



**ISSN 1605-2730**

**E-ISSN 1605-8119**

# **MATERIALS PHYSICS AND MECHANICS**

**Vol. 51, No. 1, 2023**



# MATERIALS PHYSICS AND MECHANICS

## Principal Editors:

**Alexander Belyaev**

*Institute for Problems in Mechanical Engineering  
of the Russian Academy of Science (RAS), Russia*

**Andrei Rudskoi**

*Peter the Great St.Petersburg Polytechnic University, Russia*

## Founder and Honorary Editor: Ilya Ovid'ko (1961-2017)

*Institute for Problems in Mechanical Engineering  
of the Russian Academy of Sciences (RAS), Russia*

## Associate Editor:

**Anna Kolesnikova**

*Institute for Problems in Mechanical Engineering  
of the Russian Academy of Sciences (RAS), Russia*

## Editorial Board:

**E.C. Aifantis**

*Aristotle University of Thessaloniki, Greece*

**K.E. Aifantis**

*University of Florida, USA*

**U. Balachandran**

*Argonne National Laboratory, USA*

**A. Bellosi**

*Research Institute for Ceramics Technology, Italy*

**A.K. Belyaev**

*Institute for Problems in Mechanical Engineering (RAS), Russia*

**S.V. Bobylev**

*Institute for Problems in Mechanical Engineering (RAS), Russia*

**A.I. Borovkov**

*Peter the Great St.Petersburg Polytechnic University, Russia*

**G.-M. Chow**

*National University of Singapore, Singapore*

**Yu. Estrin**

*Monash University, Australia*

**A.B. Freidin**

*Institute for Problems in Mechanical Engineering (RAS), Russia*

**Y. Gogotsi**

*Drexel University, USA*

**I.G. Goryacheva**

*Institute of Problems of Mechanics (RAS), Russia*

**D. Hui**

*University of New Orleans, USA*

**G. Kiriakidis**

*IESL/FORTH, Greece*

**D.M. Klimov**

*Institute of Problems of Mechanics (RAS), Russia*

**G.E. Kodzhaspirov**

*Peter the Great St.Petersburg Polytechnic University, Russia*

**S.A. Kukushkin**

*Institute for Problems in Mechanical Engineering (RAS), Russia*

**T.G. Langdon**

*University of Southampton, U.K.*

**V.P. Matveenko**

*Institute of Continuous Media Mechanics (RAS), Russia*

**A.I. Melker**

*Peter the Great St.Petersburg Polytechnic University, Russia*

**Yu.I. Meshcheryakov**

*Institute for Problems in Mechanical Engineering (RAS), Russia*

**N.F. Morozov**

*St.Petersburg State University, Russia*

**R.R. Mulyukov**

*Institute for Metals Superplasticity Problems (RAS), Russia*

**Yu.V. Petrov**

*St.Petersburg State University, Russia*

**N.M. Pugno**

*Politecnico di Torino, Italy*

**B.B. Rath**

*Naval Research Laboratory, USA*

**A.E. Romanov**

*Ioffe Institute (RAS), Russia*

**A.M. Sastry**

*University of Michigan, Ann Arbor, USA*

**B.A. Schrefler**

*University of Padua, Italy*

**N.V. Skiba**

*Institute for Problems in Mechanical Engineering (RAS), Russia*

**A.G. Sheinerman**

*Institute for Problems in Mechanical Engineering (RAS), Russia*

**R.Z. Valiev**

*Ufa State Aviation Technical University, Russia*

**K. Zhou**

*Nanyang Technological University, Singapore*

## "Materials Physics and Mechanics" Editorial Office:

**Phone:** +7(812)552 77 78, ext. 224 **E-mail:** mpmjournal@spbstu.ru **Web-site:** <http://www.mpm.spbstu.ru>

International scientific journal "Materials Physics and Mechanics" is published by Peter the Great St.Petersburg Polytechnic University in collaboration with Institute for Problems in Mechanical Engineering of the Russian Academy of Sciences in both hard copy and electronic versions.

The journal provides an international medium for the publication of reviews and original research papers written in English and focused on the following topics:

- Mechanics of composite and nanostructured materials.
- Physics of strength and plasticity of composite and nanostructured materials.
- Mechanics of deformation and fracture processes in conventional materials (solids).
- Physics of strength and plasticity of conventional materials (solids).
- Physics and mechanics of defects in composite, nanostructured, and conventional materials.
- Mechanics and physics of materials in coupled fields.

Owner organizations: Peter the Great St. Petersburg Polytechnic University; Institute of Problems of Mechanical Engineering RAS.

*Materials Physics and Mechanics is indexed in Chemical Abstracts, Cambridge Scientific Abstracts, Web of Science Emerging Sources Citation Index (ESCI) and Elsevier Bibliographic Databases (in particular, SCOPUS).*

© 2023, Peter the Great St. Petersburg Polytechnic University

© 2023, Institute for Problems in Mechanical Engineering RAS



# **МЕХАНИКА И ФИЗИКА МАТЕРИАЛОВ**

**Materials Physics and Mechanics**

**Том 51, номер 1, 2023 год**

Учредители:

ФГАОУ ВО «Санкт-Петербургский политехнический университет Петра Великого»  
ФГБУН «Институт проблем машиноведения Российской Академии Наук»

## Редакционная коллегия журнала

### Главные редакторы:

д.ф.-м.н., чл.-корр. РАН **А.К. Беляев**  
*Институт проблем машиноведения Российской Академии Наук (РАН)*

д.т.н., академик РАН **А.И. Рудской**  
*Санкт-Петербургский политехнический университет Петра Великого*

**Основатель и почетный редактор:** д.ф.-м.н. **И.А. Овидько (1961-2017)**  
*Институт проблем машиноведения Российской Академии Наук (РАН)*

### Ответственный редактор

д.ф.-м.н. **А.Л. Колесникова**  
*Институт проблем машиноведения Российской Академии Наук (РАН)*

### Международная редакционная коллегия:

д.ф.-м.н., проф. **А.К. Беляев**  
*Институт проблем машиноведения РАН, Россия*  
д.ф.-м.н. **С.В. Бобылев**  
*Институт проблем машиноведения РАН, Россия*  
к.т.н., проф. **А.И. Боровков**  
*Санкт-Петербургский политехнический у-т Петра Великого, Россия*  
д.ф.-м.н., проф. **Р.З. Валиев**  
*Уфимский государственный технический университет, Россия*  
д.ф.-м.н., академик РАН **И.Г. Горячева**  
*Институт проблем механики РАН, Россия*  
д.ф.-м.н., академик РАН **Д.М. Климов**  
*Институт проблем механики РАН, Россия*  
д.т.н., проф. **Г.Е. Коджаспиров**  
*Санкт-Петербургский политехнический у-т Петра Великого, Россия*  
д.ф.-м.н., проф. **С.А. Кукушкин**  
*Институт проблем машиноведения РАН, Россия*  
д.ф.-м.н., академик РАН **В.П. Матвеев**  
*Институт механики сплошных сред РАН, Россия*  
д.ф.-м.н., проф. **А.И. Мелькер**  
*Санкт-Петербургский политехнический у-т Петра Великого, Россия*  
д.ф.-м.н., проф. **Ю.И. Мещеряков**  
*Институт проблем машиноведения РАН, Россия*  
д.ф.-м.н., академик РАН **Н.Ф. Морозов**  
*Санкт-Петербургский государственный университет, Россия*  
д.ф.-м.н., чл.-корр. РАН **Р.Р. Мулюков**  
*Институт проблем сверхпластичности металлов РАН, Россия*  
д.ф.-м.н., чл.-корр. РАН **Ю.В. Петров**  
*Санкт-Петербургский государственный университет, Россия*  
д.ф.-м.н., проф. **А.Е. Романов**  
*Физико-технический институт им. А.Ф. Иоффе РАН, Россия*  
д.ф.-м.н. **Н.В. Скиба**  
*Институт проблем машиноведения РАН, Россия*  
д.ф.-м.н., проф. **А.Б. Фрейдин**  
*Институт проблем машиноведения РАН, Россия*  
д.ф.-м.н. **А.Г. Шейнман**  
*Институт проблем машиноведения РАН, Россия*

Prof., Dr. **E.C. Aifantis**  
*Aristotle University of Thessaloniki, Greece*  
Dr. **K.E. Aifantis**  
*University of Florida, USA*  
Dr. **U. Balachandran**  
*Argonne National Laboratory, USA*  
Dr. **A. Bellosi**  
*Research Institute for Ceramics Technology, Italy*  
Prof., Dr. **G.-M. Chow**  
*National University of Singapore, Singapore*  
Prof., Dr. **Yu. Estrin**  
*Monash University, Australia*  
Prof., Dr. **Y. Gogotsi**  
*Drexel University, USA*  
Prof., Dr. **D. Hui**  
*University of New Orleans, USA*  
Prof., Dr. **G. Kiriakidis**  
*IESL/FORTH, Greece*  
Prof., Dr. **T.G. Langdon**  
*University of Southampton, UK*  
Prof., Dr. **N.M. Pugno**  
*Politecnico di Torino, Italy*  
Dr. **B.B. Rath**  
*Naval Research Laboratory, USA*  
Prof., Dr. **A.M. Sastry**  
*University of Michigan, Ann Arbor, USA*  
Prof., Dr. **B.A. Schrefler**  
*University of Padua, Italy*  
Prof. Dr. **K. Zhou**  
*Nanyang Technological University, Singapore*

Тел.: +7(812)552 77 78, доб. 224 E-mail: [mpmjjournal@spbstu.ru](mailto:mpmjjournal@spbstu.ru) Web-site: <http://www.mpm.spbstu.ru>

### Тематика журнала

Международный научный журнал "Materials Physics and Mechanics" издается Санкт-Петербургским политехническим университетом Петра Великого в сотрудничестве с Институтом проблем машиноведения Российской Академии Наук в печатном виде и электронной форме. Журнал публикует обзорные и оригинальные научные статьи на английском языке по следующим тематикам:

- Механика композиционных и наноструктурированных материалов.
- Физика прочности и пластичности композиционных и наноструктурированных материалов.
- Механика процессов деформации и разрушения в традиционных материалах (твердых телах).
- Физика прочности и пластичности традиционных материалов (твердых тел).
- Физика и механика дефектов в композиционных, наноструктурированных и традиционных материалах.
- Механика и физика материалов в связанных полях.

Редколлегия принимает статьи, которые нигде ранее не опубликованы и не направлены для опубликования в другие научные издания. Все представляемые в редакцию журнала "Механика и физика материалов" статьи рецензируются. Статьи могут отправляться авторам на доработку. Не принятые к опубликованию статьи авторам не возвращаются.

Журнал "Механика и физика материалов" ("Materials Physics and Mechanics") включен в систему цитирования Web of Science Emerging Sources Citation Index (ESCI), SCOPUS и РИНЦ.

© 2023, Санкт-Петербургский политехнический университет Петра Великого  
© 2023, Институт проблем машиноведения Российской Академии Наук



## Contents

<b>Epitaxial stabilization of <math>\alpha</math>-Ga<sub>2</sub>O<sub>3</sub> layers grown on r-plane sapphire</b> V.I. Nikolaev, A.Y. Polyakov, S.I. Stepanov, A.I. Pechnikov, L.I. Guzilova, M.P. Scheglov, A.V. Chikiryaka	<b>1-9</b>
<b>Deformations properties of glassy epoxy doped with SiO<sub>2</sub> and Al<sub>2</sub>O<sub>3</sub> nanoparticles of different synthesis methods</b> V. Syzrantsev	<b>10-18</b>
<b>Effect of nickel incorporation on structural and optical properties of zinc oxide thin films deposited by RF/DC sputtering technique</b> Mohibul Khan, Md Shahbaz Alam, Sk. Faruque Ahmed	<b>19-32</b>
<b>Deformation and Heat-Insulating Characteristics of Light Concrete on Porous Burned Binder Under Heating</b> V.T. Erofeev, S.A. Korotaev, N.I. Vatin	<b>33-41</b>
<b>Wave propagation in a nonlocal rotating micropolar piezoelectric solid</b> Baljeet Singh, Asha Sangwan, Jagdish Singh	<b>42-60</b>
<b>Simulation of the plastic deformation of shape memory alloys considering shear anisotropy on the slip plane</b> F.S. Belyaev, M.E. Evard, A.E. Volkov	<b>61-67</b>
<b>On the unloading dynamics in an elastic/viscoplastic material predeformed by viscometric twisting</b> A.A. Burenin, E.A. Gerasimenko, L.V. Kovtanyuk	<b>68-83</b>
<b>Gas-abrasive wear of shut-off valves and process piping of compressor and gas distribution stations</b> O.Yu. Elagina, A.G. Buklakov, Yu.S. Dubinov, D.V. Dedok	<b>84-92</b>
<b>Diffusion-induced stresses due to an impulsive mass source under non-Fickian mass transfer models</b> M. Fayik, A.R. El-Dhaba, E. Awad	<b>93-107</b>
<b>Mechanical properties and deformation curves of the 3D-printed polycarbonate</b> I.K. Andrianov, S.I. Feoktistov	<b>108-118</b>
<b>Mechanical and microstructural characteristics of underwater friction stir welded AA 6061-T6 joints using a hybrid GRA-artificial neural network approach</b> Kiran Wakchaure, Ajaykumar Thakur	<b>119-141</b>
<b>Effect of Mechanical Properties of AL7075/Mica Powder Hybrid Metal Matrix Composite</b> K. Arunprasath, P. Amuthakkannan, M. Vijayakumar, R. Sundarakannan, M. Selwin, S. Kavitha, Lavish Kumar Singh	<b>142-150</b>

<b>Effect of compression precracking on near threshold region for AISI 4340 steels considering compliance measurements</b> Salim Çalışkan, Rıza Gürbüz	<b>151-167</b>
<b>Mechanical properties of a soil improved with recycled demolition concrete for the construction of shallow foundations</b> S.P. Munoz Perez, T.M. Salazar Pretel, L.I. Villena Zapata	<b>168-178</b>

## Epitaxial stabilization of $\alpha$ -Ga<sub>2</sub>O<sub>3</sub> layers grown on r-plane sapphire

V.I. Nikolaev<sup>1,3</sup> , A.Y. Polyakov<sup>2</sup> , S.I. Stepanov<sup>1,3</sup>, A.I. Pechnikov<sup>1,3</sup> ,

L.I. Guzilova<sup>3</sup> , M.P. Scheglov<sup>3</sup> , A.V. Chikiryaka<sup>3</sup>

<sup>1</sup> Perfect Crystals LLC, Saint Petersburg, Russia

<sup>2</sup> National University of Science and Technology MISiS, Moscow, Russia

<sup>3</sup> Ioffe Institute, Saint Petersburg, Russia

 nikolaev.v@mail.ioffe.ru

**Abstract.** In this work, we study the thermal stabilization of metastable  $\alpha$ -Ga<sub>2</sub>O<sub>3</sub> in growth experiments. Gallium oxide films are grown on c- and r-plane sapphire substrates by halide vapor phase epitaxy (HVPE) at the temperature range of 450-690 °C. The surface morphology is investigated by scanning electron microscopy. The structural quality and phase composition of the grown films is studied by X-ray diffraction. It is found that the use of r-plane sapphire substrates prevents the formation of the orthorhombic  $\kappa$ -Ga<sub>2</sub>O<sub>3</sub> and monoclinic  $\beta$ -Ga<sub>2</sub>O<sub>3</sub> and thus extends the growth process window for the deposition of the rhombohedral  $\alpha$ -phase of gallium oxide.

**Keywords:** gallium oxide, HVPE, epitaxial layers, c-plane and r-plane sapphire substrates

**Acknowledgements.** The research was supported by Russian Science Foundation, Grant No. 19-19-00409.

**Citation:** Nikolaev VI, Polyakov AY, Stepanov SI, Pechnikov AI, Guzilova LI, Scheglov MP, Chikiryaka AV. Epitaxial stabilization of  $\alpha$ -Ga<sub>2</sub>O<sub>3</sub> layers grown on r-plane sapphire. *Materials Physics and Mechanics*. 2023;51(1): 1-9. DOI: 10.18149/MPM.5112023\_1.

### Introduction

Gallium oxide is a prospective ultra-wideband gap semiconductor having a bandgap of about 5 eV. It has gained considerable interest recently for applications in high-power electronics, chemical sensors, and ultraviolet detectors [1]. Ga<sub>2</sub>O<sub>3</sub> exists in many polymorphic forms denoted as monoclinic  $\beta$ , corundum  $\alpha$ , defective spinel  $\gamma$ , orthorhombic (hexagonal)  $\kappa(\epsilon)$ , and bixbyite  $\delta$  polymorphs. In some early studies, the  $\epsilon$ -phase was erroneously ascribed to a hexagonal P63mc space group. However, more recent studies revealed that the  $\epsilon$ -phase actually consists of nanoscale domains of the orthorhombic structure rotated 120° relatively to each other [2]. The  $\beta$ -Ga<sub>2</sub>O<sub>3</sub> polymorph is the most stable form and can be obtained by melt crystallization. However, the low symmetry of the monoclinic structure presents evident drawbacks for device applications.

Besides the monoclinic polymorph, other crystal forms of Ga<sub>2</sub>O<sub>3</sub> such as the orthorhombic  $\kappa$ -phase and the rhombohedral corundum  $\alpha$ -phase have attracted considerable interest due to their unique physical properties. The  $\kappa$ -phase has large spontaneous polarization which can be used to generate high-density two-dimensional electron gas. Among other polymorphs,  $\alpha$ -Ga<sub>2</sub>O<sub>3</sub> has the widest bandgap of 5.3 eV and is isostructural to sapphire substrates. Epitaxial stabilization can be used as an effective tool for the growth of metastable polymorphs of Ga<sub>2</sub>O<sub>3</sub>. Metastable polymorphs can be grown by epitaxial methods on foreign



substrates. In most papers, *c*-plane sapphire was used as a substrate for the Ga<sub>2</sub>O<sub>3</sub> growth, and only a few reports used *a*, *r*, and *m*-plane sapphire as the substrate.

The stability of  $\alpha$ -Ga<sub>2</sub>O<sub>3</sub> epitaxial films on sapphire substrates is governed by a large number of factors. On one hand,  $\alpha$ -Ga<sub>2</sub>O<sub>3</sub> is the best lattice-matched polymorph and has the same corundum structure as sapphire. The lattice mismatches between  $\alpha$ -Ga<sub>2</sub>O<sub>3</sub> and  $\alpha$ -Al<sub>2</sub>O<sub>3</sub> (sapphire) are only 4.81% and 3.54% in the *a*- and *c*-axis directions. For that reason,  $\alpha$ -phase can be energetically more preferable to other polymorphs when grown epitaxially on sapphire substrates. On the other hand, the thermal stability of  $\alpha$ -Ga<sub>2</sub>O<sub>3</sub> is less than that of  $\kappa$ -Ga<sub>2</sub>O<sub>3</sub> and  $\beta$ -Ga<sub>2</sub>O<sub>3</sub>. In the temperature range of 600–650 °C, all three phases can coexist and compete with each other.

In the previous studies, pressure, temperature, substrate type and orientation, gallium and oxygen precursors, additional hydrogen chloride flow, and doping with tin, silicon, and boron have been identified as the main factors which determine the preferential nucleation of one or another phase.

It has been observed by many authors that the growth of phase pure  $\alpha$ -Ga<sub>2</sub>O<sub>3</sub> on sapphire substrates is limited by the film thicknesses. High-resolution transmission electron microscopy studies revealed that independent of the growth method a few-monolayer thick  $\alpha$ -Ga<sub>2</sub>O<sub>3</sub> can be stabilized by strain during the growth of Ga<sub>2</sub>O<sub>3</sub> on *c*-plane sapphire [3]. For thicker layers, the  $\alpha$ -phase transforms to  $\beta$ -phase due to a large in-plane lattice mismatch between  $\alpha$ -Ga<sub>2</sub>O<sub>3</sub> and the sapphire substrate.

The thermal stability of  $\alpha$ -(Al<sub>x</sub>Ga<sub>1-x</sub>)<sub>2</sub>O<sub>3</sub> is expected to be higher than that of pure  $\alpha$ -Ga<sub>2</sub>O<sub>3</sub> because  $\alpha$ -phase is the stable polymorph of Al<sub>2</sub>O<sub>3</sub>. Surprisingly, even a small Al doping is sufficient to increase the growth temperature and resistance to thermal annealing. According to Lee *et al.*, slight doping with Al (1–2.5%) allows the growth at higher temperatures (e.g. 50–150 °C higher) without the marked appearance of the  $\beta$ -phase and enhances thermal stability for successive thermal treatments [4].

Several research groups reported that the Sn doping growth could facilitate the preferential growth of the  $\kappa$ -phase [5–7]. This phenomenon was observed with MBE, PLD, and mist-CVD. Kang *et al.* investigated the Sn-induced phase stabilization of  $\kappa$ -Ga<sub>2</sub>O<sub>3</sub> and the thermal stability of the films grown by mist chemical vapor deposition [7]. They found that Sn doping promotes the  $\kappa$ -phase even under low temperature (*T<sub>g</sub>* = 450 °C) growth conditions that strongly favor the  $\alpha$ -phase. The post-growth annealing tests at 800–1000 °C showed that the thermal stability of the  $\kappa$ -phase also depends on the Sn concentration. The higher the Sn concentration, the more stable the phase. The one with the highest Sn content showed no phase transition from  $\kappa$  to  $\beta$  after annealing at 800 °C, 900 °C, and 1000 °C for 30 min each. The exact mechanism of the Sn-induced phase stabilization of  $\kappa$ -Ga<sub>2</sub>O<sub>3</sub> remains elusive.

The addition of boron stabilizes the MOVPE growth of the  $\alpha$ -phase on *c*-, *a*-, and *r*-plane sapphire substrates [8]. A preferred growth of the  $\alpha$ -phase without boron addition could only be observed on *r*-plane Al<sub>2</sub>O<sub>3</sub>. While most of the growths of  $\alpha$ -Ga<sub>2</sub>O<sub>3</sub> thin films have been investigated on *c*-plane sapphire substrates, there are a few publications of  $\alpha$ -Ga<sub>2</sub>O<sub>3</sub> on sapphire substrates of other orientations.

Cheng *et al.* systematically investigated the differences of  $\alpha$ -Ga<sub>2</sub>O<sub>3</sub> films grown on *a*-, *c*-, and *r*-plane sapphire substrates using the mist-CVD method [9]. They reported that the quality of *c*-plane  $\alpha$ -Ga<sub>2</sub>O<sub>3</sub> films is better than both *a*-plane and *r*-plane epilayers, corresponding to the results of XRD 2 $\theta$  scans and optical absorption. They claimed to have a higher growth rate on the *c*-plane (11.44 nm/min) than on the *a*- and *r*-plane sapphire (5.74 and 5.26 nm/min).

Oshima *et al.* reported the growth of ten-period binary  $\alpha$ -Al<sub>2</sub>O<sub>3</sub>/Ga<sub>2</sub>O<sub>3</sub> superlattices on *r*-plane sapphire substrates by plasma-assisted molecular beam epitaxy [10]. The superlattice with  $\alpha$ -Ga<sub>2</sub>O<sub>3</sub> thickness up to >1 nm had coherent interfaces without misfit dislocation despite

the large lattice mismatches.

Hu *et al.* studied the growth of Ga<sub>2</sub>O<sub>3</sub> thin films on various oriented (*c*-, *a*-, *m*-, *r*-plane) sapphire substrates by plasma-enhanced chemical vapor deposition (PECVD) is investigated using high-purity metallic Ga and oxygen (O<sub>2</sub>) as precursor materials and argon (Ar) as carrier gas. The film grown on the *c*-plane sapphire substrates exhibits the  $\beta$ -phase with a preferred growth plane of ( $\bar{2}01$ ), while these grown on the *m*- and *r*-planes are amorphous.

The achievable film thickness of phase pure  $\alpha$ -Ga<sub>2</sub>O<sub>3</sub> is limited by the formation of *c*-plane facets on the  $\alpha$ -Ga<sub>2</sub>O<sub>3</sub> surface.

Phase stabilization of  $\alpha$ -Ga<sub>2</sub>O<sub>3</sub> on *r*-plane sapphire was studied by Kracht *et al.* who observed no indication for  $\beta$ -Ga<sub>2</sub>O<sub>3</sub> in  $\alpha$ -Ga<sub>2</sub>O<sub>3</sub> layers on *r*-plane sapphire with a thickness up to 117 nm thickness [11]. This layer thickness is much higher than the values reported for MBE growth on the *a* and *c* planes, respectively. If growth time is further extended the nucleation of  $\beta$ -Ga<sub>2</sub>O<sub>3</sub> on *c*-plane facets that are increasingly exposed during the growth of  $\alpha$ -Ga<sub>2</sub>O<sub>3</sub> is observed.

Here, we investigate the effect of substrate temperature on the growth in the  $\alpha$ -Ga<sub>2</sub>O<sub>3</sub> on *c*- and *r*-plane sapphire substrates.

## Experiment

Ga<sub>2</sub>O<sub>3</sub> films were grown by HVPE on (0001) *c*-plane and (10 $\bar{1}2$ ) *r*-plane single-side polished sapphire substrate of 400  $\mu$ m thickness. Oxygen gas (O<sub>2</sub>) and gallium chloride (GaCl) were used as precursors with argon (Ar) used as a carrier gas. The GaCl vapor was synthesized *in situ* through the chemical reaction between metallic gallium and gaseous hydrogen chloride upstream in the reactor. The growth of the Ga<sub>2</sub>O<sub>3</sub> films was performed at temperatures varying from 450 °C to 690 °C and a fixed O/Ga mole flow ratio of 4.2. The growth rate varied from 1.7 to 6.9  $\mu$ m/hr. The overall thickness of the films was 1-5  $\mu$ m. A more detailed description of the epitaxial growth procedures can be found in our earlier papers [12-14].

The phase composition and crystal structure of the produced Ga<sub>2</sub>O<sub>3</sub> films were investigated by X-ray diffraction (XRD). The surface morphology and the cross-section of the films were studied by scanning electron microscopy (SEM).

## Results and discussion

The comparison of the surface morphology for different samples was performed by SEM imaging (Fig. 1,2). Compared to specimens grown on *r*-plane sapphire, Ga<sub>2</sub>O<sub>3</sub> films grown on *c*-plane substrates exhibit flatter surface morphology. This tendency becomes even more pronounced at higher growth temperatures. For example, it can be seen that Ga<sub>2</sub>O<sub>3</sub> grown on *c*-plane sapphire at 670 °C forms a continuous film. Most of the film is composed of oriented crystal blocks of 120° symmetry, a few crystallites with hexagonal symmetry can be also observed. In contrast, the specimen grown on *r*-plane sapphire is clearly polycrystalline composed of agglomerated prismatic crystallites of various orientations. The observed crystal habit is typical for the monoclinic polymorph.

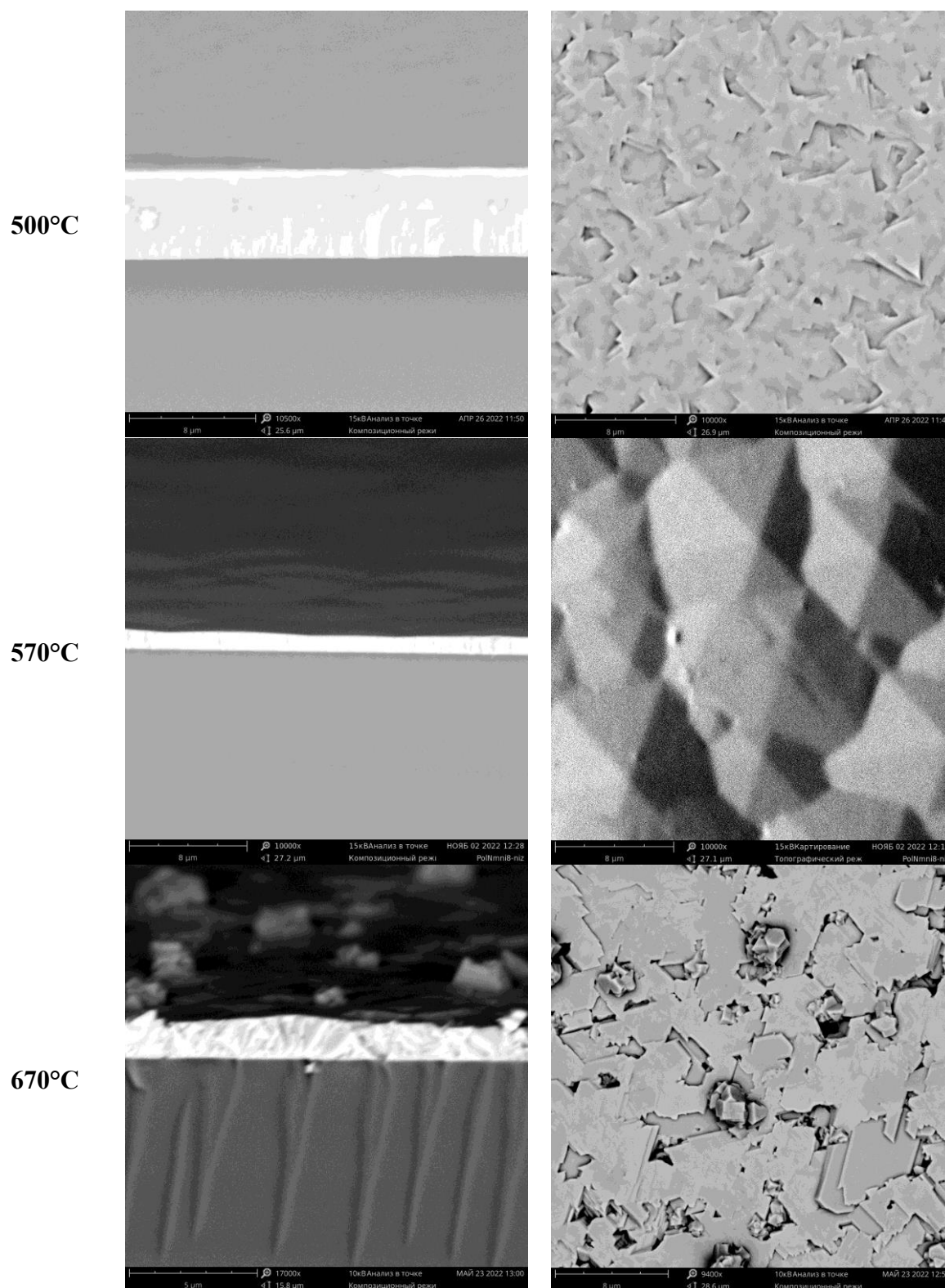
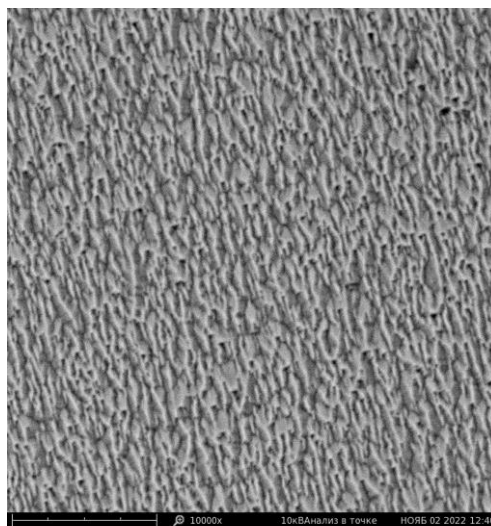
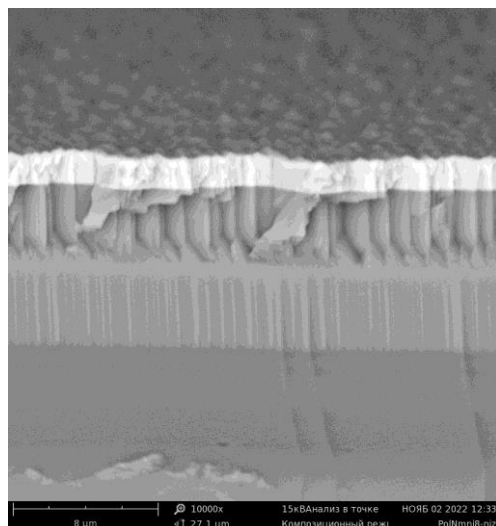


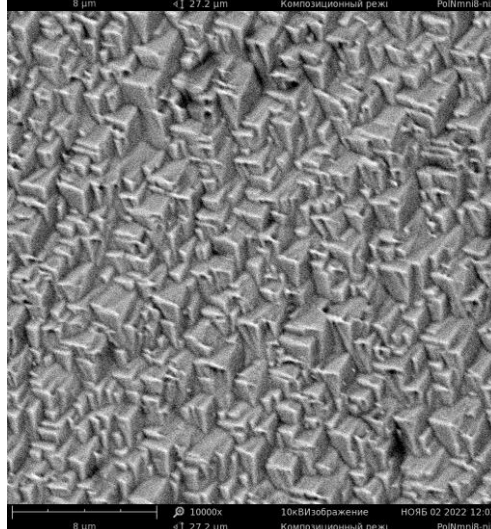
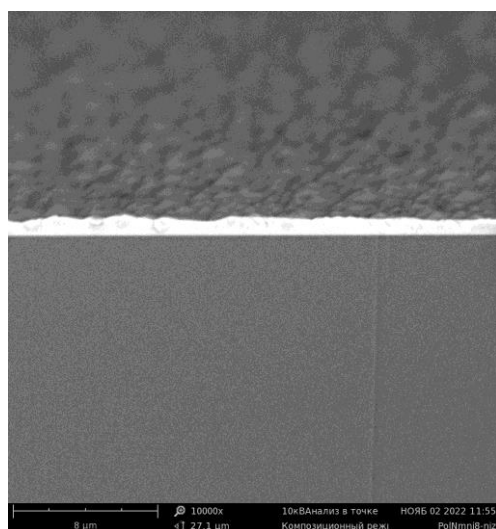
**Fig. 1.** Cross-sectional and plan view SEM images for  $\text{Ga}_2\text{O}_3$  layers on c-plane sapphire at different temperatures



500°C



570°C



670°C

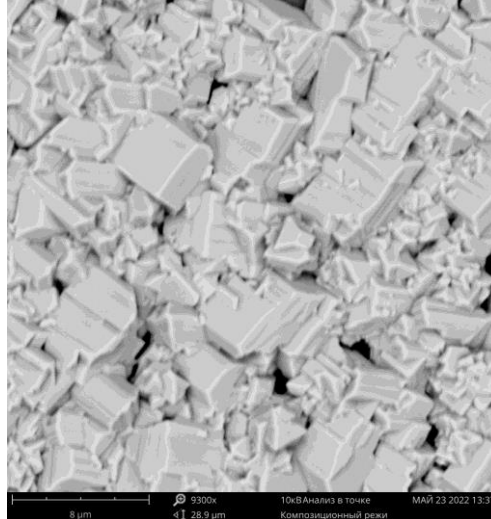
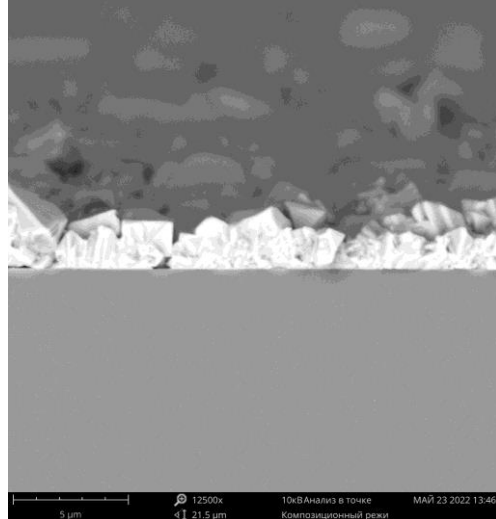


**Fig. 2.** Cross-sectional and plan view SEM images for Ga<sub>2</sub>O<sub>3</sub> layers on r-plane sapphire at different temperatures

The XRD  $\omega$ – $2\theta$  scans of  $\text{Ga}_2\text{O}_3$  films grown on *c*-plane sapphire at different temperatures are shown in Fig. 3. All XRD spectra show reflexes from the sapphire substrate that can be indexed as 0006 at  $2\theta \approx 41.65^\circ$  and 00012 at  $2\theta \approx 90.85^\circ$ . The other two well-pronounced diffraction peaks can be assigned to the 0006 and 00012 reflections of  $\alpha$ - $\text{Ga}_2\text{O}_3$ . The specimens grown at temperatures below  $530^\circ\text{C}$  showed diffraction peaks which can be assigned to 004 and 006 reflections of  $\kappa$ - $\text{Ga}_2\text{O}_3$ . The specimens grown at higher temperatures exhibit  $\beta$ - $\text{Ga}_2\text{O}_3$  peaks that can be indexed as 402 at  $2\theta \approx 38^\circ$ , 603 at  $2\theta \approx 59^\circ$  and 804 at  $2\theta \approx 82^\circ$ . Interestingly, the intensity of diffraction peak related to  $\kappa$ - $\text{Ga}_2\text{O}_3$  decrease with increasing temperature, on the contrary, the intensity of  $\beta$ - $\text{Ga}_2\text{O}_3$  diffraction peaks increases as the growth temperature increases. The XRD pattern from the specimen grown at  $670^\circ\text{C}$  also shows a variety of minor peaks which can be attributed to  $\beta$ - $\text{Ga}_2\text{O}_3$  phase. The growth temperature is a key factor in controlling the balance between  $\alpha$ ,  $\beta$ , and  $\kappa$  phases. Under the given growth conditions, the HVPE deposition of  $\alpha$ - $\text{Ga}_2\text{O}_3$  on *c*-plane sapphire substrates is possible only within a very narrow temperature window at about  $530^\circ\text{C}$ . It can be speculated that low growth temperature conditions result in  $\kappa$ - $\text{Ga}_2\text{O}_3$  because this phase has a smaller lattice mismatch with *c*-plane sapphire. On the other hand, at a higher temperature, the diffusion length is longer, and atoms reach the step edges. Therefore, the formation of the  $\alpha$ - $\text{Ga}_2\text{O}_3$  phase which has the same structure as the sapphire substrate becomes energetically more favorable.

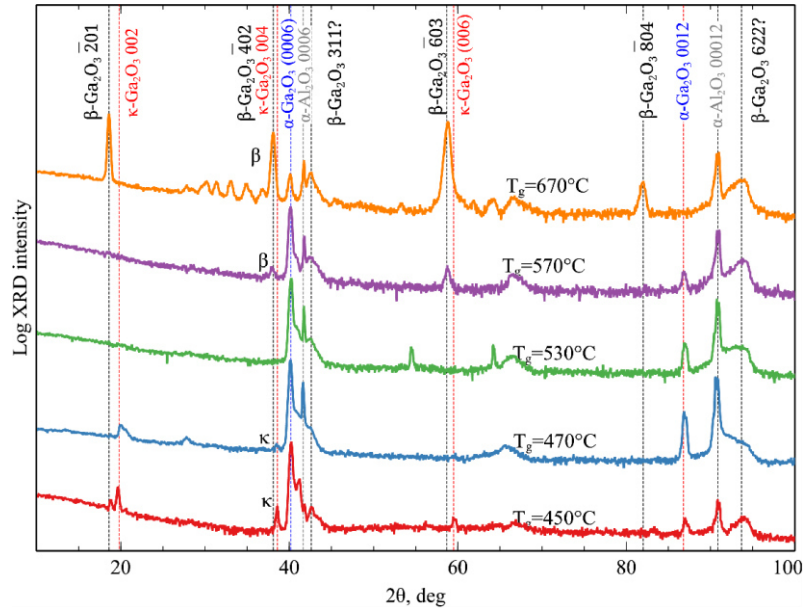


**Fig. 3.** Symmetrical  $\omega$ – $2\theta$  XRD scans of  $\text{Ga}_2\text{O}_3$  epilayers grown on *c*-plane sapphire substrates at different growth temperatures

The upper-temperature limit is in line with previous publications, as metastable  $\alpha$ - $\text{Ga}_2\text{O}_3$  has the propensity to revert to the stable  $\beta$ -phase upon heating. The transition temperature to the  $\beta$ -phase is from  $600^\circ\text{C}$  to  $650^\circ\text{C}$  and depends on the film thickness. As reported by Lee et al.,  $\alpha$ - $\text{Ga}_2\text{O}_3$  films thicker than  $1\ \mu\text{m}$  on *c*-plane sapphire substrates remained  $\alpha$ -phase upon annealing up to  $550^\circ\text{C}$  but gradually changed to  $\beta$ -phase at a temperature higher than  $600^\circ\text{C}$  [15]. The phase stability of  $\alpha$ - $\text{Ga}_2\text{O}_3$  on *c*-plane sapphire can be enhanced by decreasing the film thickness. According to Jinno *et al.*, an  $\alpha$ - $\text{Ga}_2\text{O}_3$  film around  $20\ \text{nm}$  thick maintained the corundum structure at an annealing temperature of  $750^\circ\text{C}$  [16].

On the other hand, the lower temperature limit defined by the formation of the  $\kappa$ -phase is apparently of a less fundamental nature and is related to the particular features of the employed

growth technique. For example, mist-CVD shows the opposite trend where the low-temperature growth (<550 °C) favors the formation of  $\alpha$ -Ga<sub>2</sub>O<sub>3</sub>, while higher temperatures result in the deposition of  $\kappa$ -Ga<sub>2</sub>O<sub>3</sub> films. A similar trend has been reported for the HVPE technique, where deposition at a relatively high temperature ( $T_g = 650$  °C) resulted in  $\kappa$ -Ga<sub>2</sub>O<sub>3</sub> [17]. On the other hand, Son *et al.* Reported that the growth at 470–650 °C resulted in preferentially  $\alpha$ -phase epilayers, while the deposition at 450 °C produced a mixture of  $\alpha$ - and  $\kappa$ -Ga<sub>2</sub>O<sub>3</sub> polymorphs [18]. In the case of the MOCVD technique, the balance between  $\alpha$  and  $\kappa$  polymorphs is governed not solely by temperature, but by multiple factors. Typically, MOCVD growth at low temperatures (550 °C) results in polycrystalline Ga<sub>2</sub>O<sub>3</sub> because precursors do not have sufficient energy to form crystalline Ga<sub>2</sub>O<sub>3</sub> film.

Figure 4 presents XRD  $\omega$ -2 $\theta$  scans of Ga<sub>2</sub>O<sub>3</sub> films grown on *r*-plane sapphire at different temperatures. The specimens grown in the temperature range 450 °C – 650 °C showed only 1012, 2024, and 3036 reflexes of the *r*-plane  $\alpha$ -Al<sub>2</sub>O<sub>3</sub> and  $\alpha$ -Ga<sub>2</sub>O<sub>3</sub>. Therefore, the film is composed mainly of the (1012)-oriented  $\alpha$ -Ga<sub>2</sub>O<sub>3</sub> phase, with little or no detectable admixture of other polymorphic phases.

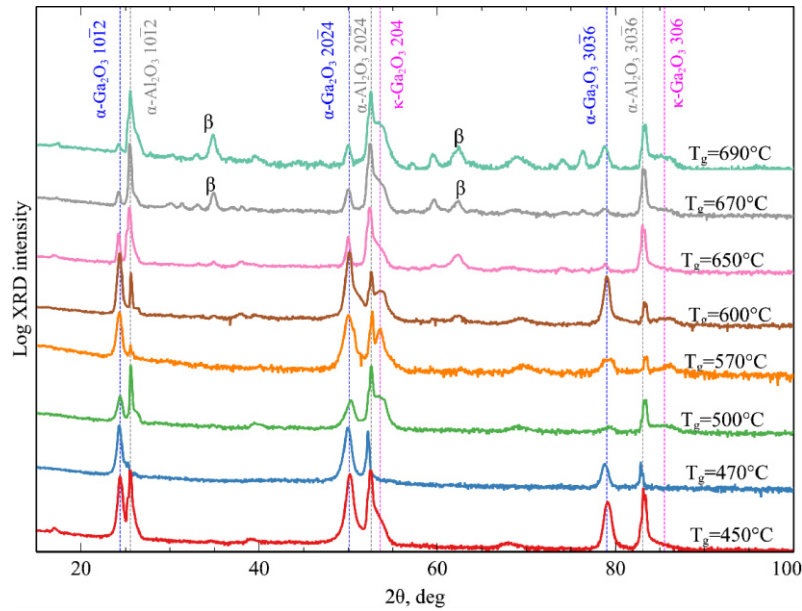


**Fig. 4.** Symmetrical  $\omega$ -2 $\theta$  XRD scans of Ga<sub>2</sub>O<sub>3</sub> epilayers grown on *r*-plane sapphire substrates at different growth temperatures

It should be noted that the growth of  $\alpha$ -Ga<sub>2</sub>O<sub>3</sub> layers on the *r*-plane of sapphire is characterized by a much wider temperature process window. First, in contrast to the Ga<sub>2</sub>O<sub>3</sub> films on the *c*-plane sapphire, specimens on the *r*-plane do not exhibit the inclusion of the  $\kappa$ -phase. Secondly, the upper temperature limit which is marked by the onset of the  $\beta$ -phase formation is increased from 570 °C to 670 °C.

## Conclusion

In summary, the HVPE growth of Ga<sub>2</sub>O<sub>3</sub> on *c* and *r*-plane sapphire substrates has been studied. We show that the use of *r*-plane sapphire substrates facilitates the growth of phase-pure  $\alpha$ -Ga<sub>2</sub>O<sub>3</sub> films. At low temperatures, Ga<sub>2</sub>O<sub>3</sub> films grown on *r*-plane sapphire do not exhibit an inclusion of the  $\kappa$ -phase. At high temperatures, up to about 700 °C the use of *r*-plane sapphire substrates prevents the thermal decomposition of the  $\alpha$ -Ga<sub>2</sub>O<sub>3</sub> and its transformation into  $\beta$ -Ga<sub>2</sub>O<sub>3</sub>.



## References

1. Biswas M, Nishinaka H. Thermodynamically metastable  $\alpha$ -,  $\epsilon$ - (or  $\kappa$ -), and  $\gamma$ -Ga<sub>2</sub>O<sub>3</sub>: From material growth to device applications. *APL Mater.* 2022;10(6): 060701.
2. Cora I, Mezzadri F, Boschi F, Bosi M, Čaplovičová M, Calestani G, Dódoni I, Pécz B, Fornari R. The real structure of  $\epsilon$ -Ga<sub>2</sub>O<sub>3</sub> and its relation to  $\kappa$ -phase. *CrystEngComm.* 2017;19(11): 1509-1516.
3. Schewski R, Wagner G, Baldini M, Gogova D, Galazka Z, Schulz T, Remmele T, Markurt T, von Wenckstern H, Grundmann M, Bierwagen O, Vogt P, Albrecht M. Epitaxial stabilization of pseudomorphic  $\alpha$ -Ga<sub>2</sub>O<sub>3</sub> on sapphire (0001). *Appl. Phys. Express.* 2015;8(1): 011101.
4. Lee SD, Ito Y, Kaneko K, Fujita S. Enhanced thermal stability of alpha gallium oxide films supported by aluminum doping. *Jpn. J. Appl. Phys.* 2015;54(3): 030301.
5. Kneiß M, Hassa A, Splith D, Sturm C, von Wenckstern H, Schultz T, Koch N, Lorenz V, Grundmann M. Tin-assisted heteroepitaxial PLD-growth of  $\kappa$ -Ga<sub>2</sub>O<sub>3</sub> thin films with high crystalline quality. *APL Mater.* 2019;7(2): 022516.
6. Kracht M, Karg A, Schörmann J, Weinhold M, Zink D, Michel F, Rohnke M, Schowalter M, Gerken B, Rosenauer A, Klar PJ, Janek J, Eickhoff M. Tin-Assisted Synthesis of  $\epsilon$ -Ga<sub>2</sub>O<sub>3</sub> by Molecular Beam Epitaxy. *Phys. Rev. Appl.* 2017;8(5): 054002.
7. Kang HY, Kang H, Lee E, Lee GR, Chung RBK. Sn-Induced Phase Stabilization and Enhanced Thermal Stability of  $\kappa$ -Ga<sub>2</sub>O<sub>3</sub> Grown by Mist Chemical Vapor Deposition. *ACS Omega.* 2021;6(46): 31292–31298.
8. Gottschalch V, Merker S, Blaurock S, Kneiß M, Teschner U, Grundmann M, Krautscheid H. Heteroepitaxial growth of  $\alpha$ -,  $\beta$ -,  $\gamma$ - and  $\kappa$ -Ga<sub>2</sub>O<sub>3</sub> phases by metalorganic vapor phase epitaxy. *J. Cryst. Growth.* 2019;510: 76–84.
9. Cheng Y, Xu Y, Li Z, Zhang J, Chen D, Feng Q, Xu S, Zhou H, Zhang J, Hao Y, Zhang C. Heteroepitaxial growth of  $\alpha$ -Ga<sub>2</sub>O<sub>3</sub> thin films on a-, c- and r-plane sapphire substrates by low-cost mist-CVD method. *J. Alloys Compd.* 2020;831: 154776.
10. Oshima T, Kato Y, Imura M, Nakayama Y, Takeguchi M.  $\alpha$ -Al<sub>2</sub>O<sub>3</sub>/Ga<sub>2</sub>O<sub>3</sub> superlattices coherently grown on r -plane sapphire. *Appl. Phys. Express.* 2018;11(6): 065501.
11. Kracht M, Karg A, Feneberg M, Bläsing J, Schörmann J, Goldhahn, R, Eickhoff M. Anisotropic Optical Properties of Metastable (0112)  $\alpha$ -Ga<sub>2</sub>O<sub>3</sub> Grown by Plasma-Assisted Molecular Beam Epitaxy. *Phys. Rev. Appl.* 2018;10(2): 024047.
12. Nikolaev VI, Stepanov SI, Pechnikov AI, Shapenkov SV, Scheglov MP, Chikiryaka AV, Vyvenko OF. HVPE Growth and Characterization of  $\epsilon$ -Ga<sub>2</sub>O<sub>3</sub> Films on Various Substrates. *ECS J. Solid State Sci. Technol.* 2020;9(4): 045014.
13. Pechnikov AI, Stepanov SI, Chikiryaka AV, Scheglov MP, Odnobludov MA, Nikolaev VI, Thick  $\alpha$ -Ga<sub>2</sub>O<sub>3</sub> Layers on Sapphire Substrates Grown by Halide Epitaxy. *Semiconductors.* 2019;53(6): 780–783.
14. Stepanov SI, Nikolaev VI, Almaev AV, Pechnikov AI, Scheglov MP, Chikiryaka AV, Kushnarev BO, Polyakov AY. HVPE growth of corundum-structured  $\alpha$ -Ga<sub>2</sub>O<sub>3</sub> on sapphire substrates with  $\alpha$ -Cr<sub>2</sub>O<sub>3</sub> buffer layer. *Materials Physics and Mechanics.* 2021;47(4): 577-581.
15. Lee S, Akaiwa K, Fujita S. Thermal stability of single crystalline alpha gallium oxide films on sapphire substrates. *Phys. Status Solidi C.* 2013;10(11): 1592–1595.
16. Jinno R, Kaneko K, Fujita S. Thermal stability of  $\alpha$ -Ga<sub>2</sub>O<sub>3</sub> films grown on c-plane sapphire substrates via mist-CVD. *AIP Adv.* 2020;10(11): 115013.
17. Bosi M, Mazzolini P, Seravalli L, Fornari R. Ga<sub>2</sub>O<sub>3</sub> polymorphs: tailoring the epitaxial growth conditions. *J. Mater. Chem. C.* 2020;8(32): 10975–10992.
18. Son H, Jeon DW. Optimization of the growth temperature of  $\alpha$ -Ga<sub>2</sub>O<sub>3</sub> epilayers grown by halide vapor phase epitaxy. *J. Alloys Compd.* 2019;773: 631–635.

## THE AUTHORS

**V.I. Nikolaev** 

e-mail: nikolaev.v@mail.ioffe.ru

**S.I. Stepanov**

e-mail: s.i.stepanov@gmail.com

**Guzilova L.I.** 

e-mail: guzilova@mail.ioffe.ru

**A.V. Chikiryaka**

e-mail: chikiryaka@mail.ru

**A.Y. Polyakov** 

e-mail: aypolyakov@gmail.com

**A.I. Pechnikov** 


e-mail: alpechn@yahoo.com

**M.P. Scheglov** 

e-mail: m.scheglov@mail.ioffe.ru

## Deformations properties of glassy epoxy doped with SiO<sub>2</sub> and Al<sub>2</sub>O<sub>3</sub> nanoparticles of different synthesis methods

V. Syzrantsev 

Grozny State Oil Technical University named after Academician M.D. Millionshchikov,  
Chechen Republic, Grozny, Russia  
 [vvveliga@mail.ru](mailto:vvveliga@mail.ru)

**Abstract.** The variation in the deformation properties of epoxy polymers doped with of SiO<sub>2</sub> and Al<sub>2</sub>O<sub>3</sub> nanoparticles obtained by four different methods was experimentally investigated. It was shown that the doping of nanoparticles leads to structural changes in the polymer similar to the effect of plasticization (an increase in the mobility of the polymer chain). The variation of the types of nanoparticles contained in the composite significantly changes the process of the kinetics of microindentation stress relaxation. In particular, the complete recovery from microindentation (healing of the indentation) occurs at different concentrations by varying the method of nanoparticle synthesis.

**Keywords:** Microindentation, thermally stimulated relaxation, delocalization, epoxy polymer, nanoparticles

**Citation:** Syzrantsev V. Deformations properties of glassy epoxy doped with SiO<sub>2</sub> and Al<sub>2</sub>O<sub>3</sub> nanoparticles of different synthesis methods. *Materials Physics and Mechanics*. 2023;51(1): 10-18. DOI: 10.18149/MPM.5112023\_2.

### Introduction

Polymers are currently used in many industries, including biomedicine, batteries, ceramics, composites, magnetism, electronics packaging, solid fuels, and adhesives [1,2]. The inclusion of various fillers [3,4] can significantly change such properties as mechanical strength [5,6], thermal [7] and electrical conductivity [8], thermal stability [9], magnetic characteristics [10,11], and other properties.

Based on polymers, in particular epoxy-polymer materials, composite materials are formed with granular fillers, dyes, or other additives that give the material specific properties. The properties of such composites depend on the size, shape, and nature of the particles, the interaction between their components, and the distribution of particles in the matrix [12,13]. Epoxy resins have a cross-linked structure; they have covalent bonds linking polymer chains together. In addition to them, the presence of other types of molecular interactions, such as hydrogen bonding, can also affect the properties of the epoxy resin [14].

Under mechanical stresses exceeding the yield pressure (plastic yield), in silicate and other inorganic glasses, plastic inelastic deformations occur, which can persist for a long time after the external pressure is removed. However, when the material is heated below the glass transition temperature (T<sub>g</sub>), this deformation is restored to its original undeformed state. That is, it exhibits the behavior of reversible viscoelastic deformation [15-17].

Similar behavior is found in many amorphous polymers. After pressure is removed at room temperature, the deformation persists and is visually indistinguishable from residual plastic deformation. However, when heated below T<sub>g</sub>, the deformed polymer returns to the



undeformed state [18-20], similar to inorganic glasses [21]. Consequently, the effect of plasticity turns out to be a universal property of such glassy materials.

Previously, it was assumed that a large "residual" deformation of amorphous polymers in the glassy state is fixed since thermal motion at room temperature is not enough to return distorted-chain macromolecules to their original state. Only during heating, when the intensity of thermal motion is high enough to give sufficient mobility to flexible macromolecules, can stress be relieved. Since this phenomenon also manifests itself in low molecular weight inorganic and metallic glasses, where chain macromolecules are absent, the "polymeric" approach to the nature of this deformation should be reconsidered.

Paper [19] developed an idea that a new structure arises in a region that is plastically deformed and subsequently relaxed as a result of thermal action; it is a structure different from the original one. The main carriers of these processes are local microshears, which appear under the action of external loads and disappear upon heating.

In the explanation given in [22], great importance was attached to the appearance of an interface in a deformable structure and the "healing" of interfacial boundaries during thermally stimulated strain relaxation. The elementary act of "plastic" deformation of glass was reduced to the displacement of the link from the equilibrium position associated with the rearrangement of the neighboring particles. In particular, in inorganic glass, this refers to the displacement of the bridge oxygen atom in the Si-O-Si bridging group, which leads to local deformations in the network of amorphous filaments. The process of delocalization of atoms in amorphous polymers corresponds to the displacement of a small portion of the main chain of the macromolecule (the main group of atoms in the crosslink) from its equilibrium position and is associated with the local deformation of intermolecular bonds [23,24]. An analysis of the recovery curves for the residual deformation of glasses during heating provides useful information both from a purely scientific and practical point of view.

The main role of a dispersed filler is to create an additional force that prevents the displacement of the macromolecule chain fragments. The feature of nanoparticles is that their surface has a significant number of active sites, which depend on the conditions and method of particle synthesis. The presence and strength of the active sites of the filler surface play a decisive role here since the active sites resist indentation and contribute to the healing of cracks. Strengthening effects can be observed when using the same nanoparticles in combination with different matrices or different nanoparticles with the same matrix. It was shown that different synthesis methods form nanoparticle surfaces with different properties while maintaining the phase composition of the material [25,26]. The relationship between the types of surface sites, their strength, and the interaction of nanoparticles with a dispersion medium was also shown. In particular, there was a significant difference in the strength of the active sites for the studied samples, which was reflected in the rheology of nanofluids based on epoxy resin and water.

## Materials and methods of experiment

Table 1 lists the properties of the nanoparticles used.

To study the kinetics of deformation, an industrial epoxy resin ED-20 (PolyMax (Russia)) was used. After doping nanoparticles into it, the suspension was subjected to ultrasonic treatment for 30 minutes in an ultrasonic bath Sapphire (Russia) as a measure for particle deagglomeration. After that, the PEPA hardener was added in a ratio of 1:10 to the resin weight. The mixtures were then poured into molds lightly lubricated with silicone grease. Curing took place within 24 hours at room temperature. ED-20 is a commercial cross-linked polymer in a glassy state at room temperature ( $T_g \approx 80^\circ\text{C}$ ) [14]. For microscopic analysis, it was cut into pieces  $10 \times 10 \times 3$  mm in size and additionally polished. Ten samples were prepared and tested for each concentration.

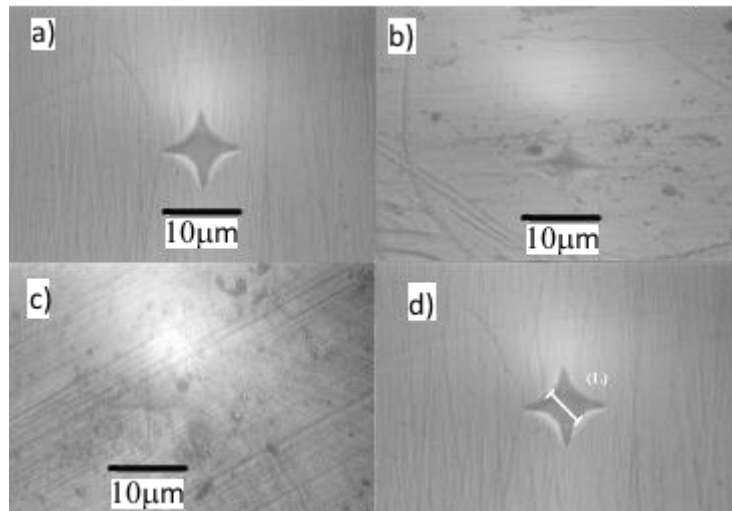
**Table 1.** Samples under study

Sample	Origin	Producer	Average particle diameter, nm
Aluminum oxide			
Aa	Flame hydrolysis of a mixture of aluminum chloride, hydrogen, and air	Evonik Industries AG, (Germany)	27.7
Ta	Evaporation of material by an electron beam	Bardakhanov LLC, (Russia)	34.3
La	Liquid phase synthesis	Nanjing XFNANO Materials Tech Co., (China)	27.2
Ea	Electric explosion of a thin wire in an argon atmosphere	Advanced powder technologies LLC, (Russia)	64.3
Silicon dioxide			
As	Flame hydrolysis of high-purity $\text{SiCl}_4$	Evonik Industries AG, (Germany)	22.7
Ts	Evaporation of material by an electron beam	Bardakhanov LLC, (Russia)	28.2
Ls	Liquid phase synthesis	Nanjing XFNANO Materials Tech Co., (China)	24.3
Ps	Plasma-chemical synthesis in arc plasma	Plasmotherm, (Russia)	23.8

The samples were subjected to microindentation and visualization on an HVS-1000A microhardness tester with a Vickers quadrangular diamond pyramid (apex angle 136 degrees). The samples were indented with a load of 1.96 N (200 g) for 20 s. After indentation, the samples were placed on a hot plate (the indentation surface was in contact with the hot plate) at a given temperature for a given period of time, and then photographed again. The temperatures used were 20, 60, 70, 75, and 80°C. At temperatures above 80°C, the samples began to break down.

When microindentation is performed on a sample at room temperature, a square imprint with concave sides is formed (Figs. 1(a), 1(d)). However, for current samples with some elasticity, when the indenter is removed, part of the samples returns to the space occupied by the indenter resulting in an imprint with concave sides. However, full recovery was prevented by "plastic" deformation.

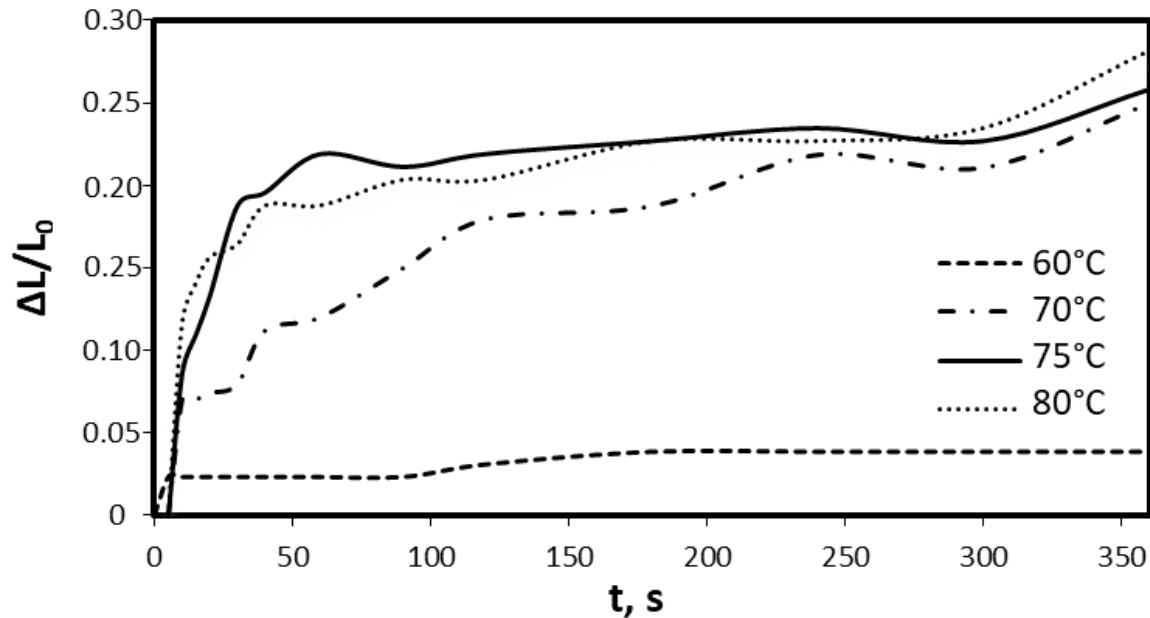
When the samples were heated, the filling of the cavity was observed, as shown in Figs. 1(a-c). The recesses were deformed inward from the sides, and the corners of the recess were not deformed. Thus, to quantify the deformation, the width of the central point between the two walls of the microindent (L) was measured (Fig. 1(d)).



**Fig. 1.** Microindentation of ED-20 with Ts (1.6 wt %) at 75°C after a) 0 s, b) 5 s, c) 30 s, d) measured value L, imprint width

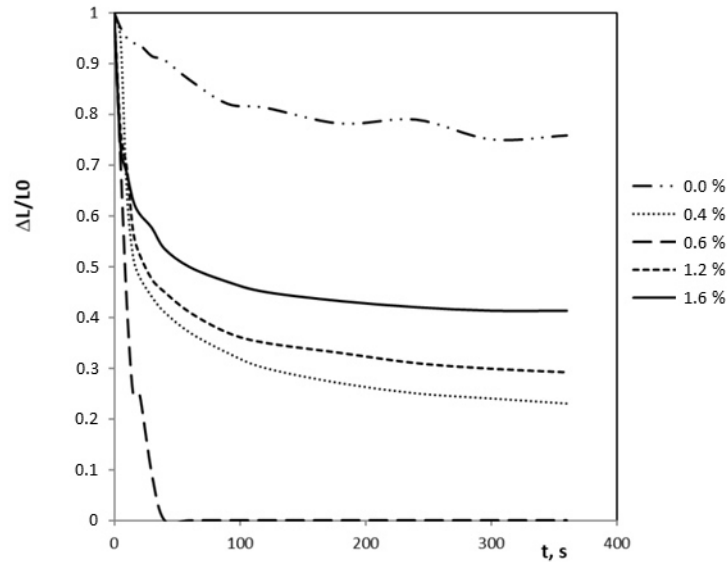
## Results

Figure 2 shows the deformation kinetics of ED-20 without additives (control sample) at various temperatures.  $L_0$  is the initial width after indentation, and  $\Delta L$  is the change in width after heating. At room temperature, no change in the imprint size with time was observed. At 60°C, slight shrinkage is observed. When the temperature was within 10°C of  $T_g$ , a stronger indentation deformation was observed. However, none of the temperatures resulted in a complete recovery of the imprint.



**Fig. 2.** Thermal permanent deformation of imprints on epoxy resins at different temperatures

When nanoparticles were added to the epoxy resin, the recovery performance improved, as shown in Fig. 3, for 75°C. As with the control, maximum recovery occurs within 10°C of the  $T_g$  of the epoxy; although the amount of the recovery is much larger.



**Fig. 3.** Thermal residual deformation of indentations on epoxy resins ED-20 with As nanoparticles at 75°C

However, only the composite with a concentration in a small range showed complete recovery after microindentation at 75°C (Fig. 1(c)). Although all other concentrations of nanoparticles increased their recovery in comparison with the control, they reached a maximum recovery of only about 30%. This indicates that there is an optimal concentration of nanoparticles that ensures complete recovery. At 80°C, the range of concentrations where complete recovery occurred somewhat expanded, but still remained limited.

Figures 4 and 5 show the specific behavior of permanent deformation at a certain concentration, which varied depending on the nanoparticles doped in ED-20.

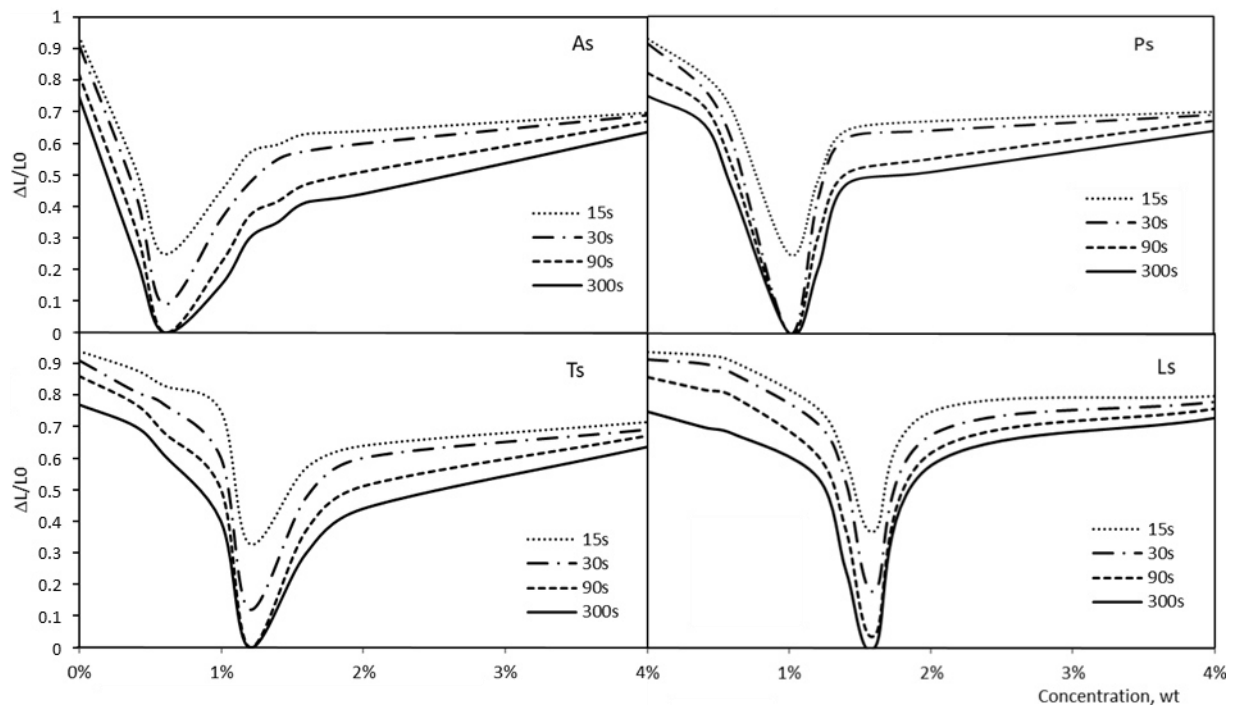


**Fig. 4.** Thermal residual deformation of imprints on epoxy resins ED-20 with SiO<sub>2</sub> nanoparticles depending on the concentration at 75°C

It can be seen from the obtained data that the minimum residual deformation of the composites is located at different concentrations of nanoparticles. That is, the particle-resin interaction has a different meaning for particles obtained by different synthesis methods. The intensity of the interaction introduced by nanoparticles coincides with the assumptions obtained in [26], i.e., it is due to the strength of surface sites formed during the synthesis of nanoparticles. The fastest hardening effect among silica is produced by As particles having strong Lewis acid sites. While the weakest and most delayed effect is shown by Ls particles, the surface of which has only Brønsted main sites.

A similar situation arises for samples containing aluminum oxide nanoparticles. The Aa particles, having a more active surface [26], strengthen the composite faster than other particles. At the same time, La particles having the most passive surface strengthen the composite at the highest concentration of particles. In the same way, the efficiency of the particle-resin interaction can be traced when changing the method of particle synthesis [27,28]. The variation in the activity of the particle surface leads to a change in their concentration at which the maximum recovery of the deformation is achieved.

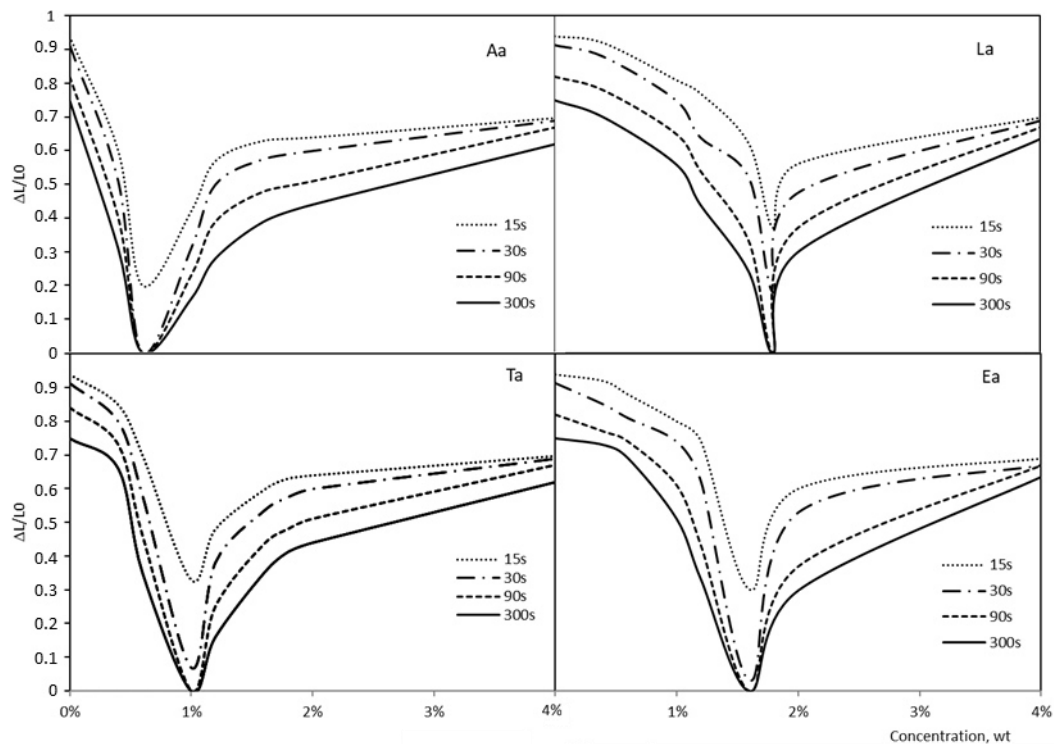


**Fig. 5.** Thermal residual deformation of imprints on epoxy resins ED-20 with Al<sub>2</sub>O<sub>3</sub> nanoparticles depending on the concentration at 75°C.

In [29], a correlation was traced between the dependences of the activation energy of the deformation process and the microindentation deformation itself on the concentration of nanoparticles. Both values have a clear minimum at the concentration, when there is maximum healing of the deformation and a much smaller change in the activation energy at other concentrations. Apparently, at such a concentration, a change in the structure of the polymer occurs. At low concentrations, there are few additional polymer-nanoparticle bonds, and the polymer is relatively easily deformed. As the concentration increases, the number of strengthened bonds increases, reaching a maximum at the optimum value. That is, the number of doped nanoparticles can use all the free bonds of the polymer creating an additional structural network. With a further increase in concentration, forced bonds appear between



nanoparticles (agglomeration), which are much weaker. It is important to note that the number of additional polymer-nanoparticle bonds depends on the activity of the nanoparticle surface [26] and varies depending on the method of their synthesis.

Within the framework of the model of delocalized atoms [23], the relaxation of plastic deformation during heating (thermal stimulation) is explained by the return of exciting delocalized atoms to their main undeformed state [17]. The volumes of delocalization of atoms for pure ED-20 and the one consisting of 1.6 wt% SiO<sub>2</sub> [29] were approximately 97 and 63 Å<sup>3</sup>, respectively.

Therefore, it can be assumed that a group of atoms in the conjugation site of the system of covalent bonds is responsible for the viscous strain of epoxy polymers. Its molecular mechanism is reduced to local displacements (delocalization) of the bridge oxygen atom in the Si-O-Si bond [16,17]. Depending on the activity of the surface of nanoparticles and the intensity of the bonding of O-Si or O-Al groups, which can be determined using IR spectroscopy [30,31], the activation energy of composites with particles of the same chemical composition but different synthesis methods may vary. A smaller volume of delocalization of atoms means that in a given volume, where the polymer has been deformed, there are more units of delocalization, i.e. the volume of fluctuations is larger at any given temperature.

## Conclusions

The kinetics of thermally stimulated relaxation of inelastic strains in an epoxy polymer with SiO<sub>2</sub> and Al<sub>2</sub>O<sub>3</sub> nanoparticles was studied by restoring imprints in epoxy resin samples at elevated temperatures. For all samples, the maximum relaxation value was observed at 75°C, which is 10°C below the glass transition temperature.

We showed that although pure epoxy samples received a maximum recovery of 20%, samples with certain concentrations of nanoparticles had complete relaxation (disappearance of imprints). At higher concentrations, complete relaxation was not achieved.

It is shown that a change in the method of nanoparticle synthesis leads to a change in the concentration at which the relaxation maximum is reached.

## References

1. May CA. (ed.) *Epoxy resins: Chemistry and Technology*. 2nd ed. New York: CRC Press; 2018.
2. Kumar SK, Benicewicz BC, Vaia RA, Winey KI. 50th Anniversary Perspective: Are Polymer Nanocomposites Practical for Applications? *Macromolecules*. 2017;50(3): 714-731.
3. Rueda MM, Auscher MC, Fulchiron R, Périé T, Martin G, Sonntag P, Cassagnau P. Rheology and applications of highly filled polymers: A review of current understanding. *Progress in Polymer Science*. 2017;66: 22-53.
4. Bailey EJ, Winey KI. Dynamics of polymer segments, polymer chains, and nanoparticles in polymer nanocomposite melts: A review. *Progress in Polymer Science*. 2020;105: 101242.
5. Liang JZ. Reinforcement and quantitative description of inorganic particulate-filled polymer composites. *Composites Part B*. 2013;51: 224-232.
6. Mohandesi AJ, Refahi A, Meresht SE, Berenji S. Effect of temperature and particle weight fraction on mechanical and micromechanical properties of sand-polyethylene terephthalate composites: a laboratory and discrete element method study. *Composites Part B*. 2011;42(6): 1461-467.
7. Takahashi S, Imai Y, Kan A, Hotta Y, Ogawa H. Dielectric and thermal properties of isotactic polypropylene/hexagonal boron nitride composites for high-frequency applications. *Journal of Alloys and Compounds*. 2014; 615: 141-145.

8. Tanaka T, Kozako M, Okamoto K. Toward high thermal conductivity nanomicro epoxy composites with sufficient endurance voltage. *Journal of International Council on Electrical Engineering*. 2012;2: 90-98.
9. Bikiaris D. Can nanoparticles really enhance thermal stability of polymers? Part II: an overview on thermal decomposition of polycondensation polymers. *Thermochimica Acta*. 2011;523: 25-45.
10. Peinado F, Medel E, Silvestre R, Garcia A. Open-grade wearing course of asphalt mixture containing ferrite for use as ferromagnetic pavement. *Composites Part B*. 2014;57: 262-268.
11. Hunyek A, Sirisathitkul C. Electromagnetic and dynamic mechanical properties of extruded cobalt ferrite-polypropylene composites. *Polymer - Plastics Technology and Engineering*. 2011;50: 593-598.
12. Kozlov GV, Dolbin IV. The interconnection of efficiency and the degree of aggregation of nanofiller in polymer nanocomposites. *Condensed Matter and Interphases*. 2022;24(1): 45-50.
13. Filippov AA, Fomin VM, Karpov EV. Experimental determination of the elastic characteristics of filled polymers using mechanical tests for constrained compression. *AIP Conference Proceedings*. 2019;2125: 020014.
14. Khozin VG. *Epoxy polymer reinforcement*. Kazan: Printing house; 2004. (In Russian)
15. Benzine O, Bruns S, Pan Zh, Durst K, Wondraczek L. Local deformation of glasses mediated by rigidity fluctuation on nanometer scale. *Advanced Science*. 2018;5(10): 1800916.
16. Sanditov DS. Thermally-stimulated low-temperature relaxation of plastic deformation in glassy organic polymers and silicate glass. *Polymer Science A*. 2007;49(5): 549-557.
17. Sanditov DS. Model of viscous flow of glass forming liquids and glasses. *Doklady Physical Chemistry*. 2013;451(2): 187-191.
18. Arzhakov MS, Zhirnov AE, Lukovkin GM, Arzhakov SA. Universal character of the physicochemical behavior of polymer glasses under compressive deformation conditions. *Russian metallurgy (Metally)*. 2010;2010(10): 851-856.
19. Oleinik ETF, Rudnev SN, Salamatina OB, Kotelyanskii MI. Mechanisms of anelastic deformation in solid polymers: solid-like and liquid-like processes. *Polymer Science. Series A*. 2008;50(5): 494-506.
20. Magafurov IS, Topolkaraev VA, Oleinik EF. Inelastic deformation of glassy polymers under creep conditions. *Mechanics of Composite Materials*. 1990;26: 14-18.
21. Khonik VA, Mitrofanov YuP, Lyakhov SA, Vasiliev AN, Khonik SV, Khoviv DA. Relationship between the shear modulus G, activation energy, and shear viscosity  $\eta$  in metallic glasses below and above T<sub>g</sub>: direct in situ measurements of G and  $\eta$ . *Physical Review B: Condensed Matter and Materials Physics*. 2009;79(13): 132204.
22. Volynskii AL, Bakeev NF. Structural aspects of deformation of amorphous polymers. *Russian Chemical Bulletin*. 2005;54(1): 1-15.
23. Sanditov DS, Ojovan MI. On relaxation nature of glass transition in amorphous materials. *Physica B*. 2017;523: 96-113.
24. Argon AS. *The physics of deformation and fracture of polymers*. Cambridge: Cambridge University Press; 2013.
25. Bardakhanov SP, Vasiljeva IV, Kuksanov NK, Mjakin SV. Surface functionality features of nanosized silica obtained by electron beam evaporation at ambient pressure. *Advances in Materials Science and Engineering*. 2010;241695: 5.
26. Syzrantsev VV. Analysis of variation in the properties of the surface of SiO<sub>2</sub> and Al<sub>2</sub>O<sub>3</sub> nanoparticles obtained by different methods. *Condensed Matter and Interphases*. 2022;24(3): 369-378.

27. Syrkov AG, Silivanov MO, Sychev MM, Rozhkova NN. Alteration of the acid-base properties of the oxidized surface of disperse aluminum during the adsorption of ammonium compounds and the antifriction effect. *Glass Physics and Chemistry*. 2018;44(5): 474-479.
28. Syzrantsev VV, Arymbaeva AT, Zavjalov AP, Zobov KV. The nanofluids' viscosity prediction through particle-media interaction layer. *Materials Physics and Mechanics*. 2022;48(3): 386-396.
29. Nomoev AV, Sanditov DS, Syzrantsev VV, Radnaev BR, Schreiber M. Deformations of microindentations on glassy epoxy mixed with silica nanoparticles. *Physica B: Condensed Matter*. 2019;560: 23-27.
30. Syzrantsev VV, Larina TV, Abzaev YA, Paukstis EA, Kostyukov AI. Structural, surface and optical properties of nanoalumina produced by various ways. *IOP Conference Series: Materials Science and Engineering*. 2020;1000(1): 012001.
31. Syzrantsev VV, Paukstis EA, Larina TV. Surface polymorphism of silica nanoparticles. *IOP Conference Series: Materials Science and Engineering*. 2020;1008(1): 012030.

## THE AUTHOR

Syzrantsev V. 

e-mail: vvveliga@mail.ru

## Effect of nickel incorporation on structural and optical properties of zinc oxide thin films deposited by RF/DC sputtering technique

Mohibul Khan, Md Shahbaz Alam, Sk. Faruque Ahmed 

Nanoscience Laboratory, Department of Physics, Aliah University, IIA/27, Newtown, Kolkata -700160, India

\*e-mail: fahmed.phys@aliah.ac.in

**Abstract:** Reactive co-sputtering technique has been used to fabricate pure zinc oxide and nickel doped zinc oxide thin films on glass substrate at room temperature 30° C. The actual target of this experimental work was to investigate the effect of nickel incorporation on structural and optical properties of nickel doped zinc oxide thin films. The deposited samples were characterized by using Energy-Dispersive Analysis X-ray, X-Ray Diffractometer, Atomic Force Microscope, Fourier Transform Infrared Spectroscopy and Ultraviolet-visible spectrophotometer to investigate the doping growth, structural crystallinity, surface morphology, chemical bonding information and optical properties. Scanning electron microscope has been used to measure the thickness of all deposited films. The X-Ray Diffractometer study of all deposited films reveals that the highly intensive peak has been found near glancing angle at 34.48° corresponds to miller indices (002), which confirmed the wurtzite hexagonal crystallite structure of zinc oxide that matched with JCPDS card no 36-1451. Crystallite size of deposited thin films is increased from 8 nm to 15 nm with the increasing of atomic % of nickel from 0 to 7.5 respectively in zinc oxide. The Fourier Transform Infrared Spectroscopy peak found at 432 cm<sup>-1</sup> confirmed the deposited films are zinc oxide thin films. Optical band gap energy decreases from 3.15 eV to 2.21 eV where as the Urbach energy increases from 118meV to 243meV with increasing of atomic % of nickel from 0 to 7.5 respectively.

**Keywords:** Ni-ZnO thin films; RF/DC sputtering technique; XRD; AFM; Optical Property; Urbach energy.

**Acknowledgement.** The authors wish to acknowledge the University Grants Commission, New Delhi, India for the financial support under Maulana Azad National Fellowship (MANF) scheme during the execution of the work.

**Citation:** Khan M., Alam M S, Ahmed S F. Effect of nickel incorporation on structural and optical properties of zinc oxide thin films deposited by RF/DC sputtering technique. *Materials Physics and Mechanics*. 2023;51(1): 19-32. DOI: 10.18149/MPM.5112023\_3.

### Introduction

Among all II–VI chalcogenide type semiconductors materials, nanocrystalline zinc oxide (whose direct wide band gap and exciton binding energy are 3.37 eV and 60 meV respectively) is one of the greatest acceptable interests for their environmentally safe and versatile application in the field of nanoscience and nanotechnology [1-3]. Past few decades, many researchers from different part of the world have been chosen zinc oxide (ZnO) materials for its multi-functional behaviors like as chemical stability, opto-electric, well luminescence property, good transparency, prominent electron mobility and piezoelectric properties [1-5]. Piezoelectric properties of ZnO thin films depend on its hexagonal crystalline structure [5]. Applications of ZnO thin films are most striking because of their low cost and

also for the non-toxic behavior which is comparable with some oxides like CdO,  $\text{In}_2\text{O}_3$  and  $\text{SnO}_2$  [2,6]. Also, the low resistivity and high transmittance properties of ZnO have been found in the visible region [6]. This type of nano-range ZnO thin films has been used due to its extensively applications in optoelectronic devices [2,3,6]. Nowadays nano-range ZnO films are used in extensive area of science and technology like as UV protectors, solar cell, gas sensing devices, transparent FETs, antibacterial coatings, drug delivery devices, cancer treatment, transparent conducting oxides, photo catalysis, Schottky diodes, light emitting diodes, flat panel displays, spintronics, computer screen, high mobility transistor, laser diodes, surface acoustic devices, smart windows, smartphone display, varistors, high electron mobility, chemical sensors, photo voltaic cells and transparent electrodes [1-11]. The doping effect of different elements such as Au, Al, Sb, N, Ga, Cu, Mn, Ti, Ag, Co, Mo, In, Sn, Fe, and V with pure ZnO on physical, optical, electrical, and dielectric properties have been reported [1-16]. The position of metal element nickel (Ni) in the periodic table is 10<sup>th</sup> group of 4<sup>th</sup> period along with Fe and Co. This transition metal which gradually loses its strong metallic behavior is a very good conductor of electric and heat. Ni has three oxidation states which are +2, +3 and +4. Among all oxidation states +2 is the most significant state [17]. The electro negativity behavior of Ni suggests a suitable bonding attraction for with other elements. 0.69 Å is the ionic radii of  $\text{Ni}^{+2}$  which is familiar with  $\text{Zn}^{+2}$  (0.74 Å) [17]. The structure and valance of Ni and Zn elements are similar. This can be presumed that the hexagonal crystalline structure of ZnO is not changing if  $\text{Ni}^{+2}$  ion replaced by  $\text{Zn}^{+2}$  ion in pure ZnO lattice. The changing effect of Ni on different properties that i.e, physical, optical, electrical, and dielectric with ZnO have been reported earlier [17,18]. In this experimental work, the changes in structural and optical properties of ZnO thin film with Ni incorporation have been studied in detail.

Nickel doped ZnO (NZO) thin films are deposited by several physical and chemical techniques such as chemical bath deposition, photochemical deposition, cyclic voltammetry, sol-gel preparation, low temperature aqueous solution route, spray pyrolysis, metal organic chemical vapor deposition, Radio Frequency (RF) sputtering, screen printing, Direct Current (DC) sputtering, molecular beam epitaxy, DC and RF magnetron sputtering techniques [1-19]. In this scientific work, RF and DC co-reactive magnetron sputtering technique has been chosen to prepare pure ZnO and NZO thin films on glass substrate. This physical technique has been used due to its various advantageous properties like as low-temperature growth, good quality of nano-range thin films, large film area and controllable thickness of film [2,3].

In this current scientific research work, pure ZnO and NZO thin films deposited by reactive co sputtering technique where ZnO and Ni targets were used in RF shutter and DC shutter simultaneously. ZnO films have been doped with different atomic % of Ni for the better improvement of the structural and optical properties of the newly formed nano crystal thin films. Deposited nano-range pure ZnO and NZO films were characterized and analyzed by using X-Ray Diffractometer (XRD), Energy-Dispersive Analysis X-ray (EDAX), Fourier Transform Infrared Spectroscopy (FT-IR), Atomic Force Microscope (AFM), Scanning Electron Microscope (SEM) and Ultraviolet-visible (UV-VIS) Spectrophotometer. Optical characteristics as well as the optical band gap energy ( $E_g$ ) measured from the transmittance spectra of the deposited films by using UV-VIS spectrophotometer. The change in optical transmittance,  $E_g$  and urbach energy ( $E_u$ ) with different atomic % of Ni in the ZnO thin films has been explored in detail.

## Experimental Details

**Materials and deposition techniques.** Pure ZnO and NZO nano-range films have been deposited for 30 min on commercial glass substrate by using DC/RF magnetron co-sputtering technique with the variation of atomic % of Ni from 0 to 7.5% respectively at room temperature 30°C. Source materials (ZnO and Ni targets) and commercial glass substrate of size 75 mm × 25 mm × 1.45 mm were purchased from Sigma-Aldrich Company. Purity, diameter, and thickness of both targets are 99.999%, 54 mm and 2 mm respectively. At 45 °C temperature, all substrates were ultrasonically cleaned by acetone and double distilled water separately and finally soaked with hot air gun.

Only ZnO target was used in RF gun and only Ni target was used in DC gun. Before making the film's deposition, Argon gas was used to clean the impurities of two targets by pre sputtering for 10 minutes. The Rotary pump and Turbo pump of the system has been used simultaneously to maintain the chamber pressure at  $3.5 \times 10^{-4}$  Pa. Argon (Ar) gas and Oxygen gas were used 15 sccm and 5 sccm respectively by mass flow controller (MFC) for deposition purpose. Argon gas has been used for its good sputtering behavior, whereas oxygen gas has been used to maintain oxygen rich growth during deposition. Oxygen gas is also important to reduce the intrinsic donor defects during deposition. The working pressure of the deposition chamber was maintained at 2.0 Pa. Three rotations per minute of all deposition substrates have been used to maintained uniform thickness and good surface morphology of films. Cathode shutters to substrate holder distance was kept at 70 mm for good quality of thin films deposition. During the deposition, RF power set at 100 watt which was fixed and DC voltage, which varies from 180 V to 240 V respectively. The atomic % of Ni varies from 2.6 to 7.5 with the variation of DC voltages from 180 V to 240 V respectively. Only RF power has been used in ZnO target for the formation of pure ZnO thin films. Details of deposition conditions are given below the Table 1.

**Characterizations.** The compositional, structural, morphological, chemical and optical properties of pure ZnO and NZO thin films have been investigated. The compositional property of pure ZnO and NZO thin films has been tested by EDAX (Oxford, model-7582). The crystallite structure of all deposited films has been investigated by using XRD (Bruker, D-8 Advance). Ambient based multimode AFM (Bruker, MultiMode-8) has been used to characterize the surface morphology of all deposited thin films. AFM measurements have been done in contact mode. A silicon probe has been used for scanning purpose which have a radius of curvature 10 nm, height 15 microns and standard chip size  $1.6 \times 1.6 \times 0.4$  mm. A cross sectional scanning electron microscope has been used to calculate the thickness of all deposited films. The FT-IR spectroscopy (IR Affinity-1S, Shimadzu, Japan) has been used to study the chemical bonding information of all deposited thin films. The optical characteristics of the deposited films have been study using a UV-Vis spectrophotometer (V-770, Jasco, Japan).

**Table 1.** Deposition conditions were maintained for the formation of crystallite thin films.

Parameters	Corresponding values
Base pressure / (Pa)	$3.5 \times 10^{-4}$
Working pressure / (Pa)	2.0
Target	ZnO, Ni
Ar flow / (cm <sup>3</sup> /min)	15
O <sub>2</sub> flow / (cm <sup>3</sup> /min)	5
Deposition temperature / (°C)	30
Substrate rotate / (r/min)	3
RF power / (W)	100
DC voltage / (V)	180, 210, 240
Deposition time / (min)	30
Distance between target and substrate holder / (mm)	70



## Results and discussions

**Energy-Dispersive Analysis X-ray (EDAX) analysis.** EDAX has been used to understand the doping growth of atomic % of Ni in ZnO nano-range thin film. The EDAX results of pure ZnO and 7.5 atomic % of Ni doped ZnO nano-range thin films are shown in Fig. 1(a, b). The confirmation of pure ZnO nano-range thin films has been confirmed by EDAX after finding sharp peak of Zinc (Zn) and Oxygen (O) in the thin film respectively, which shown in Fig 1(a). An additional peak of Ni has been found together with Zn and O peaks in the current deposited thin film, which confirmed the NZO nano-range thin film as shown in Fig. 1(b). Ni is a minor intense peak in the NZO nano-range thin film, whereas Zn and O is major intense peak. It has been identified that after incorporation of Ni in the NZO nano-range thin film decreased the atomic % of both Zn and O respectively.

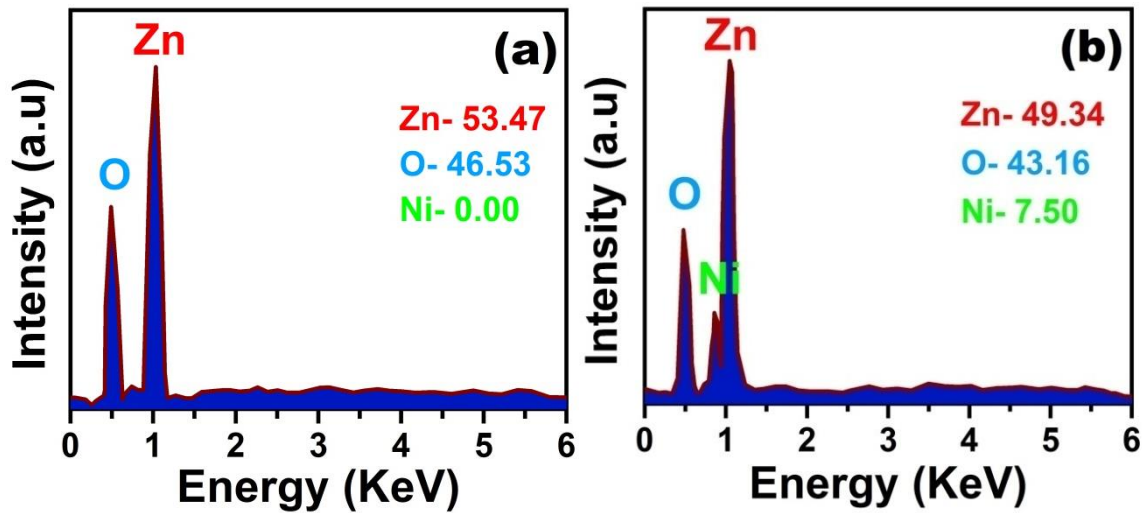


**Fig. 1.** EDAX spectra of NZO thin films: (a) 0.0 atomic % of Ni and (b) 7.5 atomic % Ni

**X-Ray Diffractometer (XRD) study.** The nature of structural crystalline property of pure ZnO and NZO films has been studied by XRD analysis. Cu-K $\alpha$  radiation of wavelength  $\lambda = 1.5406 \text{ \AA}$  has been used to capture the XRD spectra of all deposited thin films in between  $20^\circ$  to  $70^\circ$  glancing angle. During the capturing of XRD spectra, the source voltage kept at 40 kV and source current kept at 40 mA. XRD patterns of deposited all films has been shown in Figs. 2 (a-d). The XRD pattern of all films has been recorded with the scan rate  $2^\circ$  per minute. Crystal structures of deposited thin films are two types like hexagonal wurtzite or cubic zinc blende which is depends on few deposition parameters [2,3]. The highly intensive peak has been found near glancing angle at  $34.48^\circ$  corresponds to miller indices (002), which confirmed the wurtzite hexagonal crystalline structure of ZnO that matched with JCPDS card no 36-1451 [2,3,16,18,20]. Peak intensity of deposited films increased slowly with the increasing of atomic % of Ni from 0 to 7.5 respectively. Debye-Scherrer formula has been used to calculate the crystallite sizes (D) of all films [2,3,21,22]

$$D^{-1} = \frac{\beta \cos \theta}{K \lambda}, \quad (1)$$

where  $K$  (0.94),  $\lambda$  (1.5406  $\text{\AA}$ ),  $\beta$  and  $\theta$  are known as Scherrer constant, wavelength of X-ray, full width of half maximum (FWHM) and Bragg's angle or glancing angle respectively.

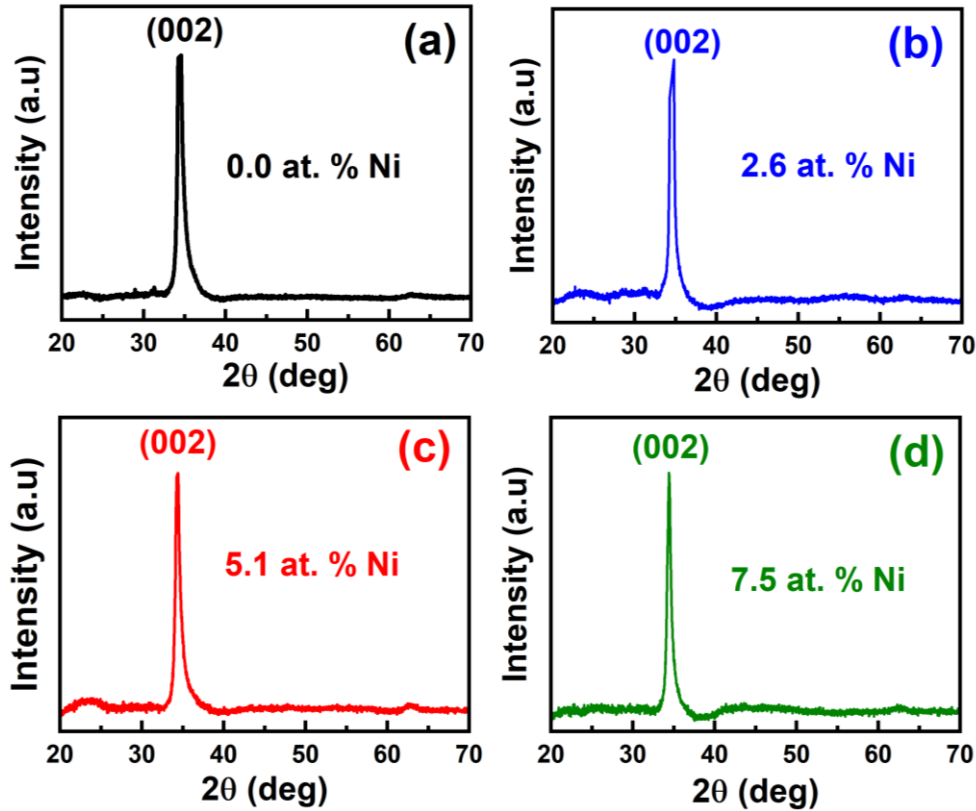


**Fig. 2.** (a-d). XRD patterns of NZO thin films deposited on glass substrates at different atomic % of Ni from; (a) Ni = 0, (b) Ni = 2.6, (c) Ni = 5.1, (d) Ni = 7.5% respectively

It is found that after increasing of atomic % of Ni from 0 to 7.5 the crystallite sizes of deposited films increased from 8 nm to 15 nm which are due to predominantly shifting of  $\text{Ni}^{2+}$  ion into the ZnO host lattice sites. As there is an inverse relation between crystallite size and FWHM, crystallites size increases from 8 nm to 15 nm where as  $\beta$  decreases from  $1.06073^\circ$  to  $0.56425^\circ$  respectively [22]. Equation 2 has been used to calculate the strain of all deposited films [20,22,23]

$$\varepsilon^{-1} = \frac{4}{(\beta \cos \theta)} \quad (2)$$

After calculating the strain of all deposited films, it has been found that it is decreased from  $44.18 \times 10^{-4}$  to  $23.5 \times 10^{-4}$  with the increasing of atomic % of Ni from 0 to 7.5 respectively. Equation 3 is known as Bragg's equation, which has been used to calculate the interplanar spacing (d) of pure ZnO and NZO all films [8,23,24]

$$\frac{1}{d} = \frac{(2 \sin \theta)}{n \lambda}, \quad (3)$$

where  $n$  is diffraction order. Equation 4 has been used to calculate the lattice constants of deposited all films [8,24]

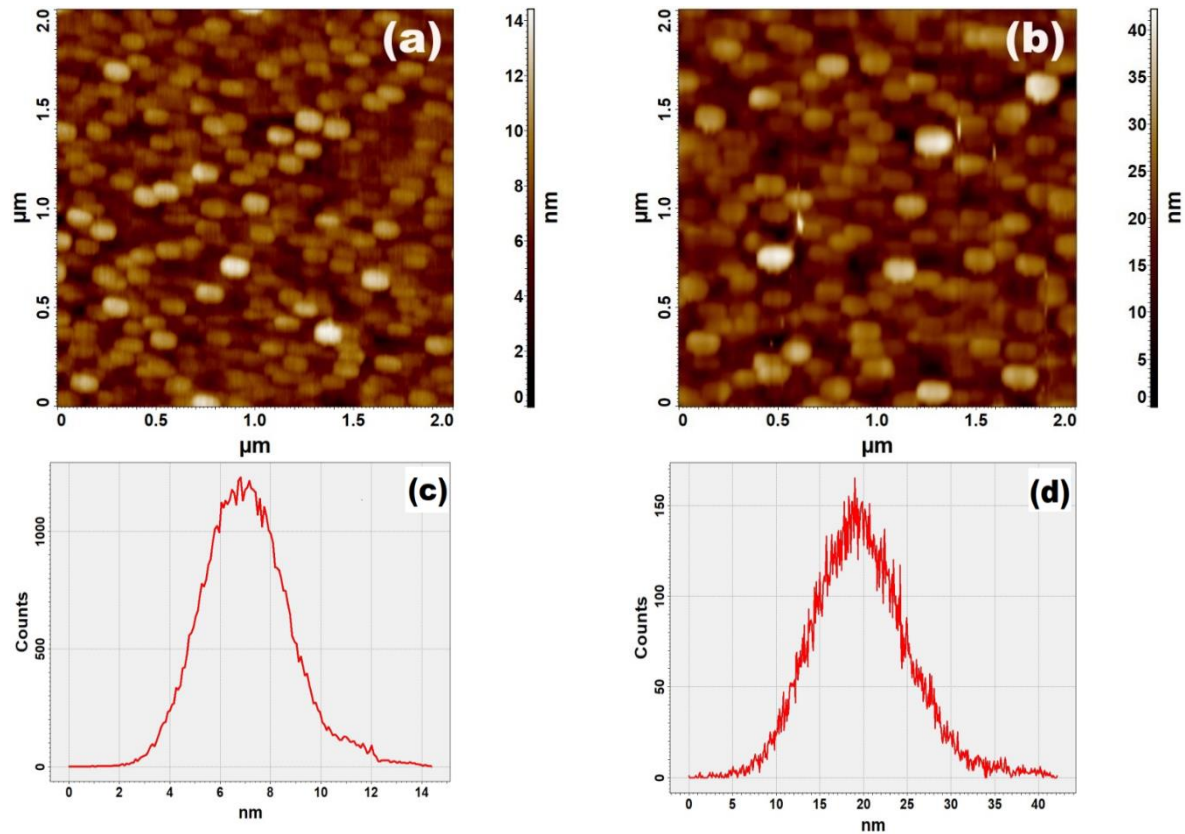
$$d^{-2} = \left[ \frac{4}{3a^2} (h^2 + hk + k^2) \right] + \frac{l^2}{c^2}, \quad (4)$$

where  $(a, c)$  and  $(hkl)$  are lattice constant and miller indices. The lattice constant  $c$  slightly varies from  $5.198 \text{ \AA}$  to  $5.206 \text{ \AA}$  due to the substitution of  $\text{Ni}^{2+}$  ion instead of  $\text{Zn}^{2+}$  ion at their respective lattice sites. It was clearly observed that decrease in strain causes increased in crystallite size and increased in lattice constants [17,23]. The values of glancing angles ( $2\theta$ ), Full Width Half Maxima ( $\beta$ ), crystallite sizes ( $D$ ), strain ( $\varepsilon$ ), interplanar spacing ( $d$ ) and lattice constant ( $c$ ) are shown in Table 2.

**Table2.** XRD data of NZO thin films at different atomic % of Ni.

Atomic % of Ni	2 $\theta$ (deg)	$\beta$ (deg)	D (nm)	d ( $\text{\AA}$ )	$\epsilon \times 10^{-4}$	c ( $\text{\AA}$ )
0.0	34.48	1.06073	8	2.599	44.18	5.198
2.6	34.46	0.86254	10	2.600	35.93	5.200
5.1	34.44	0.70253	12	2.602	29.26	5.204
7.5	34.42	0.56425	15	2.603	23.50	5.206

**Atomic Force Microscope (AFM) study.** Scanning probe AFM has been used to study the morphological property of deposited pure ZnO and NZO films surface. The surface image which has been captured by highly resolute AFM micrograph is homogeneous and uniform. Two-dimensional (2-D) AFM surface images of pure ZnO and NZO thin films and their corresponding histograms are shown in Fig. 3 (a-d). AFM images of all films display that the surface morphological characteristic varies with adding atomic % of Ni from 0 to 7.5 with pure ZnO respectively is shown in Fig. 3(a, b). The reflecting and scattering characteristic of transmitted light depend on the surface of morphological roughness of all deposited films. It has been found that the grain sizes of all films increases with increasing the roughness of the morphological surfaces, where the roughness of the morphological surfaces increases with adding atomic % of Ni from 0 to 7.5 with pure ZnO respectively. Histogram which is shown in Fig. 3 (c-d) exhibits that grain sizes of deposited films increased from 7 nm to 19 nm with adding atomic % of Ni from 0 to 7.5 with pure ZnO respectively. Grain size which has measured by AFM of ZnO film is lower than that calculated from XRD of same film. Grain size which has measured by AFM of NZO films is greater than the grain size calculated from XRD of same films. The bigger grain size which has been found in AFM of all films is caused by the agglomeration of lesser crystals, where XRD gives report about the mean grain size which coherently scatters the X-rays [25,26].

**Fig. 3.** Two-dimensional AFM images of NZO thin films: (a) 0.0 atomic % of Ni, (b) 7.5 atomic of Ni (c) and (d) the corresponding histogram

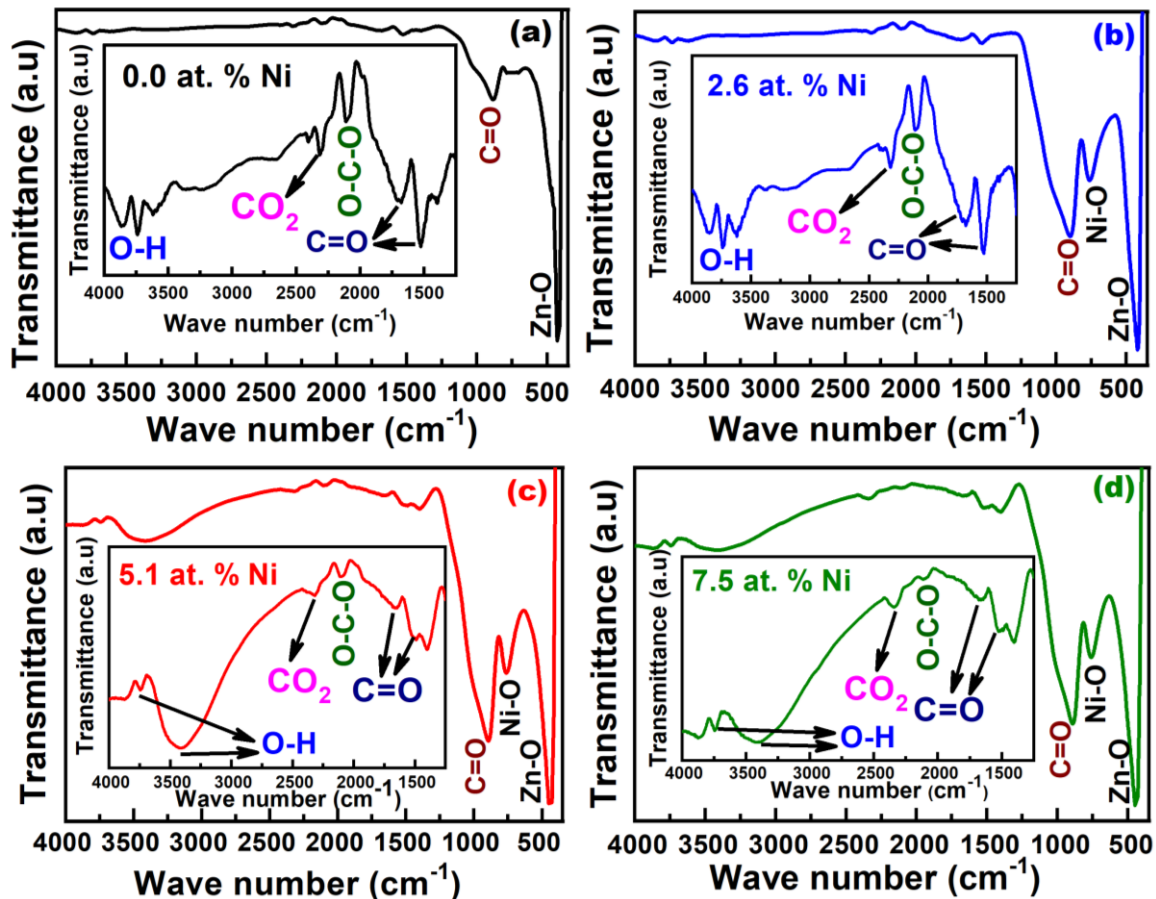


**Fig. 4.** (a-d) FT-IR spectra of NZO thin films with variation of atomic % of Ni from; (a) Ni = 0, (b) Ni = 2.6, (c) Ni = 5.1, (d) Ni = 7.5 respectively

**Fourier Transform Infrared Spectroscopy (FT-IR) study.** Chemical compositions of pure ZnO and NZO films have been observed by using FT-IR spectrum in  $400\text{ cm}^{-1}$  to  $4000\text{ cm}^{-1}$  the frequency at room temperature  $30^\circ\text{C}$  is shown in Fig. 4 (a-d). As all films deposited on glass substrate, so plane glass substrate has been used as reference for the measurement of FT-IR absorption spectra to eliminate the absorption peak. The structural and molecular arrangements of pure and Ni doped ZnO thin films on glass substrates have been examined by using FT-IR spectrum. The FT-IR frequency  $400\text{ cm}^{-1}$  to  $4000\text{ cm}^{-1}$  separated in two parts. The first part is  $400\text{ cm}^{-1}$  to  $1600\text{ cm}^{-1}$ . This part is known as fingerprint region and in this region stretching and bending vibrations are occurs. Whereas the second part is  $1600\text{ cm}^{-1}$  to  $4000\text{ cm}^{-1}$ , which part is known as functional group region and in this region only stretching vibration is occurs. The FT-IR peaks which are shown in Fig. 4 (a-d) have been found due to the stretching and bending vibration of atom and molecules or functional groups. The FT-IR peaks intensity does not fix, it is depends on different deposition materials. Due to the stretching vibration of Zn-O bond in all deposited films a peak has been identified at near  $432\text{ cm}^{-1}$ , which confirmed the deposited films are ZnO thin films [18,19,24]. One peak has been identified except Fig. 4(a) closed to  $720\text{ cm}^{-1}$  due to stretching vibration of Ni-O band [27]. The stretching absorption peak has been found in all deposited films at near  $890\text{ cm}^{-1}$  assigned as C=O peak. Two absorption peaks have been found at near  $1528\text{ cm}^{-1}$  and  $1680\text{ cm}^{-1}$ , which were assigned due to symmetric strong C=O bond and asymmetric C=O bond respectively [2,3,27]. One FT-IR peak has been found near at  $2060\text{ cm}^{-1}$  assigned to O-C-O bond, which decreased very slowly with the increase of atomic % of Ni from 2.6 to 7.5 respectively [18]. The absorption peak of  $\text{CO}_2$  molecules has been identified at near  $2310\text{ cm}^{-1}$ , which attributed due to the run time of deposition or atmosphere during the FT-IR



analysis [24]. The absorption peak of O-H band has been found between  $3740\text{ cm}^{-1}$  to  $3830\text{ cm}^{-1}$  and  $3420\text{ cm}^{-1}$  to  $3450\text{ cm}^{-1}$ , which assigned for atmosphere during the FT-IR analysis [28,29]. These FT-IR results of all deposited films state that  $\text{Ni}^{2+}$  ions successfully incorporated into pure ZnO lattice site and also confirmed the wurtzite crystalline nature of all films.

**Optical band gap energystudy.** UV-Visible spectrophotometer has been used to study the optical property of pure ZnO and NZO thin films in the wavelength between 300 nm to 800 nm at room temperature of  $30^\circ\text{C}$  are shown in Fig. 5. Optical property of deposited films depends on transmittance spectra. Highly transmittance films are important for good quality optical property. Transmittance spectra of deposited films depends on deposition conditions. In visible region deposited films are showed a transmittance nearly 85 % due to low scattering or absorption losses. Transmittance spectra of all deposited films gradually decreases with adding atomic % of Ni from 2.6 to 7.5 within pure ZnO are shown in Fig. 5 as well as it shifts towards from visible region to near UV region. Optical transmittance is related to film thickness. It is decreases with increasing of film thickness [30]. Thickness of the deposited films increased from 250 nm to 350 nm with increasing atomic % of Ni from 0 to 7.5 respectively.

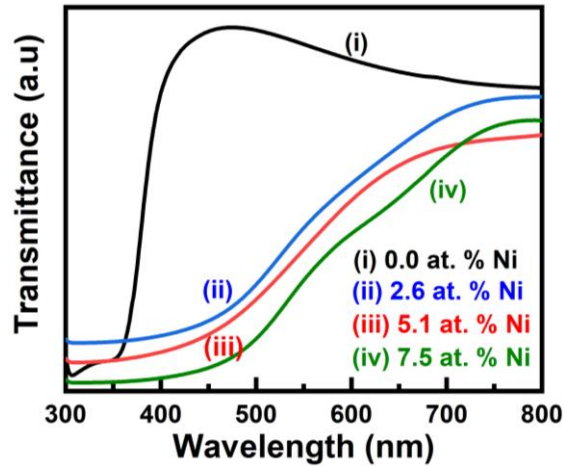


**Fig. 5.** Transmission spectra of NZO thin films with the variation of different atomic % of Ni from 0 to 7.5 respectively

The film thickness is calculated by using cross-sectional Scanning Electron Microscope images. Beer-Lambert law, which is getting from band theory of solid has been used to calculate the absorption coefficient ( $\alpha$ ) using the equation [8,22]

$$\alpha = \frac{1}{t} \ln \left( \frac{I_0}{I_t} \right), \quad (5)$$

where  $I_0$ ,  $I_t$  and  $t$  are the intensity of incident light, intensity of transmitted light and thickness of deposited films respectively. The transmittance relation  $T = \frac{I_t}{I_0}$  is known as the simplified form of Beer-Lambert formula. The energy of the optical band gap ( $E_g$ ) of pure ZnO and NZO films has been calculated by using the Tauc expression [21,22,31]

$$(\alpha h\nu)^{1/m} = A(h\nu - E_g), \quad (6)$$

where  $A$ ,  $h\nu$  and  $m$  are constant, energy of the incident photon ( $h$  and  $\nu$  are Planck's constant and frequency of the incident light respectively) and the different type of transition value. The value of  $m$  is different for different deposition semiconductor material. In this case the value of  $m$  is  $1/2$  as ZnO is directly allowed band gap materials [2,3,8]. In the case of directly allowed transition semiconductor material, the  $E_g$  of pure ZnO and NZO films has been

determined from the extrapolation of the straight line on the x-axis using  $(\alpha h\nu)^2$  against  $h\nu$  graph of different atomic % of Ni as shown in Fig. 6 (a-d). It is observed that the  $E_g$  of the deposited films decreases lightly with entering Ni into the ZnO layer. The obtained  $E_g$  of pure ZnO, ZnO: 2.6 at. % Ni, ZnO: 5.1 at. % Ni and ZnO: 7.5 at. % Ni films are 3.15, 2.59, 2.40 and 2.21 eV, respectively. It is observed that the  $E_g$  of pure and NZO films decreases due to increase in the grain size when atomic % of Ni increases [22]. The variation of  $E_g$  against different atomic % of Ni is shown in Fig. 7. It has been observed from Fig. 7 that the variation of the optical band gap energy of ZnO thin films is 0.94 eV (3.15 eV to 2.21 eV) by nickel doping which is better than other reported value such as 0.05 eV (3.33eV to 3.28eV), 0.08 eV (3.28eV to 3.20eV) and 0.51 eV (3.26 eV to 2.75 eV) respectively [32-34]. The potential advantage of NZO as an optical coating can be taken with controlling its optical band gap by changing the Ni content independently from other parameters.

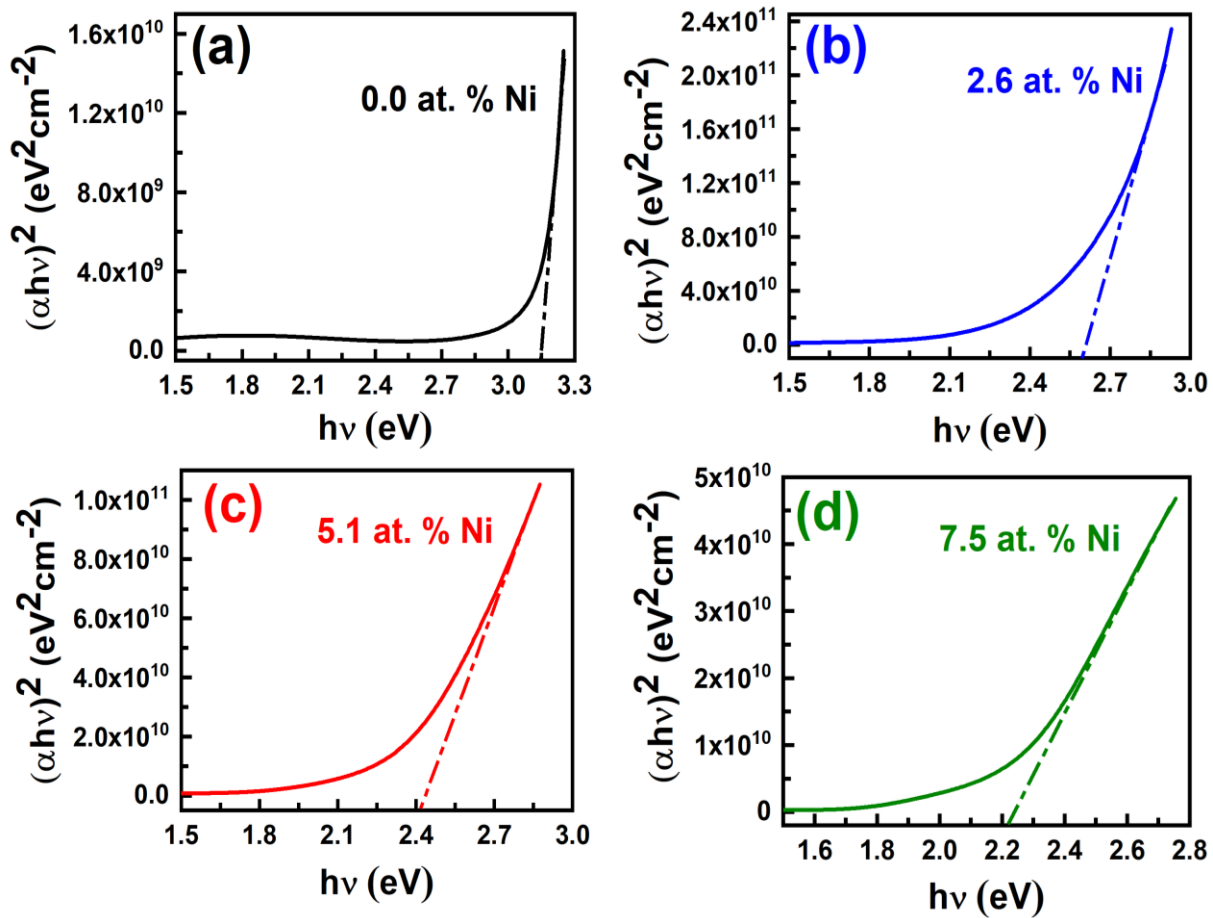


**Fig. 6.** (a-d) Tauc plot of  $(\alpha h\nu)^2$  against  $h\nu$  at a different atomic % of Ni

**Urbach energy.** UV-vis spectrophotometers also been used to calculated Urbach energy ( $E_u$ ) of deposited pure ZnO and NZO thin film. The  $E_u$  of deposited thin films has been found for the structural disorder of crystal, which is familiar as "band tail width" of localized energy states. The schematic band tail diagram of  $E_u$  of deposited films has been shown in Fig. 8(a). The diagrammatic expression of  $E_u$  of deposited crystalline film is shown by the formula

$$E_u = \Delta E_g - \Delta E_{g'}, \quad (7)$$

where  $\Delta E_g$  and  $\Delta E_{g'}$  are familiar as valence band to conduction band energy gap and valence band tail to conduction band tail energy gap respectively [3,22]. The  $E_u$  of deposited film is also familiar as disorder liness of phonon states or defect density. The  $E_u$  of deposited films is



calculated by using an exponential function below the slope of absorption of band edge [35,36].

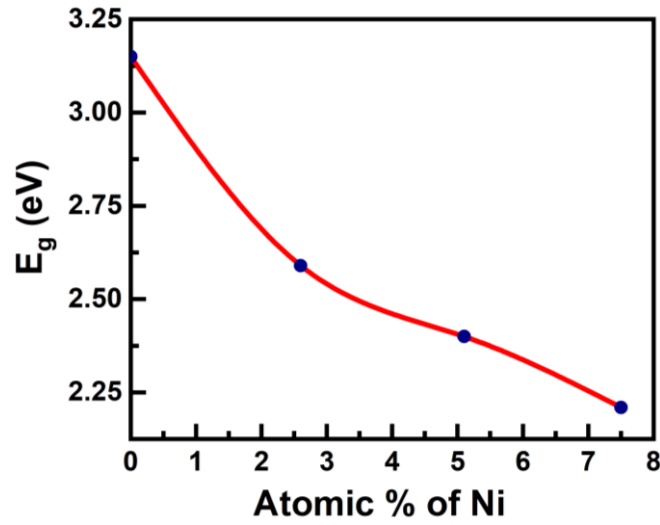


**Fig. 7.** Variation of  $E_g$  against different atomic % of Ni from 0 to 7.5 respectively

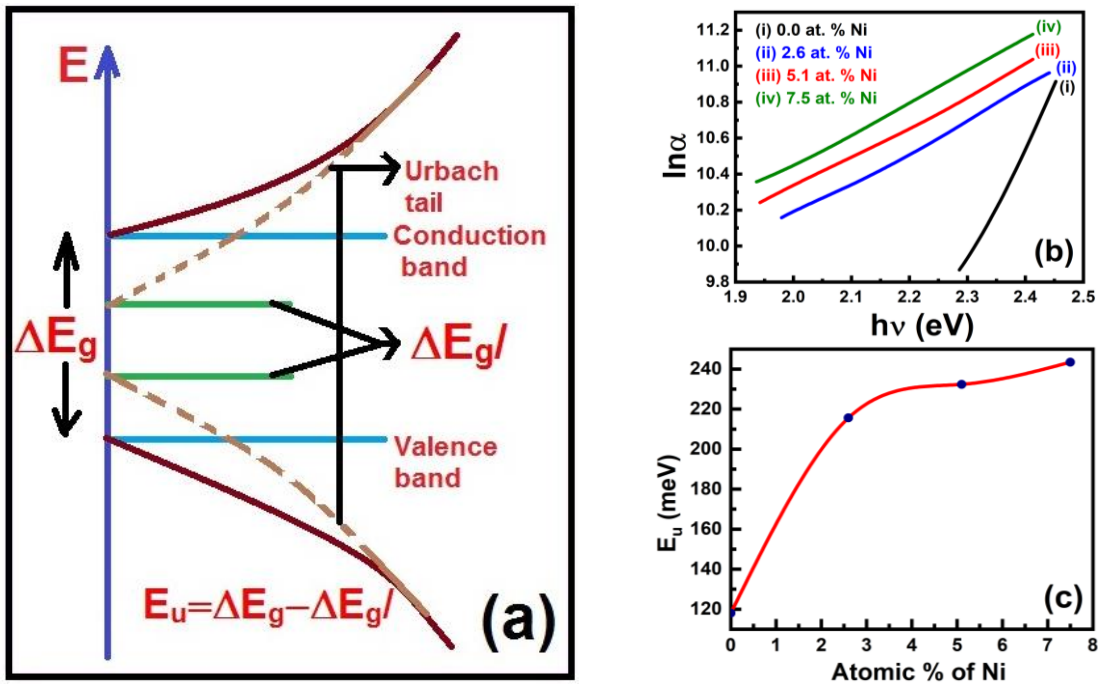


**Fig. 8.** (a) Schematic diagram of band tail of Urbach energy, (b) a plot of  $\ln\alpha$  vs.  $h\nu$  of pure ZnO and NiO thin films with different at. % of Ni, (c) Variation of Urbach energy ( $E_u$ ) of Ni doped ZnO thin films with atomic % of Ni

The absorption band edge of deposited films has been generated for the interaction of electron-phonon or exciting-phonon. The optical-electronic transitions of the compound which happened in between excited and near localized states is calculated from steepness parameter of absorption band edge. The band of the compound which bending slowly is depending on the reduction of optical band gap. In the phonon states, the disorder of pure ZnO and NiO films will be high if  $E_u$  is also higher. The band tail of Urbach of deposited films has been expressed by the formula [37-39]

$$\ln\alpha_0 = \ln\alpha + \frac{h\nu}{E_u}, \quad (8)$$

where  $\alpha_0$ ,  $\alpha$  and  $h\nu$  are constant, absorption coefficient and photon energy of the incident ray of light respectively. Band tail of  $E_u$  of pure ZnO and NZO films has been determined using the  $\ln\alpha$  versus  $h\nu$  plot, which shown in Fig. 8 (b). Semiconductor Group (II-VI) chalcogenide materials Urbach band tail depends on several workable defects which are structural disorder, interaction between carrier-impurity and carrier-phonon etc. [2,40]. In the phonon states of crystalline structure, the  $E_u$  of deposited films directly provides several efficient information about thermal disorderliness and the occupancy level [40]. The exponential increasing of  $\alpha$  of deposited pure ZnO and NZO films can be stated from the transitions of the density of states between valence to conduction band and also the shape and size of tails. The structural and thermal disorderliness of deposited films can be determined from Skettrup's theory, which modeled as an Einstein oscillator [40].

Generally, the  $E_g$  of deposited films is inversely related to  $E_u$  [40]. It is found that  $E_u$  of deposited films increases with increasing of atomic % of Ni from 0 to 7.5 respectively within pure ZnO. The graph between  $E_u$  versus atomic % of Ni shown in Fig. 8(c). The  $E_u$  of deposited films increases from 118 meV to 243 meV with the increasing of atomic % of Ni from 0 to 7.5 respectively within ZnO. The disorderliness of deposited pure ZnO and NZO films also increases with the increase of  $E_u$ . The slowly increasing state of  $E_u$  indicate that from tail to tail and band to tail transitions and redistribution of states severally [41]. Moreover it was found that the  $E_g$  of deposited films decrease due to the increase of the band tail of  $E_u$  [3,41].

## Conclusions

In this experimental research work, pure ZnO and NZO thin films have been synthesized on the glass substrates via RF/DC reactive co-sputtering technique. XRD, AFM and FT-IR spectroscopy have been used to characterize the nanostructure crystallinity, surface morphology and chemical compositions of the pure ZnO and NZO thin films respectively. Crystallite sizes of deposited thin films which are measured by XRD are increased from 8 nm to 15 nm with the increasing of atomic % of Ni from 0 to 7.5 respectively in ZnO. Grain sizes of deposited films which are determined by AFM increased from 7 nm to 19 nm with adding atomic % of Ni from 0 to 7.5 with pure ZnO respectively. The FT-IR peaks which are found near  $432\text{ cm}^{-1}$  and  $755\text{ cm}^{-1}$  confirmed the deposited films are pure ZnO and NZO thin films. The  $E_g$  of pure and NZO thin films has been investigated by UV-Vis spectrophotometer which decreased from 3.15 eV to 2.21 eV with increasing the atomic % of Ni from 0 to 7.5 respectively at room temperature  $30^\circ\text{C}$ . It is found that with increasing of atomic % of Ni from 0 to 7.5 the  $E_u$  increases from 118 meV to 243 meV respectively. The potential advantage of NZO as an optical coating can be taken with controlling its transparency and optical band gap by changing the Ni content independently of other parameters.

## References

1. Sajjad M, Ullah I, Khan MI, Khan J, Khan MY, Qureshi MT. Structural and optical properties of pure and copper doped zinc oxide nanoparticles. *Results Phys.* 2018;9: 1301-1309.
2. Khan M, Ahmed SF. Effect of the distance between cathode and substrate on structural and optical properties of zinc oxide thin films deposited by rf sputtering technique. *Mater. Phys. Mech.* 2021;47(6): 872-884.
3. Khan M, Alam MS, Ahmed SF. Synthesis and Characterization of Copper Doped Zinc Oxide Thin Films Deposited by RF/DC Sputtering Technique. *J. Shanghai Jiao Tong Univ. (Sci.)*. 2022.
4. Imran M, Ahmed R, Afzal N, Rafique M. Copper ion implantation effects in ZnO film

deposited on flexible polymer by DC magnetron sputtering. *Vacuum*. 2019;165: 72-80.

5. Maiti UN, Ghosh PK, Ahmed SF, Mitra MK, Chattopadhyay KK. Structural, optical and photoelectron spectroscopic studies of nano/micro ZnO: Cd rods synthesized via sol-gel route. *J. Sol-Gel Sci. Technol.* 2007;41: 87-92.
6. Saha B, Das NS, Chattopadhyay KK. Combined effect of oxygen deficient point defects and Ni doping in radio frequency magnetron sputtering deposited ZnO thin films. *Thin solid Films*. 2014;562: 37-42.
7. Pandey B, Ghosh S, Srivastava P, Kabiraj D, Shripati T, Lalla NP. Synthesis of nanodimensional ZnO and Ni-doped ZnO thin films by atom beam sputtering and study of their physical properties. *Physica E*. 2009;41(7): 1164-1168.
8. Yusof AS, Hassan Z, Zainal N. Fabrication and characterization of copper doped zinc oxide by using Co-sputtering technique. *Mater. Res. Bull.* 2018;97: 314-318.
9. Hafdallah A, Djefailia F, Saidane N. Structural and Optical Properties of ZnO Thin Films Deposited by Pyrolysis Spray Method: Effect of Substrate Temperature. *Optics*. 2018;7(2): 68-73.
10. Mukherjee N, Ahmed SF, Chattopadhyay KK, Mondal A. Role of solute and solvent on the deposition of ZnO thin films. *Electrochimica Acta*. 2009;54(16): 4015-4024.
11. Dietl T, Ohno H. Diluted ferromagnetic semiconductors: Physics and spintronic structures. *Rev. Mod. Phys.* 2014;86(1): 187-251.
12. Caglar Y, Caglar M, Ilican S, Aksoy S, Yakuphanoglu F. Effect of channel thickness on the field effect mobility of ZnO-TFT fabricated by sol gel process. *J. Alloys Compd.* 2015;621: 189-193.
13. Al-Hardan NH, Abdullah MJ, Ahmad H, Aziz AA, Low LY. Investigation on UV photo detector behaviour of RF-sputtered ZnO by impedance spectroscopy. *Solid State Electron.* 2011;55(1): 59-63.
14. Khosravi P, Karimzadeh F, Salimijazi HR, Abdi Y. Structural, optical and electrical properties of co-sputtered p-type ZnO: Cu thin-films. *Ceram. Int.* 2019;45(6): 7472-7479.
15. Kim H, Pique A, Horwitz JS, Murata H, Kafafi ZH, Gilmore CM, Chrisey DB. Effect of aluminum doping on zinc oxide thin films grown by pulsed laser deposition for organic light-emitting devices. *Thin Solid Films*. 2000;377-378: 798-802.
16. Zargar RA, Khan SUD, Khan MS, Arora M, Hafiz AK. Synthesis and Characterization of Screen Printed Zn<sub>0.97</sub>Cu<sub>0.03</sub>O Thick Film for Semiconductor Device Applications. *Phys. Res. Int.* 2014;2014: 464809.
17. Ali MY, Khan MKR, Karim AMMT, Rahman MM, Kamruzzaman M. Effect of Ni doping on structure, morphology and opto-transport properties of spray pyrolysed ZnO nanofiber. *Heliyon*. 2020;6(3): e03588.
18. Husain S, Rahman F, Ali Nasir, Alvi PA. Nickel Sub-lattice Effects on the Optical Properties of ZnO Nanocrystals. *J. Optoelectron. Engineer.* 2013;1: 28-32.
19. Fattah ZA. Synthesis and characterization of nickel doped zinc oxide nanoparticles by sol-gel method. *Int. J. Engineer. Sci. Res. Technol.* 2016;5: 418-429.
20. Muthukumaran S, Gopalakrishnan R. Structural, FTIR and photoluminescence studies of Cu doped ZnO nanopowders by co-precipitation method. *Opt. Mat.* 2012;34: 1946-1953.
21. Ghosh PK, Maiti UN, Ahmed SF, Chattopadhyay KK. Photoluminescence and field emission properties of ZnS:Mn nanoparticles synthesized by rf-magnetron sputtering technique. *Opt. Mater.* 2007;29(12): 1584-1590.
22. Khan M, Alam MS, Saha B, Ahmed SF. Synthesis and characterization of cadmium sulfide (CdS) thin films by cyclic voltammetry technique. *Mater. Today: Proceed.* 2021;47: 2351-2357.
23. Raja K, Ramesh PS, Geetha D. Synthesis, structural and optical properties of ZnO and Ni-doped ZnO hexagonal nanorods by Co-precipitation method. *Spectrochim. Acta. A Mol.*

*Biomol. Spectrosc.* 2014;120: 19-24.

24. Elhamdi I, Souissi H, Taktak O, Elghoul J, Kammoun S, Dhahri E, Costa FO. Experimental and modeling study of ZnO:Ni nanoparticles for near-infrared light emitting diodes. *RSC Adv.* 2022;12: 13074-13086.
25. Abuelwafa AA, Denglawey AE, Dongol M, Nahass MME, Soga T. Influence of annealing temperature on structural and optical properties of nanocrystalline Platinum octaethylporphyrin (PtOEP) thin films. *Opt. Mater.* 2015;49: 271-278.
26. Ghosh PK, Maiti UN, Ahmed SF, Chattopadhyay KK. Highly conducting transparent nanocrystalline Cd<sub>1-x</sub>Sn<sub>x</sub>S thin film synthesized by RF magnetron sputtering and studies on its optical, electrical and field emission properties. *Sol. Energy Mater. Sol. Cells.* 2006;90(16): 2616-2629.
27. Siddique MN, Ali T, Ahmed A, Tripathi P. Enhanced electrical and thermal properties of pure and Ni substituted ZnO Nanoparticles. *Nano-Struct. Nano-Objects.* 2018;16: 156-166.
28. Alamdari S, Ghamsari MS, Lee C, Han W, Park HH, Tafreshi MJ, Afarideh H, Ara MHM. Preparation and Characterization of Zinc Oxide Nanoparticles Using Leaf Extract of Sambucusebulus. *Appl. Sci.* 2020;10(10): 1-19.
29. Khan Z R, Khan M S, Zulfeqar M, Khan M S. Optical and Structural Properties of ZnO Thin Films Fabricated by Sol-Gel Method. *Mater. Sci. App.* 2011;2: 340-345.
30. Shukla RK, Kumar N, Srivastava A. Pandey A. Pandey M. Optical and sensing properties of Al doped ZnO nanocrystalline thin films prepared by spray pyrolysis. *Mater Today: Proceed.* 2018;5(3): 9102- 9107.
31. Alam MS, Khan M, Ahmed SF. Nanostructure wrinkle thin films on flexible substrate: Tunable optical properties. *Mater. Today: Proceed.* 2022;49: 1401-1407.
32. Khalfallah B, Chaabouni F, AbaabM. Ni-doped ZnO films deposited by RF magnetron sputtering using raw powder target. *Indian. J. Physics.* 2019;93: 439–447.
33. Owwoye VA, Ajenifuja E, Adeoye EA, Osinkolu GA, Popoola AP. Microstructural and optical properties of Ni-doped ZnO thin films prepared by chemical spray pyrolysis technique. *Mater. Res. Express.* 2019;6(8): 086455.
34. Ma Z, Ren F, Deng Y, Volinsky AA. Structural, electrochemical and optical properties of Ni doped ZnO: Experimental and theoretical investigation. *Optik.* 2020;219: 165204.
35. Rai RC. Analysis of the Urbach tails in absorption spectra of undoped ZnO thin films. *J. Appl. Phys.* 2013;113(15): 153508.
36. Alam MS, Mukherjee N, Ahmed SF. Optical Properties of Diamond Like Carbon Nanocomposite Thin films. *AIP Conf. Proceed.* 2018;1953(1): 090018.
37. Ahmed SF, Banerjee D, Chattopadhyay KK. The influence of fluorine on the optical properties in diamond like carbon thin films. *Vacuum.* 2010;84(6): 837-842.
38. Ahmed SF, Moon MW, Lee KR. Effect of silver doping on optical property of diamond like carbon films. *Thin Solid Films.* 2009;517(14): 4035-4038.
39. Alam MS, Ghosh CK, Mukherjee N, Ahmed SF. Nanostructure evolution and optical properties of silver doped diamond like carbon thin film on soft polymer. *Adv.Sci.Lett.* 2018;24: 5731–5736.
40. Islam MA, Hossain MS, Aliyu MM, Chelvanathan P, Huda Q, Karim MR, Sopian K, Amin N. Comparison of Structural and Optical Properties of CdS Thin Films Grown by CSVT, CBD and Sputtering Techniques. *Energy Procedia.* 2013;33: 203-213.
41. Vettumperumal R, Kalyanaraman S, Santoshkumar B, Thangavel R. Estimation of electron–phonon coupling and Urbach energy in group-I elements doped ZnO nanoparticles and thin films by sol–gel method. *Mater. Res. Bull.* 2016;77: 101-110.

**THE AUTHORS****Mohibul Khan** 

e-mail: khanmohibul2@gmail.com

**Md Shahbaz Alam** 

e-mail: 786shahbaz92@gmail.com

**Sk. Faruque Ahmed** 

e-mail: faruquekist@gmail.com

## Deformation and Heat-Insulating Characteristics of Light Concrete on Porous Burned Binder Under Heating

V.T. Erofeev <sup>1</sup> , S.A. Korotaev <sup>1</sup> , N.I. Vatin <sup>2</sup> 

<sup>1</sup> National Research Mordovia State University, Saransk, The Republic of Mordovia, Russia

<sup>2</sup> Peter the Great St. Petersburg Polytechnic University, St. Petersburg, Russia

✉ [vatin@mail.ru](mailto:vatin@mail.ru)

**Abstract.** It is known to use heat-insulating materials with a rigid cellular structure on cement, gypsum, liquid glass binders as a constructive fire protection. The described technologies for the manufacture of such materials do not allow combining a binder with an aggregate. The use of frame technology made it possible to obtain a material with an aggregate on a porous burned soda-lime-silicate waterproof binder. The article presents the results of studies of the fire-proof properties of samples from the obtained material. The deformation and heat-insulating characteristics of the material when heated are used as criteria for fire-proof properties. Volumetric heating of the material to a maximum temperature of 892 °C was carried out when studying the deformation characteristics. The heat-insulating characteristics of the material were studied during one-sided heating of a material sample in the form of a tile to a maximum temperature of 1050 °C. The characteristics obtained indicate that the material can be used for fire-proof lining of building structures and as for the construction of screen walls and as a filling material in fire barriers.

**Keywords:** coarse aggregate, liquid glass, soda-lime-silicate glass, burned binder, fire-proof characteristics of the material

**Acknowledgements.** *This research was supported by a grant from the Russian Science Foundation No. 21-19-00324, <https://rscf.ru/project/21-19-00324/>*

**Citation:** Erofeev VT, Korotaev SA, Vatin NI. Deformation and Heat-Insulating Characteristics of Light Concrete on Porous Burned Binder Under Heating. *Materials Physics and Mechanics*. 2023;51(1): 33-41. DOI: 10.18149/MPM.5112023\_4.

### Introduction

An effective way to protect geometrically simple building structure elements from fire is by covering them with fire-resistant materials with low thermal conductivity.

The commonly used measure is to use insulation materials with low thermal conductivity to delay the increase in the structure's temperature. This phenomenon prevents structural failures due to fire, including intumescent fire-proof paints [1,2], coatings and plasters of semiliquid compositions [3], and insulation boards with a rigid structure [3,4].

Fire protection thermal insulation materials with a rigid structure can be bricks, stones, sheets, slabs, panels, and shells. The materials are fabricated from cement [5], gypsum [4,6], sodium silicate [7], calcium silicate [8,9,11,16,17], magnesium oxide [10,11], and vermiculite [12]. The polarization of the binder reduces the density and thermal conductivity of the material [4,13] and the inclusion of porous fire-resistant aggregates in its composition [14], for example, perlite and vermiculite [15-17].



Cellular silicate glass or glass foam is recognized for its unique operational and thermal insulation properties and desirable fire resistance. Using different wastes in glass foam production reduces material costs and makes it competitive. The literature [18-20] indicated the critical parameters for material selection and sintering of glass foams produced using waste glass and the glass foam properties. Technologies for obtaining cellular glass from the recycled waste of soda-lime-silicate glass formed in the sphere of consumption have been developed and discussed by several researchers [21-26]. Most conventional soda-lime-silicate glasses have a sufficient high softening temperature of 550-700 °C, so cellular silicate glass can also be used as a fire-retardant material, but with the inclusion of fire-resistant fillers in its composition are not currently implemented.

A study examined the glass-ceramic foams for thermal insulation based on alkali-activation and sintering of zeolite-poor rock [27,28]. The alkali-activation and reactive sintering technology produced the acquired foams by adding powdered eggshell or zeolite-poor rock. A similar technology obtained foam glass from solid waste of flat glass and exhausted alkaline batteries [29].

The frame technology is proposed [30,31] for producing fire protection material with expanded clay as a coarse aggregate. A glass powder was selected for forming a fired porous vitreous binder. The glass powder was obtained by grinding the utilized container and building glass and liquid sodium glass. The obtained material had water resistance, and fire safety properties make it possible to use it as a rigid insulating or structural-insulating construction material. However, the physical and mechanical characteristics of the material have not been studied in detail.

Therefore, a review of existing technologies for manufacturing fire-retardant heat-insulating materials with a rigid structure shows that, at the moment, there are no scientific results and technologies that allow combining the cellular structure of coarse aggregate with a binder.

This study aims to obtain a material with expanded clay filler on a porous calcined soda-lime-silicate waterproof binder and determine its fire-retardant properties. The deformation and heat-insulating characteristics of the samples under heating evaluated the fire-proof properties.

## Materials and methods

Expanded clay with a fraction of 5-10 mm with a bulk density of 530 kg/m<sup>3</sup> was used as a filler for the developed material on a firing binder. The expanded clay fraction with the smallest grain size was selected to reduce the stresses at the interfaces between the grains of the filler and the binder since these stresses increase with an increase in the grain size.

Soda liquid glass with a density of 1.48 g/cm<sup>3</sup> and a suspension of finely ground cullet from the secondary waste of soda-lime-silicate glass were used as components for synthesizing the firing binder. The fineness of glass grinding was characterized by a residue on grid No. 0063 of 5-6%. The chemical composition of glass is presented in Table 1.

**Table 1.** Chemical composition of glass, %

SiO <sub>2</sub>	Al <sub>2</sub> O <sub>3</sub>	Fe <sub>2</sub> O <sub>3</sub>	CaO	MgO	Na <sub>2</sub> O	K <sub>2</sub> O	SO <sub>3</sub>	Mn <sub>3</sub> O <sub>4</sub>	TiO <sub>2</sub>	BaO
60.4	11.8	1.4	8.0	0.3	13.9	2.5	0.3	1.3	1.4	—

The frame technology [30,31] was developed by the authors and used to prepare the samples. The preparation of frame molding technology includes the following operations. Initially, the aggregate's grains were mixed with sodium liquid glass. Then the aggregate with a liquid glass-coated surface was placed in the mold. Further, the mold with the aggregate was placed in an electric airing cupboard and exposed to heat treatment at a temperature of 60-80°C, during which the adhesive bond made of liquid glass hardened. The glued hardened frame of

aggregate grains was removed from the mold and soaked with a water slurry of finely ground cullet from the secondary waste of soda-lime-silicate glass. If the volume of intergranular voids of the cured framework was filled partly with an impregnating suspension of finely ground glass, then the materials macrostructure turned out to be large-porous (Fig. 1, a). A combined macrostructure sample cross section with two layers (monolithic and large-porous) was obtained by completely filling the framework voids on one side with glass suspension and not completely on the other side (Fig. 1, b).

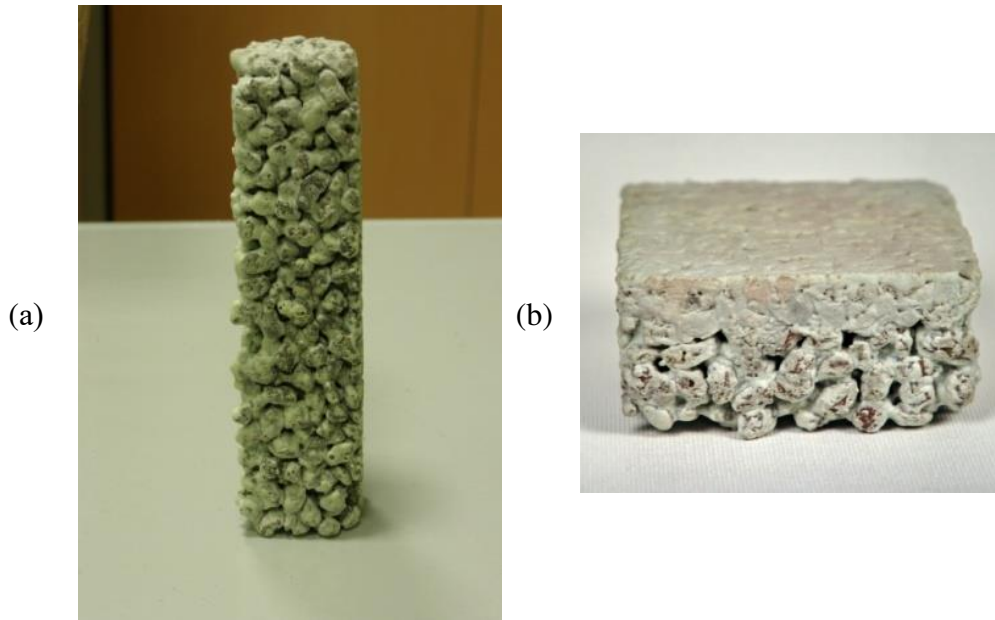
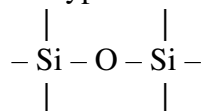


**Fig. 1.** The sample of a large-porous structure size  $42 \times 41 \times 167$  mm (a) and a combined structure sample with large-porous and monolithic layers size  $84 \times 84 \times 40$  mm (b)

The advantage of the board material of the combined structure is the increased adhesion of the coarse-porous layer to the solution of the connecting layer due to the mechanical engagement of the coarse-porous side. After impregnating the glued frame suspension of finely ground glass, it was dried repeatedly at a temperature of  $60-80$  °C. After drying, the molded samples were burned in an electric furnace on a refractory pallet. The frame molding technology burns a raw product without heat-resistant forms. The firing temperature was limited to  $780$  °C.

The material's porous burned binder with the aggregate was synthesized in successive drying and burning operations of the molded sample from two components – sodium liquid glass and a suspension of finely ground cullet. The binder synthesis mechanism obtained by firing including the following stages. The hardening of the frame's liquid-glass glue from aggregate grains during drying is accompanied by the appearance of supersaturated metastable solutions, followed by the transition of hydrate forms of sodium silicates when moisture evaporates into a vitreous state and polymerization of silicon-containing chemical bonds with removing hydroxyl-hydrogen groups with the formation of a silicon polymer frame of a volumetric mesh structure with cells of the type:



After soaking the glued hardened frame with a suspension of cullet, during the initial drying period at the interface of the phases. The partial dissolution of the liquid-glass binder of the frame occurs, accompanied by the transition of sodium cations into the solution due to its

solvation interaction and hydrolysis of the binder's anionic skeleton, leading to the release of monomeric and polymer anions of hydrated silica. At a particular stage of drying, the decrease in the pH of the medium and the increase in the concentration of hydrated silica leads to polymerization of the latter with the formation of viscous gel layers that slow down the dissolution of the liquid-glass binder of the frame. Slowing down the binder's dissolution process contributes to preserving a certain strength by the glued frame and allows the frame to dry off the soaked frame without mold. Simultaneously with the interaction of the suspension of finely ground cullet with the frame's liquid glass glue, leaching and watering of the initial glass structure of the suspension particles occur, the mechanism of which is based on the interaction of aqueous solutions of alkalis with silica. Glass watering occurs during its hydration and hydrolysis. The glass watering is accompanied by the adsorption of hydrated alkali metal cations on the active areas of the silica surface that arise during glass grinding, followed by depolymerization of silica due to the hydrolysis of  $\equiv\text{Si}-\text{O}-\text{Si}\equiv$  bonds with the formation of silanol groups  $\text{Si}-\text{OH}$ . Hydrated silica is transferred during drying to the surface of glass particles. With the increase in its concentration during drying, silicic acid polymerization occurs with a thick elastic gel film with astringent properties. As free water is removed from the dried material, sodium hydro silicates are formed in the volume of the binder from the degradation products of the frame's adhesive binder and the glass particles of the suspension. The free water is remaining after drying forms hydrogen bonds with silanol water. The dried semifinished product's heated up to 400 °C is accompanied by water removal from sodium hydro silicates. Further increasing the temperature to the limiting burning temperature of 740-780 °C resulting the silicic acid bonds are destroyed, the silicic-oxygen tetrahedra polymerize, and water is released during the dehydration of the hydroxyl cover of the glass. In the same temperature range, the eutectic mixture of the  $\text{Na}_2\text{O}-\text{CaO}-\text{SiO}_2$  system formed from the components of the complex binder ensures that during melting, the accumulation of a significant amount of melt with the necessary pyroplastic mobility and the formation of closed pores in the volume of the firing binder. The coincidence of the processes of gas release and the appearance of closed pores in the melt creates conditions for the swelling of the binder due to a sharp increase in vapor pressure in the pores. It is not advisable to increase the firing temperature above 780 °C due to a decrease in the binder viscosity and disturbance of the pore formation process. According to the results of the microscopic examination, the diameter of the pores from the fired binder ranged between 0.02 and 0.5 mm. The swelling of the binder leads to an inevitable volume increase, and the aggregate's grains move apart without changing the product's shape.

The developed technology offers a waterproof material with a large-pore structure and a combined structure with large-pore and monolithic layers with a density of 567 and 710 kg/m<sup>3</sup>, respectively, Fig. 1. The compressive strength of the material in large-pore structure is 1.5 MPa. Prismatic samples of size 42×41×167 mm (Fig. 1, a) were used to determine the deformation of the longitudinal bending under the action of their dead weight during heating in an electric resistance furnace, Fig. 2, a. The increase in temperature rate in the furnace was 14.0 °C/min at the beginning of heating and 4.5 °C/min at the end.

Samples in the form of tiles of a combined structure with large-porous and monolithic layers 84×84×40 mm in size (Fig. 1, b) were used to determine the heat-insulating characteristics of the sample under the influence of temperature from one side. A unilateral effect on the temperature sample was carried out by sealing the opening of the electric resistance furnace with a tile so that the coarsely porous layer of the tile was facing inside the furnace, Fig. 2, b. After sealing the furnace opening with tiles, the temperature in the furnace was raised. The temperature change on the surface of the tile facing outward was recorded with a pyrometer. The heat-insulating characteristics of the tile sample were evaluated by the temperature on the surface of the tile facing outward.

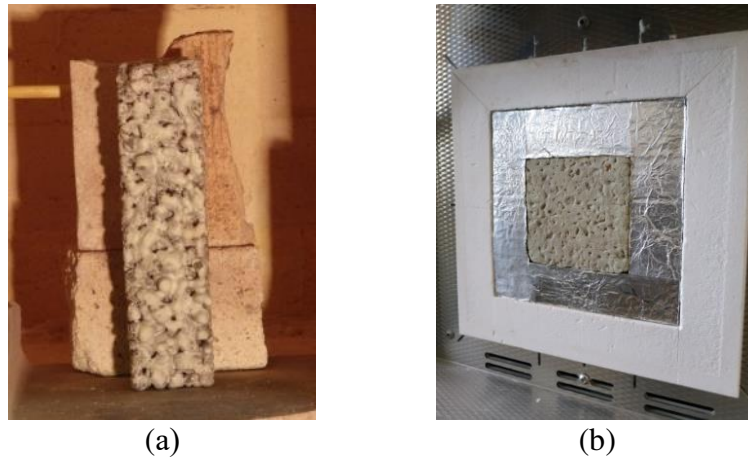


**Fig. 2.** Testing samples for deformation of the longitudinal bending (a) and the heat-insulating characteristics (b) in electric resistance furnaces

### Results and discussion

The following results were obtained for the deformation of longitudinal bending of the samples under study. Visual observation of the samples during their heating in an oven for 70 min up to a temperature of 788 °C; no changes were found in the samples. With a further rise in temperature for 10 min. from 788 °C to 835 °C, buckling deformations of the samples developed due to a decrease in the viscosity of the vitreous binder and its viscous flow. The growth of deformations ended with the loss of stability of the samples at a temperature of about 835 °C, Fig. 3, a. It should be noted that the temperature of 788 °C at the beginning of sample deformation is higher than the temperature range of 550–700 °C at the beginning of softening typical soda-lime-silicate glasses. The interaction of the binder with the surface of the filler, which resists the viscous flow of the binder, contributes to more excellent temperature resistance.

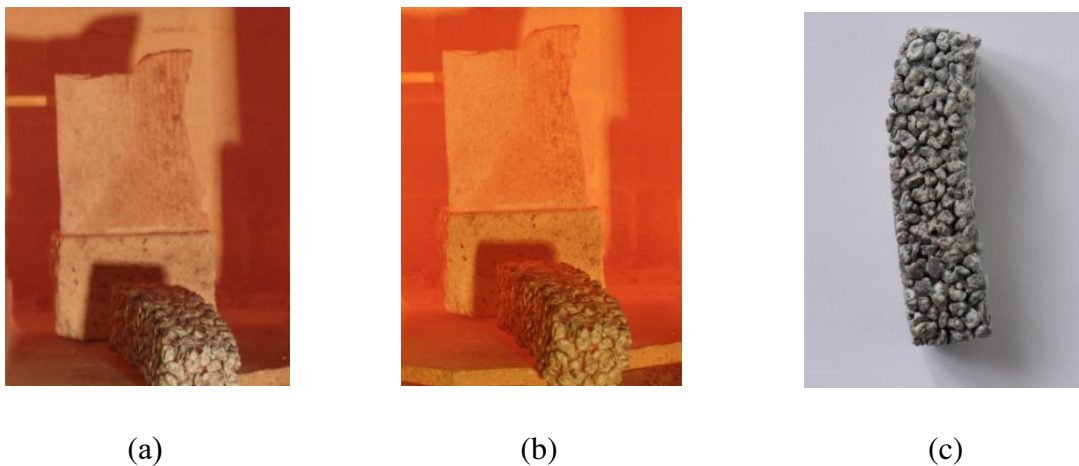


**Fig. 3.** Testing of a sample for refractoriness: a) the sample that has lost stability due to longitudinal bend deformation in a furnace; at a temperature of 835 °C; b) the sample in the furnace at a maximum firing temperature of 892 °C; c) the sample's view after testing

Therefore, the filler increases the material's resistance to deformations under heating. With a further rise in temperature for 20 minutes from 835 °C to 892 °C, no visible changes in the shape of the deformed and buckling specimens were observed (Fig. 3, b, c). Therefore, the resistance of the material of prismatic samples to deformation, caused by the binder's softening

during heating, is maintained up to a temperature of 788 °C, which exceeds the softening point of typical soda-lime-silicate glasses by at least 100 °C. The integrity of the material is preserved when it is heated to even higher temperatures, at least up to 892 °C, under the termination of the longitudinal force from its dead weight on the sample. The preserving of integrity indicates the positive effect of the filler on the increase in the structural strength of the material when heated due to the interaction of the binder with the surface of the filler. Table 2 shows the heat-insulating characteristics of a combined structure tile (Fig. 1, b).

**Table 2.** The tile's heat-insulating characteristics

Time from the beginning of the temperature increase in the heating chamber of the furnace, min	0	5	10	15	30	45	60	75	76
The temperature in the heating chamber, °C	25	320	455	730	900	1020	1050	1050	Trial terminated
Facing the outward sample's surface temperature, °C	25	37	56	147	220	286	324	329	–

The temperature regime in the heating chamber of the furnace complies with the Russian State Standard GOST 30247.0-94 (ISO 834-75) "Elements of building constructions. Fire-resistance test methods. General requirements" [32], used for testing building structures for fire resistance. This dependence determines the temperature regime:

$$T - T_0 = 345 \lg (8t + 1),$$

where  $T$  is the temperature in the furnace corresponding to the time  $t$ , °C;  $T_0$  is the temperature in the furnace before the start of thermal exposure (assumed to be equal to the ambient temperature), °C;  $t$  is the time calculated from the beginning of the test, min.

As a criterion for the limiting state of the enclosing structure in terms of the loss of heat-insulating ability, an increase in temperature on the unheated surface of the structure by more than 220 °C was taken following the fire resistance test methods of Russian State Standard GOST 30247.1–94 "Elements of building constructions. Fire-resistance tests methods. Load-bearing and separating constructions" [33]. Experimental data showed (Table 2) that a temperature increase on the tile's unheated surface by more than 220 °C was recorded after the 30th minute of the test. Following the accepted criterion, 30 min is a required time to reach the limit state based on the loss of the heat-insulating ability of the prototype tile. No visible changes were found in the unheated surface of the sample tile during the test. Inspection after the test of the surface of the sample tile facing the heating chamber of the furnace also showed no visible changes in this surface, except for a change in color towards darkening. Insignificant, by 5 °C, increase in the temperature of the unheated surface of the sample tile while maintaining the maximum temperature of 1050 °C in the heating chamber of the furnace for 15 min. (Table 2) testifies to the high heat-shielding characteristics of the material.

## Conclusion

The object of the study was material with expanded clay filler on a porous calcined soda-lime-silicate waterproof binder (expanded glass concrete). The fire-retardant properties of the material were evaluated by the deformation and heat-insulating characteristics of the samples during heating. According to the research results, water-resistant material with a large-pore

structure and a combined structure with large-pore and monolithic layers with a density of 567 and 710 kg/m<sup>3</sup>, respectively, was proposed. The material of a large-pore structure has a compressive strength of 1.5 MPa. The deformation characteristics of the samples of expanded clay-glass concrete during their heating in an electric furnace were determined by visual observation of the deformations of the buckling of the samples under the action of their dead weight. Deformations develop due to the softening of the porous glassy binder during the heating of the samples. The heat-insulating characteristics of expanded clay-glass concrete were evaluated by the surface temperature of the sample tile during the heating of the opposite tile surface. A hole in the electric furnace was sealed with a sample tile, the temperature in the furnace was raised to 1050 °C, and the temperature was measured with a pyrometer on the surface of the sample facing outward.

The following conclusions are drawn from studying the deformation and heat-insulating characteristics of samples of expanded clay-glass concrete during heating.

1. No deformations were recorded in the samples when it is heated up to 788 °C. When the sample heated above 788 °C, buckling deformations occurred in the samples due to the softening of the porous vitreous binder. The developed deformations lead to the loss of stability of the samples when it reaches a temperature of about 835 °C.

2. The softened glassy binder's interaction with the filler surface leads to an increase in the material's structural strength, as a result of which the temperature of 788 °C at the beginning of the deformation of the samples exceeds the softening point of typical soda-lime-silicate glasses by at least 100 °C.

3. The heating of samples after deformation and stability loss happened at a temperature of 892 °C, exceeding the beginning of softening the glassy binder of expanded clay-glass concrete by about 200 °C, which does not lead to loss of samples integrity.

4. The limiting state of the sample tile of expanded clay-glass concrete in terms of loss of heat-insulating ability was recorded after the 30th minute of the test. The limiting state criterion is an increase in temperature on the unheated surface of the sample tile by more than 220 °C.

5. Insignificant, by 5 °C, increase in the temperature of the unheated surface of the sample tile while maintaining the maximum temperature of 1050 °C for 15 minutes. The furnace's heating chamber indicates the material's high heat-shielding characteristics. The obtained deformation and heat-insulating characteristics of expanded clay-glass concrete during heating show that this material can be used for fire-protective cladding of building structures and fire-protective material in fire-proof partitions and screen walls.

## References

1. Silva D, Nuzzo I, Nigro E, Occhiuzzi A. Intumescent Coatings for Fire Resistance of Steel Structures: Current Approaches for Qualification and Design. *Coatings*. 2022;12(5): 696.
2. Zielecka M, Rabajczyk A, Cygańczuk K, Pastuszka Ł, Jurecki L. Silicone Resin-Based Intumescent Paints. *Materials*. 2020;13(21): 4785.
3. Gao L, Zheng G, Nie X, Wang Y. Thermal performance, mechanical property and fire behavior of epoxy thermoset based on reactive phosphorus-containing epoxy monomer. *Journal of Thermal Analysis and Calorimetry*. 2017;127(2): 1419–1430.
4. Soloveiko S, Pulkis K, Skujans J, Aboltins A. Composite Sandwich-type panel made of foamgypsum. *Engineering for Rural Development*. 2018;17: 1482–1487.
5. Ma X, Pan J, Cai J, Zhang Z, Han J. A review on cement-based materials used in steel structures as fireproof coating. *Construction and Building Materials*. 2022;315: 125623.
6. Nassif AY, Yoshitake I, Allam A. Full-scale fire testing and numerical modelling of the transient thermo-mechanical behaviour of steel-stud gypsum board partition walls. *Construction and Building Materials*. 2014;59: 51–61.



7. Khlystov A, Isaev D, Suldin V. Claydite dust - a unique technogenic raw material for heat-resistant concretes production. *IOP Conference Series: Materials Science and Engineering*. 2021;1015(1): 012070.
8. Qi F, Sun J, Zhu G, Li H, Wu Y, Li S, Yang C, Zheng J, Zhang Y. Recycling of blast furnace slag to prepare calcium silicate hydrate by mechanical-chemical co-activation and its application to calcium silicate fireproof board. *Process Safety and Environmental Protection*. 2022;165: 1–12.
9. Diederichs U, Jäntschi S, Sklenářová D. Thermo-Mechanical Behavior of Fire Protection Boards. *Solid State Phenomena*. 2021;325: 209–214.
10. Vaz G, Raposo J, Reis L, Monteiro P, Viegas D. Rigid Protection System of Infrastructures against Forest Fires. *Fire*. 2022;5(5): 145.
11. Tomar MS, Khurana S, Chowdhury S. A numerical method for studying the effect of calcium silicate lining on road tunnel fires. *Thermal Science and Engineering Progress*. 2022. 29: 101245.
12. Tikhomirova IN, Makarov AV, Htet ZM. Thermal Insulation Materials Based on Expanded Vermiculite and Foamed Liquid Glass. *Refractories and Industrial Ceramics*. 2020;61(4): 451–455.
13. Zhigulina AY, Mizuryaev SA, Chiknovoryan AG. Fire-resistant Heat Insulating Material with Variable Rheology. *IOP Conference Series: Materials Science and Engineering*. 2019;661(1): 012106.
14. Semenov V, Bessonov I, Zhukov A, Mednikova E, Govryakov I. Thermal insulation systems for road bases with foam glass gravel. *Magazine of Civil Engineering*. 2022;110(2): 11003.
15. Jong KYJ, Yew MC, Yew MK, Ting CH, Saw LH, Ng TC, Yeo WH, Beh JH. Fire Resistance and Mechanical Properties of the Fire-Resistant Board. In: *Advances in Material Science and Engineering*. Springer; 2021. p.249–256.
16. Chistova NG, Matyugulina VN, Vititnev AY. The effect of vermiculite on the fire protection of composite materials. *AIP Conference Proceedings*. 2022;2467: 080036.
17. Zhurtov AV, Khezhev TA, Chepurnenko AS, Saibel AV. Two-layer ferrocement shells stress-strain state modeling under the fire conditions. *Materials Science Forum*. 2020;974: 515–520.
18. Siddika A, Hajimohammadi A, Sahajwalla V. Powder sintering and gel casting methods in making glass foam using waste glass: A review on parameters, performance, and challenges. *Ceramics International*. 2022;48(2): 1494–1511.
19. Zhang J, Liu B, Zhang S. A review of glass ceramic foams prepared from solid wastes: Processing, heavy-metal solidification and volatilization, applications. *Science of The Total Environment*. 2021;781: 146727.
20. Siddika A, Hajimohammadi A, Mamun MAA, Alyousef R, Ferdous W. Waste Glass in Cement and Geopolymer Concretes: A Review on Durability and Challenges. *Polymers*. 2021;13(13): 2071.
21. Vaisman YI, Ketov AA, Ketov PA. The scientific and technological aspects of foam glass production. *Glass Physics and Chemistry*. 2015;41(2): 157–162.
22. Bulgakov A, Erofeev V, Bogatov A., Smirnov V, Schach R. Innovative production technology of binding and building composite materials on the basis of glass wastes. In: *Insights and Innovations in Structural Engineering, Mechanics and Computation - Proceedings of the 6th International Conference on Structural Engineering, Mechanics and Computation, SEMC 2016*. 2016. p.1583–1586.
23. Lesovik VS, Bessonov IV, Bulgakov BI, Larsen OA, Puchka OV, Vaysera SS. Approach on Improving the Performance of Thermal Insulating and Acoustic Glass

Composites. *IOP Conference Series: Materials Science and Engineering*. 2018;463(4): 042030.

24. Bessonov I, Zhukov A, Shokodko E, Chernov A. Optimization of the technology for the production of foam glass aggregate. *E3S Web of Conferences*. 2020;164: 14016.

25. Panov YT, Ermolaeva EV, Nikonov AV, Timakov EA. High-Performance Thermal Insulation Material Based on Waste Glass. *IOP Conference Series: Materials Science and Engineering*. 2020;896: 012074 .

26. Ji R, Zheng Y, Zou Z, Chen Z, Wei S, Jin X, Zhang M. Utilization of mineral wool waste and waste glass for synthesis of foam glass at low temperature. *Construction and Building Materials*. 2019;215: 623–632.

27. Ibrahim JFM, Gömze LA, Koncz-Horvath D, Filep Á, Kocserha I. Preparation, characterization, and physicochemical properties of glass-ceramic foams based on alkali-activation and sintering of zeolite-poor rock and eggshell. *Ceramics International*. 2022;48(18): 25905–25917.

28. Ibrahim JEFM, Tihtih M, Kurovics E, Gömze LA, Kocserha I. Innovative glass-ceramic foams prepared by alkali activation and reactive sintering of clay containing zeolite (zeolite-poor rock) and sawdust for thermal insulation. *Journal of Building Engineering*. 2022;59: 105160.

29. Cruz GM, Murr CG, Stafin G, Grzebielucka EC, Ferreira Borges CP, Arrúa MEP, de Souza ECF, Alves SA, Masetto Antunes SR. A novel foam glass obtained from solid waste: A sustainable strategy for application in the degradation of an environmental pollutant. *Ceramics International*. 2022;48(18): 26351–26360.

30. Erofeev VT, Korotaev SA. Frame technology of the fired material with aggregate on a glasslike binder. *Construction Materials*. 2014;3: 88–91.

31. Erofeev V, Korotaev S, Bulgakov A, Tretiakov I, Rodin A. Getting Fired Material with Vitreous Binder Using Frame Technology. *Procedia Engineering*. 2016;164: 166–171.

32. Russian State Standard GOST 30247.0-94 (ISO 834-75). *Elements of building constructions. Fire-resistance test methods. General requirements*. Moscow: IPK Standard Publishing; 2003. (In Russian)

33. Russian State Standard GOST 30247.1–94. *Elements of building constructions. Fire-resistance tests methods. Load-bearing and separating constructions*. Moscow: IPK Standard Publishing; 1995. (In Russian)

## THE AUTHORS

**Erofeev V.T.** 

e-mail: yerofeevvt@mail.ru

**Korotaev S.A.** 

e-mail: korotaevc@yandex.ru

**Vatin NI.** 

e-mail: vatin@mail.ru

## Wave propagation in a nonlocal rotating micropolar piezoelectric solid

Baljeet Singh <sup>1</sup>✉ , Asha Sangwan <sup>2</sup> , Jagdish Singh <sup>3</sup> 

<sup>1</sup>Department of Mathematics, Post Graduate Government College, Sector-11, Chandigarh-160011, India

<sup>2</sup>Department of Mathematics, Government College, Sampla, Rohtak-124001, Haryana, India

<sup>3</sup>Department of Mathematics, Maharshi Dayanand University, Rohtak, -124001, Haryana, India

✉ [bsinghgc11@gmail.com](mailto:bsinghgc11@gmail.com)

**Abstract.** The nonlocal theory of elasticity is applied to formulate the governing equations of nonlocal micropolar piezoelectric material in a rotating frame. The governing equations are specialized for a plane and solved to show the existence of three coupled plane waves. Reflection of a coupled longitudinal displacement wave is considered at a stress-free surface of half-space containing the micropolar piezoelectric material. For the incidence of coupled longitudinal displacement waves, the expressions of reflection coefficients and energy ratios for reflected waves are derived. A quantitative example is set up to illustrate the effects of rotation and nonlocal parameters on the reflection coefficients and energy ratios in a given range of the angle of incidence.

**Keywords:** plane waves, nonlocality, rotation, reflection coefficients, energy ratios

**Citation:** Singh Baljeet, Sangwan Asha, Singh Jagdish. Wave propagation in a nonlocal rotating micropolar piezoelectric solid. *Materials Physics and Mechanics*. 2023;51(1): 42-60. DOI: 10.18149/MPM.5112023\_5.

### Introduction

Plane wave reflection and refraction phenomenon are extensively used to conduct non-destructive testing or non-destructive evaluation of composites for characterizing/mapping subsurface defects and assessing the in-situ condition of structural components without reforming the original features of the composites in a non-tarnish way. Elastic wave propagation problems in layered media have been discussed by several authors. Prominent among them are Knott [1], Jeffreys [2], Gutenberg [3], Ergin [4], Ewing et al. [5], and Achenbach [6].

Piezoelectric materials find their utility as sensors and actuators in many applications involving signal transmission. Various analytical studies on wave characteristics in piezoelectric materials were investigated (Kyame [7], Pailloux [8], Cheng and Sun [9], Auld [10], Alshits et al. [11], Parton and Kudryavtsev [12], Every and Neiman [13], Alshits and Shuvalov [14], Wang [15], Yang [16], Pang et al. [17], Darinskii et al. [18], Burkov et al. [19], Abd-alla and Al-sheikh [20], Singh [21], Kuang and Yuan [22], Yuan and Zhu [23], Guo and Wei [24], Guo et al. [25], Othman et al. [26], Singh and Singh [27], Jiao et al. [28], Sahu et al. [29], Singh et al. [30], Liu et al. [31].

The translation and rotation of a moving object can be sensed by accelerometers and gyroscopes, respectively. These motion sensors are used as an important tool in smart weapon systems, video cameras, automobiles, robotics, navigation, and machine control. Recently, vibratory gyroscopes made up of piezoelectric materials have been a centre of research. The governing equations with Centrifugal and Coriolis accelerations for a rotating piezoelectric body are responsible for observing the fundamental nature of the piezoelectric gyroscope. The

rotational effects on plane waves in an isotropic medium were observed by Schoenberg and Censor [32]. According to White [33], the rotational effect on frequency or wave speed provides valuable inputs for acoustic sensors design. In particular, the rotation-induced frequency shifts have been applied to manufacture the gyroscopes (Tiersten et al. [34], Tiersten et al. [35], Wren and Burdett [36]).

In recent years, the materials and structures have been considered on a nano-scale to meet the requirement of various acoustic devices to have greater sensitivity and storage within the smaller structure. The applications of nonlocal theory help to explain and predict physical phenomena at small length scales. Edelen et al. [37], Eringen and Edelen [38], and Eringen [39] developed the nonlocal elasticity theory characterized by the presence of nonlocality residuals fields like body force, mass, entropy, and internal energy. Eringen [40,41] applied the nonlocal elasticity theory to investigate plane waves in elastic media. Thereafter, various researchers investigated wave propagation problems by using nonlocal elasticity theories. More recent works are cited as Roy et al. [42], Khurana and Tomar [43,44], Singh [45,46], Kaur and Singh [47], Liu et al. [31] and Tung [48].

The micropolar elasticity extends classical elasticity with extra independent degrees of freedom for local rotation. Eringen [49-51] introduced linear micropolar elasticity, where the motions of the particles are represented by the displacement and micro-rotation vectors. The theory of micropolar elasticity was further applied by various researchers in piezoelectric materials. For example, the works of Craciun [52], Ciomasu and Vieru [53], Vieru and Ciomasu [54], Zhilin and Kolpakov [55], Aouadi [56], and Gales [57] are cited for reference. Recently, the piezoelectricity of micropolar materials was used to explore the plane and surface wave characteristics by Singh and Sindhu [58,59], Sangwan et al. [60], Singh et al. [61] and Bijarnia et al. [62]. The main motivation of this paper is to apply the nonlocal elasticity theory for the investigation of rotational effects on plane waves in the micropolar piezoelectric medium.

In section 2, the governing equations of a transversely isotropic, rotating, nonlocal micropolar piezoelectric medium are specialized for a plane. In section 3, the existence of three coupled plane waves is discussed. In section 4, a reflection phenomenon of coupled longitudinal displacement wave from a traction-free boundary of a semi-infinite space is considered. The expressions for reflection coefficients and energy ratios are derived. In section 5, some special cases are discussed. In section 6, a quantitative example of the model is set up to graphically illustrate the effects of rotation and nonlocality on the speeds, amplitude ratios, and energy ratios in a given range of propagation angles.

## Governing equations

We consider a nonlocal rotating micropolar piezoelectric solid material with constant angular velocity  $\vec{\Omega} = \Omega \hat{n}$ , where  $\hat{n}$  is a unit vector along the axis of rotation. The fixed coordinate system in the rotating solid introduces Centripetal acceleration  $\vec{\Omega} \times (\vec{\Omega} \times \vec{u})$  by virtue of time-changing motion only and Coriolis acceleration  $(2\vec{\Omega} \times \vec{\dot{u}})$ . According to Schoenberg and Censor [32], Eringen and Edelen [38], Eringen [39], and Aouadi [56], the fundamental system of field equations without body forces and body couples for the linear theory of rotating nonlocal micropolar piezoelectric solids are formulated as

(a) The equations of the motion

$$\sigma_{ji,j} = \rho \left[ \ddot{u}_i + \left\{ \vec{\Omega} \times (\vec{\Omega} \times \vec{u}) \right\}_i + (2\vec{\Omega} \times \vec{\dot{u}})_i \right], \quad (1)$$

$$m_{ik,i} + \varepsilon_{ijk} \sigma_{ij} = \rho j \ddot{\phi}_k, \quad (2)$$

(b) The equations of the electric fields

$$D_{j,j} = q_e, \quad E_k = -\psi_{,k}, \quad (3)$$

(c) The constitutive equations

$$(1 - \varepsilon^2 \nabla^2) \sigma_{ij} = c_{ijkl} e_{kl} + b_{ijkl} \kappa_{kl} + \lambda_{ijk} E_k, \quad (4)$$

$$(1 - \varepsilon^2 \nabla^2) m_{ij} = b_{klij} e_{kl} + a_{ijkl} \kappa_{kl} + \beta_{ijk} E_k, \quad (5)$$

$$D_k = -\lambda_{ijk} e_{ij} - \beta_{ijk} \kappa_{ij} + \gamma_{jk} E_j, \quad (6)$$

(d) The geometrical equations

$$e_{ij} = u_{j,i} + \varepsilon_{ijk} \phi_k, \quad \kappa_{ij} = \phi_{j,i}, \quad (7)$$

where  $\rho$  is the mass density,  $\varepsilon$  is the nonlocal parameter,  $\vec{u}$  is the displacement vector,  $\vec{\phi}$  is the microrotation vector,  $\sigma_{ij}$  is the stress tensor,  $m_{ij}$  is the couple stress tensor,  $j$  is the micro-inertia,  $\varepsilon_{ijk}$  is the alternating symbol,  $D_k$  is the dielectric displacement vector,  $q_e$  is the volume charge density,  $E_j$  is the electric field vector,  $\psi$  is the electrostatic potential,  $e_{ij}$  and  $\kappa_{ij}$  are kinematic strain measures and  $a_{ijkl}$ ,  $b_{ijkl}$ ,  $c_{ijkl}$ ,  $\lambda_{ijk}$ ,  $\beta_{ijk}$  and  $\gamma_{jk}$  are constitutive coefficients. The symbol  $\nabla^2$  is the Laplace operator. Subscripts preceded by a comma denote space partial derivatives. The superposed dot denotes time partial derivatives. The constitutive coefficients satisfy the following symmetry relations

$$c_{ijkl} = c_{klij}, \quad a_{ijkl} = a_{klij}, \quad \gamma_{ij} = \gamma_{ji}. \quad (8)$$

Now, we consider an infinite linear, homogeneous, and transversely isotropic nonlocal rotating micropolar piezoelectric solid half-space. We take the origin of the rectangular Cartesian coordinate system  $(x_1, x_2, x_3)$  on the free surface  $x_3 = 0$  and  $x_3$ -axis is taken normal to the half-space. The plane of isotropy is taken perpendicular to  $x_3$ -axis and the rotation is assumed with constant angular velocity  $\vec{\Omega}$  about  $x_2$ -axis. For a two-dimensional problem, we consider the following components of displacement vector  $\vec{u}$ , microrotation vector  $\vec{\phi}$ , and angular velocity  $\vec{\Omega}$

$$\vec{u} = (u_1, 0, u_3), \quad \vec{\phi} = (0, \phi_2, 0), \quad \vec{\Omega} = (0, \Omega, 0). \quad (9)$$

Using Equation (9) in Equations (1-8), the governing equations for transversely isotropic rotating nonlocal micropolar piezoelectric medium in  $x_1 - x_3$  plane reduce to the following system of four partial differentials equations in  $u_1, u_3, \phi_2$  and  $\psi$

$$A_{11} \frac{\partial^2 u_1}{\partial x_1^2} + (A_{13} + A_{56}) \frac{\partial^2 u_3}{\partial x_1 \partial x_3} + A_{55} \frac{\partial^2 u_1}{\partial x_3^2} + K_1 \frac{\partial \phi_2}{\partial x_3} - (\lambda_{15} + \lambda_{31}) \frac{\partial^2 \psi}{\partial x_1 \partial x_3} = \rho (1 - \varepsilon^2 \nabla^2) \left[ \frac{\partial^2 u_1}{\partial t^2} - \Omega^2 u_1 + 2\Omega \frac{\partial u_3}{\partial t} \right] \quad (10)$$

$$A_{66} \frac{\partial^2 u_3}{\partial x_1^2} + (A_{13} + A_{56}) \frac{\partial^2 u_1}{\partial x_1 \partial x_3} + A_{33} \frac{\partial^2 u_3}{\partial x_3^2} + K_2 \frac{\partial \phi_2}{\partial x_1} - \lambda_{15} \frac{\partial^2 \psi}{\partial x_1^2} - \lambda_{33} \frac{\partial^2 \psi}{\partial x_3^2} = \rho (1 - \varepsilon^2 \nabla^2) \left[ \frac{\partial^2 u_3}{\partial t^2} - \Omega^2 u_3 - 2\Omega \frac{\partial u_1}{\partial t} \right] \quad (11)$$

$$B_{77} \frac{\partial^2 \phi_2}{\partial x_1^2} + B_{66} \frac{\partial^2 \phi_2}{\partial x_3^2} - \chi \phi_2 - K_1 \frac{\partial u_1}{\partial x_3} - K_2 \frac{\partial u_3}{\partial x_1} = \rho j (1 - \varepsilon^2 \nabla^2) \frac{\partial^2 \phi_2}{\partial t^2} \quad (12)$$

$$\lambda_{15} \frac{\partial^2 u_3}{\partial x_1^2} + \lambda_{33} \frac{\partial^2 u_3}{\partial x_3^2} + (\lambda_{15} + \lambda_{31}) \frac{\partial^2 u_1}{\partial x_1 \partial x_3} + \gamma_{11} \frac{\partial^2 \psi}{\partial x_1^2} + \gamma_{33} \frac{\partial^2 \psi}{\partial x_3^2} = 0 \quad (13)$$

where

$$\nabla^2 = \frac{\partial^2}{\partial x_1^2} + \frac{\partial^2}{\partial x_3^2},$$

$$\begin{aligned} A_{11} &= C_{1111}, A_{55} = C_{3131}, A_{13} = C_{1133} = C_{3311}, A_{56} = C_{3113} = C_{1331}, A_{66} = C_{1313}, A_{33} = C_{3333}, \\ K_1 &= A_{56} - A_{55} = C_{3113} - C_{3131}, K_2 = A_{66} - A_{56} = C_{1313} - C_{1331}, \chi = K_2 - K_1, B_{77} = a_{1212}, \\ B_{66} &= a_{3232}, \lambda_{31} = \lambda_{311}, \lambda_{33} = \lambda_{333}, \lambda_{45} = \lambda_{431} = \lambda_{413}, \lambda_{35} = \lambda_{313} = \lambda_{331}. \end{aligned}$$

### Plane waves

The plane harmonic solutions of Equations (10-13) are considered as

$$\{u_1, u_3, \phi_2, \psi\} = \{u_1^*, u_3^*, \phi_2^*, \psi^*\} \exp\{ik(x_1 \sin \theta + x_3 \cos \theta) - i\omega t\}, \quad (14)$$

where  $i = \sqrt{-1}$ ,  $k$  is the wave number,  $\omega$  is the circular frequency,  $\theta$  is propagation angle, and  $v$  is the propagation speed.

Using Equation (14) in Equations (10-13), we obtain a homogenous system of four equations in  $u_1^*, u_3^*, \phi_2^*$  and  $\psi^*$  the non-zero solutions of which require the following condition

$$D_0 \Lambda^3 - D_1 \Lambda^2 + D_2 \Lambda - D_3 = 0, \quad (15)$$

where  $\Lambda = \rho \left( \frac{v}{\omega} \right)^2$  and the expressions for  $D_j$  ( $j = 0, 1, 2, 3$ ) are given as

$$D_0 = \alpha_5 M_3 (M_1^2 + M_2^2),$$

$$D_1 = \alpha_5 M_1 M_3 (\alpha_1 + \alpha_2) + \alpha_5 M_1 \left[ (K_1^*)^2 + (K_2^*)^2 \right] + M_1 M_3 (\alpha_3^2 + B_3^2)$$

$$- \alpha_5 M_2 M_3 (B_2 - B_1) - \alpha_4 \alpha_5 (M_1^2 + M_2^2),$$

$$D_2 = (\alpha_2 \alpha_5 + \alpha_3^2) (K_1^*)^2 + (\alpha_1 \alpha_5 + B_3^2) (K_2^*)^2 - (2\alpha_3 B_3 + \alpha_5 B_1 + \alpha_5 B_2) K_1^* K_2^*$$

$$- \alpha_4 M_1 (\alpha_3^2 + B_3^2) - \alpha_4 \alpha_5 M_1 (\alpha_1 + \alpha_2) - (B_1 + B_2) \alpha_3 B_3 M_3$$

$$+ (\alpha_1 \alpha_3^2 + \alpha_2 B_3^2) M_3 + (\alpha_1 \alpha_2 - B_1 B_2) \alpha_5 M_3 + \alpha_4 \alpha_5 M_2 (B_2 - B_1),$$

$$D_3 = \alpha_4 \alpha_5 B_1 B_2 + (B_1 + B_2) \alpha_3 \alpha_4 B_3 - \alpha_1 \alpha_4 \alpha_3^2 - \alpha_2 \alpha_4 B_3^2 - \alpha_1 \alpha_2 \alpha_4 \alpha_5,$$

where

$$\alpha_1 = A_{11} \sin^2 \theta + A_{55} \cos^2 \theta - \left[ 1 + (\Omega^*)^2 \right] \rho \varepsilon^2 \omega^2,$$

$$\alpha_2 = A_{66} \sin^2 \theta + A_{33} \cos^2 \theta - \left[ 1 + (\Omega^*)^2 \right] \rho \varepsilon^2 \omega^2, \quad \alpha_3 = \lambda_{15} \sin^2 \theta + \lambda_{33} \cos^2 \theta,$$

$$\alpha_4 = B_{77} \sin^2 \theta + B_{66} \cos^2 \theta - \rho j \varepsilon^2 \omega^2, \quad \alpha_5 = \gamma_{11} \sin^2 \theta + \gamma_{33} \cos^2 \theta,$$

$$B_1 = (A_{13} + A_{56}) \sin \theta \cos \theta - 2i \Omega^* \rho \varepsilon^2 \omega^2, \quad B_2 = (A_{13} + A_{56}) \sin \theta \cos \theta + 2i \Omega^* \rho \varepsilon^2 \omega^2,$$

$$B_3 = (\lambda_{45} + \lambda_{31}) \sin \theta \cos \theta, \quad K_1^* = i K_1 \cos \theta, \quad K_2^* = i K_2 \sin \theta,$$

$$\Omega^* = \frac{\Omega}{\omega}, \quad M_1 = \left[ 1 + (\Omega^*)^2 \right] \rho \omega^2, \quad M_2 = 2i \Omega^* \rho \omega^2, \quad M_3 = \chi - \rho j \omega^2.$$

The dispersion Equation (15) is a cubic equation in  $v^2$ . Three roots  $v_1, v_2$  and  $v_3$  of Equation (15) are found to be real and positive with inequality  $v_1 > v_2 > v_3$ . These three roots suggest the existence of three plane waves, namely, Coupled Longitudinal Displacement

(CLD), Coupled Transverse Displacement (CTD), and Coupled Transverse Microrotational (CTM) waves with distinct speeds  $v_1$ ,  $v_2$  and  $v_3$ , respectively.

### Reflection of Coupled Longitudinal Displacement (CLD) wave

An incident CLD wave propagating with velocity  $v_1$  through the transversely isotropic rotating nonlocal micropolar piezoelectric solid half-space (M) strikes the free surface  $x_3 = 0$  making an angle  $\theta_o$  with negative  $x_3$ -axis. The incident CLD wave will generate three reflected waves as CLD, CTD, and CTM waves in medium M. The geometry showing the directions of striking waves and reflected waves is illustrated in Fig. 1.

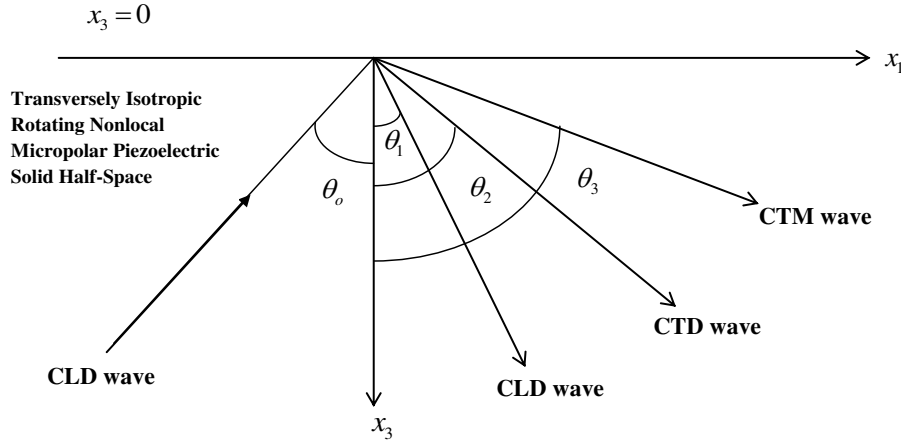


**Fig. 1.** Geometry of the problem illustrating the striking and reflected waves

The appropriate displacement components  $u_1, u_3$ , microrotation component  $\phi_2$ , and electric potential  $\psi$  for the incident and reflected waves in medium M are

$$u_1 = A_o \exp\{ik_1(x_1 \sin \theta_o + x_3 \cos \theta_o) - i\omega t\} + \sum_{j=1}^3 A_j \exp\{ik_j(x_1 \sin \theta_j - x_3 \cos \theta_j) - i\omega t\}, \quad (16)$$

$$u_3 = \xi_1^* A_o \exp\{ik_1(x_1 \sin \theta_o + x_3 \cos \theta_o) - i\omega t\} + \sum_{j=1}^3 \xi_j A_j \exp\{ik_j(x_1 \sin \theta_j - x_3 \cos \theta_j) - i\omega t\}, \quad (17)$$

$$\phi_2 = \eta_1^* A_o \exp\{ik_1(x_1 \sin \theta_o + x_3 \cos \theta_o) - i\omega t\} + \sum_{j=1}^3 \eta_j A_j \exp\{ik_j(x_1 \sin \theta_j - x_3 \cos \theta_j) - i\omega t\}, \quad (18)$$

$$\psi = \zeta_1^* A_o \exp\{ik_1(x_1 \sin \theta_o + x_3 \cos \theta_o) - i\omega t\} + \sum_{j=1}^3 \zeta_j A_j \exp\{ik_j(x_1 \sin \theta_j - x_3 \cos \theta_j) - i\omega t\}, \quad (19)$$

where the explicit expressions for coupling coefficients  $\xi_1^*, \eta_1^*, \zeta_1^*, \xi_j, \eta_j$  and  $\zeta_j$  ( $j=1,2,3$ ) are provided in Appendix.

The mechanical boundary conditions applied at  $x_3 = 0$  are vanishing of the normal force stress component, tangential force stress component, and tangential couple stress component i.e.,



$$\sigma_{33} = 0, \sigma_{31} = 0, m_{32} = 0, \quad (20)$$

where

$$\begin{aligned} (1 - \varepsilon^2 \nabla^2) \sigma_{33} &= A_{13} \frac{\partial u_1}{\partial x_1} + A_{33} \frac{\partial u_3}{\partial x_3} - \lambda_{35} \frac{\partial \psi}{\partial x_1} - \lambda_{33} \frac{\partial \psi}{\partial x_3}, \\ (1 - \varepsilon^2 \nabla^2) \sigma_{31} &= A_{56} \frac{\partial u_3}{\partial x_1} + A_{55} \frac{\partial u_1}{\partial x_3} + (A_{56} - A_{55}) \phi_2 - \lambda_{31} \frac{\partial \psi}{\partial x_1} - \lambda_{35} \frac{\partial \psi}{\partial x_3}, \\ (1 - \varepsilon^2 \nabla^2) m_{32} &= B_{66} \frac{\partial \phi_2}{\partial x_3}. \end{aligned}$$

The displacement components, microrotation component, and electric potential functions given by Equations (16) to (19) satisfy the boundary conditions (20) with the following relations (analogous to Snell's law)

$$k_1 \sin \theta_o = k_1 \sin \theta_1 = k_2 \sin \theta_2 = k_3 \sin \theta_3, \quad k_1 v_1 = k_2 v_2 = k_3 v_3 \quad (21)$$

and the following three relations in amplitude ratios of reflected waves are derived as

$$\sum_{j=1}^3 a_{ij} Z_j = h_i, \quad (i=1,2,3), \quad (22)$$

where  $Z_j = \frac{A_j}{A_o}$ ,  $(j=1,2,3)$  are amplitude ratios of reflected CLD wave, reflected CTD wave,

and reflected CTM wave, respectively and

$$\begin{aligned} a_{1j} &= \frac{(A_{13} - \lambda_{35} \zeta_j) \sin \theta_o - (A_{33} \xi_j - \lambda_{33} \zeta_j) f_j^*}{(A_{13} - \lambda_{35} \zeta_1^*) \sin \theta_o + (A_{33} \xi_1^* - \lambda_{33} \zeta_1^*) \cos \theta_o}, \quad (j=1,2,3) \\ a_{2j} &= \frac{(A_{56} \xi_j - \lambda_{31} \zeta_j) \sin \theta_o - (A_{55} - \lambda_{35} \zeta_j) f_j^* - i(A_{56} - A_{55}) \left( \frac{v_1}{v_j} \right) \left( \frac{\eta_j}{k_j} \right)}{(A_{56} \xi_1^* - \lambda_{31} \zeta_1^*) \sin \theta_o + (A_{55} - \lambda_{35} \zeta_1^*) \cos \theta_o - i(A_{56} - A_{55}) \left( \frac{\eta_1}{k_1} \right)}, \quad (j=1,2,3) \\ a_{3j} &= \frac{\left( \frac{\eta_j}{k_j} \right) \left( \frac{v_1}{v_j} \right) f_j^*}{\left( \frac{\eta_1}{k_1} \right) \cos \theta_o}, \quad (j=1,2,3) \end{aligned}$$

$$h_1 = -1, h_2 = -1, h_3 = 1,$$

where

$$f_j^* = \sqrt{\left( \frac{v_1}{v_j} \right)^2 - \sin^2 \theta_o}, \quad (j=1,2,3).$$

Following Achenbach [6], the rate of energy transmission at the interface  $x_3 = 0$  is

$$P^* = (1 - \varepsilon^2 \nabla^2) \sigma_{33} \frac{\partial u_3}{\partial t} + (1 - \varepsilon^2 \nabla^2) \sigma_{31} \frac{\partial u_1}{\partial t} + (1 - \varepsilon^2 \nabla^2) m_{32} \frac{\partial \phi_2}{\partial t}. \quad (23)$$

The time rate of average energy transmission for the respective wave to that of the incident wave, denoted by  $E_j (j=1,2,3)$  for reflected CLD, reflected CTD, and reflected CTM, respectively, are given as

$$E_j = \frac{\langle P_j^* \rangle}{\langle P_0^* \rangle}, \quad (j=1,2,3), \quad (24)$$

where  $\langle P_0^* \rangle$  denotes the average energy transmission per unit surface area per unit time for incident CLD wave in rotating nonlocal micropolar piezoelectric medium M.

The expressions for energy ratios at the interface  $x_3 = 0$  are given as

$$E_j = \left( \frac{\hbar_{1j} + \hbar_{2j} - \hbar_{3j}}{\hbar_0} \right) Z_j^2, \quad (j=1,2,3) \quad (25)$$

where

$$\begin{aligned} \hbar_{1j} &= (A_{13}\xi_j + A_{56}\xi_j - \lambda_{35}\xi_j\zeta_j - \lambda_{31}\zeta_j) \sin \theta_o, \\ \hbar_{2j} &= -(A_{55} + A_{33}\xi_j^2 - \lambda_{33}\xi_j\zeta_j - \lambda_{35}\zeta_j + B_{66}\eta_j^2) \sqrt{\left(\frac{v_1}{v_j}\right)^2 - \sin^2 \theta_o}, \\ \hbar_{3j} &= i(A_{56} - A_{55}) \left(\frac{v_1}{v_j}\right) \left(\frac{\eta_j}{k_j}\right), \\ \hbar_0 &= \left\{ \begin{aligned} &(A_{13}\xi_1^* + A_{56}\xi_1^* - \lambda_{35}\xi_1^*\zeta_1^* - \lambda_{31}\zeta_1^*) \sin \theta_o + \\ &(A_{55} + A_{33}\xi_1^{*2} - \lambda_{33}\xi_1^*\zeta_1^* - \lambda_{35}\zeta_1^* + B_{66}\eta_1^{*2}) \cos \theta_o - i(A_{56} - A_{55}) \left(\frac{\eta_1^*}{k_1}\right) \end{aligned} \right\}. \end{aligned}$$

### Particular cases

- (a) In the absence of nonlocal parameter ( $\varepsilon = 0$ ), the above theoretical analysis reduces for the case when a plane wave is incident at a traction-free boundary of a transversely isotropic rotating micropolar piezoelectric solid half-space.
- (b) In the absence of rotation rate ( $\Omega^* = 0$ ), the above theoretical analysis reduces for the case when a plane wave is incident at a traction-free boundary of a transversely isotropic nonlocal micropolar piezoelectric solid half-space.
- (c) In absence of rotation and nonlocality ( $\Omega^* = 0, \varepsilon = 0$ ), the above theoretical analysis reduces for the case when a plane wave is incident at a traction-free boundary of a micropolar piezoelectric solid half-space of transversely isotropic type.

### Numerical results and discussion

For illustrations of speeds, amplitude ratios, and energy ratios, the following physical constants of a micropolar piezoelectric material are considered (Singh and Sindhu [59], Sangwan et al. [60])

$$\begin{aligned} A_{11} &= 17.8 \times 10^{10} \text{ Nm}^{-2}, A_{33} = 18.43 \times 10^{10} \text{ Nm}^{-2}, A_{13} = 7.59 \times 10^{10} \text{ Nm}^{-2}, A_{56} = 1.89 \times 10^{10} \text{ Nm}^{-2}, \\ A_{55} &= 4.357 \times 10^{10} \text{ Nm}^{-2}, A_{66} = 4.42 \times 10^{10} \text{ Nm}^{-2}, B_{77} = 2.78 \times 10^{10} \text{ N}, B_{66} = 2.68 \times 10^{10} \text{ N}, \\ \lambda_{15} &= 1 \times 10^{-5} \text{ Cm}^{-2}, \lambda_{31} = 3.9 \text{ Cm}^{-2}, \lambda_{33} = 1.33 \text{ Cm}^{-2}, \lambda_{35} = 0.23 \text{ Cm}^{-2}, \omega = 10^5 \text{ Hz}, \\ \gamma_{11} &= 85.2 \text{ C}^2 \text{ N}^{-1} \text{ m}^{-2}, \gamma_{33} = 28.7 \text{ C}^2 \text{ N}^{-1} \text{ m}^{-2}, \rho = 1740 \text{ Kg m}^{-3}, j = 0.196 \text{ m}^2. \end{aligned}$$

For the above physical constants, Equations (15), (22), and (25) are solved numerically with the help of programming in MATLAB. The propagation speeds, the modulus of amplitude ratios, and energy ratios of various reflected waves are computed for different values of nonlocal parameter  $\varepsilon$  and rotation rate  $\Omega^*$ . The CLD and CTM waves are observed as the fastest and slowest waves, respectively.

### Speeds of plane waves

*Speeds versus rotation parameter.* To illustrate the effects of rotation and nonlocal parameters, the speeds of CLD, CTD, and CTM waves are plotted against rotation rate  $\Omega^*$  ( $0 \leq \Omega^* < 1$ ) in Fig. 2 for three distinct nonlocal parameters when the angle of incidence  $\theta_o$  is fixed as  $45^\circ$ . The solid, dashed, and dotted curves in Fig. 2 correspond to the speed variations of CLD, CTD, and CTM waves for the nonlocal parameter  $\varepsilon = 0, 0.007, 0.008$ , respectively. For  $\varepsilon = 0, 0.007$  and  $0.008$ , the speed of CLD wave as shown in Fig. 2(a) is approximately  $0.96 \times 10^4 \text{ ms}^{-1}$  at  $\Omega^* = 0$  and it increases uniformly as the rotation parameter  $\Omega^*$  increases from 0 to 0.9. Beyond  $\Omega^* = 0.9$ , the speed of CLD wave increases very sharply to a maximum value  $8.045 \times 10^5 \text{ ms}^{-1}$  at  $\Omega^* = 0.99$ . The speeds of CTD and CTM waves as illustrated in Fig. 2 decrease uniformly as  $\Omega^*$  increases from 0 to 0.99. However, the rate of decrease in speed of CTM wave is very low as compared to CTD wave. From Figure 2, it is noticed that the speeds of CLD, CTD, and CTM waves become slow in the presence of nonlocal parameters.

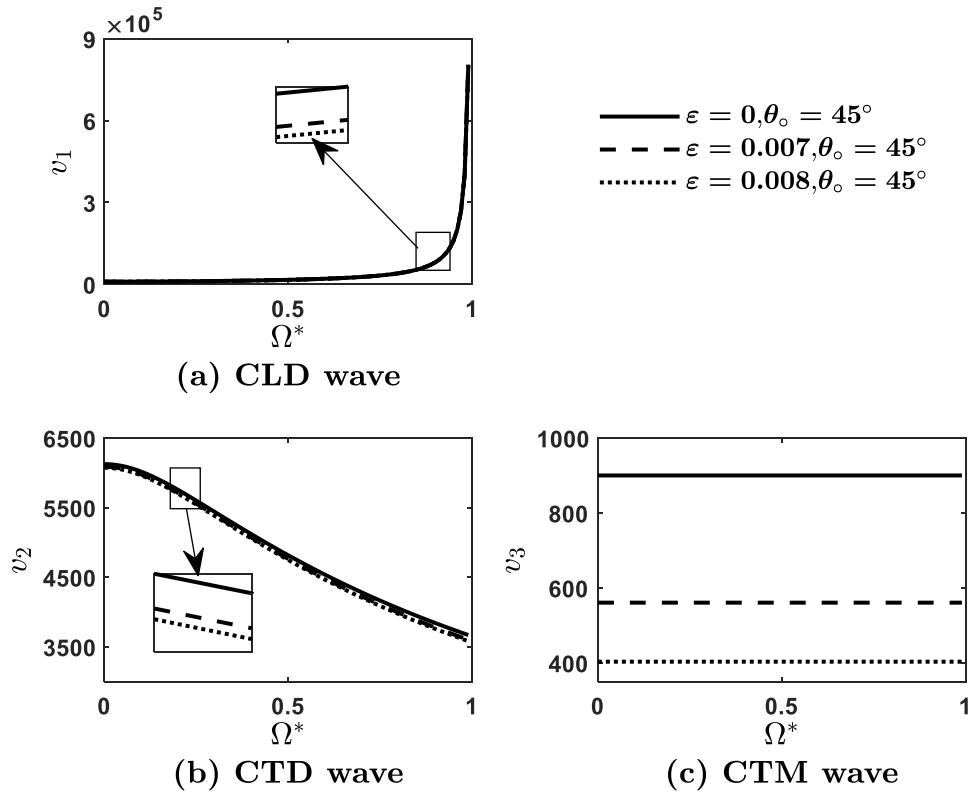


**Fig. 2.** The speed variations of CLD, CTD, and CTM waves against rotational rate for distinct nonlocal parameters

*Speeds versus nonlocal parameters.* To validate the rotation and nonlocality effects shown in Fig. 2 the speeds of CLD, CTD, and CTM waves are also plotted against nonlocal parameter  $\varepsilon$  shown in Fig. 3 for three different values of  $\Omega^*$  when  $\theta_o = 45^\circ$ . The solid, dashed, and dotted curves in Fig. 3 correspond to variations in speeds of reflected CLD, CTD, and CTM waves for  $\Omega^* = 0.1, 0.4, 0.8$ , respectively. For each value of  $\Omega^*$ , the speeds of CLD, CTD and CTM waves decrease as nonlocal parameter  $\varepsilon$  increases. Beyond the critical

values of nonlocal parameters, these waves do not exist. The range of nonlocal parameters for the propagation of these waves depends on the rotation parameter  $\Omega^*$ . The range of nonlocal parameters for the existence of CLD increases as  $\Omega^*$  increases, whereas the range of nonlocal parameters for the existence of CTD decreases as  $\Omega^*$  increases. The CTM wave is little affected due to nonlocal as well as rotation parameters.

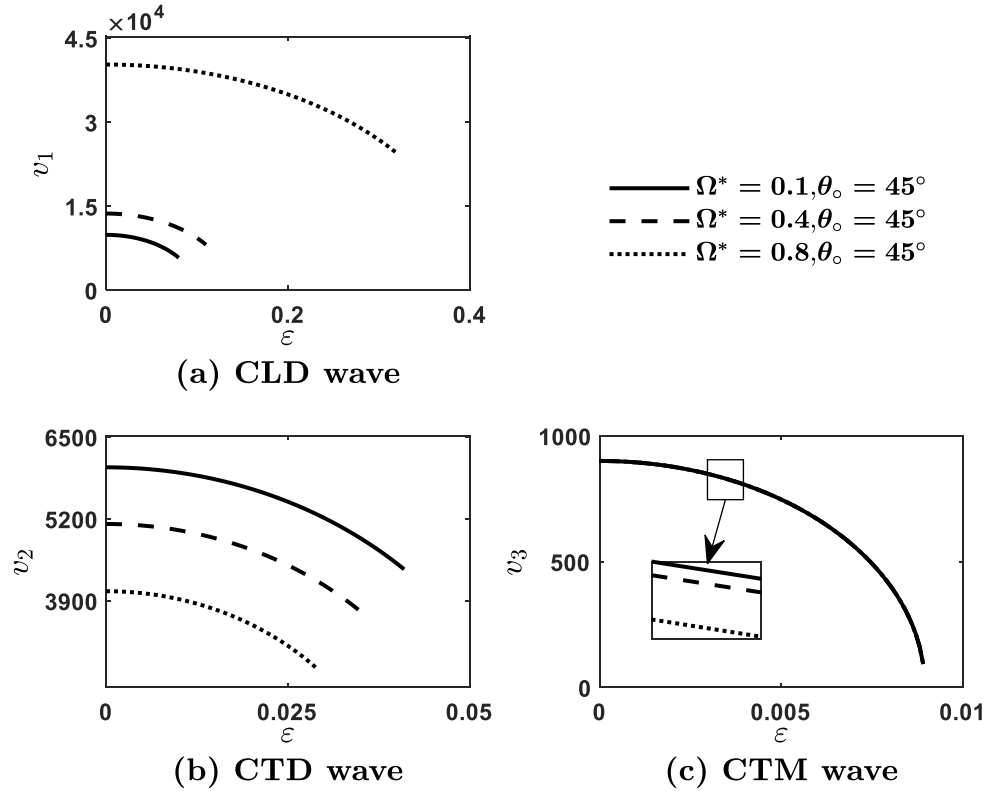


**Fig. 3.** The speed variations of CLD, CTD, and CTM waves against nonlocal parameters for distinct rotation rates

*Speeds versus propagation angle.* The speeds of CLD, CTD, and CTM waves are plotted against the propagation angle in Fig. 4 for three different nonlocal parameters when rotation rate  $\Omega^* = 0.8$ . The solid, dashed and dotted curves in these figures correspond to speed variations for  $\epsilon = 0, 0.007$  and  $0.008$ , respectively. For  $\epsilon = 0$ , the speed of CLD wave decreases from  $4.0571 \times 10^4 \text{ ms}^{-1}$  at  $\theta_o = 0.01^\circ$  (near normal incidence) to value  $4.0060 \times 10^4 \text{ ms}^{-1}$  at  $\theta_o = 89.99^\circ$  (near grazing incidence). For  $\epsilon = 0$ , the speed of CTD wave first increases from  $3533.74 \text{ ms}^{-1}$  at  $\theta_o = 0.01^\circ$  to its maximum value  $4051.05 \text{ ms}^{-1}$  at  $\theta_o = 45.30^\circ$  and then decreases to value  $3542.78 \text{ ms}^{-1}$  at  $\theta_o = 89.99^\circ$ . For  $\epsilon = 0$ , the speed of CTM wave increases slightly from  $891.08 \text{ ms}^{-1}$  at  $\theta_o = 0.01^\circ$  to  $907.48 \text{ ms}^{-1}$  at  $\theta_o = 89.99^\circ$ . Similar speed variations of CLD, CTD, and CTM waves are also obtained for  $\epsilon = 0.007$  and  $0.008$  as shown in Fig. 4. The comparison of solid, dotted and dashed curves in these figures show the nonlocal effects on the speed of these waves at each propagation angle. A similar analysis of speed variations of CLD, CTD, and CTM waves is also shown in Fig. 5 to illustrate the effect of rotation in a given range of propagation angle when  $\epsilon = 0.001$ .

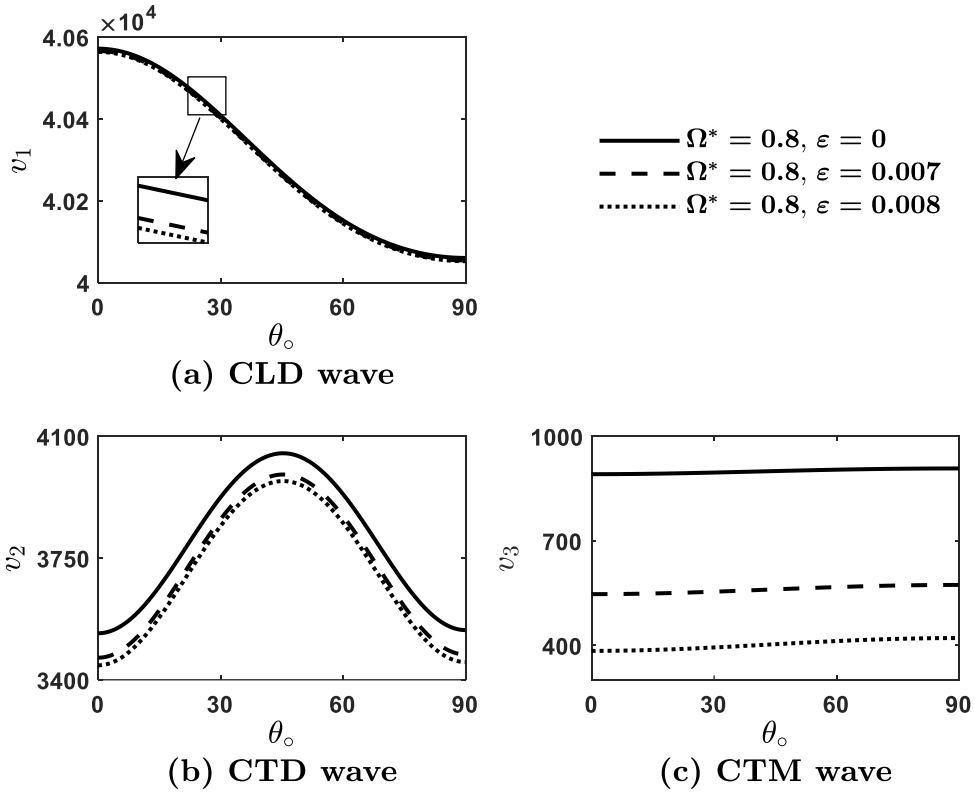


**Fig. 4.** The speed variations of CLD, CTD, and CTM waves against the incident angle of CLD wave for distinct nonlocal parameters when  $\Omega^* = 0.8$

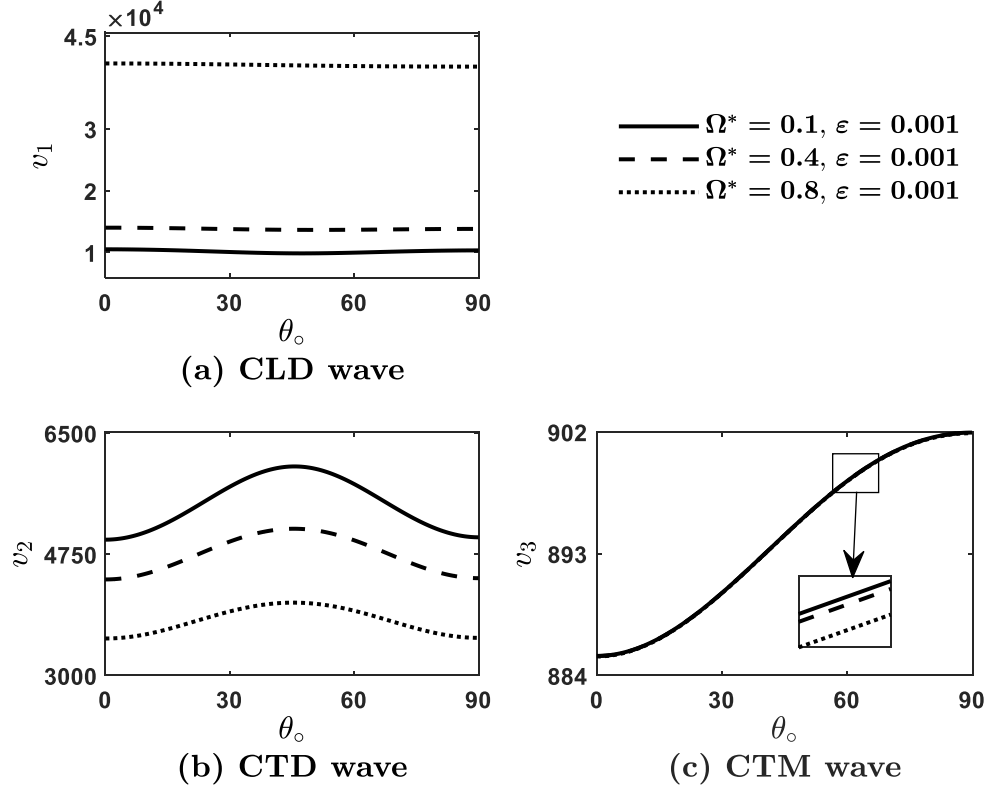


**Fig. 5.** The speed variations of CLD, CTD, and CTM waves against the incident angle of CLD wave for distinct rotation rates when  $\varepsilon = 0.001$

### Amplitude and energy ratios versus angle of incidence of CLD wave

The amplitude ratios  $|Z_1|$ ,  $|Z_2|$ , and  $|Z_3|$  of reflected CLD, CTD, and CTM waves are plotted against the incident angle  $\theta_o$  of CLD wave in Fig. 6 for  $\varepsilon = 0$  (solid curve),  $\varepsilon = 0.007$  (dashed curve), and  $\varepsilon = 0.008$  (dotted curve) when  $\Omega^* = 0.8$ .

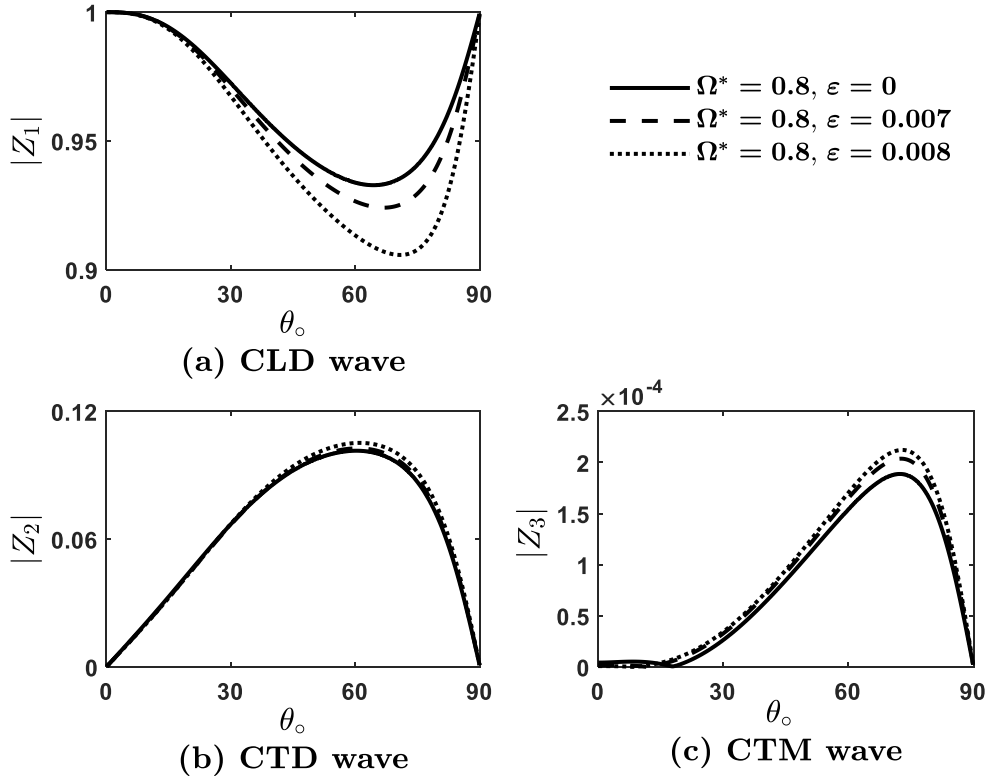


**Fig. 6.** The amplitude ratio variations of CLD, CTD, and CTM waves against the incident angle of CLD wave for distinct nonlocal parameters when  $\Omega^* = 0.8$

For  $\varepsilon = 0$ , the amplitude ratio of reflected CLD wave decreases from 0.9999 at  $\theta_o = 0.01^\circ$  to its minimum value 0.9328 at  $\theta_o = 64.36^\circ$  and then increases to a value 0.9999 at  $\theta_o = 89.99^\circ$ . For  $\varepsilon = 0$ , the reflected CTD wave amplitude ratio increases from  $2.1279 \times 10^{-5}$  at  $\theta_o = 0.01^\circ$  to its maximum value 0.1015 at  $\theta_o = 60.23^\circ$  and then decreases to value  $8.6324 \times 10^{-5}$  at  $\theta_o = 89.99^\circ$ . For  $\varepsilon = 0$ , the amplitude ratio of the reflected CTM wave oscillates in the given range of incident angle. In the presence of nonlocality, the amplitude ratio of reflected CLD wave drops, and the amplitude ratios of CTD and CTM waves rise at each angle of incidence except the normal and grazing incidences. The maximum effect of nonlocality on these amplitude ratios is observed in the range between  $60^\circ$  to  $80^\circ$  of the incident angle. Similar amplitude ratio variations of reflected CLD, CTD, and CTM waves are also shown in Fig. 7 to illustrate the effect of rotation at each incident angle. The amplitude ratio of CLD wave rises and the amplitude ratios of CTD and CTM waves drop at each incident angle except the normal and grazing incidences.

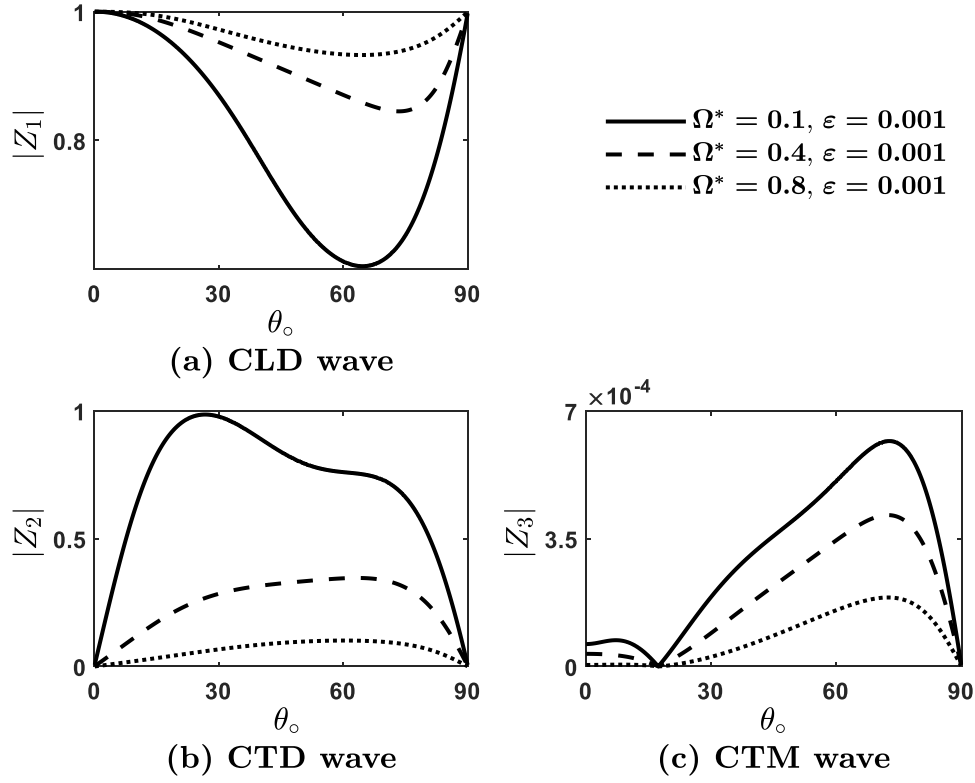


**Fig. 7.** The amplitude ratio variations of CLD, CTD, and CTM waves against the incident angle of CLD wave for distinct rotation rates when  $\varepsilon = 0.001$

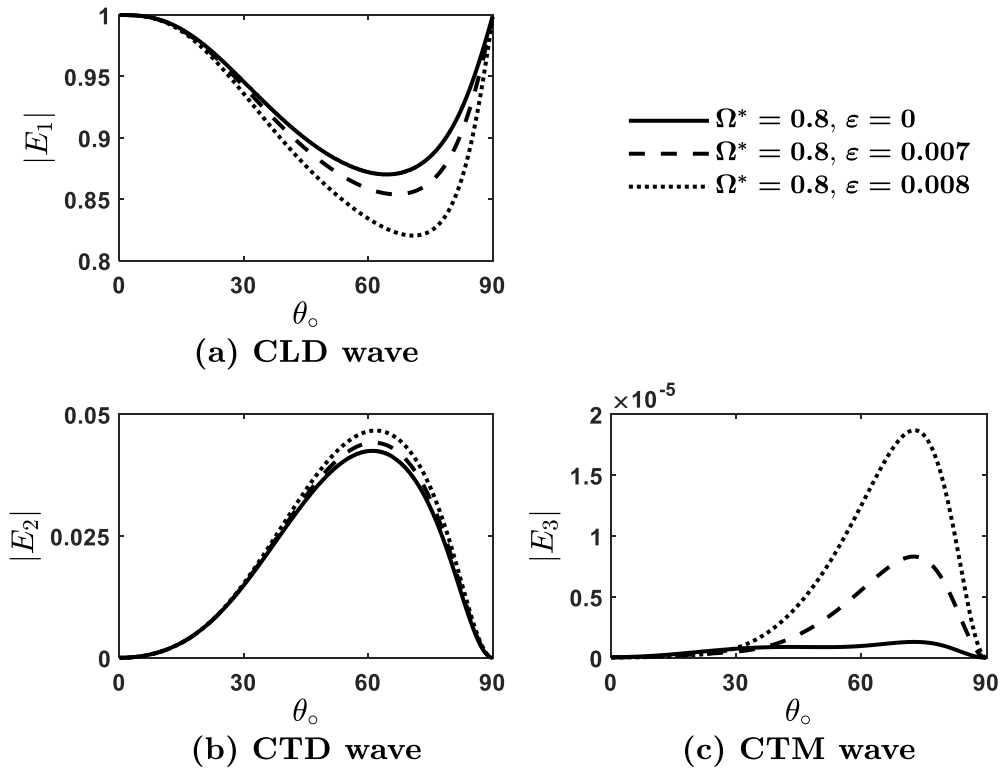


**Fig. 8.** The energy ratio variations of CLD, CTD, and CTM waves against the incident angle of CLD wave for distinct nonlocal parameters when  $\Omega^* = 0.8$



The energy ratio variations of the reflected CLD, CTD, and CTM are shown in Figs. 8 and 9 are observed similar to those of amplitude ratios. The nonlocality and rotation parameters affect the energy ratios of these reflected waves in a similar pattern as these parameters affect the amplitude ratios. The main aim of illustrating the energy ratio in Figs. 8 and 9 is to validate the numerical correctness of the amplitude ratio variations. From these figures, it is also noticed that the reflected CLD wave shares the maximum part of the energy ratio, and the reflected CTM wave shares the minimum and very little share of the energy ratio compared to other reflected waves. However, the energy shares of each reflected wave change with the incident angle.

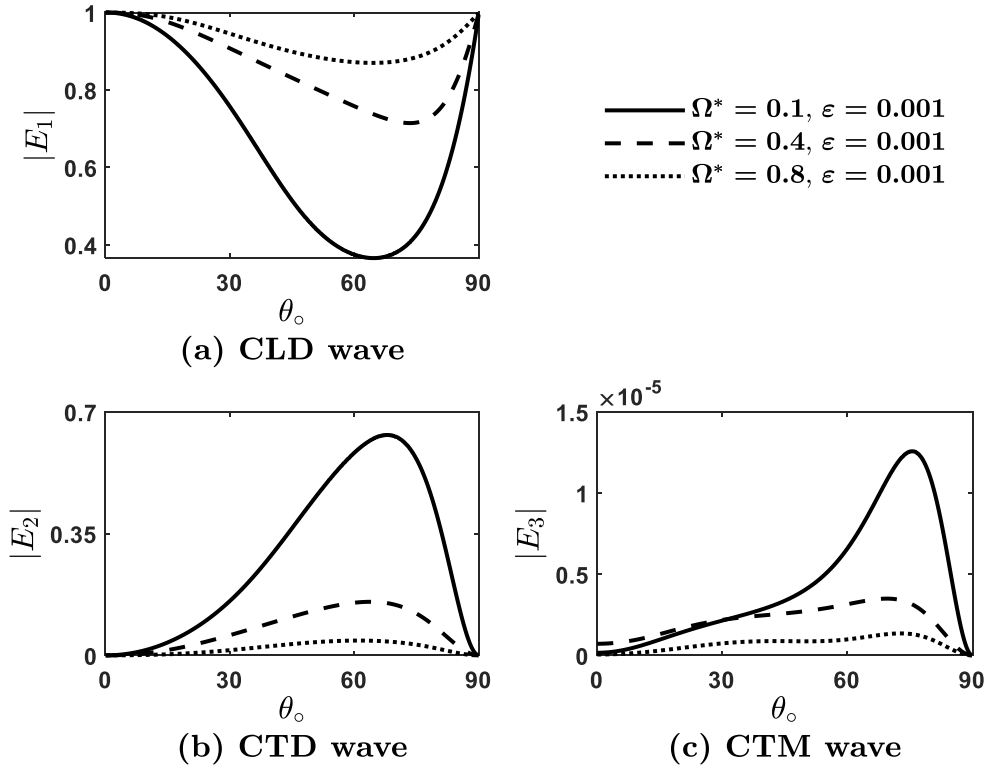


**Fig. 9.** The energy ratio variations of CLD, CTD, and CTM waves against the incident angle of CLD wave for distinct rotation rates when  $\varepsilon = 0.001$

## Conclusions

Plane waves in a rotating nonlocal micropolar piezoelectric medium are investigated. There exist three coupled waves, namely Coupled Longitudinal Displacement (CLD) wave, Coupled Transverse Displacement (CTD) wave and Coupled Transverse Microrotational (CTM) wave. The CLD and CTM waves are observed as the fastest and slowest waves, respectively. A reflection phenomenon of incident CLD wave from a tractions-free surface is considered. The relations between various reflected waves amplitude ratios are derived. The energy ratio expressions of these reflected waves are also derived. A numerical example is considered to illustrate the dependence of the speeds, amplitude, and energy ratios on the nonlocality and rotation parameters in a given range of the angle of incidence. Some specific observations from the numerical example are derived as follows:

1. For given rotation parameter  $\Omega^*$  and propagation angles, the speeds of CLD, CTD, and CTM waves decrease as the nonlocal parameter  $\varepsilon$  increases.
2. For given nonlocal parameter  $\varepsilon$  and propagation angle, the speed of CLD wave increases, and the speeds of CTD and CTM waves decreases.

3. Beyond the critical values of the nonlocal parameter, the CLD, CTD, and CTM waves do not propagate. The range of nonlocal parameters for the propagation of these waves depends on the rotation parameter  $\Omega^*$ . The range of nonlocal parameters for the existence of CLD increases as  $\Omega^*$  increases, whereas the range of nonlocal parameters for the existence of CTD decreases as  $\Omega^*$  increases. The CTM wave is little affected due to nonlocal as well as rotation parameters.
4. The speeds, amplitude ratios, and energy ratios vary with the change in propagation angle and the nonlocal and rotation effects are also found dependent on the propagation angle.  
The present theoretical and numerical analysis may be used to estimate the possible nonlocal parameters for various nonlocal micropolar piezoelectric materials.

## References

1. Knott CG. Reflexion and refraction of elastic waves with seismological applications. *Lond Edinb Dublin Philos Mag J Sci*. 1899;48: 64-97.
2. Jeffreys H. The reflexion and refraction of elastic waves. *Geophysical Suppl Mon Notices Royal Astron*. 1926;1(7): 321-334.
3. Gutenberg B. Energy ratio of reflected and refracted seismic waves. *Bull Seismol Soc Am*. 1944;34(2): 85-102.
4. Ergin K. Energy ratio of the seismic waves reflected and refracted at a rock-water boundary. *Bull Seismol Soc Am*. 1950;42(4): 349-372.
5. Ewing WM, Jardetzky WS, Press F. *Elastic waves in layered media*. New York: McGraw-Hill; 1957.
6. Achenbach JD. *Wave propagation in elastic solids*. New York: North-Holland; 1973.
7. Kyame JJ. Wave Propagation in piezoelectric crystals. *J Acoust Soc Am*. 1949;21(3): 159-167.
8. Pailloux PMH. Piézoélectricité Calcul des vitesses de propagation [Piezoelectricity. Calculation of propagation velocities]. *Le Journal De Physique Et Le Radium*. 1958;19:523-526. (In French)
9. Cheng NC, Sun CT. Wave propagation in two-layered piezoelectric plates. *J Acoust Soc Am*. 1975;57(3): 632-638.
10. Auld BA. Wave propagation and resonance in piezoelectric materials. *J Acoust Soc Am*. 1981;70(6): 1577-1585.
11. Alshits VI, Lothe J, Lyubimov VN. The phase shift for reflection of elastic waves in hexagonal piezoelectric crystals. *Wave Motion*. 1984;6(3): 259-264.
12. Parton VZ, Kudryavtsev BA. *Electromagnetoelasticity: piezoelectrics and electrically conductive solids*. New York: Gordon and Beach; 1988.
13. Every AG, Neiman VI. Reflection of electroacoustic waves in piezoelectric solids: Mode conversion into four bulk waves. *J Appl Phys*. 1992;71(12): 6018-6024.
14. Alshits VI, Shuvalov AL. Resonance reflection and transmission of shear elastic waves in multilayered piezoelectric structures. *J Appl Phys*. 1995;77(6): 2659-2665.
15. Wang Q. Wave propagation in a piezoelectric coupled solid medium. *J Appl Mech*. 2002;69: 819-824.
16. Yang JS. A review of a few topics in piezoelectricity. *Appl Mech Rev*. 2006;59: 335-345.
17. Pang Y, Wang YS, Liu JX, Fang DN. Reflection and refraction of plane waves at the interface between piezoelectric and piezomagnetic media. *Int J Eng Sci*. 2008;46(11): 1098-1110.
18. Darinskii AN, Clezio EL, Feuillard G. The role of electromagnetic waves in the reflection of acoustic waves in piezoelectric crystals. *Wave Motion*. 2008;45(4): 428-444.

19. Burkov SI, Sorokin BP, Aleksandrov KS, Karpovich AA. Reflection and refraction of bulk acoustic waves in piezoelectrics under uniaxial stress. *Acoust Phys*. 2009;55: 178–185.
20. Abd-alla AN, Al-sheikh FA. Reflection and refraction of plane quasi-longitudinal waves at an interface of two piezoelectric media under initial stress. *Arch Appl. Mech*. 2009;79: 843–857.
21. Singh B. Wave propagation in a prestressed piezoelectric half-space. *Acta Mech*. 2010;211: 337–344.
22. Kuang ZB, Yuan XG. Reflection and transmission of waves in pyroelectric and piezoelectric materials. *J Sound Vib*. 2011;330(6): 1111–1120.
23. Yuan X, Zhu ZH. Reflection and refraction of plane waves at interface between two piezoelectric media. *Acta Mech*. 2012;223: 2509–2521.
24. Guo X, Wei P. Effects of initial stress on the reflection and transmission waves at the interface between two piezoelectric half spaces. *Int J Solids Struct*. 2014;51(21–22): 3735–3751.
25. Guo X, Wei P, Li L, Tang Q. Influences of mechanically and dielectrically imperfect interfaces on the reflection and transmission waves between two piezoelectric half spaces. *Int J Solids Struct*. 2015;63: 184–205.
26. Othman MIA, Elmaklizi YD, Ahmed EAA. Influence of magnetic field on generalized piezo-thermoelastic rotating medium with two relaxation times. *Microsyst Technol*. 2017;23: 5599–5612.
27. Singh B, Singh B. Reflection from free surface of a rotating generalized thermo-piezoelectric solid half space. *J Solid Mech*. 2018;10(1): 57–66.
28. Jiao F, Wei P, Zhou Y, Zhou X. Wave propagation through a piezoelectric semiconductor slab sandwiched by two piezoelectric half-spaces. *Eur J Mech A Solids*. 2019;75: 70–81.
29. Sahu SA, Nirwal S, Mondal S. Reflection and transmission of quasi-plane waves at the interface of piezoelectric semiconductors with initial stresses. *Appl Math Mech*. 2021;42(7): 951–968.
30. Singh S, Singh AK, Guha S. Impact of interfacial imperfections on the reflection and transmission phenomenon of plane waves in a porous-piezoelectric model. *Appl Math Model*. 2021;100: 656–675.
31. Liu C, Yu J, Wang X, Zhang B, Zhang X, Zhou H. Reflection and transmission of elastic waves through nonlocal piezoelectric plates sandwiched in two solid half-spaces. *Thin-Walled Struct*. 2021;168: 108306.
32. Schoenberg M, Censor D. Elastic waves in rotating media. *Q Appl Math*. 1973;31: 115–125.
33. White RW. Acoustic sensors for physical, chemical and biochemical applications. In: *Proceedings of the 1998 IEEE International Frequency Control Symposium*. 1998. p.587–594.
34. Tiersten HF, Stevens DS, Das PK. Acoustic surface wave accelerometer and rotation rate sensor. In: *1980 Ultrasonics Symposium*. Boston (MA): IEEE; 2005. p.692–695.
35. Tiersten HF, Stevens DS, Das PK. Circulating flexural wave rotation rate sensor. In: *1981 Ultrasonics Symposium*. Chicago (IL): IEEE; 2005. p.163–166.
36. Wren T, Burdess JS. Surface waves perturbed by rotation. *ASME J. Appl Mech*. 1987;54: 464–466.
37. Edelen DGB, Green AE, Laws N. Nonlocal continuum mechanics. *Arch Ration Mech Anal*. 1971;43: 36–44.
38. Eringen AC, Edelen DGB. On nonlocal elasticity. *Int J Eng Sci*. 1972;10: 233–248.
39. Eringen AC. *Nonlocal continuum field theories*. New York: Springer; 2001.
40. Eringen AC. Linear theory of nonlocal elasticity and dispersion of plane waves. *Int J Eng Sci*. 1972;10(5): 425–435.

41. Eringen AC. Plane waves in nonlocal micropolar elasticity. *Int J Eng Sci.* 1984;22: 1113-1121.
42. Roy I, Acharya DP, Acharya S. Rayleigh wave in a rotating nonlocal magnetoelastic half-plane. *J Theor Appl Mech.* 2015;45: 61-78.
43. Khurana A, Tomar SK. Reflection of plane longitudinal waves from the stress-free boundary of a nonlocal, micropolar solid half-space. *J Mech Mater Struct.* 2013;8: 95-107.
44. Khurana A, Tomar SK. Wave propagation in nonlocal microstretch solid. *Appl Math Model.* 2016;40: 5858-5875.
45. Singh B. Rayleigh-type surface waves in a nonlocal thermoelastic solid half space with voids. *Waves Random Complex Media.* 2021;31(6): 2103-2114.
46. Singh B. Propagation of waves in an incompressible rotating transversely isotropic nonlocal elastic solid. *Vietnam J Mech.* 2021;43(3): 237-252.
47. Kaur B, Singh B. Rayleigh-type surface wave in nonlocal isotropic diffusive materials. *Acta Mech.* 2021;232: 3407-3416.
48. Tung DX. The reflection and transmission of a quasi-longitudinal displacement wave at an imperfect interface between two nonlocal orthotropic micropolar half-space. *Arch Appl Mech.* 2021;91: 4313-4328.
49. Eringen AC. Linear theory of micropolar elasticity. *J Math Mech.* 1966;15: 909-923.
50. Eringen AC. *Theory of micropolar elasticity. Fracture 2.* New York: Academic Press; 1968.
51. Eringen AC. *Microcontinuum field theories I: foundations and solids.* New York: Springer; 1999.
52. Cracium IA. Uniqueness theorem in the linear theory of piezoelectric micropolar thermoelasticity ion. *Int J Eng Sci.* 1995;33: 1027-1036.
53. Ciumasu SG, Vieru D. Variational formulations for the vibration of a micropolar piezoelectric body. *J Acoust Soc Am.* 1999;105: 1240.
54. Vieru D, Ciumasu SG. Love waves in non-classical micropolar piezoelectricity. *J Acoust Soc Am.* 1999;105: 1241.
55. Zhilin PA, Kolpakov YE. A micro-polar theory for piezoelectric materials. In: *Lecture at XXXIII Summer School–Conference-Advanced Problems in Mechanics.* St. Petersburg, Russia; 2015.
56. Aouadi M. Aspects of uniqueness in micropolar piezoelectric bodies. *Math Mech Solids.* 2008;13: 499-512.
57. Gales C. Some results in micromorphic piezoelectricity. *Eur J Mech A Solids.* 2012;31: 37-46.
58. Singh B, Sindhu R. On propagation of Rayleigh type surface wave in a micropolar piezoelectric medium. *Open J Acoust.* 2016;6(4): 35-44.
59. Singh B, Sindhu R. Rotational effects on propagation of Rayleigh wave in a micropolar piezoelectric medium. *J Theor Appl Mech.* 2018;48: 93-105.
60. Sangwan A, Singh B, Singh J. Reflection and transmission of plane waves at an interface between elastic and micropolar piezoelectric solid half-spaces. *Tech Mech.* 2018;38(3): 267-285.
61. Singh B, Sangwan A, Singh J. Reflection and transmission of elastic waves at an interface between two micropolar piezoelectric half-spaces. *J Ocean Eng Sci.* 2019;4(3): 227-237.
62. Bijarnia R, Singh B, Awrejcewicz J. Reflection at non-free boundary of a micropolar piezoelectric half-space. *Forces Mech.* 2021;3: 100019

**THE AUTHORS****Baljeet Singh** 

e-mail: bsinghgc11@gmail.com

**Jagdish Singh** 

e-mail: jsnandal2k15@gmail.com

**Asha Sangwan** 

e-mail: aashisangwan53@gmail.com

## Appendix

The expressions for  $\xi_1^*, \eta_1^*, \zeta_1^*, \xi_p, \eta_p$  and  $\zeta_p$  ( $p=1,2,3$ ) using Snell's law are given as

$$\xi_1^* = \frac{\Delta_1^*}{\Delta}, \frac{\eta_1^*}{k_1} = \frac{\Delta_2^*}{\Delta}, \zeta_1^* = \frac{\Delta_3^*}{\Delta}, \xi_p = \frac{\Delta_{1p}}{\Delta_p}, \frac{\eta_p}{k_p} = \frac{\Delta_{2p}}{\Delta_p}, \zeta_p = \frac{\Delta_{3p}}{\Delta_p},$$

where

$$\Delta_p = \begin{vmatrix} C_p & K_{1p} & G_p \\ Q_p & K_{2p} & T_p \\ K_{2p}^* & R_p & 0 \end{vmatrix}, \Delta_{1p} = \begin{vmatrix} P_p & K_{1p} & G_p \\ F_p & K_{2p} & T_p \\ K_{1p}^* & R_p & 0 \end{vmatrix},$$

$$\Delta_{2p} = \begin{vmatrix} C_p & P_p & G_p \\ Q_p & F_p & T_p \\ K_{2p}^* & K_{1p}^* & 0 \end{vmatrix}, \Delta_{3p} = \begin{vmatrix} C_p & K_{1p} & P_p \\ Q_p & K_{2p} & F_p \\ K_{2p}^* & R_p & K_{1p}^* \end{vmatrix},$$

$$\Delta = \begin{vmatrix} C_0 & -K_{11} & -G_1 \\ Q_1 & K_{21} & T_1 \\ K_{21}^* & R_1 & 0 \end{vmatrix}, \Delta_1^* = \begin{vmatrix} P_1 & -K_{11} & -G_1 \\ F_0 & K_{21} & T_1 \\ -K_{11}^* & R_1 & 0 \end{vmatrix},$$

$$\Delta_2^* = \begin{vmatrix} C_0 & P_1 & -G_1 \\ Q_1 & F_0 & T_1 \\ K_{21}^* & -K_{11}^* & 0 \end{vmatrix}, \Delta_3^* = \begin{vmatrix} C_0 & -K_{11} & P_1 \\ Q_1 & K_{21} & F_0 \\ K_{21}^* & R_1 & -K_{11}^* \end{vmatrix},$$

where

$$P_p = \left[1 + (\Omega^*)^2\right] (\rho v_p^2 + \rho \varepsilon^2 \omega^2) - A_{11} \sin^2 \theta_o \left(\frac{v_p}{v_1}\right)^2 - A_{55} \left[1 - \sin^2 \theta_o \left(\frac{v_p}{v_1}\right)^2\right],$$

$$Q_p = \left[1 + (\Omega^*)^2\right] (\rho v_p^2 + \rho \varepsilon^2 \omega^2) - A_{66} \sin^2 \theta_o \left(\frac{v_p}{v_1}\right)^2 - A_{33} \left[1 - \sin^2 \theta_o \left(\frac{v_p}{v_1}\right)^2\right],$$

$$R_p = \frac{B_{77}}{j} \sin^2 \theta_o \left(\frac{v_p}{v_1}\right)^2 + \frac{B_{66}}{j} \left[1 - \sin^2 \theta_o \left(\frac{v_p}{v_1}\right)^2\right] + \frac{\chi}{jk_p^2} - (\rho v_p^2 + \rho \varepsilon^2 \omega^2),$$

$$T_p = \lambda_{15} \sin^2 \theta_o \left(\frac{v_p}{v_1}\right)^2 + \lambda_{33} \left[1 - \sin^2 \theta_o \left(\frac{v_p}{v_1}\right)^2\right],$$

$$C_p = -(A_{13} + A_{56}) \sin \theta_o \left(\frac{v_p}{v_1}\right) \sqrt{1 - \sin^2 \theta_o \left(\frac{v_p}{v_1}\right)^2} - 2i \Omega^* (\rho v_p^2 + \rho \varepsilon^2 \omega^2),$$

$$C_0 = (A_{13} + A_{56}) \sin \theta_o \cos \theta_o - 2i \Omega^* (\rho v_1^2 + \rho \varepsilon^2 \omega^2),$$

$$F_p = -(A_{13} + A_{56}) \sin \theta_o \left(\frac{v_p}{v_1}\right) \sqrt{1 - \sin^2 \theta_o \left(\frac{v_p}{v_1}\right)^2} + 2i \Omega^* (\rho v_p^2 + \rho \varepsilon^2 \omega^2),$$

$$F_0 = (A_{13} + A_{56}) \sin \theta_o \cos \theta_o + 2i \Omega^* (\rho v_1^2 + \rho \varepsilon^2 \omega^2),$$

$$G_p = (\lambda_{15} + \lambda_{31}) \sin \theta_o \left(\frac{v_p}{v_1}\right) \sqrt{1 - \sin^2 \theta_o \left(\frac{v_p}{v_1}\right)^2}, \quad \Omega^* = \frac{\Omega}{\omega},$$

$$K_{1p} = iK_1 \sqrt{1 - \sin^2 \theta_o \left( \frac{v_p}{v_1} \right)^2}, \quad K_{2p} = iK_2 \sin \theta_o \left( \frac{v_p}{v_1} \right),$$

$$K_{1p}^* = i \frac{K_1}{jk_p^2} \sqrt{1 - \sin^2 \theta_o \left( \frac{v_p}{v_1} \right)^2}, \quad K_{2p}^* = i \frac{K_2}{jk_p^2} \sin \theta_o \left( \frac{v_p}{v_1} \right).$$



# Simulation of the plastic deformation of shape memory alloys considering shear anisotropy on the slip plane

F.S. Belyaev <sup>1</sup> , M.E. Evard <sup>2</sup>, A.E. Volkov <sup>2</sup> 

<sup>1</sup>Institute for Problems of Mechanical Engineering RAS, 61, Bolshoi Pr. V.O., St. Petersburg, Russia, 199178

<sup>2</sup>St. Petersburg State University, Universitetskaya emb., 7-9, St. Petersburg, Russia, 199034

✉ belyaev\_fs@mail.ru

**Abstract.** The plastic deformation of a TiNi single crystal was modeled, taking into account the anisotropy of the yield stress in the slip plane. The material parameters (initial yield stress and hardening factor) were selected for each slip system. Deformation curves were obtained for different orientations of the single crystal. It is shown that Schmid's law prevents obtaining a correct description of deformation for all orientations of single crystals. Good agreement with experiments was observed for the crystal orientations  $\langle 001 \rangle$ ,  $\langle 111 \rangle$ , and  $\langle 123 \rangle$  but not  $\langle 011 \rangle$ , for which the deformation mechanism was different. In the case of the deformation of a polycrystalline sample, the anisotropy in the slip plane is not significant.

**Keywords:** shape memory alloys, microstructural modeling, plastic deformation, TiNi, single crystal, polycrystal

**Acknowledgments.** This research was funded by Russian Foundation for Basic Research (RFBR), project number 19-31-60035.

**Citation:** Belyaev FS, Evard ME, Volkov AE. Simulation of the plastic deformation of shape memory alloys considering shear anisotropy on the slip plane. *Materials Physics and Mechanics*. 2023;51(1): 61-67. DOI: 10.18149/MPM.5112023\_6.

## Introduction

Shape memory alloys (SMA) are intelligent materials that can exhibit functional properties such as shape memory and superelasticity. Due to their unique properties, these alloys are widely applied in the fields of aerospace, biomedical and micro-electromechanical systems (MEMS) and so on [1-4]. Plastic deformation is an important phenomenon associated with the thermomechanical properties of SMA. This association is because the dislocation slip in these materials is not only one of the deformation mechanisms but also leads to the formation of several specific effects, such as two-way shape memory and the “training” of the material. Plastic deformation under certain conditions makes it possible to purposefully improve the properties of materials. The influence of plastic deformation on the mechanical behavior of SMA is of considerable interest to researchers [5-9].

Successful development of devices with SMA parts requires a reliable method for calculating their mechanical behavior. Most of the existing models of SMA aim to describe phase transformations since phase deformations and the realization of functional properties are associated with them. However, some models also describe plastic deformation. Phenomenological models describing plastic deformation include [10-12]. In the one-dimensional model of Tanaka et al. [10], plastic deformation is associated with residual stresses under cyclic loading. In the model used by Bo et al. [11], thermally induced

transformation and its interaction with plastic deformation under cyclic loading conditions are considered. The model in [12] describes stress-induced phase transformations and plastic strain. In this model, the development of the plastic strain is associated with detwinned martensite and is induced by cyclic loading conditions. The earliest microstructural models describing plastic strain are [13-15]. These models describe only microplastic deformation, that is, plastic deformation associated with the accommodation of growing martensite plates. In [13], it is assumed that microplastic deformation increases with the motion of the interphase boundaries. In [14-15], microplastic flow conditions similar to the flow conditions in the one-dimensional case with isotropic hardening are proposed. The models in [16-17] describe active plastic deformation, that is, plastic deformation associated with dislocation slip. The model in [16] describes the martensite plasticity present only after the austenite–martensite transformation is complete. The model in work [17] accounts for both phase transformations and plasticity at the crystallographic level and allows their simultaneous realization. The most recent works on the microstructural modeling of SMA that consider plastic deformation include [18-27]. In works [18-21] a microstructural model is presented that describes the plastic deformation of austenite and martensite, as well as the accumulation of plastic deformation under cyclic loading. The models of [22-25] describe dislocation slip in austenite but not the deformation twinning of martensite. The model of Xu et al. [26] describes the austenitic plasticity caused by dislocation slipping, and the martensitic plasticity caused by dislocation slipping and deformation twinning. It also describes the effect of grain size on martensitic transformations. The model of Ju et al. [27] describes the SMA deformation in terms of finite deformations. It takes into account both microplastic deformation and plastic deformation of austenite and martensite.

Earlier authors developed the model to describe microplastic strain and its effect on the functional properties of SMA [28-29], but it was unable to describe active plastic strain. Based on this, the purpose of this work is to describe the active plastic deformation of the SMA as a separate deformation mechanism. Moreover, the model should be able to describe the deformation of both single crystals and polycrystalline samples. During the deformation of single crystal samples, the flow stress depends on the orientation of the tension axis. To account for this when describing SMA deformation, it is necessary to include an elementary act of plastic deformation in the model: dislocation shear and its anisotropy on the slip plane.

## Model

The model material is a single crystal (one grain with an orientation of crystallographic axes  $\omega$ ) with several slip systems. In metals and alloys, the dislocation slip occurs only on certain crystallographic planes. On other planes, it is difficult for shearing to occur, since the corresponding flow stresses exceed the ultimate strength of the material. All active slip planes can be divided into  $M$  families of crystallographically equivalent planes. Let us denote  $K_m$  as the number of planes of the family  $m$ . Then, we propose that Reuss's hypothesis is applicable. The plastic strain of model material  $\varepsilon_{\omega}^{p(m,k)}$  is the sum of the strains on each of the slip planes:

$$\dot{\varepsilon}_{\omega}^{gr p} = \sum_{m=1}^M \sum_{k=1}^{K_m} \dot{\varepsilon}^{p(m,k)}, \quad (1)$$

where  $\varepsilon_{\omega}^{p(m,k)}$  is the shear strain in the  $k$ -th plane from the  $m$ -th family.

Shear on the slip plane is assumed to occur only in the direction of the smallest Burgers vector. To formulate the flow conditions, we introduce local basis coordinate systems on the slip planes. The first axis of this local coordinate system lies in the sliding plane and is directed along the possible shear direction; the second axis lies in the same plane, and the third axis is perpendicular to it. We assume that the only components of the stress related to this local basis, which produce slip on this plane, are  $\tau_{31}^{(m,k)}$  and  $\tau_{32}^{(m,k)}$ . If we denote the stress

applied to the single crystal by  $\sigma^{gr}$  then the two stress components can be found using the formulae:

$$\begin{aligned}\tau_{31}^{(m,k)} &= A_{p3}^{(m,k)} A_{q1}^{(m,k)} \sigma_{pq}^{gr}, \\ \tau_{32}^{(m,k)} &= A_{p3}^{(m,k)} A_{q2}^{(m,k)} \sigma_{pq}^{gr},\end{aligned}\quad (2)$$

where  $A^{(m,k)}$  is the rotation matrix that transforms the crystallographic basis  $\omega$  into the local basis of the  $k$ -th slip plane of the  $m$ -th family.

The condition for the onset of plastic shear was formulated based on Schmid's law: plastic flow begins when the shear component of the stress,  $\tau_{31}^{(m,k)}$  or  $\tau_{32}^{(m,k)}$ , reaches a critical value,  $\tau^{s(m,k)}$ , for the given slip system:

$$\tau^{s(m,k)} = \begin{cases} \tau_{31}^{(m,k)}, & \text{if } \tau_{31}^{(m,k)} \geq \tau_{32}^{(m,k)}, \\ \tau_{32}^{(m,k)}, & \text{if } \tau_{31}^{(m,k)} < \tau_{32}^{(m,k)}. \end{cases} \quad (3)$$

We assume that the flow stress  $\tau^{s(m,k)}$  is the sum of the initial (equilibrium) value  $\tau^{s(m,k)}_{eq}$  and the deformation additive  $\tau^{s(m,k)}_{def}$  is responsible for the strain hardening:

$$\tau^{s(m,k)} = \tau^{s(m,k)}_{eq} + \tau^{s(m,k)}_{def}. \quad (4)$$

The value of the initial flow stress  $\tau^{s(m,k)}_{eq}$  is the same for all planes belonging to the given  $m$ -th family. To calculate the value of  $\tau^{s(m,k)}_{def}$ , we assume that the hardening factor  $h^m$  does not depend on the shear value and the strain rate. It is equal to the product of the hardening factor  $h^m$  and the maximum plastic shear rate,  $\dot{\beta}_{31}$  or  $\dot{\beta}_{32}$ :

$$\tau^{s(m,k)}_{def} = \begin{cases} h^m |\dot{\beta}_{31}^{(m,k)}|, & \text{if } |\dot{\beta}_{31}^{(m,k)}| > 0, \\ h^m |\dot{\beta}_{32}^{(m,k)}|, & \text{if } |\dot{\beta}_{32}^{(m,k)}| > 0. \end{cases} \quad (5)$$

The solution of the system of equations (2)-(5) makes it possible to calculate the  $\varepsilon^p(m,k)$  components. Then the sum (1) will give the total plastic deformation of the model single crystal. To solve the system of differential equations, a direct finite-difference scheme was used.

## Simulation results

To test the model, numerical experiments were conducted by stretching single crystals of TiNi alloy with different crystal lattice orientations. This alloy is very popular and widely used. It is known that plastic shear in the austenitic B2 phase of TiNi SMA slip occurs on the planes belonging to two families:  $\{110\}$  and  $\{100\}$ . The first family consists of 6 planes, and the second consists of 3 planes [30]. For the TiNi slip systems, the following material constants were selected: the initial flow stress  $\tau^{s}_{eq}$  and the hardening coefficient  $h$  (Table 1).

**Table 1.** Flow stress and hardening factor for existing slip systems

Slip plane family	Initial flow stress $\tau^{s}_{eq}$ , MPa	Hardening coefficient $h$ , MPa
$\{100\}$	85	100
$\{110\}$	100	3000

All calculations were performed at 600 K, which is much higher than the final temperature of the reverse martensitic transformation. The choice of temperature is because an increase in stress does not cause a martensitic transformation, and plastic shear remains the only active mechanism of inelastic deformation. Figure 1 shows the results of modeling the behavior of a TiNi single crystal under tension along the  $\langle 001 \rangle$ ,  $\langle 111 \rangle$ ,  $\langle 123 \rangle$ , and  $\langle 011 \rangle$  directions and the corresponding experimental dependences [30].

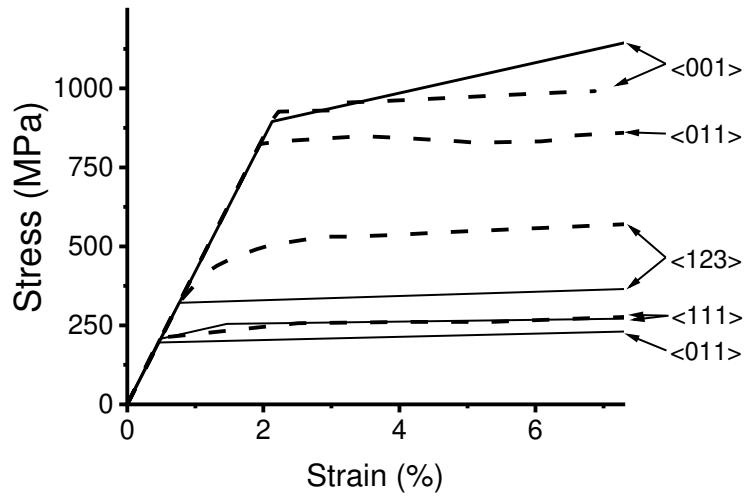


**Fig. 1.** Experimental [30] (dashed lines) and calculated (solid lines) tension curves of a TiNi single crystal

Comparing the calculated tension curves of a TiNi single crystal with the experimental data (Fig. 1) shows that the selected values of the material constants correctly describe the model alloy behavior with the tension oriented along the  $\langle 001 \rangle$  and  $\langle 111 \rangle$  axes. For the  $\langle 123 \rangle$  direction, the calculated yield stress coincides with that observed experimentally [30]. For the orientation of the tension along the  $\langle 011 \rangle$  direction, the calculated curve does not substantially coincide with the experimental one.

Experimental data show that under tension applied along the  $\langle 011 \rangle$  direction, the crystals are "hard", that is, they have a high yield point,  $\sigma_{0.1} \approx 920$  MPa [30]. In works [30-31], it was suggested that when the orientation of the tension axis changes to directions near  $\langle 011 \rangle$ , the deformation mechanism changes at the microscale. In particular, with the orientation  $\langle 011 \rangle$ , volumetric splitting of the screw dislocation core occurs, which obstructs the onset of plastic shear. Therefore, within the framework of this model, considering only the anisotropy in the slip plane does not allow an adequate description of the behavior of a TiNi single crystal for all directions of tension.

### Deformation of polycrystals

The proposed model can be adapted to the calculation of the plastic deformation of a polycrystalline sample. We assume that the described representative volume consists of grains of equal size with different orientations of the crystallographic axes: 1, 2,...,  $\omega$ ,...,  $\Omega$ . Then we can calculate the deformations of individual grains according to the proposed model and obtain the deformation of the representative volume through orientational averaging:

$$\varepsilon^p = \frac{1}{\Omega} \sum_{\omega=1}^{\Omega} R_{\omega} \varepsilon_{\omega}^{gr p} R_{\omega}^{-1}, \quad (6)$$

where  $R_{\omega}$  is the rotation matrix that transforms the laboratory basis to the crystallographic basis of the grain  $\omega$ .

Figure 2 shows the tension curve of the polycrystal calculated by our model (solid line). The relatively low yield stress of the TiNi polycrystal is due to the action of a large number of slip systems; deformation occurs along those with lower microscopic yield stress.

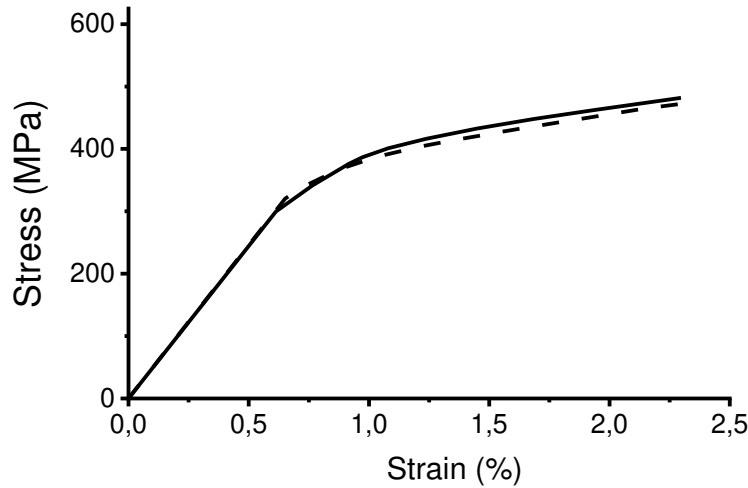


**Fig. 2.** Tension curves of a TiNi polycrystal calculated by a model with anisotropic (solid line) and isotropic (dashed line) shear on the slip plane

To calculate the deformation of the polycrystal, a simplified version of the model can be used that does not account for the shear anisotropy on the slip plane. A condition similar to the von Mises yield criterion but for the two-dimensional case is used for the determination of the initiation of plastic flow:

$$T_\tau = \sqrt{(\tau_{31})^2 + (\tau_{32})^2} = \tau^s. \quad (7)$$

The hardening law also changes:

$$\dot{\tau}_{def}^s = h \sqrt{(\dot{\beta}_{31})^2 + (\dot{\beta}_{32})^2}. \quad (8)$$

This version of the model assumes that the shear on the slip plane can occur isotropically and not only in the direction of the smallest Burgers vector. This model can describe the polycrystal behavior well, but it is not suitable for calculating the deformation of a single crystal, in which shear can occur only in certain crystallographic directions.

The calculated tension curve of a polycrystalline sample obtained by the model with isotropic shear is shown in Fig. 2 (dashed line). The results of modeling the deformation of the polycrystalline sample obtained by both models almost coincide. Accounting for anisotropy does not play an important role in modeling the polycrystal deformation because the difference in shear directions in these models ceases to significantly affect the material behavior after averaging over all grains.

## Conclusions

A model of the plastic deformation of a TiNi single crystal is formulated, which accounts for dislocation shear on slip planes occurring only in the direction of the smallest Burgers vector. The material parameters were selected: yield strength and hardening factor for TiNi slip systems. The deformation curves are calculated for different directions of the tensile axis. Comparison with the experimental data showed that the model correctly describes the deformation of TiNi single crystals for different orientations of the tension axis, except for directions close to  $\langle 011 \rangle$ . This exception is due to the failure of the applied condition of the onset of plastic shear to account for possible changes in the deformation mechanism, particularly the splitting of the dislocation core.

A comparison of the results of the calculation according to the proposed model and according to the model allowing isotropic shear in the slip plane showed that, in the case of a polycrystalline sample, the inclusion of the anisotropy in the slip plane is not significant.

## References

1. Mohd JJ, Leary M, Subic A, Gibson MA. A review of shape memory alloy research, applications and opportunities. *Mater. Des.* 2014;56: 1078-1113.
2. Choudhary N, Kaur D. Shape memory alloy thin films and heterostructures for MEMS applications: a review. *Sen. Act. A: Phys.* 2016;242: 162-181.
3. Velmurugan C, Senthilkumar V, Dinesh S, Arulkirubakaran D. Machining of NiTi-shape memory alloys - A review. *Mach. Sci. Tech.* 2018;22(3): 355-401.
4. Patel SK, Behera B, Swain B, Roshan R, Sahoo D, Behera A. A review on NiTi alloys for biomedical applications and their biocompatibility. *Mater. Today: Proc.* 2020;33: 5548-5551.
5. Levitas VI, Javanbakht M. Interaction of phase transformations and plasticity at the nanoscale: phase field approach. *Mater. Today: Proc.* 2015;2: S493-S498.
6. Prokoshkin SD. Regulation of the functional properties of shape memory alloys using thermomechanical treatment. In: Trochu F, Brailovski V, Galibois A (eds.) *Shape Memory Alloys: Fundamentals, Modeling and Industrial Applications, Proceedings of COM 1999, Canadian Institute of Mining, Metallurgy and Petroleum*. Montreal: Canada; 1999. p.267-277.
7. Shoichi E. Two-way shape memory effect generated by deformation of parent phase in Ni-Ti. In: *Proceedings of ICOMAT 1992, Monterey Institute for Advanced Studies*. Monterey, California: USA; 1993. p.965-970.
8. Zel'dovich VI, Sobyana GA, Rinkevich OS. Influence of prestrain on the shape-memory effect and martensite structure in titanium nickelide: I. Dilatometric effects of martensitic transformations. *Phys. Met. Metallogr.* 1996;81: 305-312.
9. Belyaev SP, Resnina NN, Volkov AE. Influence of irreversible plastic deformation on the martensitic transformation and shape memory effect in TiNi alloy. *Mater. Sci. Eng.: A.* 2006;438-440: 627-629.
10. Tanaka K, Nishimura F, Hayashi T, Tobushi H, LExcellent C. Phenomenological analysis on subloops and cyclic behavior in shape memory alloys under mechanical and/or thermal loads. *Mech. Mater.* 1995;19: 281-292.
11. Bo Z, Lagoudas DC. Thermomechanical modeling of polycrystalline SMAs under cyclic loading. Part I. Theoretical derivations. *Int. J. Eng. Sci.* 1999;37(9): 1089-1140.
12. Lagoudas DC, Entchev PB. Modeling of transformation-induced plasticity and its effect on the behavior of porous shape memory alloys. Part I. Constitutive model for fully dense SMAs. *Mech. Mater.* 2004;36(9): 865-892.
13. Sun Q-P, LExcellent C. On the unified micromechanics constitutive description of one-way and two-way shape memory effects. *J. Phys. IV.* 1996;06(C1): 367-375.
14. Evard ME, Volkov AE. Modeling of martensite accommodation effect on mechanical behavior of shape memory alloys. *J. Eng. Mater. Technol.* 1999;121(1): 102-104.
15. Volkov AE, Casciati F. Simulation of dislocation and transformation plasticity in shape memory alloy polycrystals. In: Auricchio F, Faravelli L, Magonette G, Torra V. (eds.) *Shape memory alloys. Advances in modelling and applications, Proceedings of CIMNE*. Barcelona: Spain; 2001. p.88-104.
16. Wang XM, Xu BX, Yue ZF. Micromechanical modelling of the effect of plastic deformation on the mechanical behaviour in pseudoelastic shape memory alloys. *Int. J. Plast.* 2008;24(8): 1307-1332.
17. Manchiraju S, Anderson PM. Coupling between martensitic phase transformations and plasticity: a microstructure-based finite element model. *Int. J. Plast.* 2010;26(10): 1508-1526.
18. Yu C, Kang G, Song D, Kan Q. Micromechanical constitutive model considering plasticity for super-elastic NiTi shape memory alloy. *Computational Mater. Sci.* 2012;56: 1-5.

19. Yu C, Kang G, Kan Q, Song D. A micromechanical constitutive model based on crystal plasticity for thermo-mechanical cyclic deformation of NiTi shape memory alloys. *Int. J. Plasticity*. 2013;44: 161-191.
20. Yu C, Kang G, Kan Q. Crystal plasticity based constitutive model of NiTi shape memory alloy considering different mechanisms of inelastic deformation. *Int. J. Plasticity*. 2014;54: 132-162.
21. Yu C, Kang G, Song D, Kan Q. Effect of martensite reorientation and reorientation-induced plasticity on multiaxial transformation ratchetting of super-elastic NiTi shape memory alloy: New consideration in constitutive model. *Int. J. Plasticity*. 2015;67: 69-101.
22. Dhala S, Mishra S, Tewari A, Alankar A. Modeling of finite deformation of pseudoelastic NiTi shape memory alloy considering various inelasticity mechanisms. *Int. J. Plast.* 2019;115: 216-237.
23. Xie X, Kang G, Kan Q, Yu C, Peng Q. Phase field modeling to transformation induced plasticity in super-elastic NiTi shape memory alloy single crystal. *Modelling Simul. Mater. Sci. Eng.* 2019;27(4): 045001.
24. Xie X, Kang G, Kan Q, Yu C. Phase-field theory based finite element simulation on thermo-mechanical cyclic deformation of polycrystalline super-elastic NiTi shape memory alloy. *Comput. Mater. Sci.* 2020;184: 109899.
25. Hossain M, Baxevanis T. A finite strain thermomechanically-coupled constitutive model for phase transformation and (transformation-induced) plastic deformation in NiTi single crystals. *Int. J. Plast.* 2021;139: 102957.
26. Xu B, Yu C, Kang G. Phase field study on the microscopic mechanism of grain size dependent cyclic degradation of super-elasticity and shape memory effect in nano-polycrystalline NiTi alloys. *Int. J. Plast.* 2021;145: 103075.
27. Ju X, Moumni Z, Zhang Y, Zhang F, Zhu J, Chen Z, Zhang W. A multi-physics, multi-scale and finite strain crystal plasticity-based model for pseudoelastic NiTi shape memory alloy. *Int. J. Plast.* 2022;148: 103146.
28. Belyaev FS, Evard ME, Volkov AE, Volkova NA. A microstructural model of SMA with microplastic deformation and defects accumulation: application to thermocyclic loading. *Mater. Today: Proc.* 2015;2(3): S583-S587.
29. Belyaev FS, Volkov AE, Evard ME. Microstructural modeling of fatigue fracture of shape memory alloys at thermomechanical cyclic loading. *AIP Conf. Proc.* 2018;1959: 070003.
30. Chumlyakov YI, Surikova NS, Korotaev AD. Orientation dependence of strength and plasticity of titanium nickelide single crystals. *Phys. Met. Metallogr.* 1996;82(1): 102-109.
31. Surikova NS, Chumlyakov YI. Mechanisms of plastic deformation of the titanium nickelide single crystals. *Phys. Met. Metallogr.* 2000;89(2): 98-107.

## THE AUTHORS

**Belyaev F.S.** 

e-mail: belyaev\_fs@mail.ru

**Evard M.E.**

e-mail: m.evard@spbu.ru

**Volkov A.E.** 

e-mail: a.volkov@spbu.ru




# On the unloading dynamics in an elastic/viscoplastic material predeformed by viscometric twisting

A.A. Burenin <sup>1</sup> , E.A. Gerasimenko <sup>2</sup>  , L.V. Kovtanyuk <sup>2</sup> 

<sup>1</sup> Khabarovsk federal research center of the Far Eastern Branch of the Russian Academy of Sciences, Turgenev  
St. 51, Khabarovsk, Russia, 680000

<sup>2</sup> Institute of Automation and Control Processes Far Eastern Branch of the Russian Academy of Sciences, 5,  
Radio St., Vladivostok, Russia, 690041

 gerasimenko@iacp.dvo.ru

**Abstract.** Solving the problem of large elastic-plastic deformation theory, the present paper addresses, involved two stages. We first derive the exact solution to the problem of slow strain growth in a cylindrical layer consisting of an incompressible elastic/viscoplastic material and experiencing viscometric motion subject to no-slip contact between the material and the rigid instrument's walls. Then a striking stick-slip transition at one of the material-instrument interfaces poses the problem of unloading dynamics. Stress jump at the boundary surface causes a shear cylindrical unloading shock wave, which advances into the material and interacts with the elastic-plastic boundary separating viscoplastic flow from reversible deformation region. To solve this dynamic problem the ray method for constructing approximate solutions is adjusted to the case of elastic/viscoplastic material.

**Keywords:** large strains, elasticity, viscoplasticity, viscometric strains, unloading wave, ray method

**Citation:** Burenin AA, Gerasimenko EA, Kovtanyuk LV. On the unloading dynamics in an elastic/viscoplastic material predeformed by viscometric twisting. *Materials Physics and Mechanics*. 2023;51(1): 68-83. DOI: 10.18149/MPM.5112023\_7.

## Introduction

The dynamics of solids under impulse or shock loading remains one of the primary concerns of modern mechanics and mathematical physics. Such problems arise when dealing with issues of ensuring the reliability of critical units in mechanisms and machines, upon improving technology for processing materials and manufacturing products, in nonlinear acoustics and acoustic diagnostics, in seismology and seismic exploration. Unsteady impact on the boundaries of deformable bodies causes the propagation of velocity (shock waves) or acceleration (weak waves) discontinuities through the material. They are generally induced by discontinuous initial and boundary conditions; although, a weak wave may terminate into a shock one [1,2] due to the unbounded growth of its strength [3,4]. This phenomenon is essentially nonlinear [5], as also is the dependence of wave velocities on the preliminary strains [6] and shock wave velocities on the amplitude of discontinuities [7-9].

Originally, these and other nonlinear phenomena used to be observed in gas dynamics, which, unlike dynamics of solids, was developed as a nonlinear theory. The situation is more complicated for solids because they exhibit both volumes (as in gas dynamics) and shape-

changing strains. Volume and shape-changing deformations propagate independently only in the scope of linear elasticity, but they are coupled in the nonlinear case. Sometimes, in order to focus on the aspects of propagating shear strains solely, the material is assumed to be incompressible [10-12]. Herein, we introduce this simplifying constraint too.

When the plastic properties of material should be taken into account along with elastic ones, the problem is getting more challenging. J. Mandel [13] noted that in the context of the Prandtl-Reuss elastoplastic flow model [14] shock waves cannot be uniquely described by a closed system of equations in terms of discontinuities. To avoid this uncertainty, the auxiliary thermodynamic hypothesis on the maximum mechanical energy dissipation on the surfaces across which plastic strains are discontinuous had to be introduced [15,16]. With this hypothesis accepted and small deformations assumed, the first simplest problems of the perfect elastoplasticity [17-20] were solved; algorithms and programs for numerical calculations were developed [21-25]. Among the latter, finite-difference, characteristics, and finite-element calculation methods evolved. But in all cases, the main challenge in calculating the deformation dynamics was associated with discontinuity surfaces traveling through a deformable body, especially the surfaces of velocity discontinuities.

In gas dynamics [3], special shock-fitting algorithms were developed to calculate the location and the amplitude of discontinuities. They typically constitute a two-step scheme of predictor-corrector type relying on the solution of the discontinuity decomposition problem at the intermediate step. In solid dynamics, due to interacting processes of shear and volumetric strain propagation, the problem of the decomposition of a combined discontinuity is hardly ever tractable [17,20]; therefore, various modifications of shock-capturing methods are employed [22]. Nevertheless, it is worth remarking that discontinuities in solids can be fitted by the methods based on integral generalizations of variational inequalities [21] and the methods for embedding near-front asymptotics into finite-difference schemes [26-28]. Asymptotic expansions of solutions behind discontinuity surfaces are constructed either using the perturbation method [29] or the ray method [27]. By so doing, the location of discontinuities and their amplitudes are corrected at each time step of calculations.

The method for constructing approximate solutions of essentially unsteady dynamic problems in the form of near-front expansions was proposed in papers [30] and [31], in which it was termed the ray method. Achenbach and Reddy [30] constructed an approximate solution as a power series with respect to time, while Babicheva et al. [31] did so with respect to the ray coordinate. Obeying compatibility conditions for discontinuities [15,32-34] one can recurrently deduce ordinary differential equations (decay equations) for coefficients of these power series. The recurrence is violated only if the velocity of the discontinuity surface depends on the variable amplitude of discontinuity, i.e., for shock waves in the nonlinear media. Peculiarities of the ray method employment and approximate solutions obtained by means of it were reviewed in [35]. Burenin et. al. [36-38] tailored the method of ray expansions for constructing solutions behind shock wave fronts. In the present paper, we use the ray method in the dynamics of large elastic/viscoplastic deformations [39,40] to construct a ray expansion of a solution behind the front of the unloading shock wave.

Dynamics of elastic/viscoplastic medium unloading was studied in [41-43], where authors obtained the exact solutions of the problems on instantaneous unloading of a material that had undergone large elastic/viscoplastic strains under quasistatic deforming prior to that. The interaction of the unloading shock wave with the moving elastic-plastic boundary was investigated. The success in solving these problems was gained by applying the theory of large elastic-plastic deformations [44,45], in which reversible and irreversible strains were specified by differential equations of their change (transfer). The foundations of the mathematical model for this theory [44,45] were proposed in [46,47]. The content of [44], thus, constitutes analytical and numerical-analytical solutions of boundary-value problems of the large strain theory just

mentioned along with a detailed description of the way to obtaining model relations. Herein, we also solve the boundary-value problem in the context of the theory [44], but our concern is constructing an approximate solution behind the front of the unloading shock wave by means of the ray expansions.

We should stress that allowing for the viscous resistance to plastic flow has even facilitated deriving exact solutions [42,43]. Herein, we also take it into account when constructing the ray expansion. Such a simplification is associated with the fact that, due to the viscosity of the material under plastic flow, irreversible deformations are continuous across the surfaces of velocity discontinuities. This leads to the effect that, in contrast to the elastic-plastic medium [16,21], the elastic/viscoplastic one cannot transmit discontinuity surfaces other than those moving with elastic wave velocities [48-50].

Reversible and irreversible deformations are interdependent in the course of deforming. Therefore, the initial stress-strain state cannot be prescribed arbitrarily [42-44] when posing unloading problems. It must be a result of the preliminary loading process. So, any problem of unloading a deformable body that has accumulated large strains must be preceded by solving the problem on the loading of this body providing data on the resulting distribution of reversible and irreversible strains over the body. Such a loading problem can be a quasistatic one, in which inertia forces can be neglected due to the slow process of active deformation. It is precisely such a loading process that we consider here.

### Mathematical model of elastic/viscoplastic material

Flow plasticity theory demands decomposing strains in a body into reversible and irreversible parts, which, unlike total strains, are not measurable experimentally. Therefore, introducing them into the theory is hypothetical. However, they are highly important for the theory as they are thermodynamic parameters of state for a deformable body. According to the concept of constructing the thermodynamics of processes, it is reversible and irreversible strains that one should formulate differential equations of their change (transfer) for [44,45,51]. These equations may serve as a definition for the parts of deformation or accompany such parameters of state if the latter is defined out of other considerations. It only matters while doing so that the relations formulated are geometrically consistent.

When deformations are small, the problem of constructing equations of total deformation transfer does not arise because its solution is obvious. In the case of large deformations, [52,53] such a problem is most often reduced to "choosing" the objective derivative of the hypothetically constructed tensor of plastic strains.

For the present study, we adopt the mathematical model proposed in [46,47] and thoroughly discussed in [44,45]. Equations of change in the tensors of reversible  $\mathbf{e}$  and irreversible  $\mathbf{p}$  strains can be written in the form [44,45]

$$\frac{D\mathbf{e}}{Dt} = \boldsymbol{\varepsilon} - \boldsymbol{\varepsilon}^p - \frac{1}{2}((\boldsymbol{\varepsilon} - \boldsymbol{\varepsilon}^p + \mathbf{z}) \cdot \mathbf{e} + \mathbf{e} \cdot (\boldsymbol{\varepsilon} - \boldsymbol{\varepsilon}^p - \mathbf{z})), \quad (1)$$

$$\frac{D\mathbf{p}}{Dt} = \boldsymbol{\varepsilon}^p - \mathbf{p} \cdot \boldsymbol{\varepsilon}^p - \boldsymbol{\varepsilon}^p \cdot \mathbf{p}, \quad (2)$$

where

$$\frac{D\mathbf{n}}{Dt} = \frac{d\mathbf{n}}{dt} - \mathbf{r} \cdot \mathbf{n} - \mathbf{n} \cdot \mathbf{r}^T, \quad \boldsymbol{\varepsilon} = \frac{1}{2}(\nabla \mathbf{v} + \nabla^T \mathbf{v}), \quad \boldsymbol{\omega} = \frac{1}{2}(\nabla \mathbf{v} - \nabla^T \mathbf{v}),$$

$$\mathbf{v} = \frac{d\mathbf{u}}{dt} = \frac{\partial \mathbf{u}}{\partial t} + \mathbf{v} \nabla \mathbf{u}, \quad \mathbf{r} = \boldsymbol{\omega} + \mathbf{z},$$

$$\mathbf{z} = A^{-1}\{B^2(\boldsymbol{\varepsilon} \cdot \mathbf{e} - \mathbf{e} \cdot \boldsymbol{\varepsilon}) + B(\boldsymbol{\varepsilon} \cdot \mathbf{e}^2 - \mathbf{e}^2 \cdot \boldsymbol{\varepsilon}) + \mathbf{e} \cdot \boldsymbol{\varepsilon} \cdot \mathbf{e}^2 - \mathbf{e}^2 \cdot \boldsymbol{\varepsilon} \cdot \mathbf{e}\},$$

$$A = 8 - 8E_1 - 3E_1^2 - E_2 - \frac{E_1^3}{3} + \frac{E_3}{3}, \quad B = 2 - E_1,$$

$$E_1 = \text{tr}(\mathbf{e}), \quad E_2 = \mathbf{e} \cdot \mathbf{e}, \quad E_3 = \mathbf{e}^2 \cdot \mathbf{e}.$$

In the transfer equations for reversible (1) and irreversible (2) strains,  $\mathbf{u}$  and  $\mathbf{v}$  are the displacement and the velocity vectors respectively. The terms  $(\boldsymbol{\varepsilon} - \boldsymbol{\varepsilon}^p)$  and  $\boldsymbol{\varepsilon}^p$  in the right parts of equations (1)-(2) are the sources of strains. The remaining terms in the right parts are the flux terms. They define the interdependence of the thermodynamic parameters  $\mathbf{e}$  and  $\mathbf{p}$  in the course of their change. The geometrical consistency of this interdependence requires the definite objective time derivative in (1) and (2). The form of this derivative is indicated for an arbitrary tensor  $\mathbf{n}$ . If the nonlinear part  $\mathbf{z}$  of the tensor  $\mathbf{r}$  is null, the objective derivative  $D/Dt$  in (1) and (2) becomes the Jaumann derivative [44,45].

The sources in transfer equations (1) and (2) define the growth of reversible  $\mathbf{e}$  and irreversible  $\mathbf{p}$  strains and must be related to the reasons for this growth by governing laws. According to (2), there is a possibility for the deformation process with  $\boldsymbol{\varepsilon}^p = 0$ , when  $D\mathbf{p}/Dt = 0$ . In this case, the tensor of irreversible strains is invariable, but its components change as if the body would move without getting deformed. Dependencies (1) and (2) endow the regions of preliminary reversible (elastic) deformation  $\mathbf{p} = 0$  and the unloading regions  $\mathbf{p} = \text{const} \neq 0$  with this property.

Recalling (1) and (2), the Almansi tensor of total strains  $\mathbf{d}$  is defined as follows [44,45,47]

$$\mathbf{d} = \mathbf{e} + \mathbf{p} - \frac{1}{2} \mathbf{e} \cdot \mathbf{e} - \mathbf{e} \cdot \mathbf{p} - \mathbf{p} \cdot \mathbf{e} + \mathbf{e} \cdot \mathbf{p} \cdot \mathbf{e}. \quad (3)$$

Reasoning from (3), rather it is the tensor  $\mathbf{s} = \mathbf{e} - \mathbf{e} \cdot \mathbf{e}/2$  that should have been referred to as a tensor of reversible (elastic) strains, in which the tensor  $\mathbf{e}$  is a main linear part. The tensor  $\mathbf{e}$  is the one of small elastic strains; it turned out to be convenient for writing transfer equations (1) and (2) by means of it. It also proved to be more useful when writing a counterpart of the Murnaghan formula [44,45,54] in the case of perfect elastoplasticity under study. This formula for the case of an incompressible medium considered below reads [44,45]

$$\begin{aligned} \boldsymbol{\sigma} &= -p_1 \mathbf{I} - \frac{\partial W}{\partial \mathbf{d}} (\mathbf{I} - 2\mathbf{d}) \text{ if } \mathbf{p} = 0, \\ \boldsymbol{\sigma} &= -p_2 \mathbf{I} - \frac{\partial W}{\partial \mathbf{e}} (\mathbf{I} - \mathbf{e}) \text{ if } \mathbf{p} \neq 0. \end{aligned} \quad (4)$$

In (4),  $\boldsymbol{\sigma}$  is the Euler-Cauchy stress tensor,  $p_1$  and  $p_2$  are the additional hydrostatic pressures,  $\mathbf{I}$  is the second-order unit tensor,  $W = W(J_1, J_2)$  is the elastic potential (free energy density in the isothermal case). For proceeding calculations, we designate  $W = W(J_1, J_2)$  as follows

$$W = -2\mu J_1 - \mu J_2 + b J_1^2 + (b - \mu) J_1 J_2 - \chi J_1^3 + \dots, \quad (5)$$

$$J_k = \begin{cases} L_k & \text{if } \mathbf{p} \equiv 0 \\ I_k & \text{if } \mathbf{p} \neq 0 \end{cases}, \quad k = 1, 2,$$

$$L_1 = \text{tr}(\mathbf{d}), \quad L_2 = \mathbf{d} \cdot \mathbf{d}, \quad I_1 = \text{tr}(\mathbf{e}) - \frac{1}{2} \mathbf{e} \cdot \mathbf{e}, \quad I_2 = \mathbf{e} \cdot \mathbf{e} - \mathbf{e}^2 \cdot \mathbf{e} + \frac{1}{4} \mathbf{e}^2 \cdot \mathbf{e}^2.$$

In (5),  $\mu$  is the shear modulus;  $b$  and  $\chi$  are the higher-order elastic moduli. The invariants  $I_1$  and  $I_2$  of the reversible strain tensor are specified in such a way as to ensure the limiting transition from the second formula in (4) to the first one as the plastic strains tend to zero.

The relation (2) allows deforming without the growth of irreversible strains, i.e. elastic deforming. We remark that this assumption idealizes the deformable material. This is achievable only in the scope of perfect elastoplasticity. The real body possesses viscosity, so upon imposing stress it acquires unrecoverable strains due to the creeping onset. However, differential equation (2) does not contradict this either. Ignoring this phenomenon, we further assume the deformable material to be perfectly elastic-plastic [14]. In such a material, irreversible (plastic) strains begin going up when the stresses reach the loading surface  $f(\boldsymbol{\sigma}, \boldsymbol{\varepsilon}^p, k) = 0$ . As a loading surface, we take the unified condition of maximum tangential stresses [14]

$$f(\sigma_i, \varepsilon_k^p, k) = \max |\sigma_i - \sigma_j| - 2k - 2\eta \max |\varepsilon_k^p|. \quad (6)$$

In (6),  $\sigma_i$  and  $\varepsilon_k^p$  are the principal values of the stress and the strain rate tensors respectively,  $k$  is the yield stress, and  $\eta$  is the coefficient of viscous resistance to plastic flow. Imposing the condition of the von Mises maximum principle [14], we have the associated law of plastic flow

$$\varepsilon^p = \lambda \frac{\partial f}{\partial \sigma}, \quad \lambda > 0. \quad (7)$$

In order to get the closed system of equations both in the region of elastic deformation and in the region of plastic flow it suffices to complete the preceding relations with the equation of motion or the balance equation

$$\nabla \cdot \sigma = \rho \frac{dv}{dt}, \quad (8)$$

$$\nabla \cdot \sigma = 0. \quad (9)$$

Whenever forces of inertia are feasible to be ignored in (8) so as to have (9), a quasistatic approximation is allowed in solving the problem.

### Quasistatic deformation

Let the material, the deformation properties of which obey the relations stated in Section 2, fills the layer between two coaxial rigid surfaces. The equations of these surfaces in the cylindrical coordinate system  $(r, \varphi, z)$  are the following:  $r = r_0$ ,  $r = R$  ( $r_0 < R$ ). Deforming is caused by revolving the inner cylinder  $r \leq r_0$  about its axis  $r = 0$  while the surface  $r = R$  is motionless. The material is considered to be initially unstrained. Assume that the no-slip conditions are satisfied at the boundary surfaces  $r = r_0$  and  $r = R$  until the shear stress exceeds some given threshold value  $|\sigma_{r\varphi}| \leq \sigma_0$

$$u(R, t) = v(R, t) = 0, \quad \sigma_{r\varphi}(r_0, t) = -\alpha t. \quad (10)$$

The latter condition specifies the load on the deformable material;  $\sigma_0$  and  $\alpha$  are the prescribed constants of the problem. We put  $\sigma_0 > k$ . Due to the imposed condition of incompressibility, the paths of the material's particles are concentric circles, and the only nonzero component of the velocity vector is  $v_\varphi$ . According to (1)-(3), the kinematics of the medium in this case is determined by the relations

$$u_r = r(1 - \cos\psi), \quad u_\varphi = r \sin\psi, \quad (11)$$

$$d_{rr} = -\frac{f^2}{2}, \quad d_{r\varphi} = \frac{f}{2}, \quad f = r \frac{\partial \psi}{\partial r}, \quad v_\varphi = r\omega = r \frac{\partial \psi}{\partial t},$$

$$\varepsilon_{r\varphi} = \frac{r}{2} \frac{\partial^2 \psi}{\partial r \partial t}, \quad \omega_{r\varphi} = -\frac{\partial \psi}{\partial t} - \frac{r}{2} \frac{\partial^2 \psi}{\partial r \partial t}, \quad r_{r\varphi} = -\frac{\partial \psi}{\partial t} + \frac{2\varepsilon_{r\varphi}(1 - e_{\varphi\varphi})}{e_{rr} + e_{\varphi\varphi} - 2},$$

where  $\psi = \psi(r, t)$  is the central angle of twisting of medium particles, and  $\omega = v_\varphi/r$  is the angular velocity.

Taking into account that for such problems diagonal components of the strain tensors are small quantities of a higher order of smallness compared to off-diagonal components [44], hereinafter we restrict ourselves to terms of the first order with respect to diagonal components and of the second order with respect to off-diagonal components. Such a restriction, though not mandatory, allows us to obtain analytical relations for the displacements. From (4) and (5) we derive stress components

$$\sigma_{rr} = -p - 2\mu + 2(b + \mu)e_{rr} + 2be_{\varphi\varphi} + \mu e_{r\varphi}^2, \quad (12)$$

$$\sigma_{\varphi\varphi} = -p - 2\mu + 2(b + \mu)e_{\varphi\varphi} + 2be_{rr} + \mu e_{r\varphi}^2,$$

$$\sigma_{zz} = -p - 2\mu + 2b(e_{rr} + e_{\varphi\varphi}) - 2\mu e_{r\varphi}^2, \quad \sigma_{r\varphi} = 2\mu e_{r\varphi}, \quad \frac{\sigma_{rr} - \sigma_{\varphi\varphi}}{\sigma_{r\varphi}} = \frac{e_{rr} - e_{\varphi\varphi}}{e_{r\varphi}}.$$

At the beginning of the loading process (from the instant  $t = 0$ ), the material deforms reversibly ( $p_{ij} = 0$ ). According to relations (12) and (3), the stress components, in this case, can be written as follows

$$\begin{aligned}\sigma_{rr} = \sigma_{zz} &= -(p + 2\mu) - \frac{(b+\mu)}{2}f^2 = -s(r, t), \\ \sigma_{\varphi\varphi} &= -s(r, t) + \mu f^2, \quad \sigma_{r\varphi} = \mu f.\end{aligned}\quad (13)$$

Substituting (13) into (9), we get two balance equations

$$\frac{\partial \sigma_{rr}}{\partial r} + \frac{\sigma_{rr} - \sigma_{\varphi\varphi}}{r} = 0, \quad \frac{\partial \sigma_{r\varphi}}{\partial r} + 2 \frac{\sigma_{r\varphi}}{r} = 0. \quad (14)$$

Then, integrating equations (14) subject to the boundary conditions (10), we obtain a solution for the case when material acquires the elastic deformation

$$\psi = \frac{c(t)}{2\mu} \left( \frac{1}{R^2} - \frac{1}{r^2} \right), \quad \omega = \frac{\dot{c}(t)}{2\mu} \left( \frac{1}{R^2} - \frac{1}{r^2} \right), \quad \dot{c}(t) = \frac{dc(t)}{dt}, \quad (15)$$

$$\sigma_{r\varphi} = \frac{c(t)}{r^2}, \quad \sigma_{rr} = \sigma_{zz} = \frac{c^2(t)}{4\mu} \left( \frac{1}{r_0^4} - \frac{1}{r^4} \right) + \sigma_{rr}^0,$$

$$\sigma_{\varphi\varphi} = \frac{c^2(t)}{4\mu} \left( \frac{1}{r_0^4} + \frac{3}{r^4} \right) + \sigma_{rr}^0, \quad c(t) = -\alpha t r_0^2,$$

$$e_{r\varphi} = d_{r\varphi} = \frac{c(t)}{2\mu r^2}, \quad e_{rr} = -\frac{3}{2}e_{r\varphi}^2, \quad e_{\varphi\varphi} = \frac{e_{r\varphi}^2}{2},$$

where  $\sigma_{rr}^0 = \sigma_{rr}(r_0, t)$  is a prescribed value of the stress component  $\sigma_{rr}$  at the surface  $r = r_0$ .

Solution (15) is valid within the time interval from  $t = 0$  to  $t = t_0$  until the plasticity condition (6) is fulfilled at the rigid wall  $r = r_0$ , which, under the restrictions applied, takes the form  $\sigma_{r\varphi}(r_0, t_0) = -k$ . Substituting the value  $\sigma_{r\varphi}(r_0, t_0)$  into the last equation and using (15), we find the moment of the plastic flow onset  $t_0 = k/\alpha$ .

Thenceforth, the region of viscoplastic flow  $V^{(P)}: r_0 \leq r \leq m(t)$  develops from the boundary  $r = r_0$ . The surface  $r = m(t)$  is an elastic-plastic boundary. In the region  $V^{(E)}: m(t) \leq r \leq R$  reversible deforming continues.

By integrating the balance equations (14) in the region of recoverable deforming and using condition (10), we find

$$\sigma_{r\varphi}^{(E)} = \frac{c(t)}{r^2}, \quad \psi^{(E)} = \frac{c(t)}{2\mu} \left( \frac{1}{R^2} - \frac{1}{r^2} \right), \quad \omega^{(E)} = \frac{\dot{c}(t)}{2\mu} \left( \frac{1}{R^2} - \frac{1}{r^2} \right). \quad (16)$$

Hereinafter, the superscript "E" is related to the region  $V^{(E)}$  while the superscript "P" denotes the region  $V^{(P)}$ .

In the case under study, the yielding criterion (6) reads

$$f(\sigma_{r\varphi}, \varepsilon_{r\varphi}^p) = \sigma_{r\varphi}^2 - (k - \eta |\varepsilon_{r\varphi}^p|)^2 = 0. \quad (17)$$

In virtue of the associated flow rule (7), the condition (17) leads to

$$\sigma_{r\varphi} = -k + \eta \varepsilon_{r\varphi}^p, \quad \lambda = \frac{\varepsilon_{r\varphi}^p}{\eta \varepsilon_{r\varphi}^p - k}. \quad (18)$$

By integrating the balance equations (14) in conjunction with the continuity conditions for the stress components at the elastic-plastic boundary  $r = m(t)$ , we obtain the components  $\sigma_{r\varphi}$ ,  $e_{r\varphi}$  in the plastic flow region

$$\sigma_{r\varphi}^{(P)} = \frac{c(t)}{r^2}, \quad e_{r\varphi} = \frac{c(t)}{2\mu r^2}. \quad (19)$$

Comparing (18) and (19), we calculate the plastic strain rate

$$\varepsilon_{r\varphi}^p = \frac{1}{\eta} \left( k + \frac{c(t)}{r^2} \right). \quad (20)$$

The unknown function of integration  $c(t)$  has to be determined from the condition of zero plastic strain rate at the elastic-plastic boundary  $r = m(t)$

$$c(t) = -k m(t)^2. \quad (21)$$

On the other hand, following the last boundary condition in (10)

$$c(t) = -\alpha t r_0^2, \quad (22)$$

that allows us to get the expression for the surface  $m(t)$

$$m(t) = r_0 \sqrt{\alpha t / k}. \quad (23)$$

According to the relations (1)-(3), the yielding criterion (17), and the associated flow rule (18), in the region of plastic flow the kinematics of the medium are determined by the relations

$$\begin{aligned} \varepsilon_{r\varphi} &= \varepsilon_{r\varphi}^e + \varepsilon_{r\varphi}^p = \frac{\partial e_{r\varphi}}{\partial t} + \frac{\partial p_{r\varphi}}{\partial t}, \quad \varepsilon_{rr}^p = \frac{\partial p_{rr}}{\partial t} + 2p_{r\varphi}(r_{\varphi r} + \varepsilon_{r\varphi}^p) - 2p_{r\varphi} \frac{\partial \psi}{\partial t}, \\ \varepsilon_{\varphi\varphi}^p &= \frac{\partial p_{\varphi\varphi}}{\partial t} + 2p_{r\varphi}(r_{\varphi\varphi} + \varepsilon_{r\varphi}^p) + 2p_{r\varphi} \frac{\partial \psi}{\partial t}, \quad \varepsilon_{rr}^p = -\varepsilon_{\varphi\varphi}^p = \frac{\varepsilon_{r\varphi}^p(e_{rr} - e_{\varphi\varphi})}{2e_{r\varphi}}. \end{aligned} \quad (24)$$

Components of the velocity and the strain rate tensor are determined by (11).

Utilizing kinematic relations (24) and formula (20), we obtain the component of plastic strains  $p_{r\varphi}$

$$p_{r\varphi} = \frac{1}{\eta} \left( kt - \frac{\alpha r_0^2 t^2}{2r^2} \right) + g(r). \quad (25)$$

Recalling the condition of zero plastic strain rate at the elastic-plastic boundary  $r = m(t)$  and relation (23), we derive the unknown function  $g(r)$

$$g(r) = -\frac{k^2 r^2}{2\alpha\eta r_0^2}. \quad (26)$$

In accordance with relations (3), we have  $d_{r\varphi} = e_{r\varphi} + p_{r\varphi}$ . Then, combining (11) and (23)-(26), we deduce the differential equation governing the twist angle  $\psi(r, t)$  in the region of plastic flow

$$\frac{r}{2} \frac{\partial \psi}{\partial r} = \frac{1}{\eta} \left( kt - \frac{\alpha t^2 r_0^2}{2r^2} \right) - \frac{k^2 r^2}{2\alpha\eta r_0^2} - \frac{\alpha t r_0^2}{2\mu r^2}.$$

After integration in conjunction with the condition of continuity of function  $\psi(r, t)$  across the elastic-plastic boundary  $r = m(t)$ , we find  $\psi(r, t)$  in the yielding region

$$\psi^{(p)} = \frac{2kt}{\eta} \ln \frac{r}{m(t)} + \frac{\alpha r_0^2 t}{2\mu} \left( \frac{1}{r^2} - \frac{1}{R^2} \right) + \frac{\alpha r_0^2 t^2}{2\eta} \left( \frac{1}{r^2} - \frac{1}{m(t)^2} \right) + \frac{k^2}{2\alpha\eta r_0^2} (m(t)^2 - r^2). \quad (27)$$

Referring to (25) and (26), we have

$$p_{r\varphi} = \frac{1}{\eta} \left( kt - \frac{\alpha r_0^2 t^2}{2r^2} - \frac{k^2 r^2}{2\alpha r_0^2} \right). \quad (28)$$

Using equations of variation of strain components (1)-(2) and conditions (17)-(18), we obtain a system of equations for diagonal components of elastic  $e_{rr}$ ,  $e_{\varphi\varphi}$  and plastic  $p_{rr}$ ,  $p_{\varphi\varphi}$  strain tensors in the yielding region. These components are small quantities of a higher order of smallness compared to off-diagonal ones

$$\begin{aligned} \frac{\partial p_{r\varphi}}{\partial t} &= \varepsilon_{r\varphi}^p, \quad \frac{\partial p_{\varphi\varphi}}{\partial t} = -\varepsilon_{r\varphi}^p \frac{p_{\varphi\varphi} - e_{r\varphi}^2}{e_{r\varphi}} + \frac{4\varepsilon_{r\varphi} p_{r\varphi}}{2 + e_{r\varphi}^2} \left( 1 + p_{\varphi\varphi} - \frac{1}{2} e_{r\varphi}^2 - 2e_{r\varphi} p_{r\varphi} \right), \\ e_{rr} &= p_{\varphi\varphi} - \frac{3e_{r\varphi}^2}{2} - 2e_{r\varphi} p_{r\varphi}, \quad p_{rr} + p_{\varphi\varphi} = -2p_{r\varphi}^2, \quad e_{rr} + e_{\varphi\varphi} = -e_{r\varphi}^2. \end{aligned} \quad (29)$$

System (29) can be integrated numerically. The stress component  $\sigma_{rr}$  is found from the first balance equation (14) with the account of its value at the surface  $r = r_0$ . Then, from the relations (12), the hydrostatic pressure  $p$  and the stress components  $\sigma_{\varphi\varphi}$  and  $\sigma_{zz}$  are determined.

### Unloading wave. Ray method

The moment the stress  $|\sigma_{r\varphi}|$  at the surface  $r = r_0$  touches the critical value  $\sigma_0$ , the stick boundary condition shifts abruptly to the condition of friction between the material and the rigid cylindrical surface. Various conditions of dry or viscous friction can be taken as a law of friction. Here, we adopt the friction condition according to Prandtl law:  $|\sigma_{r\varphi}(r_0, t)| = \sigma_s$ ,  $\sigma_s = \text{const}$ ,  $\sigma_s < k$ .

According to (19), a change in the boundary condition occurs at the instant of time  $t = t_s = \sigma_0/\alpha$ . The jump in the boundary condition  $[\sigma_{r\varphi}(r_0, t_s)] = \sigma_s - \sigma_0 \neq 0$  causes the cylindrical shock wave  $\Sigma_1$ , which location in space is determined by the equation  $r = r_1(t) = r_0 + \int_{t_s}^t G(\xi) d\xi$ .

A shock wave is thought to be a surface of strong discontinuity, i.e. such a surface that displacements are continuous over it, while velocities and stresses suffer a finite discontinuity. The surface of strong discontinuity [48] could be interpreted as a limiting layer of thickness  $\Delta S$  ( $\Delta S \rightarrow 0$ ); within this layer velocities and stresses change from the values  $v_i^+$ ,  $\sigma_{ij}^+$  to the values  $v_i^-$ ,  $\sigma_{ij}^-$ , remaining monotonic and continuous inside the layer. Across the surfaces of weak discontinuity that also emerge in what follows, stresses and velocities remain continuous, but some of their partial derivatives undergo a discontinuity. As is customary, the surface of weak discontinuity, across which a discontinuity in the first-order derivative of the velocity occurs, is called a weak wave of the first order or an acceleration wave.

Thus, since the emergence of shock wave, the material of the deformable layer is divided into three parts. It keeps deforming reversibly in the region  $V^{(E)}: m(t) \leq r \leq R$ , while viscoplastic flow proceeds in the region  $V^{(P)}: r_1(t) \leq r \leq m(t)$ . In the unloading domain  $V^{(1)}: r_0 \leq r \leq r_1(t)$  material deforms reversibly anew, but with previously accumulated unrecoverable strains. According to (28) and (29), the component of irreversible strains  $p_{r\phi}(r)$  alone is invariable upon unloading process

$$p_{r\phi}(r) = \frac{1}{\eta} \left( k\tau_1(r) - \frac{\alpha r_0^2 \tau_1^2(r)}{2r^2} - \frac{k^2 r^2}{2\alpha r_0^2} \right), \quad (30)$$

where  $\tau_1(r) = t_s + \int_{r_0}^r d\xi/G(\xi)$  is the time the wave front  $\Sigma_1$  reaches a position  $r$ . Other components of plastic strain tensor  $p_{rr}(r, t)$ ,  $p_{\phi\phi}(r, t)$  keep changing with time due to changing elastic strains  $e_{r\phi}(r, t)$ . Hence, there is an internal redistribution between elastic and plastic strains; components  $p_{rr}(r, t)$ ,  $p_{\phi\phi}(r, t)$  can both increase and decrease in magnitude. Behind the unloading shock wave equations of motion may be written as

$$\frac{\partial \sigma_{r\phi}}{\partial r} + 2 \frac{\sigma_{r\phi}}{r} = \rho r \ddot{\psi}, \quad \frac{\partial \sigma_{rr}}{\partial r} + \frac{\sigma_{rr} - \sigma_{\phi\phi}}{r} = -\rho r \dot{\psi}^2. \quad (31)$$

The former equation in (31) is meant for determining the kinematics of unloading deforming, while the latter can be used for calculating the additional hydrostatic pressure  $p(r, t)$  based on the solution obtained for the function  $\psi(r, t)$ . Therefore, the boundary-value problem for the former equation in (31) should be solved first. From (11), (12), and (30), we get the following expression for the stress component  $\sigma_{r\phi}$

$$\sigma_{r\phi} = \mu r \psi_{,r} - \frac{2\mu}{\eta} \left( k\tau_1(r) - \frac{\alpha r_0^2}{2r^2} \tau_1^2(r) - \frac{k^2 r^2}{2\alpha r_0^2} \right). \quad (32)$$

Substituting (32) into the former equation in (31), we obtain a second-order partial differential equation of a hyperbolic type. The boundary conditions for such an equation will be the condition of displacement continuity across the unloading wave  $r = r_1(t)$  and the friction condition at the boundary surface  $r = r_0$ , respectively

$$[\psi]_{\Sigma_1} = (\psi^+ - \psi^-)|_{r=r_1(t)} = 0, \quad (33)$$

$$\sigma_{r\phi}(r_0, t) = -\sigma_s. \quad (34)$$

Hereinafter, square brackets denote the jump across the discontinuity surface for any function enclosed in them;  $\psi^+ = \psi^+(r_1(t), t)$  and  $\psi^- = \psi^-(r_1(t), t)$  are the values of function  $\psi(r, t)$  just ahead of the discontinuity surface and immediately behind it, respectively.

In an elastic/viscoplastic medium, irreversible strains are continuous across the discontinuity surface  $[p_{r\phi}] = 0$  [48-50]. Therefore, the velocity  $G(t)$  of the unloading shock wave can depend only on preliminary strains and jumps of reversible strains [42,50]. In all the previous relations, terms of third and higher powers of  $e_{r\phi}$  were omitted. If we restrict ourselves only to the preceding relations, we derive that the unloading wave speed is constant  $G = \sqrt{\mu/\rho}$  and  $\tau_1(r) = t_s + (r - r_0)/G$ . The equation of motion in this case takes the simplest form

$$\psi_{,rr} + \frac{3}{r} \psi_{,r} - \frac{\ddot{\psi}}{G^2} = \frac{2}{\eta} \left( \frac{k}{Gr} - \frac{\alpha r_0^2 \tau_1(r)}{Gr^3} + \frac{2k\tau_1(r)}{Gr^2} - \frac{k^2 r^2}{2\alpha r_0^2} \right). \quad (35)$$



Even such a simplified equation (35) is not exactly solvable. Therefore, we solve it approximately by means of the ray method subject to the boundary conditions (33) and (34). It is worth remarking that the ray method allows for solving the problem even without simplifying assumptions made. They are not required for the method. If one includes in (12) third and higher order powers of  $e_{r\varphi}$ , the velocity of the unloading shock wave  $G$  will not be constant. Such a case for a nonlinear elastic medium was considered in [26-28,36-38]. A review of publications devoted to the features of applying the ray method to constructing approximate solutions of solid dynamics problems one can find in [35]. In the case being considered, to construct an approximate solution for equation (35) with boundary conditions (33) and (34), it is convenient to apply the ray method in its classical form, as it was proposed more than half a century ago [30]. In addition, since the ray is a curve invariably orthogonal to the discontinuity surface, for the problem in question it coincides with the coordinate axis  $Or$ .

The function  $\psi(r, t)$  is continuous across the discontinuity surface  $[\psi] = 0$ , but its derivatives and, hence, velocity, strains, and stresses undergo ordinary discontinuity. Let us introduce a ray series for the function  $\omega(r, t) = \dot{\psi}(r, t)$  behind the unloading shock wave as follows

$$\begin{aligned}\omega(r, t) &= \omega^-|_{t=\tau_1} + \dot{\omega}^-|_{t=\tau_1}(t - \tau_1) + \frac{1}{2}\ddot{\omega}^-|_{t=\tau_1}(t - \tau_1)^2 + \dots = \\ &= (\omega^+ - [\omega])|_{t=\tau_1} + (\dot{\omega}^+ - [\dot{\omega}])|_{t=\tau_1}(t - \tau_1) + \frac{1}{2}(\ddot{\omega}^+ - [\ddot{\omega}])|_{t=\tau_1}(t - \tau_1)^2 + \dots.\end{aligned}\quad (36)$$

Expansion (36) is Taylor's series in time  $t$  about the instant of arrival of the wave front at a given point of space. The ray series for the stresses and the angle of twisting are written similarly to (36), and all the quantities desired are expressed in terms of jumps in the angular velocity and its derivatives  $[\partial^{n-1}\omega/\partial t^{n-1}]$  ( $\omega = \dot{\psi}$ ,  $n = 1, 2, \dots$ ). All the quantities ahead of the discontinuity surface (marked by index "+") are considered to be known. They are provided by the solution of the quasistatic problem on viscoplastic flow in the region  $r_1(t) \leq r \leq m(t)$ . In order to calculate the jump of  $\omega(r, t)$  and discontinuities of its derivatives of order  $n$  over the shock wave, one should differentiate the former equation in (31)  $n - 1$  times with respect to time, then write the result on other sides of the discontinuity surface and take a difference of the expressions obtained employing geometrical and kinematical conditions of compatibility [14,32-34]. Thus, we obtain a system of first-order inhomogeneous linear differential equations  $\frac{\delta \xi_n}{\delta t} + \frac{3G}{2r_1} \xi_n = \Phi_n(t, r_1, \xi_1, \xi_2, \dots, \xi_{n-1})$ ,  $\xi_n = \left[ \frac{\partial^n \psi}{\partial t^n} \right]_{\Sigma_1}$ .

In (37),  $\delta/\delta t$  is the  $\delta$ -derivative with respect to time (Thomas derivative [32]);  $\Phi_n$  is the recurrently calculated function that depends on discontinuities of lower-order derivatives, parameters of motion, and strain state ahead of the discontinuity surface

$$\begin{aligned}\Phi_1 &= \frac{G}{\eta r_1} \left( k - \frac{\alpha r_0^2 t}{r_1^2} \right), \quad \Phi_2 = \frac{\alpha r_0^2 G}{\eta r_1^3} - \frac{3G^2 A^{(1)}}{8r_1^{7/2}} - \frac{2kG^2}{\eta r_1^2}, \\ \Phi_3 &= -\frac{3B^{(1)}G^2}{8r_1^{7/2}} + \frac{15A^{(1)}G^3}{64r_1^{9/2}} + \frac{2kG^3}{\eta r_1^3}.\end{aligned}\quad (38)$$

Ordinary differential equations (37) are referred to as decay equations. The constants of integration  $A^{(1)}$ ,  $B^{(1)}$  and  $C^{(1)}$  arising in turn at each step are determined by virtue of boundary condition (34). Condition (33) is automatically satisfied due to the structure of the ray series. Finally, we obtain the following relations behind the unloading shock wave

$$\begin{aligned}\xi_1 &= \frac{A^{(1)}}{r_1^{3/2}} + \frac{2k}{3\eta} - \frac{2\alpha r_0^2}{\eta} \left( \frac{2}{Gr_1} - \frac{t}{r_1^2} \right), \quad \xi_2 = \frac{B^{(1)}}{r_1^{3/2}} + \frac{3A^{(1)}G}{8r_1^{5/2}} - \frac{4kG}{\eta r_1} - \frac{2\alpha r_0^2}{\eta r_1^2}, \\ \xi_3 &= \frac{C^{(1)}}{r_1^{3/2}} + \frac{3B^{(1)}G}{8r_1^{5/2}} - \frac{15A^{(1)}G^2}{128r_1^{7/2}} - \frac{4kG^2}{\eta r_1^2},\end{aligned}\quad (39)$$

$$\begin{aligned}
\psi^{(1)}(r, t) &= \psi^{(P)}|_{t=\tau_1} + (\dot{\psi}^{(P)} - \xi_1)|_{t=\tau_1}(t - \tau_1) + \frac{1}{2}(\ddot{\psi}^{(P)} - \xi_2)|_{t=\tau_1}(t - \tau_1)^2 + \\
&+ \frac{1}{6}(\dddot{\psi}^{(P)} - \xi_3)|_{t=\tau_1}(t - \tau_1)^3 + \dots, \\
\sigma_{r\varphi}^{(1)}(r, t) &= -\frac{\alpha r_0^2 \tau_1}{r^2} + \frac{\mu r \xi_1(\tau_1)}{G} + \\
&+ \left( -\frac{\alpha r_0^2}{r^2} - [\dot{\sigma}_{r\varphi}^{(1)}]|_{t=\tau_1} \right) (t - \tau_1) - \frac{1}{2} [\ddot{\sigma}_{r\varphi}^{(1)}]|_{t=\tau_1} (t - \tau_1)^2 + \dots, \\
[\dot{\sigma}_{r\varphi}^{(1)}] &= -\frac{3\mu}{2} \xi_1 - \frac{\mu r_1}{G} \xi_2 - \frac{\mu}{\eta} \left( k - \frac{\alpha r_0^2 t}{r_1^2} \right), \\
[\ddot{\sigma}_{r\varphi}^{(1)}] &= -\frac{\mu r_1}{G} \xi_3 - \frac{3\mu}{2} \xi_2 - \frac{3\mu G}{8r_1} \xi_1 + \frac{3\alpha \mu r_0^2 G t}{4\eta r_1^3} - \frac{7k\mu G}{4\eta r_1} + \frac{3\alpha \mu r_0^2}{2\eta r_1^2}, \\
A^{(1)} &= \frac{\sqrt{r_0} G (\sigma_0 - \sigma_s)}{\mu} + \frac{2r_0^{3/2}}{\eta} \left( \frac{2\alpha r_0}{G} - \alpha t_s - \frac{k}{3} \right), \\
B^{(1)} &= \frac{15G^2(\sigma_s - \sigma_0)}{8\mu\sqrt{r_0}} + \frac{\sqrt{r_0} G (13k + 7\sigma_0)}{4\eta} + \frac{\alpha\sqrt{r_0} G}{\mu} + \frac{\alpha r_0^{3/2}}{2\eta}, \\
C^{(1)} &= -\frac{15GB^{(1)}}{8r_0} - \frac{105G^2A^{(1)}}{128r_0^2} + \frac{8kG^2}{\eta\sqrt{r_0}} + \frac{6\alpha G\sqrt{r_0}}{\eta}.
\end{aligned}$$

The superscript "(1)" indicates that the value refers to the domain  $V^{(1)}: r_0 \leq r \leq r_1(t)$ . Calculations according to the above recurrent scheme can be continued if necessary. For instance, by calculating  $\Phi_4(t, r_1)$  and writing down the decay equation for  $\xi_4(t)$ , we can solve the initial-boundary value problem for this ordinary differential equation and so on. Here we restrict ourselves to three steps of the method.

Solution (39) is valid up to the instant  $t = t_m$ , at which the unloading wave encounters elastic-plastic boundary  $r = m(t)$

$$t_m = t_s + \frac{1}{2G^2} \left( \frac{\alpha r_0^2}{k} - 2r_0 G + \sqrt{\frac{4\alpha r_0^2 G}{k} (G t_s - r_0) + \frac{\alpha^2 r_0^4}{k^2}} \right). \quad (40)$$

Figures 1-3 show the distribution of the shear stress  $\sigma_{r\varphi}(r, t)$ , angle of twisting  $\psi(r, t)$ , and angular velocity  $\omega^{(1)}(r, t)$  (2a) at the instant  $t = t_m$  the wave  $\Sigma_1$  encounters elastic-plastic boundary. Figure 2(b) depicts the variation of unloading wave intensity with time. Here, we consider the case when the region with irreversible deformations is much narrower than the elastic one and makes up approximately 1/5 of the layer thickness. The calculation was carried out for the following values of the constants:  $\rho_0 = 8.96 \times 10^3 \text{ kg}\times\text{m}^3$ ,  $\mu = 41.5 \text{ GPa}$ ,  $k = 68.5 \text{ MPa}$ ,  $\eta = 4.83 \text{ GPa}\times\text{s}$ ,  $\sigma_0 = 71.5 \text{ MPa}$ ,  $\sigma_s = 58.2 \text{ MPa}$ ,  $R/r_0 = 1.1$ ,  $\alpha = 6343 \text{ Pa/s}$ .

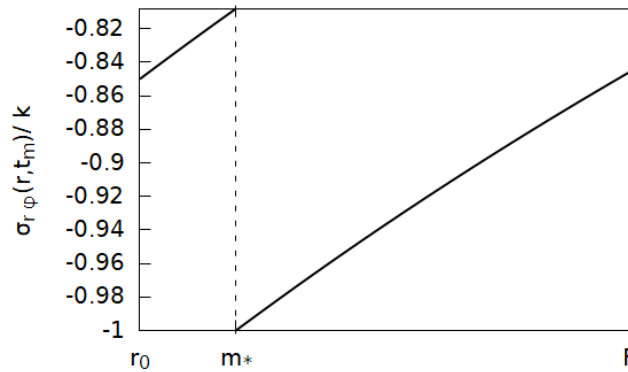


**Fig. 1.** Shear stress  $\sigma_{r\varphi}$  distribution at the moment  $\Sigma_1$  encounters elastic-plastic boundary  $r = m_*$

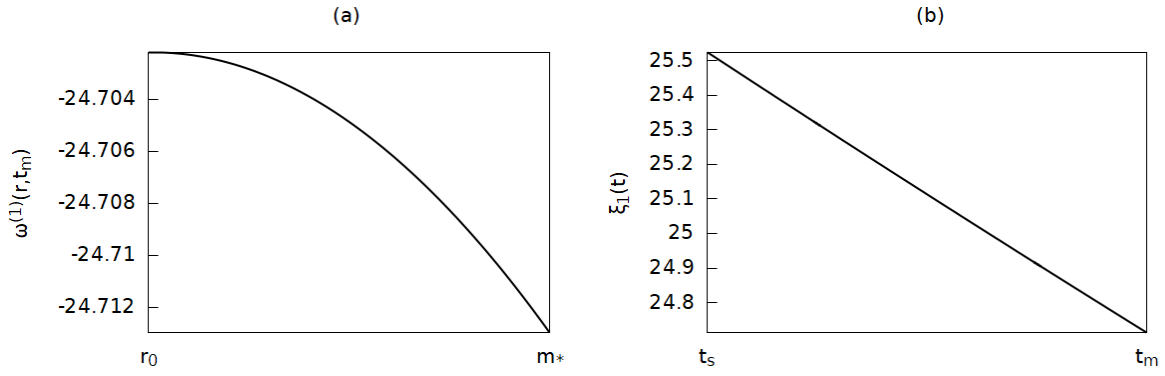


**Fig. 2.** Angular velocity  $\omega^{(1)}$  distribution at the moment  $\Sigma_1$  encounters elastic-plastic boundary  $r = m_*$  (a); variation of unloading wave intensity with time (b)

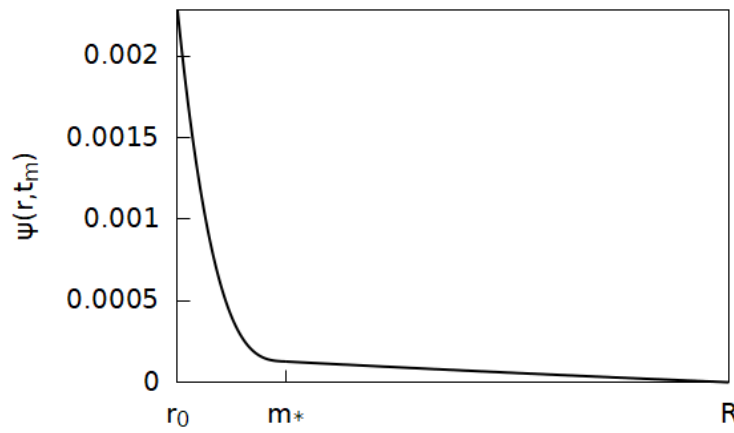


**Fig. 3.** Angle of twisting  $\psi$  distribution at the moment  $\Sigma_1$  encounters elastic-plastic boundary  $r = m_*$

### Reflection of the unloading wave from the elastic-plastic boundary

At the point of time  $t = t_m$ , plastic flow ceases, and the region with accumulated irreversible strains is bounded by the surfaces  $r = r_0$  and  $r = m_*$ , where  $m_* = m(t_m) = r_0 \sqrt{at_m/k}$ . At exactly the same time from the surface  $r = m_*$  two discontinuity surfaces, the surface  $\Sigma_2: r_2 = m_* - G(t - t_m)$ , and  $\Sigma_3: r_3 = m_* + G(t - t_m)$ , start propagating in opposite directions to the inner and to the outer cylinder respectively (Fig. 4).

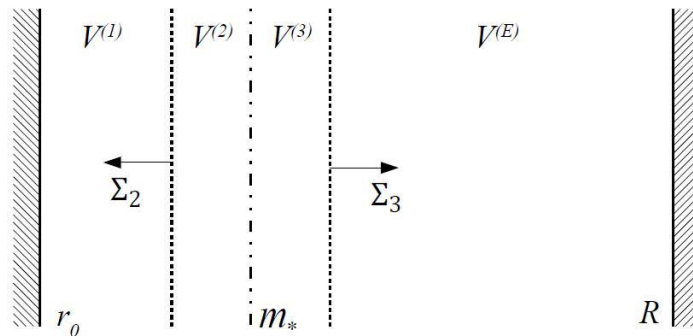


**Fig. 4.** Wave pattern after reflection of unloading wave from elastic-plastic boundary  $m_*$

In the region with accumulated irreversible strains motion of the medium is governed by equation (35), while in the region of reversible deformation the equation of motion reads

$$\psi_{,rr} + \frac{3}{r}\psi_{,r} - \frac{\ddot{\psi}}{G^2} = 0. \quad (41)$$

Boundary conditions for equations (35) and (41) are the condition of continuity of displacements across  $\Sigma_2: r = r_2(t)$  and  $\Sigma_3: r = r_3(t)$  as well as matching displacements and their derivatives at the elastic-plastic boundary  $r = m_*$ . The latter ensures the smoothness of a solution in the domain between  $\Sigma_2$  and  $\Sigma_3$  at each instant of time beyond  $t_m$

$$[\psi]_{\Sigma_2} = [\psi]_{\Sigma_3} = 0, \quad \psi^{(2)}|_{m_*} = \psi^{(3)}|_{m_*}, \quad \psi_{,r}^{(2)}|_{m_*} = \psi_{,r}^{(3)}|_{m_*}. \quad (42)$$

As above, a superscript in parentheses indicates the value is calculated in the region behind the wave with a corresponding number. The solution for the desired function  $\omega(r, t)$  behind the waves  $\Sigma_2$  and  $\Sigma_3$  is represented by the ray series similar to (36)

$$\omega^{(2)} = (\omega^{(1)} - \eta_1)|_{\tau_2} + (\dot{\omega}^{(1)} - \eta_2)|_{\tau_2}(t - \tau_2) + \frac{1}{2}(\ddot{\omega}^{(1)} - \eta_3)|_{\tau_2}(t - \tau_2)^2 + \dots, \quad (43)$$

$$\omega^{(3)} = (\omega^{(E)} - \zeta_1)|_{\tau_3} - \zeta_2|_{\tau_3}(t - \tau_3) - \frac{1}{2}\zeta_3|_{\tau_3}(t - \tau_3)^2 + \dots, \quad (44)$$

$$\eta_i = \left[ \frac{\partial^i \psi}{\partial t^i} \right]_{\Sigma_2}, \quad \tau_2 = t_m + (m_* - r)/G, \quad \zeta_i = \left[ \frac{\partial^i \psi}{\partial t^i} \right]_{\Sigma_3}, \quad \tau_3 = t_m + (r - m_*)/G.$$

Differential equations for the ray series coefficients can be obtained in accordance with the procedure described in Section 4. After integration, we substitute the result into (43), (44), compare it with the boundary conditions (42), and obtain the desired solution

$$\psi^{(2)}(r, t) = \psi^{(1)}|_{\tau_2} + \omega^{(1)}|_{\tau_2}(t - \tau_2) + \frac{1}{2}\dot{\omega}^{(1)}|_{\tau_2}(t - \tau_2)^2 + \quad (45)$$

$$+ \frac{1}{6}\left(\ddot{\omega}^{(1)}|_{\tau_2} - \eta_3(\tau_2)\right)(t - \tau_2)^3 + \dots,$$

$$\sigma_{r\varphi}^{(2)}(r, t) = \sigma_{r\varphi}^{(1)}|_{\tau_2} + \dot{\sigma}_{r\varphi}^{(1)}|_{\tau_2}(t - \tau_2) + \frac{1}{2}\left(\ddot{\sigma}_{r\varphi}^{(1)}|_{\tau_2} - \frac{\mu r}{G}\eta_3(\tau_2)\right)(t - \tau_2)^2 + \dots,$$

$$\psi^{(3)}(r, t) = \psi^{(E)}|_{\tau_3} + \left(\omega^{(E)}|_{\tau_3} - \zeta_1(\tau_3)\right)(t - \tau_3) - \frac{1}{2}\zeta_2(\tau_3)(t - \tau_3)^2 - \quad (46)$$

$$- \frac{1}{6}\zeta_3(\tau_3)(t - \tau_3)^3 + \dots,$$

$$\sigma_{r\varphi}^{(3)}(r, t) = -\frac{\alpha\tau_3 r_0^2}{r^2} + \frac{\mu r}{G}\zeta_1(\tau_3) + \left(-\frac{\alpha r_0^2}{r^2} + \frac{3\mu}{2}\zeta_1(\tau_3) + \frac{\mu r}{G}\zeta_2(\tau_3)\right)(t - \tau_3) +$$

$$+ \frac{\mu r}{2G}\left(\zeta_3(\tau_3) + \frac{3G}{2r}\zeta_2(\tau_3) + \frac{3G^2}{8r^2}\zeta_1(\tau_3)\right)(t - \tau_3)^2 + \dots,$$

$$\eta_1 = \eta_2 = 0, \eta_3 = \frac{C^{(2)}}{r_2^{3/2}}, \zeta_1 = \frac{A^{(3)}}{r_3^{3/2}}, \zeta_2 = \frac{B^{(3)}}{r_3^{3/2}} + \frac{3GA^{(3)}}{8r_3^{5/2}},$$

$$\zeta_3 = \frac{C^{(3)}}{r_3^{3/2}} + \frac{3GB^{(3)}}{8r_3^{5/2}} - \frac{15A^{(3)}G^2}{128r_3^{7/2}},$$

$$A^{(2)} = B^{(2)} = 0, \quad C^{(2)} = \frac{\alpha^2 r_0^4}{2\eta k m_*^{5/2}} + \frac{kG^2}{2\eta\sqrt{m_*}} - \frac{3G\alpha r_0^2}{4\eta m_*^{3/2}},$$

$$A^{(3)} = A^{(1)} + \frac{4\sqrt{m_*}}{\eta}\left(\frac{2}{3}km_* - \frac{\alpha r_0^2}{G}\right), \quad B^{(3)} = B^{(1)} - \frac{5kG\sqrt{m_*}}{\eta} - \frac{\alpha r_0^2}{2\eta\sqrt{m_*}},$$

$$C^{(3)} = C^{(1)} - \frac{\alpha^2 r_0^4}{2\eta k m_*^{5/2}} - \frac{21kG^2}{16\eta\sqrt{m_*}} - \frac{33\alpha r_0^2 G}{32\eta\sqrt{m_*}}.$$

As it follows from (45)-(46)  $\Sigma_3$  is a shock wave, while  $\Sigma_2$  is a weak wave of second order across which stresses and velocities remain continuous, but an acceleration derivative jump occurs. In view of the fact the region with irreversible strains occupies a small part of the layer,  $\Sigma_2$  will reflect from the cylinder wall  $r = r_0$  before  $\Sigma_3$  reaches  $r = R$ . The reflection causes propagation of the weak wave of second order  $\Sigma_4: r_4 = r_0 + G(t - t_r)$ ,  $t_r = t_m + (m_* - r_0)/G$ . If we restrict ourselves by cubic terms in the ray solution no new discontinuities occur when  $\Sigma_4$  travels through the elastic-plastic boundary  $r = m_*$ , but the calculation of preliminary deformations is implemented differently on the left/right of the elastic-plastic boundary. Preliminary deformations are given by the solution behind  $\Sigma_2$  in the region  $r_0 \leq r \leq m_*$  and by the solution behind  $\Sigma_3$  in the region  $m_* \leq r \leq r_3(t)$ . Let us write down the solution behind the wave  $\Sigma_4$

$$\begin{aligned} \psi^{(4)}(r, t) &= \psi^{(i)}|_{\tau_4} + \omega^{(i)}|_{\tau_4}(t - \tau_4) + \frac{1}{2}\dot{\omega}^{(i)}|_{\tau_4}(t - \tau_4)^2 + \\ &+ \frac{1}{6}(\ddot{\omega}^{(i)}|_{\tau_4} - \theta_3(\tau_4))(t - \tau_4)^3 + \dots, \\ \sigma_{r\varphi}^{(4)}(r, t) &= \sigma_{r\varphi}^{(i)}|_{\tau_4} + \dot{\sigma}_{r\varphi}^{(i)}|_{\tau_4}(t - \tau_4) + \frac{1}{2}(\ddot{\sigma}_{r\varphi}^{(i)}|_{\tau_4} + \frac{\mu r}{G}\theta_3(\tau_4))(t - \tau_4)^2 + \dots, \\ \theta_3 &= [\ddot{\omega}]|_{\Sigma_4} = \frac{C^{(2)}}{r_4^{3/2}}, \quad \tau_4 = t_r + (r - r_0)/G, \end{aligned} \quad (47)$$

in which  $i = 2$  in the region  $r_0 \leq r \leq m_*$  and  $i = 3$  in the region  $m_* \leq r \leq r_3(t)$ . The next change in the wave pattern occurs when the wave  $\Sigma_3$  reflects from the outer boundary  $r = R$  in the form of shock wave  $\Sigma_5: r_5 = R - G(t - t_R)$ ,  $t_R = t_m + (R - m_*)/G$ . There are no difficulties to calculate the stress-strain pattern behind  $\Sigma_5$  by means of the algorithm described and boundary condition (1) at the surface  $r = R$ , preliminary deformations ahead  $\Sigma_5$  are prescribed by (46). Further, upon weak wave  $\Sigma_4$  and shock wave  $\Sigma_5$  interaction at the instant  $\tilde{t} = t_m + (R - r_0)/G$  wave pattern remains unchanged, but from this moment one has to take into account that stress-strain state ahead  $\Sigma_4$  is determined by the solution behind  $\Sigma_5$  while preliminary deformations for the wave  $\Sigma_5$  are determined according to (47).

At this point the analytical study is considered complete, and the calculation of the further deforming, if necessary, it is advisable to carry out numerically, using the analytical expressions obtained to approximate the solution at the nodes of the near-front domain.

### Concluding remarks

The research conducted broadens our insight into the processes occurring in the material under complex deforming within a wide strain rate range. The problem considered features a two-stage deforming mechanism. In the first stage which involved slow loading of a cylindrical elastic/viscoplastic layer the exact solution of the corresponding boundary-value problem in the scope of large deformation theory has been obtained by applying the quasistatic approach. In the second stage calculation of the dynamic unloading triggered by instantaneous stress drop below the yield limit at the material and the rigid wall interface has been implemented. This event induced the cylindrical unloading shock wave, across which the plastic strain rate vanishes instantly and the viscoplastic flow ceases. Upon its reflection from the elastic-plastic boundary, a weak wave, propagating over the region with accumulated time invariable irreversible deformations, and a shock wave, moving over the elastic region, have been formed. Further unsteadiness in the layer is associated with the reflection of these waves from the instrument walls and the elastic-plastic boundary.

The solution to the dynamic problem has been constructed by means of truncated ray expansions about the time of the disturbance arrival at a given point of a domain. This method has allowed us to calculate the stress-strain state behind the discontinuity surfaces arising in the least cumbersome manner avoiding a need to solve the partial differential equation (which

cannot be integrated exactly in the case of axial symmetry), but reducing the problem of integrating a system of ordinary differential equations of the first order that determine the change of velocity jump and the jumps of its time-derivatives up to the second order over the wave fronts. Higher-order jumps can be determined according to the same algorithm with no major difficulties except for increasing computational load.

However, some limitations are worth mentioning. First of all, truncated ray series demonstrate a close approximation to the solution only in the vicinity of the wave front, which is well applicable for narrow layers, as is one considered afore, and for short time range elapsed after the moment of wave motion commence. To construct a uniformly valid solution for a domain of a more considerable extent, methods of regularization of ray expansions can be applied, both analytical [35] and numerically analytical [26-28]. In the latter case, the analytical solution is incorporated into a numerical finite-difference scheme.

Second of all, the unloading wave velocity turned out to be constant owing to allowing the reversible strains to be small. In the case of finite strains situation is more complicated; the shock wave velocity and in turn the location of the wave front will be affected by strains ahead of the wave and discontinuities amplitudes, and the evolution behavior of the discontinuity of each order is coupled with that of higher order. In addition, the wave pattern becomes more intricate because two shear shock waves will appear in a prestrained medium: plane and circularly polarized ones.

Nevertheless, despite the noted limitations, the results of the present work lay the groundwork for studying more complex unsteady boundary-value problems involving large deformations.

## References

1. Rozdestvenskii BL, Janenko NN. *Systems of quasilinear equations and their applications to gas dynamics*. Providence, Rhode Island: American Mathematical Society; 1983.
2. Gel'fand IM. Some problems of the theory of quasilinear equations. *Amer. Math. Soc. Transl. Ser.* 1963;29(2): 295-381.
3. Godunov SK, Zabrodin AV, Ivanov MY, Kraiko AN, Prokopov GP. *Numerical solution of multidimensional problems of gas dynamics*. Moscow: Nauka; 1976. (In Russian)
4. Hopf E. On the right weak solution of the Cauchy problem for a quasilinear equation of first order. *J. Math. Mech.* 1969;19(6): 483-487.
5. Engelbrecht J. *Nonlinear wave processes of deformation in solids*. London: Pitman; 1983.
6. Truesdell C. General and exact theory of waves in finite elastic strain. *Arch. Rat. Mech. Anal.* 1961;8(4): 263-296.
7. Bland DR. *Nonlinear dynamic elasticity*. Waltham, Massachusetts: Blaisdell; 1969.
8. Burenin AA, Chernyshov AD. Shock waves in an isotropic elastic space. *J. Appl. Math. Mech.* 1978;42(4): 711-717.
9. Kulikovskii A, Sveshnikova E. *Nonlinear waves in elastic media*. Boca Raton, Florida: CRC Press; 1995.
10. Chy B-T. Transverse shock waves in incompressible elastic solids. *J. Mech. Phys. Solids.* 1967;15(1): 1-14.
11. Wesolowski Z, Bürger W. Shock waves in incompressible elastic solids. *Rheol. Acta.* 1977;16(2): 155-160.
12. Fu YB, Scott NH. The evolutionary behavior of plane transverse weak nonlinear shock waves in unstrained incompressible isotropic elastic non-conductors. *Wave Motion.* 1989;11(4): 351-365.
13. Mandel J. Ondes plastique dans un milieu indéfini à trois dimensions. *J. Mec.* 1962;1(1): 3-30. (In French)
14. Bykovtsev GI, Ivlev DD. *Theory of Plasticity*. Vladivostok: Dal'nauka; 1998. (In Russian)

15. Bykovtsev GI, Kretova LD. Shock wave propagation in elastic-plastic media. *J. Appl. Math. Mech.* 1972;36(1): 94-103.
16. Burenin AA, Bykovtsev GI, Rychkov VA. Velocity discontinuity surfaces in the dynamics of irreversibly compressible media. In: *Problems of Continuum Mechanics (to the 60th anniversary of academician V.P. Myasnikov)*. Vladivostok: Inst. of Automation and Control Processes FEB RAS; 1996. p.116-127. (In Russian)
17. Kameniarzh IA. Simple waves and collapse of a discontinuity in an elastic-plastic medium with mises condition. *J. Appl. Math. Mech.* 1972; 36(2): 296-305.
18. Clifton RJ. Dynamic plasticity. *Trans ASME: J. Appl. Mech.* 1983;50(4b): 941-952.
19. Druyanov BA, Svyatova EA. The problem of the structure of a discontinuity in a strain-hardening plastic medium. *J. Appl. Math. Mech.* 1986;51(6): 808-810.
20. Balashov DB. Decay of discontinuity in linearly strain-hardening elastic-plastic medium. *Mech. Solids.* 1993; 28(2): 113-120.
21. Sadovskii VM. *Discontinuous solutions in the dynamics of elastic-plastic media*. Moscow: Fizmatlit; 1997. (In Russian)
22. Ivanov GV, Volchkov YM, Bogul'skii IO, Anisimov SA, Kurguzov VD. *Numerical solution of dynamic problems of elastic-plastic deformation of solid bodies*. Novosibirsk: Sib. Univ.; 2002. (In Russian)
23. Wilkins ML. Calculations of elastic-plastic flow. In: Adler B, Fernbach S, Rotenberg M. (eds.). *Methods of Computational Physics, Vol. 3: Fundamental Methods in Hydrodynamics*. New York: Academic Press; 1964; p.211-264.
24. Kukudzhyanov VN. *Numerical continuum mechanics*. Berlin: Walter de Gruyter; 2013.
25. Bathe K-J, Shyder MD, Cimento AP, Rolph WD. 1980, On some current procedures and difficulties in finite element analysis of elasto-plastic response. *Computers and Structures*. 1980;12: 607-624.
26. Burenin AA, Zinov'ev PV. On the problems of identifying discontinuity surfaces in numerical methods of dynamics of deformable media. In: *Problems of Mechanics (dedicated to the 90th anniversary of A.Yu. Ishlinskii)*. Moscow: Fizmatlit;2003. p.146-155. (In Russian)
27. Gerasimenko EA, Zavertan AV. Ray expansions of solutions around fronts as a shock-fitting tool for shock loading simulation. *Comput. Math. and Math. Phys.* 2009;49(4): 698-709.
28. Burenin AA, Sevastyanov GM, Shtuka VI. On the localization of discontinuities in calculations of incompressible elastic media dynamics. *Computational Continuum Mechanics*. 2016; 9(4): 400-411. (In Russian)
29. Whizam GB. *Linear and nonlinear waves*. New York: John Wiley & Sons; 1974.
30. Achenbach ID, Reddy DP. Note of wave propagation in linearly viscoelastic media. *Z. angew. Math. und. Phys. (ZAMP)*. 1967;18(1): 141-144.
31. Babicheva LA, Bykovtsev GI, Verveiko ND. Ray method of solving dynamic problems in elastic-viscoplastic media. *J. Appl. Math. Mech.* 1973;37(1): 132-141.
32. Thomas T. *Plastic flow and fracture in solids*. New York: Academic Press; 1961.
33. Grinfel'd MA. *Methods of continuum mechanics in the theory of phase transitions*. Moscow: Nauka; 1990. (In Russian)
34. Grinfel'd MA. Ray method of calculating the wave front intensity in nonlinearly elastic material. *J. Appl. Math. Mech.* 1978;42(5): 958-977.
35. Rossikhin YA, Shitikova MV. Ray method for solving dynamic problems connected with propagation of wave surfaces of strong and weak discontinuities. *Appl. Mech. Rev.* 1995;48(1): 1-39.
36. Burenin AA. Possibility of constructing approximate solutions to nonstationary problems in the dynamics of elastic media under shock impacts. *Dal'nevostochn. Mat. Sb.* 1999;8: 49-72. (In Russian)

37. Burenin AA, Rossikhin YA, Shitikova MV. A ray method for solving boundary value problems connected with the propagation of finite amplitude shock waves. In: *Proceedings of the Int. Symp. on Nonlinear Theory and its Applications*. 1993. p.1085-1088.
38. Rossikhin YA, Burenin AA, Potianikhin DA. Shock Waves Via Ray Expansions. In: Altenbach H, Öchsner A. (eds.) *Encyclopedia of Continuum Mechanics*. Berlin: Springer; 2019.
39. Kovtanyuk LV. On the forcing of an elastoviscoplastic material through an inflexible circular cylindrical die. *Doklady Physics*. 2005;50: 112-114.
40. Kovtanyuk LK, Shitikov AV. Theory of large elastoplastic deformations of materials taking account of temperature and rheological effects. *Vestnik DVO Ross. Akad. Nauk*. 2006;4: 87-93. (In Russian)
41. Burenin AA, Kovtanyuk LV, Lushpei AV. The transient retardation of rectilinear viscoplastic flow when the loading stresses are abruptly removed. *J. Appl. Math. Mech.* 2009;73(4): 478-482.
42. Burenin AA, Kovtanyuk LV, Kulaeva DV. Interaction of a one-dimensional unloading wave with an elastoplastic boundary in an elastoviscoplastic medium. *J. Appl. Mech. Tech. Phys.* 2012;53(1): 90-97.
43. Kovtanyuk LV, Rusanov MM. On collision of an unloading wave with advancing elastoplastic boundary in a flat heavy layer. *J. Appl. Ind. Math.* 2015;9: 519-526.
44. Burenin AA, Kovtanyuk LV. *Large irreversible strains and elastic aftereffect*. Vladivostok: Dal'nauka; 2013. (In Russian)
45. Begun AS, Burenin AA, Kovtanyuk LV, Lemza AO. On the mechanisms of production of large irreversible strains in materials with elastic, viscous and plastic properties. *Arch. Appl. Mech.* 2020;90: 829-845.
46. Shitikov AV, Bykovtsev GI. Finite deformations in an elastoplastic media. *Sov. Phys. Dokl.* 1990;35(3): 297-299.
47. Burenin AA, Bykovtsev GI, Kovtanyuk LV. A simple model of finite strain in an elastoplastic medium. *Doklady Physics*. 1996;41(3): 127-129.
48. Bezglasnyi PA, Verveiko ND. On the propagation of shock waves in an elastoviscoplastic medium. *Izv. Akad. Nauk SSSR, Mech. Tverd. Tela*. 1971;5: 71-76.
49. Rossikhin YA, Shitikova MV. Discontinuity Surfaces in Elasto-Visco-Plastic Media. In: Altenbach H, Öchsner A. (eds.) *Encyclopedia of Continuum Mechanics*. Berlin: Springer; 2019.
50. Verveiko ND, Shapiro AI, Krupenko SE. *The origin and motion of the tips of cracks behind the fronts of elastoviscoplastic waves*. Voronezh: Quarta Publishers; 2017. (In Russian)
51. Haase R. *Thermodynamics of irreversible processes*. Reading, Massachusetts: Addison-Welsey; 1968.
52. Lee EH. Elastic-plastic deformations at finite strains. *J. Appl. Mech.* 1969;36(1): 1-6.
53. Levitas VI. *Large deformation of materials with complex rheological properties at normal and high pressure*. New York: Nova Science Publishers; 1996.
54. Lurie AI. *Nonlinear theory of elasticity*. Amsterdam, North Holland: Elsevier; 1990.

## THE AUTHORS

**Burenin A.A.** 

e-mail: burenin@iacp.dvo.ru

**Gerasimenko E.A.** 

e-mail: gerasimenko@iacp.dvo.ru

**Kovtanyuk L.V.** 

e-mail: lk@iacp.dvo.ru



## Gas-abrasive wear of shut-off valves and process piping of compressor and gas distribution stations

O.Yu. Elagina , A.G. Buklakov , Yu.S. Dubinov  , D.V. Dedok

Gubkin Russian State University of Oil and Gas (National Research University), Moscow, Russian Federation

 dubinovys@gmail.com

**Abstract.** A high content of mechanical impurities in the gas flow causes intense gas-abrasive wear of the pipe surface, especially at the pipe bends and shut-off valves. To assess the effect of gas flow rate on the failure rate of piping elements, an installation, and a test procedure were designed. The test result was evaluated by the value of the intensity of linear wear of the material, related to the amount of abrasive that was projected on the sample for the entire time of testing. Based on the results obtained, materials were identified that have minimal wear when the gas flow is shut off and when the abrasive carrying gas flow rate changes from 24 m/s to 48 m/s. Steel 20 showed better wear resistance compared to steel 09G2S, but an increase in the flow rate leads to an increase in wear intensity.

**Keywords:** gas-abrasive wear, gas distribution station, shut-off valves, sealing materials of shutoff valves, gas medium flow rate

**Citation:** Elagina OY, Buklakov AG, Dubinov YS, Dedok DV. Gas-abrasive wear of shut-off valves and process piping of compressor and gas distribution stations. *Materials Physics and Mechanics*. 2023;51(1): 84-92. DOI: 10.18149/MPM.5112023\_8.

### Introduction

According to the requirements of state regulatory documents (GOST 54808-2011 "Pipeline valves. Leakage rates of valves" [1]) and regulatory documents of organizations (STO Gazprom 2-4.1-212-2008 "General technical requirements for pipeline valves supplied to the facilities of OAO Gazprom" [2]) for shutoff and control valves, the concentration of mechanical impurities in the natural gas flow transported in main and branch pipelines should not exceed 0.010 g/m<sup>3</sup>. An analysis of the contaminants deposited on the filters and in the cavity of the shutoff valves shows that the content of solid particles in the main gas can significantly exceed the specified requirements. Such an increase in the proportion of mechanical impurities in the gas flow is observed during the commissioning of sections of main pipelines after their repair, as well as during the period of intensive gas extraction from underground storage facilities. The composition of impurities includes abrasive particles, corrosion products of pipe metal, welding slag, and other contaminants [3]. The size of individual crystalline particles is in a wide range from 10 to 500 microns, which is shown in Fig. 1, and the chemical composition determined by X-ray fluorescence analysis is presented in Table 1.



**Fig. 1.** Photograph of the appearance of various types of contaminants in the main gas

**Table 1.** Chemical composition of mechanical impurities

Element	Element content, %		
	1	2	3
Fe	53.89	68.87	56.71
S	6.40	6.97	1.94
Ba	4.05	7.11	4.30
Si	24.03	3.53	14.57
Na	1.45	2.00	1.85
Ca	2.52	2.09	10.38
Mn	1.14	1.03	1.53
Al	1.55	1.14	1.62
Cl	0.466	0.536	0.291
K	0.632	0.504	0.661
Mg	0.434	0.385	0.517
Ti	0.251	0.162	0.263

Getting into the flow of the transported gas, mechanical impurities cause gas-abrasive wear of the pipe walls on the pipeline bends and seals of shutoff and control valves when the flow is blocked. The most significant gas-abrasive wear is manifested during the operation of the piping of compressor (CS) and gas distribution (GDS) stations. The process pipelines of these gas pipeline infrastructure facilities have a large number of bends, and ball valves with polymer seals are mainly used to shut off the gas flow [4].

The purpose of this work was to study the effect of gas-abrasive wear on the development of failures of piping elements depending on the speed of the gas flow.

### Testing method

The essence of the laboratory research on gas-abrasive wear was to test samples of steel and polymer materials subject to a stream of abrasive particles moving at a fixed speed in a gas medium at a given angle to the surface and to determine its wear indicators.

For testing, round quartz sand of 0.1-0.3 mm fineness was selected as an abrasive, the composition and properties are presented in Table 2.

Steel 20 and 09G2S were chosen to study the gas-abrasive resistance of the metal of CS and GDS process piping. Of the most widely used sealing materials for ball valves, we tested such materials as F4 fluoroplastic, F4K20 fluoroplastic, caprolon, paronite.

**Table 2.** Characteristics of quartz sand

Composition	
Clay component content	less than 1 %
Iron oxide content ( $\text{Fe}_2\text{O}_3$ )	less than 1 %
Silicon oxide content ( $\text{SiO}_2$ )	95-99.8 %
Properties of quartz sand	
Class of use by radioactivity	1
Mohs hardness	7
Bulk density (specific gravity)	1480 kg/m <sup>3</sup>

When choosing a test scheme, standardized test methods were considered in accordance with GOST 23.201-78 and GOST 23.208-79 [5,6]. The main requirement for the test setup was to ensure uniform distribution of the abrasive over the cross-section of the gas flow and maintain a given angle of attack over the entire cross-section of the sample. The use of a centrifugal accelerator according to [5] does not allow the formation of a uniform distribution of particles along the flow due to the deflecting action of the centrifugal force. Installation according to [6] does not provide the possibility of abrasive supply at different angles. Therefore, for the testing, we used a setup that simulates the movement of a gas-abrasive flow in a pipeline. The scheme and appearance of the testing installation for gas-abrasive wear are shown in Fig. 2.

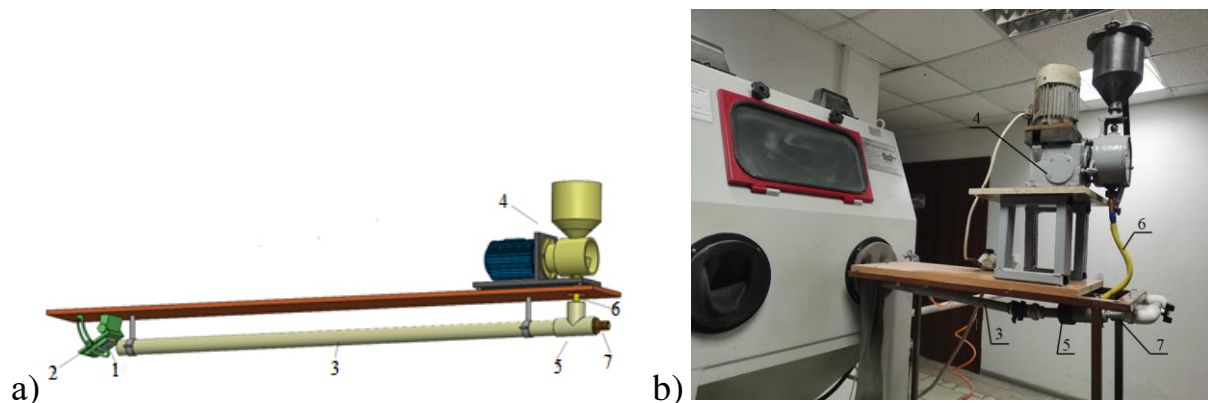


**Fig. 2.** Gas-abrasive wear test installation: a) design: 1 – sample, 2 – sample swivel holder, 3 – accelerating tube, 4 – feeder, 5 – mixing chamber, 6 – supply tube, 7 – air supply fitting, b) photograph of the external view

The principle of operation of the installation is as follows: the abrasive from feeder 4 is fed through supply tube 6 into mixing chamber 5, where it is picked up by air, which is supplied to the chamber through fitting 7. The resulting gaseous mixture enters sample 1 through pipe 3. The angle of inclination of sample 1 relative to the abrasive flow is fixed by sample holder 2 and changes from 15° to 90°.

The samples are flat rectangular plates of 110×30×4 mm in size.

The swivel holder allows deflecting and fixing the sample relative to the gas-abrasive flow. The front part of the setup with the holder, the sample, and the outlet end of the accelerating tube were placed in a sandblasting chamber (Fig. 2(b)), which was used to limit the projection and collect the waste abrasive.

The main adjustable test parameters are the gas-abrasive flow rate, the abrasive consumption per unit time, the time of a single test, and the angle of attack [7,8]. To assess the effect of the gas-abrasive flow rate on the wear process, studies were carried out at 24 m/s and 48 m/s [9,10]. The flow rate was controlled by the air pressure in the supply network and

measured using a VMA-1 digital anemometer before the abrasive was supplied. The angles of attack of the gas-abrasive flow with respect to the surface of the sample were chosen based on the data described in [11-16] and amounted to 15°, 45°, and 90°. The amount of abrasive ( $q$ ) for a single test was taken equal to 2 kg 700 g. The time of a single test cycle ( $t$ ) was taken to be 1.0 hour for a rate of 24 m/s and 30 minutes for a rate of 48 m/s. Since the air flow rate changed during the experiment, in order to obtain comparable wear values, it was decided to use the same concentration of abrasive particles per unit volume of air equal to 90 g/m<sup>3</sup>, which ensured contact of the samples with a fixed amount of abrasive per test cycle. Accordingly, the abrasive consumption was 0.75 g/s for a flow rate of 24 m/s and 1.45 g/s for a flow rate of 48 m/s.

The location of the samples during testing at different angles to the gas-abrasive flow leads to a change in the contact area. Table 3 presents the values of the actual area of the samples in contact with the gas-abrasive flow when they were located at a fixed angle of attack with respect to the flow axis.

**Table 3.** Sample area for different angles of attack

Angle of attack	90°	45°	15°
Sample area, mm <sup>2</sup>	314	440	1209

The value of wear of the samples before and after testing was determined by the gravimetric method on an electronic balance HTR-120 CE with an accuracy of 0.0001 g. The test result was evaluated:

- with respect to the specific mass loss:

$$M_n = \frac{m_1 - m_2}{F}, \quad (1)$$

- with respect to the intensity of linear wear of the material related to the amount of abrasive that got on the sample for the entire time of testing according to the following formula:

$$I_n = \frac{m_1 - m_2}{\rho \cdot F \cdot q}, \quad (2)$$

where  $\rho$  – material density, g/mm<sup>3</sup>, (in the calculation, the following density values of materials were taken: 1.6-2.0 g/cm<sup>3</sup> for paronite (PON grade according to GOST 481-80), 2.18 g/cm<sup>3</sup> for fluoroplastic (F4 grade according to GOST 10007-80), 2.17 g/cm<sup>3</sup> for carbon-filled fluoroplastic (F4K20), 1.15–1.16 g/cm<sup>3</sup> for caprolon (PA-6), 7.8 g/cm<sup>3</sup> for steel);  $F$  – sample surface area, mm<sup>2</sup>;  $q$  – amount of abrasive during testing, kg.

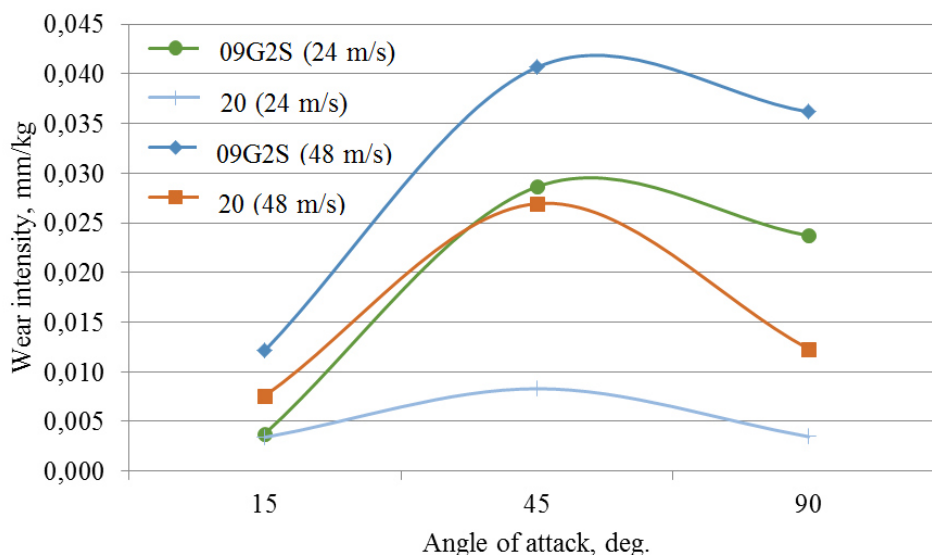
### Discussion of test results

The results of testing steels for gas-abrasive wear at different flow rates are presented in Table 4 in terms of specific mass loss, and in Fig. 4 in terms of linear wear intensity.

**Table 4.** Specific mass loss of samples to abrasive mass at different gas-abrasive flow rates (g/kg)

Angle of attack, deg	Researched Materials					
	paronite	fluoroplast	carbon-filled fluoroplast	caprolon	Steel 09G2S	Steel 20
Gas-abrasive flow rate 24 m/s						
15	0.003	0.002	0.001	-0.004	0.008	0.007
45	0.045	0.008	0.017	-0.008	0.062	0.018

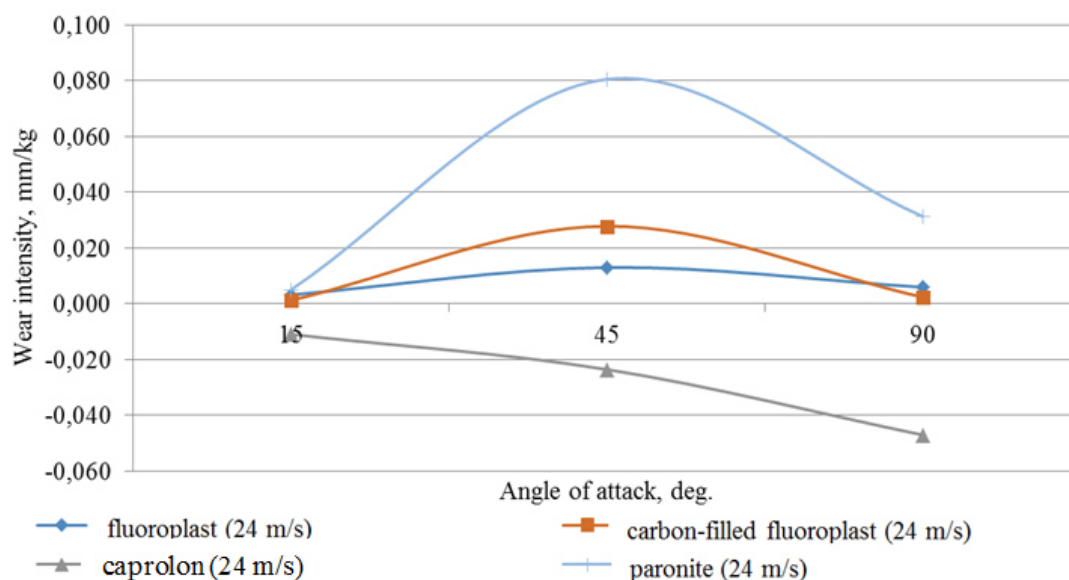
90	0.018	0.004	0.001	-0.015	0.052	0.008
Gas-abrasive flow rate 48 m/s						
15	0.088	0.006	0.006	-0.004	0.027	0.017
45	0.203	0.123	0.120	0.002	0.089	0.059
90	0.391	0.014	0.128	-0.016	0.079	0.027



**Fig. 4.** Dependences of the change in the wear intensity of pipe steels at a gas-abrasive flow rate of 24 m/s and 48 m/s

As can be seen from the data obtained for the steel pipes, the highest wear intensity is observed at an attack angle of 45°. An increase in flow rate from 24 m/s to 48 m/s has a more significant effect on steel 20: its increase in wear intensity at angles of attack of 45° and 90° was more than 3 times compared to a 1.5 times increase in 09G2S. However, at the same time, Steel 20 showed better wear resistance compared to Steel 09G2S both at a gas flow rate of 24 m/s and 48 m/s. Which agrees well with the data from [17, 18].

Graphs of changes in the wear intensity of sealing materials are shown in Fig. 5.



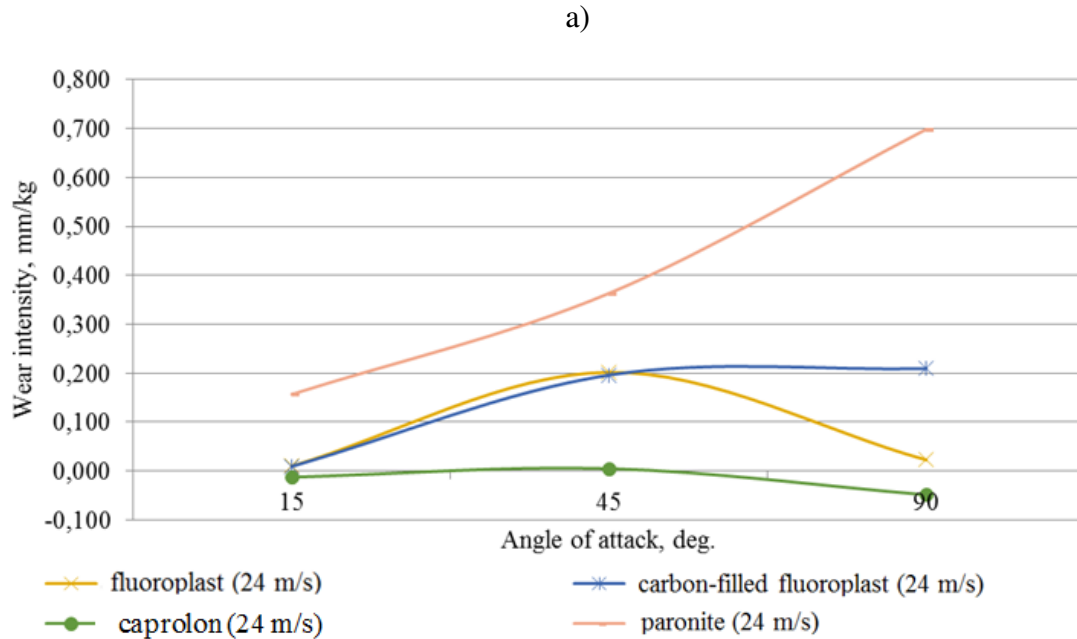


**Fig. 5.** Dependences of changes in the wear intensity of sealing materials at a gas-abrasive flow rate of a) 24 m/s, b) 48 m/s

Analysis of the obtained data shows that the maximum wear intensity is observed in paronite. Carbon-filled fluoroplastic has lower wear resistance compared to F4K fluoroplastic. Caprolon shows a tendency to abrasive charging and shows weight gain at all angles of attack.

Increasing the gas flow rate to 48 m/s leads to an increase in the wear intensity for all studied sealing materials. Paronite demonstrated the greatest increase in wear intensity with an increase in the gas-abrasive flow rate by 22-30 times. At the same time, at a gas flow rate of 24 m/s, the maximum wear is achieved at an angle of attack of 45°; with an increase in the gas flow rate to 48 m/s, the maximum wear shifts to 90°. Carbon-filled fluoroplastic demonstrated a significant increase and a similar trend in the change of wear intensity. Only for caprolon, the values of mass had practically no change.

**Method for calculating the service life of piping bends and ball valve seals in contact with a gas-abrasive flow.** The wear of piping bends in contact with a high-velocity gas flow-carrying abrasive should be evaluated to prevent wall thinning above the regulated level. The value of the ultimate wear of the pipeline wall is determined by the formula:

$$\Delta\delta^i = \delta^i - \delta_{all}^i, \quad (3)$$

where  $\Delta\delta^i$  – maximum wear of the wall of the  $i^{\text{th}}$  piping bend, mm;  $\delta_{all}^i$  – minimum allowable thickness of the wall of the  $i^{\text{th}}$  piping bend, mm;  $\delta^i$  – nominal thickness of the wall of the  $i^{\text{th}}$  piping bend, mm.

Using the experimental values of the pipe metal wear intensity at the most aggressive angle of attack of the gas-abrasive flow, the maximum allowable operation time determined by the number of months of the operation can be calculated using the following relationship:

$$T_B^i = \frac{\Delta\delta^i}{t \cdot q \cdot I_{g/a} \cdot Q_A} = \frac{\Delta\delta^i}{720 \cdot q \cdot I_{g/a} \cdot Q_A}, \quad (4)$$

where  $T_B^i$  – maximum allowable service life of a piping bend, mth;  $I_{g/a}$  – maximum intensity of gas-abrasive wear of the piping bend depending on the material, mm/kg;  $Q_A$  – actual pipeline performance, m<sup>3</sup>/h;  $q$  – abrasive content in the gas flow, kg/m<sup>3</sup>,  $t$  – duration of a single period taken equal to 1 month (720 hours).

The impact of the gas-abrasive flow on the performance of ball valves is assessed by the amount of leakage in the shut-off body. The destruction of the ball valve seals subject to the



gas flow carrying the abrasive leads to a loss of tightness and a gradual transition from class A according to GOST 54808-2011 "Pipeline valves. Leakage rates of valves" to tightness class D regarded as the limit for gas systems in accordance with STO Gazprom 2-4.1-406-2009 "Methodology for assessing the life of shut-off and control valves of main gas pipelines". The maximum allowable gap areas for shut-off valves of different nominal diameters, corresponding to the specified tightness classes, are presented in Table 5.

**Table 5.** The area of the shut-off valve gap at the maximum allowable leakage

Nominal diameter	Cross-sectional area of the gap at maximum allowable leakage at nominal pressure ( $\Delta F$ ), mm <sup>2</sup>
DN 65	0.0233
DN 80	0.0287
DN 100	0.0359
DN 125	0.0449
DN 150	0.0538
DN 200	0.0718
DN 250	0.0897
DN 300	0.1077
DN 350	0.1256
DN 400	0.1435
DN 500	0.1794
DN 600	0.2153
DN 700	0.2512

The increase in the area of the gap in the shut-off body of ball valves mainly occurs in the process of shutting off the flow and is determined by the friction of the surface of the shut-off element against the seal and the action of the gas flow carrying the abrasive. The maximum allowable number of cycles of repositioning the ball valve shutter when the gas-abrasive flow is shut off can be determined by the following formula:

$$n_{max}^i = \frac{\Delta F \cdot b \cdot \rho_{seal}}{i_{g/a} \cdot q \cdot Q_A \cdot t}, \quad (5)$$

where  $n_{max}^i$  – maximum allowable number of cycles of repositioning the ball valve shutter operating in contact with the abrasive-carrying gas flow, cycles;  $i_{g/a}$  – mass gas-abrasive wear intensity of ball valve seals, g/kg (Table 6);  $b$  – shut-off valve sealing width, mm (in the absence of data on the design of ball valves, the sealing width is assumed to be 3–5 mm);  $\rho_{seal}$  – seal material density respectively, g/mm<sup>3</sup>;  $t$  – duration of a single cycle of repositioning the shutoff valve shutter, h (Table 7).

**Table 6.** Mass intensity of gas-abrasive wear of sealing materials of valves

Material	Mass intensity of gas-abrasive wear ( $i_{g/a}$ ), g/kg	
	at flow rate of 24 m/s	at flow rate of 48 m/s
paronite	0.0709	0.4389
fluoroplast	0.0125	0.1936
carbon-filled fluoroplast	0.02	0.1432
caprolon	0	0.0024

**Table 7.** The duration of a single cycle of shifting the shutter of valves with a manual gearbox or manual override is within STO Gazprom 2-4.1-212-2008 "General technical requirements for pipeline valves supplied to the facilities of OAO Gazprom".

Size	The duration of a single cycle of shifting, h	
	seconds	hours
DN 50–150	60	0.016667
DN 200–400	180	0.05
DN 500–700	600	0.166667
DN 1000	900	0.25

An assessment of the influence of the gas flow rate on the remaining service life of shut-off valves for the pipeline section of a gas distribution station using the example of a flanged ball valve (Dn200, Ru 40, 11nzh67p) showed that with an increase in the gas flow rate containing a regulated mass concentration of mechanical impurities in the gas equal to  $0.001 \text{ g/m}^3$ , from 24 m/s to 31 m/s, the number of valve repositioning cycles was reduced from 1035 cycles to 809. A 20% reduction in the service life of shut-off valves shows the need to take into account the effect of gas flow rate when assessing the intensity of gas-abrasive wear of piping.

### Conclusions

Based on the research, the following conclusions can be drawn:

1. The presence of mechanical impurities in the natural gas flow leads to gas-abrasive wear, which is most significantly manifested in the piping bends of the CS and GDS and seals of valves due to the contact with the gas flow at variable angles from  $15^\circ$  to  $90^\circ$ .
2. The most intensive wear of the pipeline bends made of steels 20 and 09G2S is observed at an angle of attack of  $45^\circ$ . Steel 20 showed better wear resistance compared to steel 09G2S, but an increase in the gas flow rate from 24 m/s to 48 m/s contributes to a more significant increase in its wear intensity.
3. The minimum wear of the shut-off valve seals when the abrasive carrying gas flow is shut off is observed in caprolon. Carbon-filled fluoroplast has lower resistance to gas-abrasive wear compared to F4K fluoroplast.
4. Increasing the gas flow rate from 24 m/s to 48 m/s leads to an increase in the wear intensity for all studied sealing materials. At the same time, for carbon-filled fluoroplast and paronite, the wear maximum shifts from  $45^\circ$  to  $90^\circ$ .
5. The application of the proposed calculation technique makes it possible to take into account the influence of such characteristics as the gas flow rate and the abrasive content on the service life of piping bends and ball valve seals in contact with the gas-abrasive flow.

### References

1. International Standard. GOST 9544-2015. *Pipeline valves. Leakage rates of valves*. Moscow; Standartinform; 2015.
2. Public Joint Stock Company Gazprom. STO Gazprom 2-4.1-212-2008. *General technical requirements for pipeline valves supplied to the facilities of OAO Gazprom*. Moscow; 2008.
3. Ali AAH, Zalzal MKAR. An Investigation to the Abrasive Wear in Pipes Used for Oil Industry. *Journal of Engineering*. 2013;11(19): 1382-1394.
4. Łaciak M, Włodek T, Kozakiewicz T, Liszka K. Impact of flood water on the technical condition of natural gas transmission pipeline valves. *Journal of Loss Prevention in the Process Industries*. 2020;63: 103998.



5. International Standard. GOST 23.201-78. *Products wear resistance assurance. Gas abrasive wear testing of materials and coatings with centrifugal accelerator*. Moscow; Standartinform; 1978.
6. International Standard. GOST 23.208-79. *Ensuring of wear resistance of products. Wear resistance testing of materials by friction against loosely fixed abrasive particles*. Moscow; Standartinform; 1979.
7. Nasyrova M, Lipatov V, Imashev R, Savichev V, Zhonin V, Litvinenko K, Abrashov V, Skorobogach M. Numerical simulation of gas-abrasive wear of industrial equipment elements. *Petroleum Engineering*. 2021;19(5): 67-74.
8. Oka YI, Yoshida T. Practical Estimation of Erosion Damage Caused by Solid Particle Impact Part 2: Mechanical Properties of Materials Directly Associated with Erosion Damage. *Wear*. 2005;259(1-6): 102-109.
9. Shirazi SA, McLaury BS, Arabnejad H. A SemiMechanistic Model for Predicting Sand Erosion Threshold Velocities in Gas and Multiphase Flow Production. *Materials of SPE Annular Technical Conference and Exhibition: Dubai, UAE*. 2016.
10. DVNGL-RP-O501-2015. *Managing Sand Production and Erosion*. Det Norske Veritas – Germanischer Lloyd; 2015.
11. *API Recommended Practice for Design and Installation of Offshore Production Platform Piping Systems*. Washington D.C.: American Petroleum Institute; 1991.
12. Bitter JGA. A Study of Erosion Phenomena: Part I. *Wear*. 1963;6(1): 5-21.
13. Goodwin JE, Sage W, Tilly GP. Study of Erosion by Solid Particles. *Proceedings of the Institution of Mechanical Engineers*. 1969;184: 279-292.
14. Ben-Ami Y, Uzi A, Levy A. Modelling the Particles Impingement Angle to Produce Maximum Erosion. *Powder Technology*. 2016;301: 1032-1043.
15. Finnie I. Erosion of Surfaces by Solid Particles. *Wear*. 1960;3(2): 87-103.
16. Bitter JGA. A Study of Erosion Phenomena: Part I. *Wear*. 1963;6(1): 5-21.
17. Zroichikov NA, Putilov VY, Putilova IV, Fadeev SA, Malikova EA. Evaluation of the Influence of Abrasive Wear on the Service Life of Hydraulic Transport Systems. *Thermal Engineering*. 2020;9: 35–45.
18. Abrashov VN, Zhonin VV, Imashev RN, Litvinenko KV, Mikhaylov AG, Nasyrova MI, Skorobogach MA, Faritov AT. Experimental methodology for determining gas-abrasive wear of field equipment elements. *Oil Industry*. 2020;3: 78–82.

## THE AUTHORS

**Elagina O.Yu.** 

e-mail: elaguina@mail.ru

**Buklakov A.G.** 

e-mail: dron-32@mail.ru

**Dubinov Yu.S.** 

e-mail: dubinovys@gmail.com


**Dedok D.V.**

e-mail: titrngo@yandex.ru

## Diffusion-induced stresses due to an impulsive mass source under non-Fickian mass transfer models

M. Fayik<sup>1</sup> , A.R. El-Dhaba<sup>2</sup> , E. Awad<sup>1</sup> 

<sup>1</sup>Department of Mathematics, Faculty of Education, Alexandria University, Souter St. El-Shatby, Alexandria  
P.O. box 21526, Egypt

<sup>2</sup>Department of Mathematics, Faculty of Science, Damanhur University, Egypt  
 m\_fayik@alexu.edu.eg

**Abstract.** The description of the mass transfer mechanisms in various physical and engineering fields, e.g., Li-ion batteries, is of significant importance for optimizing their performance. The present work introduces a comparative study describing the different responses of a perfectly elastic material when different non-Fickian diffusion situations are considered. The uncoupled theory of elastic diffusion, in which the diffusion process is described by non-Fickian laws, such as Cattaneo, Jeffreys-type, and Burgers-type constitutive laws, is employed in this modeling. The diffusion of lithium ions inside the silicon anode is one of the physical situations in which diffusion-induced stresses may be significant. An impulsive initial value problem, consisting of an initial lithium ions amount that starts impulsively to diffuse over the entire space of a silicon material, is considered. Direct approach together with Laplace and exponential Fourier transforms techniques are employed to obtain the solution in the Laplace transformed domain. The inverse Laplace transform is computed numerically to obtain the solution in the physical domain. Comparisons among the material responses to different diffusion regimes are presented.

**Keywords:** Cattaneo equation, Jeffreys equation, linear elasticity, lithium-ion batteries, impulsive problem

**Acknowledgements.** No external funding was received for this study. E.A. is grateful to Renat Sibatov for providing his work in Ref. [44] and for fruitful discussion.

**Citation:** Fayik M, El Dhaba AR, Awad E. Diffusion-induced stresses due to an impulsive mass source under non-Fickian mass transfer models. *Materials Physics and Mechanics*. 2023;51(1): 93-107. DOI: 10.18149/MPM.5112023\_9.

### Introduction

In the middle of the last century, Nabarro [1] suggested that the self-diffusion within the grains of a polycrystalline solid can cause the solid to "Yield", resulting in a change in the shape of the solid crystal. Herring [2] developed an underlying theory, based on Nabarro's suggestion, and presented the calculations of the rate of creeping. Generally speaking, the diffusion of solute atoms or molecules in solid materials, for example, gases in metal and lithium ions in the battery, creates diffusion-induced stress (or chemical stress) [3,4] and may cause fracture or dislocation of the local structure of the solvent [5]. Prussin [3] was the first author who referred to some estimates of the phenomenon of diffusion-induced stress. As for the diffusion and chemical stress interactions, Li [4] studied the stress-induced diffusion model in elastic materials. Yang [6] presented a diffusion equation based on the

effect of stress-induced diffusion and established a relationship between hydrostatic stress and the concentration of solute atoms, see also [7-10]. All these works altered the original structure of Fick's first law by replacing the concentration with the chemical potential. In this setting, they expressed the non-Fickian diffusion induced by the lattice distortions, in other words, the coupling between lattice stresses and diffusion. Although the fundamental hypothesis, in some works, is the coupling between stresses and diffusion, i.e., stress-induced diffusion and diffusion-induced stress, it seems that neglecting the inertial term in the conservation of momentum leads eventually to uncoupling elastic diffusion (diffusion-induced stress), see e.g., [11].

One of the early investigations that had shed light on the stress distributions resulting from possible non-Fickian mass diffusion mechanisms is the work of Povstenko [12], where the author expressed this anomaly by applying a fractional diffusion-wave equation and examined the effect of this non-Fickian diffusion on the stresses with disregarding the reverse effect of solvent's strain gradient on the diffusing particle flux (i.e. chemical potential is itself the concentration), see also the monograph [13] for further perspectives and applications.

Normal diffusion processes described by the second Fick's law, owning the fame linear time-dependence law of the mean-squared displacement (MSD) of the diffusive substance  $\langle x^2(t) \rangle \propto t$ , is not dominant in all diffusion situations. Instead, fluorescence spectroscopy experiments [14] and computer simulations [15] showed a non-linear behavior for the MSD, such as ballistic behavior in the short time, or crossover from linear in the short time to non-linear in the intermediate time. We further refer the reader to the comprehensive review [16] on such non-linear behaviors. Therefore, the normal diffusion equation is no longer valid to simulate such anomalous behaviors. Furthermore, the lagged response idea [17] with its well-known fundamental concepts (flux-precedence and gradient-precedence), suggesting the non-simultaneous response between the flux and the distribution gradient that eliminates the paradox of instantaneous propagation [18], comprises many macroscopic/microscopic heat and mass transfer models, e.g., Cattaneo equation [18-22] and Jeffreys equation [23-26]. The first attempt to model non-anomalous diffusion situations using Jeffreys equation by building a connection between Jeffreys equation and the two-phase model of mass transfer [27,28] that corresponds to the two-step model of ultrafast heat transfer [29,30], has been due to [23,24]. Despite the criticism of Jeffreys equation [31] and the hyperbolic Dual-Phase-Lag (DPL) equation [32], which shows negative values for the temperature in high dimensions, which in turn prevents these equations from modeling concentration of the diffusing substances, the authors [25,26] have derived the sufficient conditions for the probabilistic interpretation of Jeffreys equation and built a connection with the continuous-time random walk scheme. In spite of the defect of the hyperbolic DPL law, yielding negative values in higher dimensions, we can adopt it and its modified version [33] (or Burgers-like equation [34]) if the problem is one-dimensional. The reader can consult Quintanilla and Racke's conditions on the DPL equations for satisfying stability and well-posedness [35,36]. For other anomalous diffusion models in higher dimensions, we refer to recent studies [37,38].

The diffusion of lithium ions in a solid-state electrolyte is an engineering environment rich with anomalous situations which are in any way do not obey the linear behavior  $\langle x^2(t) \rangle \propto t$ , see e.g., [39-44]. In [39], the authors studied the segmental motion of  $\text{CH}_2\text{CH}_2\text{O}/\text{CH}_2\text{CH}(\text{CH}_3)\text{O}$  moiety of the bulk solid-polymer electrolyte and the hopping motion of lithium ions ( $^7\text{Li}$ ) activated by this segmental motion. They reported experimentally that the anions (negative ions) diffusion exhibits an anomalous behavior following  $\langle x^2(t) \rangle \propto t^\gamma$  with  $0 < \gamma < 1$ . This anomalous behavior diminishes with the increase in temperature. Using a molecular dynamic approach, the study [42] reported different diffusion properties of lithium ions on different structure orientations of pure silicon. They emphasized the experimental results of [40, 41] that the diffusion is faster in  $\langle 110 \rangle$  orientation compared with

other orientations  $\langle 100 \rangle$  and  $\langle 111 \rangle$  and requires a smaller critical force. Moreover, during the charging process of the battery, the pure silicon anode maintains its crystalline structure for a short period, thereafter it would be transformed into Li-Si alloy. Thus, the diffusion of lithium becomes an alloy with different lithium concentrations. The low-lithium concentrations alloy was found to act as a "cage-like" for the diffusing lithium ions. When the lithium concentration increased, the pure silicon would be entirely converted to Li-Si alloy structure, hence the caging effect of the silicon structure disappeared. From a theoretical viewpoint, studying the disorder-extent of the silicon structure due to discharging/charging (lithiation/delithiation) processes, requires "resetting" the velocity of diffusing lithium to zero after a certain time for avoiding the velocity from going to infinity. One of the other anomalous behaviors observed in lithium-ion batteries is the low-frequency impedance response of LiCoO<sub>2</sub>/C batteries which makes with the real axis (in  $Z_{im}/Z_{re}$  Nyquist plot) an angle greater than  $45^\circ$  (the default angle for diffusion impedance known as the Warburg impedance). In [43], a mathematical description for the electrochemical impedance [45] based on a fractional kinetic approach was adopted for developing a model that describes the impedance response of LiCoO<sub>2</sub>/C batteries by taking into account activation of the anomalous diffusion, see also [44,46] for other perspectives of anomalous diffusion in lithium-ion batteries and solids. To perfectly capture the inertia of lithium ions transport in graphitic materials, Maiza and coworkers [47] replaced the classical Fickian approach with the non-instantaneous response assumption represented by the single-phase-lag in the particle flux, in other words, the first approximation is Cattaneo equation or Maxwell-Cattaneo-Vernotte (MCV) equation. They compared the two approaches and found that the MCV approach, or alternatively, the lagging response in the particle flux, allows providing an interpretation of observed electrochemical behaviors.

The objective of the current study is to introduce a qualitative assessment of the response of solid solvent when four main types of non-Fickian diffusion events occur: Cattaneo equation; Jeffreys equation; hyperbolic DPL equation and modified hyperbolic DPL (Burgers-like) equation. It is concluded from this study to facilitate prior knowledge to simply recognize the response of the material to possible diffusion processes. We organize the paper as follows: In the next section, we formulate and solve an initial-value problem in elastic diffusion based on the different diffusion models. The first fundamental solution is brought in the Laplace domain. Numerical schemes, graphical representations, and potential discussions are prepared in Section 0. We give a summary of the work, concluding remarks, and future generalizations in Section 0.

### Diffusion-induced stresses in an infinite domain

The diffusion of atoms or their ions (cations/anions) within a solvent medium causes distortions in the solvent lattice which could result in the development of local stresses that are known in the literature as diffusion-induced (or chemical) stresses [6-8]. Conversely, when the effect of stresses on the diffusion process is considered, then we have a stress-induced diffusion and Fick's first law is replaced with [2,48]

$$\mathbf{J}(\mathbf{r}, t) = -\frac{D_0}{R\theta} c(\mathbf{r}, t) \nabla \mu(\mathbf{r}, t), \quad (1)$$

where  $\mathbf{J}(\mathbf{r}, t)$  is the particle flux vector,  $\mathbf{r} \in \mathbb{R}^n$  denotes the position vector in the  $n$ th dimensional space,  $\mathbf{r} = \langle x_1, \dots, x_n \rangle$ , and  $t$  denotes the temporal variable,  $R$  is the gas constant,  $\theta$  is the absolute temperature,  $D_0$  is the diffusion coefficient and  $\mu(\mathbf{r}, t)$  is the chemical potential determined through the constitutive relation [4]

$$\mu(\mathbf{r}, t) = R\theta \ln c(\mathbf{r}, t) - \Omega \sigma_H(\mathbf{r}, t) \quad (2)$$

where  $\Omega$  is the partial molar volume ( $\text{m}^3/\text{mol}$ ) and  $\sigma_H(\mathbf{r}, t)$  is the hydrostatic stress defined as the mean of normal stresses, namely,

$$\sigma_H = \frac{\sigma_{xx} + \sigma_{yy} + \sigma_{zz}}{3}. \quad (3)$$

In isothermal thermodynamical processes, the generalized Fick's law (1) with the chemical potential (2) reads

$$\mathbf{J}(\mathbf{r}, t) = -D_0 \left[ \nabla c(\mathbf{r}, t) - \frac{\Omega}{R\theta} c(\mathbf{r}, t) \nabla \sigma_H(\mathbf{r}, t) \right]. \quad (4)$$

If the effect of stresses on the diffusion is negligible, or in other words, if we disregard the nonlinear terms of (4), we recover the classical Fick's first law  $\mathbf{J}(\mathbf{r}, t) = -D_0 \nabla c(\mathbf{r}, t)$ .

Because the main goal of this study is to introduce a comparative analysis that distinguishes the response of the solvent lattice to different types of non-Fickian diffusion, we assume that the lattice distortions (deformations) are very small and recoverable so that we can adopt the classical model of linear elasticity which describes the chemical stresses through the strain-stress constitutive relation [6]

$$\varepsilon_{ij} = \frac{1}{E} [(1 + \nu)\sigma_{ij} - \nu\sigma_{kk}\delta_{ij}] + \frac{\Omega}{3} c\delta_{ij}, \quad (5)$$

where  $\sigma_{ij}$  are the components of the stress tensor,  $\varepsilon_{ij}$  are the component of the strain tensor,  $i, j = 1, 2, 3$ ,  $\sigma_{kk} = \sigma_{xx} + \sigma_{yy} + \sigma_{zz}$  is the volumetric stress,  $\delta_{ij}$  is the Kronecker delta,  $E$  and  $\nu$  are Young's modulus and Poisson ratio of the elastic material. Setting  $i = j$  in (5), we get the relation

$$\frac{E}{3(1 - 2\nu)} \epsilon = \sigma_H + \frac{\Omega E}{3(1 - 2\nu)} c, \quad (6)$$

where  $\sigma_{kk} = 3\sigma_H$ ,  $\epsilon = \varepsilon_{kk} = \varepsilon_{xx} + \varepsilon_{yy} + \varepsilon_{zz}$  is the volumetric strain, and the strain components are related to the displacement through the constitutive equation

$$\varepsilon_{ij} = \frac{1}{2} (u_{i,j} + u_{j,i}), \quad (7)$$

and  $u = \langle u_x, u_y, u_z \rangle$  is the displacement vector. Now substituting from (6) into (5), we obtain the stress-strain constitutive relation

$$\sigma_{ij} = \frac{E}{1 + \nu} \varepsilon_{ij} + \frac{\nu E}{(1 + \nu)(1 - 2\nu)} \epsilon \delta_{ij} - \frac{\Omega E}{3(1 - 2\nu)} c \delta_{ij}. \quad (8)$$

Here, we consider only the diffusion-induced stress with disregarding the stress-induced diffusion. Furthermore, we assume that different non-Fickian diffusion situations could occur during the simulation, so we have altered the classical Fick's first law  $\mathbf{J}(\mathbf{r}, t) = -D_0 \nabla c(\mathbf{r}, t)$  with the following the more inclusive constitutive law [17,26]:

$$\mathbf{J}(\mathbf{r}, t + \tau_j) = -D_0 \nabla c(\mathbf{r}, t + \tau_c), \quad (9)$$

where  $\tau_j$  and  $\tau_c$  are constants of time dimension termed phase-lag in the diffusion flux and phase-lag in the concentration-gradient respectively. Equation (9) generalizes the approach followed in [47], wherein the phase lag  $\tau_c$  has been neglected from their study. The first approximation of the Taylor series expansion of (9) yields the Jeffreys-type constitutive law

$$(1 + \tau_j \partial_t) \mathbf{J}(\mathbf{r}, t) = -D_0 (1 + \tau_c \partial_t) \nabla c(\mathbf{r}, t), \quad (10)$$

which leads to a parabolic type of partial differential equation. Whilst the second approximation of the Taylor series of the left-hand side of (9) yields the constitutive law

$$\left( 1 + \tau_j \partial_t + \frac{\tau_j^2}{2} \partial_t^2 \right) \mathbf{J}(\mathbf{r}, t) = -D_0 (1 + \tau_c \partial_t) \nabla c(\mathbf{r}, t), \quad (11)$$

which gives a hyperbolic type of partial differential equation known as the hyperbolic DPL equation. Lastly, the successive lagging response of Fick's law yields the Burger-type constitutive law [33]

$$(1 + \tau_j \partial_t + \tau_m^2 \partial_t^2) \mathbf{J}(\mathbf{r}, t) = -D_0 (1 + \tau_c \partial_t) \nabla c(\mathbf{r}, t), \quad (12)$$

where that  $\tau_j = \tau_{j_1} + \tau_{j_2}$ ,  $\tau_m = \sqrt{\tau_{j_1}\tau_{j_2}}$ ,  $\tau_{j_1}$  and  $\tau_{j_2}$  are successive phase lags in the diffusion flux. Introducing the controlling parameters  $n_0$  and  $n_1$ , the above equations, (10)-(12), can be combined in the following generic constitutive law:

$$\left(1 + \tau_j \partial_t + \left(n_0 \frac{\tau_j^2}{2} + n_1 \tau_m^2\right) \partial_t^2\right) \mathbf{J}(\mathbf{r}, t) = -D_0(1 + \tau_c \partial_t) \nabla c(\mathbf{r}, t). \quad (13)$$

The numbers  $n_0$  and  $n_1$ , used in the above equation, take their values from the set  $\{0,1\}$ , and they are inserted for invoking various diffusion models from the single unphysical equation (13), that show up in the following limiting cases:

- (i) Equation (13) reduces to the well-known Fick's first law, if and only if  $n_0 = n_1 = 0$ , and the time constants are identical or neglected,  $\tau_j = \tau_c = 0$ .
- (ii) Cattaneo equation can be obtained from (13) when setting  $n_0 = n_1 = 0$  and  $\tau_c = 0$ .
- (iii) The parabolic flux-precedence (flux-driven) Jeffreys equation is produced, when  $n_0 = n_1 = 0$ , and  $\tau_j < \tau_c$ .
- (iv) The parabolic concentration gradient-precedence Jeffreys equation is obtained, when  $n_0 = n_1 = 0$ , and  $\tau_j > \tau_c$ .
- (v) For  $n_0 = 1, n_1 = 0$ , equation (13) reduces to the hyperbolic DPL diffusion model.
- (vi) Setting  $n_0 = 0, n_1 = 1, \tau_j > \tau_c$ , equation (13) reduces to the modified hyperbolic DPL diffusion model or alternatively the Burgers-type equation, such that  $\tau_j = \tau_{j_1} + \tau_{j_2}$ ,  $\tau_m = \sqrt{\tau_{j_1}\tau_{j_2}}$ , where  $\tau_{j_1}$  and  $\tau_{j_2}$  are successive phase lags in the diffusion flux.

Therefore, any local stress will be stimulated by the diffusion process only.

The conservation of momentum for the alloy (solvent and solute atoms) is given in the absence of external agents by

$$\sigma_{ji,j} = \rho \ddot{u}_i,$$

where  $\rho = \rho_0 + \rho_{\text{alloy}}(c)$  is the density and  $\rho_0$  is the density of the solvent at constant temperature (assumed constant). Because of the linearity assumption in this section, we neglect the term  $\rho_{\text{alloy}}(c)\ddot{u}_i$  and keep only the linear term  $\rho_0\ddot{u}_i$ . Therefore, the conservation of momentum reads

$$\sigma_{ji,j} = \rho_0 \ddot{u}_i. \quad (14)$$

Likewise, we ignore the dependence of  $E$  and  $\nu$  on the solute concentration and take them as material constants at a constant temperature. Under these assumptions, the initial value problem can be modeled in the one-dimensional setting where the displacement vector and the concentration of the solute are given as

$$\mathbf{u} = \langle u(x, t), 0, 0 \rangle, \quad c(\mathbf{r}, t) = c(x, t). \quad (15)$$

Thus, the normal stresses are given by

$$\sigma_{xx} = \frac{(1-\nu)E}{(1+\nu)(1-2\nu)} \epsilon - \frac{\Omega E}{3(1-2\nu)} c, \quad (16)$$

$$\sigma_{yy} = \sigma_{zz} = \frac{\nu E}{(1+\nu)(1-2\nu)} \epsilon - \frac{\Omega E}{3(1-2\nu)} c, \quad (17)$$

and the hydrostatic stress is given by

$$\sigma_H = \frac{E}{3(1-2\nu)} [\epsilon - \Omega c]. \quad (18)$$

The equation of conservation of momentum has a nonzero component in  $x$ -direction, namely  $\partial^2 \sigma_{xx} / \partial x^2 = \rho_0 \partial^2 \epsilon / \partial t^2$ , which upon combining it with the constitutive relation (16), we obtain

$$\frac{(1-\nu)E}{(1+\nu)(1-2\nu)} \frac{\partial^2 \epsilon}{\partial x^2} - \frac{\Omega E}{3(1-2\nu)} \frac{\partial^2 c}{\partial x^2} = \rho_0 \frac{\partial^2 \epsilon}{\partial t^2}, \quad (19)$$

and the concentration is given by:

$$\left(1 + \tau_j \partial_t + \left(n_0 \frac{\tau_j^2}{2} + n_1 \tau_m^2\right) \partial_t^2\right) \frac{\partial c}{\partial t} = D_0(1 + \tau_c \partial_t) \frac{\partial^2 c}{\partial x^2}, \quad (20)$$

resulted from eliminating the flux  $\mathbf{J}(\mathbf{r}, t)$  between (13) and the continuity equation:

$$\nabla \cdot \mathbf{J}(\mathbf{r}, t) + \frac{\partial c(\mathbf{r}, t)}{\partial t} = 0, \quad (21)$$

and considering the one-dimensional setting (15). For our impulsive initial value problem, we attach the following initial conditions

$$\begin{aligned} c(x, 0) &= c_0 \delta\left(\frac{x}{\sqrt{D_0 \tau_j}}\right), \quad \left.\frac{\partial c(x, t)}{\partial t}\right|_{t=0} = \frac{\tau_c D_0 c_0}{\tau_j} \partial_x^2 \left[\delta\left(\frac{x}{\sqrt{D_0 \tau_j}}\right)\right], \quad \epsilon(x, 0) \\ &= \left.\frac{\partial \epsilon(x, t)}{\partial t}\right|_{t=0} = 0. \end{aligned} \quad (22)$$

By applying the following transformations

$$\begin{aligned} \frac{x}{\sqrt{D_0 \tau_j}} &\rightarrow x, \quad \frac{u}{\sqrt{D_0 \tau_j}} \rightarrow u, \quad \frac{t}{\tau_j} \rightarrow t, \quad \frac{\Omega(1 + \nu)}{3(1 - \nu)} c \rightarrow c, \\ \frac{(1 + \nu)(1 - 2\nu)}{1 - \nu} \frac{\sigma_{ij}}{E} &\rightarrow \sigma_{ij}, \end{aligned} \quad (23)$$

the governing equations can be cast in the dimensionless form:

$$\frac{\partial^2 \epsilon}{\partial x^2} - \frac{\partial^2 c}{\partial x^2} = \kappa_M \frac{\partial^2 \epsilon}{\partial t^2}, \quad (24)$$

$$\left(1 + \partial_t + \left(\frac{n_0}{2} + n_1 \chi_1^2\right) \partial_t^2\right) \frac{\partial c}{\partial t} = (1 + \chi_0 \partial_t) \frac{\partial^2 c}{\partial x^2}, \quad (25)$$

$$\sigma_{xx} = \epsilon - c, \quad (26)$$

$$\sigma_{yy} = \sigma_{zz} = \frac{\nu}{1 - \nu} \epsilon - c \quad (27)$$

and the hydrostatic stress

$$\sigma_H = \kappa_S \epsilon - c \quad (28)$$

subject to the dimensionless initial conditions [22, 26]

$$c(x, 0) = \delta(x), \quad \left.\frac{\partial c(x, t)}{\partial t}\right|_{t=0} = \chi_0 \partial_x^2 [\delta(x)], \quad \epsilon(x, 0) = \left.\frac{\partial \epsilon(x, t)}{\partial t}\right|_{t=0} = 0 \quad (29)$$

where

$$\begin{aligned} \kappa_M &= \frac{\varrho_0 D_0 (1 + \nu)(1 - 2\nu)}{\tau_j (1 - \nu) E}, \quad \kappa_S = \frac{1 + \nu}{3(1 - \nu)}, \quad \chi_0 = \frac{\tau_c}{\tau_j}, \\ \chi_1 &= \frac{\tau_m}{\tau_j}, \quad c_0 = \frac{3(1 - \nu)}{\Omega(1 + \nu)}. \end{aligned} \quad (30)$$

The solutions of (24)-(25) subject to (29) are given in the Laplace-Fourier space as

$$\hat{\epsilon}(q, s) = \frac{L(s)}{\kappa_M s^2 - sL(s)} \left[ \frac{\kappa_M s^2}{q^2 + \kappa_M s^2} - \frac{sL(s)}{q^2 + sL(s)} \right], \quad (31)$$

$$\hat{c}(q, s) = \frac{L(s)}{q^2 + sL(s)}, \quad (32)$$

where

$$\tilde{L}(s) = \frac{\left(1 + s + \left(\frac{n_0}{2} + n_1 \chi_1^2\right) s^2\right)}{1 + \chi_0 s}. \quad (33)$$

Here, the tildes refer to the Laplace transform  $\tilde{f}(x, s) = \mathcal{L}\{f(x, t); t\}(x, s) = \int_0^\infty f(x, t) \exp(-st) dt$ , the hats refer to the Fourier transform  $\hat{f}(q, t) =$

$\mathcal{F}\{f(x, t); x\}(q, t) = \int_{-\infty}^{\infty} f(x, t) \exp(iqx) dx$ ,  $s \in \mathbb{C}$  is the Laplace parameter, and  $q \in \mathbb{R}$  is the Fourier parameter.

Finding a closed-form expression for the volumetric strain  $\hat{\epsilon}(q, s)$  in the real domain is an intractable problem to our knowledge. To extract as much information as possible from the above simulation, we shall at first invert the Fourier transform using a well-known tabulated rule, then we invoke to a familiar numerical technique to invert the Laplace transform. The solutions of the volumetric strain and the concentration are given in the Laplace space:

$$\tilde{\epsilon}(x, s) = \frac{L(s)}{2(\kappa_M s^2 - sL(s))} \left[ \sqrt{\kappa_M s^2} \exp(-\sqrt{\kappa_M s^2}|x|) - \sqrt{sL(s)} \exp(-\sqrt{sL(s)}|x|) \right] \quad (34)$$

$$\tilde{c}(x, s) = \frac{1}{2} \sqrt{\frac{L(s)}{s}} \exp(-\sqrt{sL(s)}|x|), \quad (35)$$

where we have used the rule  $\mathcal{F}^{-1}\left\{\frac{1}{a^2 + \omega^2}\right\} = \frac{1}{2a} \exp(-a|x|)$ , see [49].

## Results and discussions

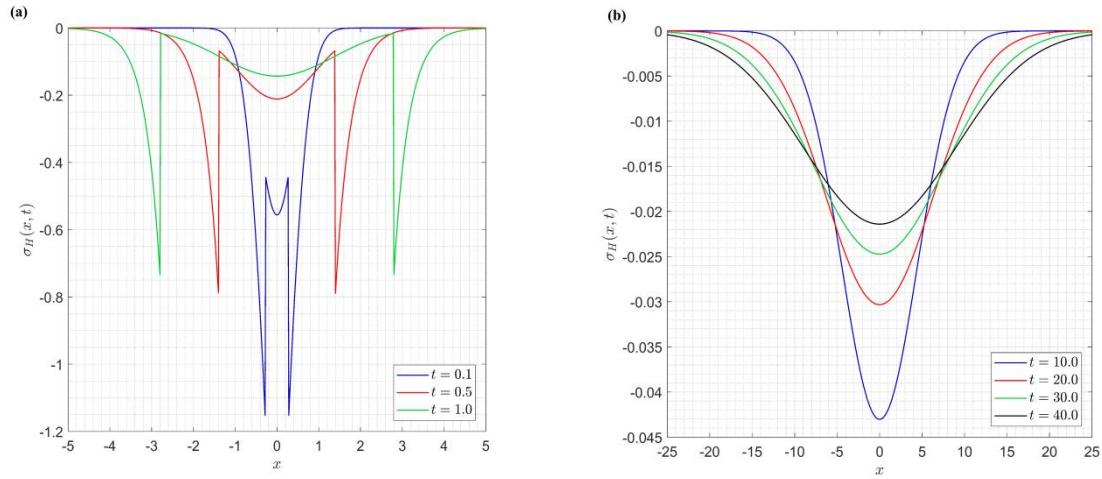
In this section we bring the solutions of concentration and volumetric strain to the real domain by inverting numerically the Laplace transform in equations (34)-(35), [17,50-55]. The diffusion of lithium ions in silicon anode is chosen for this simulation. Because of the phenomenological nature of our study, we have considered an infinite silicon medium and there has been an impulse of lithium ions distributed uniformly on the  $yz$ -plane ( $x = 0$ ). No surprising that if the phenomenon occurs on the picometer scale, the micrometer silicon film can be considered as a half-space. The crystalline silicon parameters at room temperature  $\theta_0 = 298K$  are [8]  $E = 159 GPa$ ,  $\nu = 0.22$ , and the density [56]  $\rho_0 = 2.33 \times 10^3 Kg/m^3$ . The diffusivity of lithium ions in the silicon at room temperature  $\theta_0 = 298K$  is  $D_0 = 10^{-17} m^2/s$  [8] and the partial molar volume  $\Omega = 7.69 \times 10^{-6} m^3/mol$ . Further, we have chosen the relaxation of particle flux as  $\tau_j = 10^{-15} = 1 \text{ femtosecond}$ . Using these parameters, we have

$$\kappa_M = 0.128, \kappa_S = 0.521, c_0 = 2.494 \times 10^5, \quad (36)$$

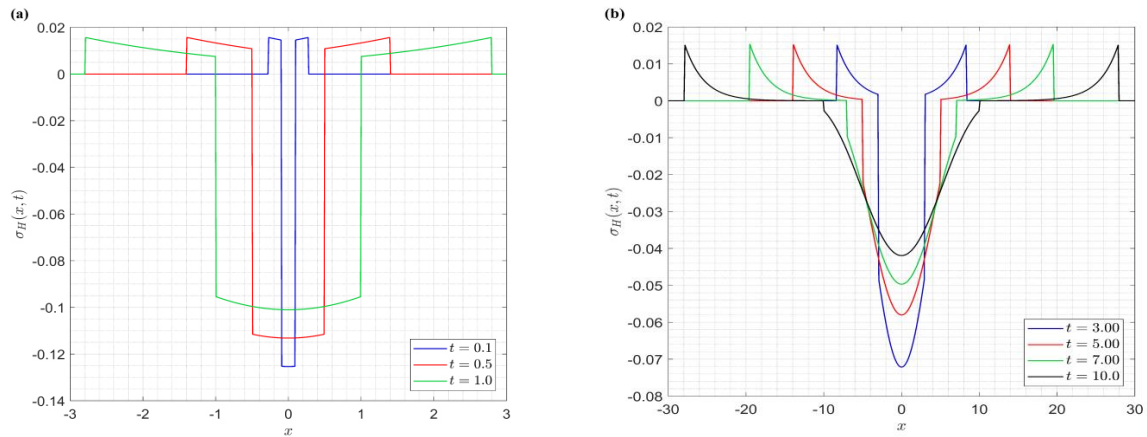
and  $\chi_0$  and  $\chi_1$  will be arbitrarily chosen to study the effects of the concentration gradient and flux diffusion delay, respectively.

Figure 1 shows the hydrostatic stress at different values of time for the Fickian diffusion. In the short time domain, the propagation of discontinuities, a characteristic property in the mathematical model of linear elasticity [57] and coupled thermoelasticity [58], is clear. As time progresses, the discontinuities go to infinity so that they do not appear in the long-time domain near the disturbances as Fig. 1(b) shows. In the finite-speed diffusion governed by the telegrapher "Cattaneo" equation, there is a characteristic discontinuity in the concentration profile in the short-time domain when the particle has had time to interact with the reflecting point [20]. This feature affects the corresponding stress distribution as shown in Fig. 2, where there are four discontinuity points for the single hydrostatic stress profile; two of them are due to the mechanical wave and the others are due to the concentration wave. With the passage of time, the wave term effect in the Cattaneo equation diminishes and the process transforms to the Fickian diffusion, thereby the discontinuity points due to finite-speed diffusion diminish in the intermediate time domain as Fig. 2(b). The long-time behavior of the hydrostatic stress due to finite-speed diffusion coincides with the long-time behavior of the Fickian diffusion, Fig. 1(b). Not only the temporal progress that lowers the sharpness of discontinuity points, but also the transition from telegrapher to telegrapher-like behavior as Fig. 3 exhibits.





**Fig. 1.** Hydrostatic stress distribution for Fickian diffusion at different values of time: (a) for a small value of time; (b) for a large value of time



**Fig. 2.** Hydrostatic stress distribution for finite-velocity diffusion at different values of time: (a) for a small value of time; (b) for a large value of time

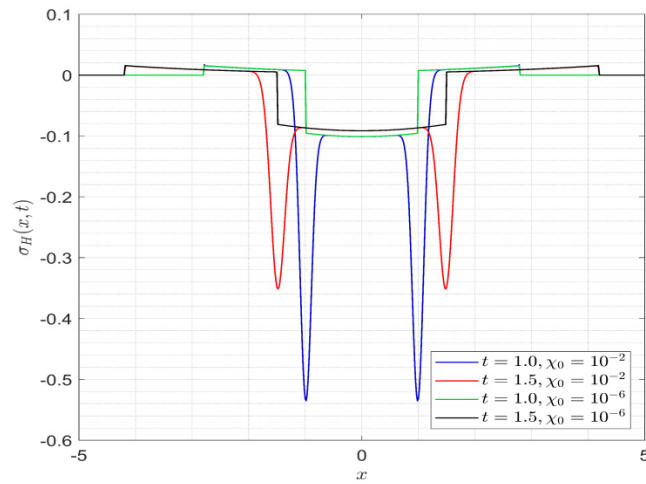


**Fig. 3.** Elimination of the discontinuity point of the finite-speed diffusion at the transition from telegrapher to telegrapher-like behavior

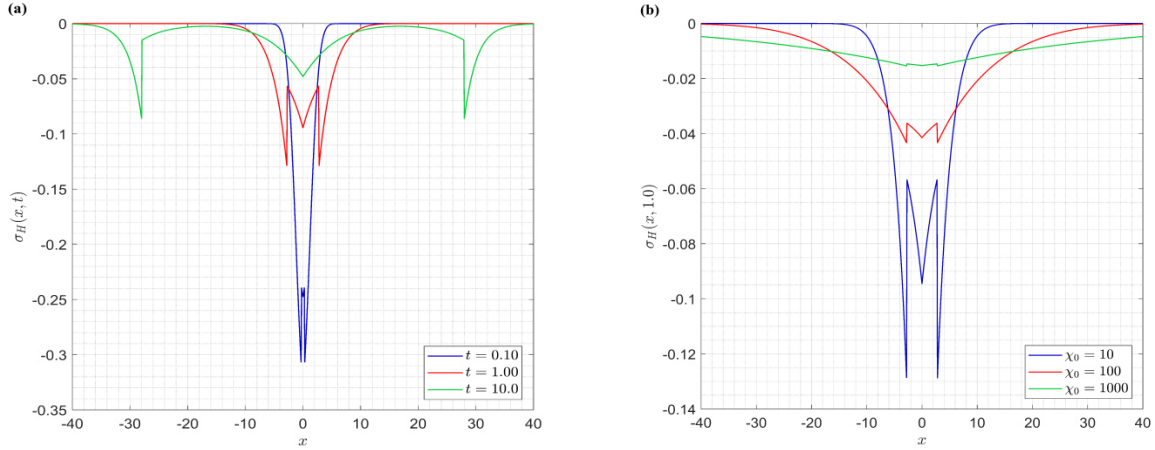


**Fig. 4.** Hydrostatic stress distribution for the DPL with flux precedence, or the cage-like diffusion: (a) for different values of time and  $\chi_0 = 10$ ; (b) for different values of  $\chi_0$  and  $t = 1.0$

As the ratio  $\chi_0$  leaves the interval  $(0,1]$ , i.e.,  $\tau_c > \tau_j$ , the concentration profile described by ordinary Jeffreys equation converts from the telegrapher-like effect to the cage-like or the labyrinth-like effects characterized by the crossover from normal diffusion  $\langle x^2(t) \rangle \propto t$  in the short-time domain to anomalous  $\langle x^2(t) \rangle \propto t^\gamma$ ,  $0 < \gamma < 1$  in the intermediate-time domain, and lastly from anomalous to normal again  $\langle x^2(t) \rangle \propto t$  in the long-time domain, see [26]. The hydrostatic stress corresponding to this cage-like phenomenon at  $\chi_0 = 10$  is depicted in Fig. 4(a) at relatively small values of the time. In comparison between the material response to the Fickian diffusion, Fig. 1(a), and to the diffusion with caging at random places within the solvent, Fig. 4(a), one concludes that the stresses in the diffusion process with caging have amplitudes less than those in the normal diffusion without caging or labyrinth, but the stresses in the case of caging reach to deeper points of the solvent compared to the normal diffusion situation. In view of Fig. 4(b) one can see that the longer the concentration gradient delays, the least-value and the deeper-distributed stresses within the solvent are.

In the ordinary wave equation, we have the dimensionless from

$$\frac{\partial^2 c}{\partial t^2} = \frac{\partial^2 c}{\partial x^2} \quad (37)$$

subject to

$$c(x, 0) = \delta(x), \quad \left. \frac{\partial c(x, t)}{\partial t} \right|_{t=0} = 0, \quad (38)$$

which can be obtained from Eq. (25) by setting  $n_0 = 0, n_1 = 1$ , and  $\chi_0 = 0$ . The first fundamental solution of the wave equation (37), i.e., the initial conditions (38) are considered, in the Laplace-Fourier domain reads  $\hat{c}(q, s) = s/(s^2 + q^2)$ , which can be solved analytically as [59]

$$c_{\text{wave}}(x, t) = \frac{1}{2} \delta(t - |x|). \quad (39)$$

The solution (39) is zero everywhere except at the points  $x = \pm t$ , where it goes to infinity at these points. Inserting this solution into Eq. (24) as an external agent stimulating the lattice strain, we get

$$\epsilon(x, t) = \frac{1}{2(1 - \kappa_M)} [\delta(t - |x|) - \sqrt{\kappa_M} \delta(t - \sqrt{\kappa_M} |x|)], \quad (40)$$

and substituting the resulting volumetric strain (40) and the concentration (39) into the hydrostatic stress (28) we obtain

$$\sigma_H(x, t) = \frac{1}{2(1 - \kappa_M)} [(\kappa_M + \kappa_S - 1)\delta(t - |x|) - \kappa_S \sqrt{\kappa_M} \delta(t - \sqrt{\kappa_M} |x|)]. \quad (41)$$

Therefore, the hydrostatic stress (41) resulting from the ballistic motion of the dispersed substance is zero everywhere except at the four points  $x = \pm t, \pm \frac{t}{\sqrt{\kappa_M}}$ , where the stresses go to infinity also, which refers to the possibility of damaging the solvent medium at these points. It is noteworthy to mention that if we replace the conditions (38) with

$$c(x, 0) = 0, \quad \left. \frac{\partial c(x, t)}{\partial t} \right|_{t=0} = \delta(x), \quad (42)$$

we get the second fundamental solution of the wave equation [12]

$$c_{\text{wave}}(x, t) = \frac{1}{2} H(t - |x|). \quad (43)$$

It is noted that the second fundamental solution (43) has not a probabilistic interpretation since  $\int_{-\infty}^{\infty} c_{\text{wave}}(x, t) dx = \frac{1}{2} \int_{-\infty}^{\infty} H(t - |x|) dx = t (\neq 1)$ . Thus, we could not classify the motion following the distribution (43) with a certain dynamical description as the case of the second Fick's law and Cattaneo, and Jeffreys equations. For the sake of completeness in this discussion, we insert the solution (43) into Eqs (24) and (28), and we obtain

$$\epsilon(x, t) = \frac{1}{2(1 - \kappa_M)} [H(t - |x|) - \sqrt{\kappa_M} H(t - \sqrt{\kappa_M} |x|)], \quad (44)$$

$$\sigma_H(x, t) = \frac{1}{2(1 - \kappa_M)} [(\kappa_M + \kappa_S - 1)H(t - |x|) - \kappa_S \sqrt{\kappa_M} H(t - \sqrt{\kappa_M} |x|)]. \quad (45)$$

The volumetric strain and the hydrostatic stress were not found in the first problem [12]. We present the hydrostatic stresses induced by the nonzero concentration-velocity at the beginning (45) in Fig. 5 at different values of the time. The four discontinuity points at  $x = \pm t, \pm \frac{t}{\sqrt{\kappa_M}}$  are obvious. The two points  $x = \pm t$  come from the wave motion, while the others  $x = \pm \frac{t}{\sqrt{\kappa_M}}$  come from the mechanical wave, refer to Eqs. (43)-(45). We note the same velocities and discontinuity points in the hydrostatic stress resulting from the finite-speed diffusion in the short-time limit, refer to Fig. 2(a).

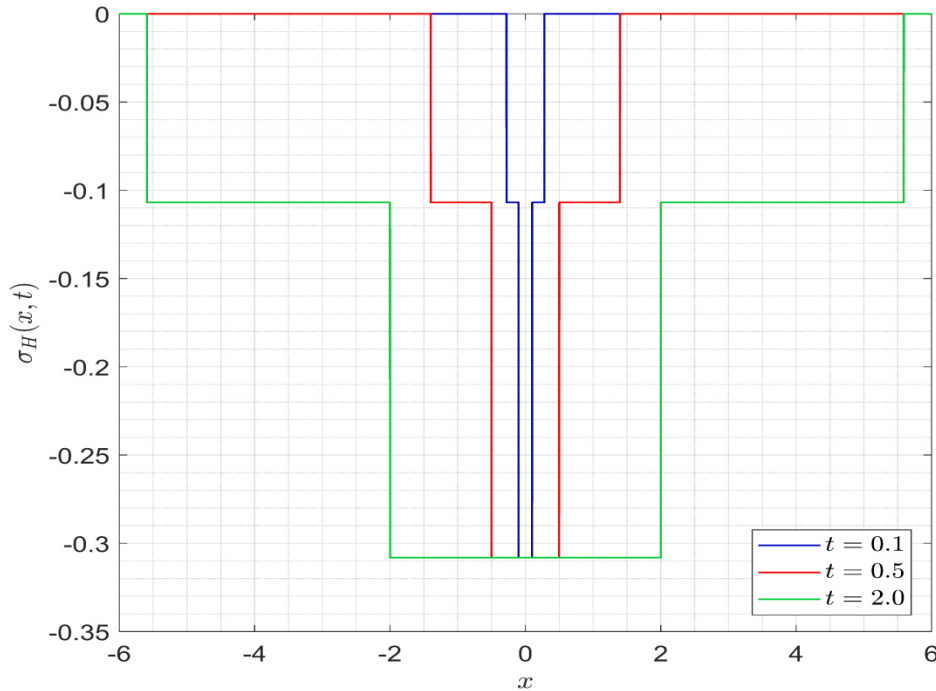


**Fig. 5.** Hydrostatic stress induced by an initial nonzero concentration velocity at different values of time

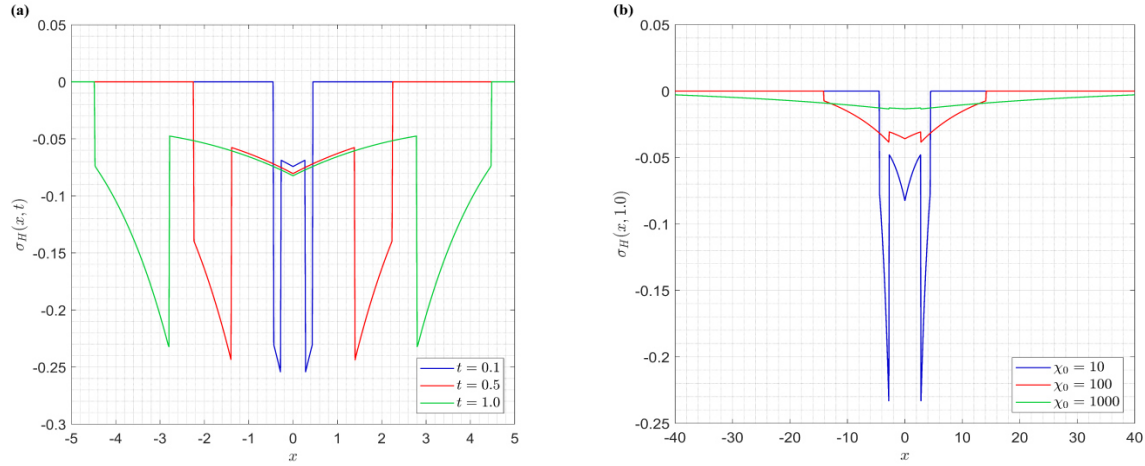


**Fig. 6.** Hydrostatic stress distribution for hyperbolic DPL diffusion model: (a) for different values of time, where  $\chi_0 = 10$ , (b) for different values of  $\chi_0$ , where  $t = 1.0$

Figure 6(a) illustrates the distributions of hydrostatic stress governed by the hyperbolic DPL diffusion model at  $\chi_0 = 10$ , for short times. It is found that for any fixed short time, the mechanical, and diffusive waves are travelling with finite speeds, namely  $\left(\frac{1}{\sqrt{\kappa_M}}, \sqrt{2\chi_0}\right)$ , respectively. i.e., the hydrostatic stress has four discontinuity points at the locations  $x = \pm\sqrt{2\chi_0}t, \pm\frac{t}{\sqrt{\kappa_M}}$ . Also, for the fixed value of  $\chi_0$ , we note that the magnitude of mechanical wavefronts is the same at different values of time (independent of time or position), but the magnitude of diffusive wavefronts decreases as time passes (exponentially decreasing with  $x$ ). Figure 6(b) shows the distributions of hydrostatic stress governed by the hyperbolic DPL diffusion model for different values of  $\chi_0 > 1$ , at instant  $t = 1.0$ . We can observe that as  $\chi_0$  increases, the hydrostatic stress records lower peaks, while the diffusive wave goes further into the medium because its speed increases,  $v_{DPL} = \sqrt{2\chi_0}$ . As far as there is a significant delay between the concentration gradient and the particle flux such that  $\tau_c \gg \tau_j$  or  $\chi_0 \gg 1$ , then the diffusive wave speed becomes greater than the mechanical wave speed, i.e.,  $v_{DPL} \gg v_{Mech}$ , which makes the diffusion process is dominant, particularly in the short-time domain. This statement is valid only for the diffusion of lithium ions in silicon medium since the coefficient  $\kappa_M$  will be different for other diffusion circumstances, and thus the mechanical wave speed will differ,  $v_{Mech} = 1/\sqrt{\kappa_M}$ . On the contrary, the case of Cattaneo diffusion equation is characterized by the relation  $v_{Cattaneo} < v_{Mech}$ , where  $v_{Cattaneo} = 1$  and  $v_{Mech} = 1/\sqrt{\kappa_M}$ , which leads to the dominance of mechanical waves in the short-time domain.

Figure 7(a) illustrates the distributions of hydrostatic stress associated with the modified hyperbolic DPL diffusion model at  $\chi_0 = 10$  and  $\chi_1 = 0.246$  as time elapses. In this case, the mechanical and the diffusive waves are travelling with finite speeds  $\left(\frac{1}{\sqrt{\kappa_M}}, \frac{\sqrt{\chi_0}}{\chi_1}\right)$ , respectively, with finite sharp jumps at the wavefronts  $x = \pm\frac{\sqrt{\chi_0}}{\chi_1}t, \pm\frac{t}{\sqrt{\kappa_M}}$ , as shown in Fig. 7(a) at  $t = 0.1, 0.5$  and  $1$ . Figure 7(b) clearly reveals that at any instant, for example at  $t = 1.0$ , the increasing of  $\chi_1$  at a fixed value of  $\chi_0$  leads to the magnitude of hydrostatics stress governed by modified hyperbolic DPL records the small values through interval domain  $|x| < \frac{t}{\sqrt{\kappa_M}}$ , and after crossing the mechanical wavefront, the increasing of  $0 < \chi_1 < 1$  has a converse effect

on the domain  $\frac{t}{\sqrt{\kappa_M}} < |x| < \frac{\sqrt{\chi_0}}{\chi_1} t$ . In addition, the magnitude of the mechanical and diffusive wavefronts increases as  $\chi_1$  increases.

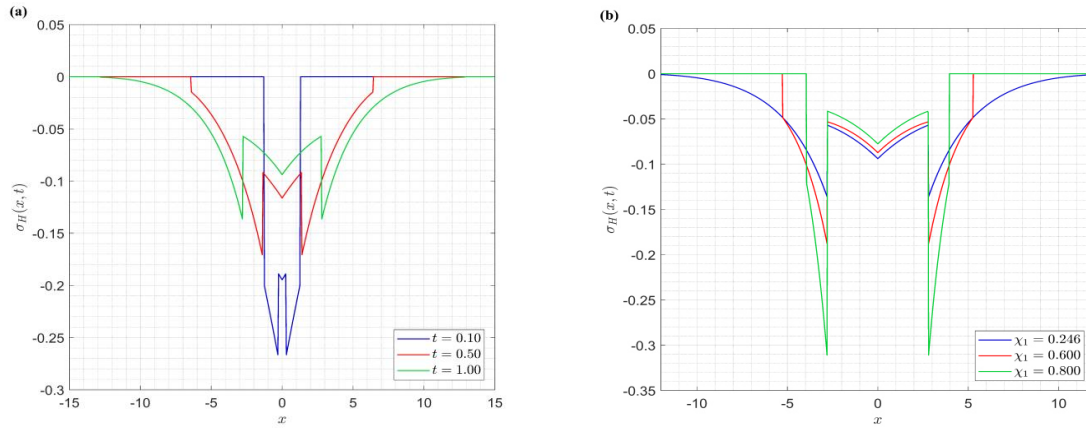


**Fig. 7.** Hydrostatic stress distribution for modified hyperbolic DPL diffusion model: (a) for different values of time,  $\chi_0 = 10.0$  and  $\chi_1 = 0.246$ ; (b) for different values of  $\chi_1$ ,  $\chi_0 = 10$  and  $t = 1.0$

We infer that the hydrostatic stress governed by the Fickian diffusion, DPL with flux-precedence  $\chi_0 \gg 1$ , hyperbolic DPL, and modified hyperbolic DPL are compressive along the whole domain. The maximum value of the compressive stress is at the location of the mechanical wavefronts. Otherwise, the hydrostatic stress is governed by the Cattaneo and the Cattaneo-like diffusion (the gradient-precedence case in which  $\chi_0 \ll 1$ ) equations is negative on the region  $|x| < t$  (compressive stress region). After crossing the point  $|x| = t$ , the hydrostatic stress values transform suddenly to be positive, i.e., tensile stress region. In addition, the maximum values of compressive and tensile stresses are at the location of the mechanical and diffusive wavefronts. In this case, fracture failure is most likely to occur [60].

## Conclusions

On a phenomenological basis, we introduced the generalized DPL equation to the uncoupled theory of elastic diffusion to compare the different responses of the material to these varieties of non-Fickian diffusion processes. We paid great attention to the hydrostatic stresses (chemical) inherent within the material. We found that the stresses record higher values in the normal and Fickian diffusion processes compared with the considered non-Fickian situations. Many investigations employed Fick's law for modeling the diffusion of solute atoms within a solid, e.g., the diffusion of lithium ions within the silicon. The stresses resulting from such investigations contain both the effect of diffusion on stress and the effect of stress on diffusion. We derived our motivation from the fundamental hypothesis of a recent investigation that studied the effect of delayed constitutive law on the diffusion of lithium ions, see [47], without discussing the stresses. Here, we discussed the stresses due to finite-speed diffusion, refer to Fig. 2, in addition to investigating the effect of other non-Fickian diffusion models on diffusion-induced stresses. We compared among the different velocities of the hyperbolic diffusion models and the mechanical wave velocities. The speed of diffusive waves governed by Cattaneo equation has apparently a velocity less than the mechanical wave speed in the case of diffusion of lithium ions within the silicon medium. Then, the mechanical waves dominate the short-time domain. On the contrary, the hyperbolic DPL diffusion models own speeds greater than the mechanical wave speed, thus, the diffusion process dominates the short-time domain.



## References

1. Nabarro F. Report of a Conference on the Strength of Solids. In: *The Physical Society*. London; 1948. p.590.
2. Herring C. Diffusional viscosity of a polycrystalline solid. *J. Appl. Phys.* 1950;21(5): 437-45.
3. Prussin S. Generation and distribution of dislocations by solute diffusion. *J. Appl. Phys.* 1961;32(10): 1876-1881.
4. Chen-Min Li J. *Physical chemistry of some microstructural phenomena*. Springer; 1978.
5. Abbaschian R, Reed-Hill RE. *Physical Metallurgy Principles-SI Version: Cengage Learning*. 2009.
6. Yang F. Interaction between diffusion and chemical stresses. *Materials Science and Engineering: A*. 2005;409(1-2): 153-159.
7. Yang F. Effect of local solid reaction on diffusion-induced stress. *J. Appl. Phys.* 2010;107(10): 103516.
8. Yang F. Insertion-induced expansion of a thin film on a rigid substrate. *Journal of Power Sources*. 2013;241: 146-149.
9. Suo Y, Yang F. Transient analysis of diffusion-induced stress: effect of solid reaction. *Acta Mechanica*. 2019;230(3): 993-1002.
10. Chiang D, Ouyang H, Yang F, Lee S. An alternative method of solvent-induced stresses in an elastic thin slab: Moutier theorem. *Polymer Engineering & Science*. 2022;62(4): 1178-1186.
11. Wang X, Liu X, Yang Q. Transient analysis of diffusion-induced stress for hollow cylindrical electrode considering the end bending effect. *Acta Mechanica*. 2021;232(9): 3591-3609.
12. Povstenko Y. Stresses exerted by a source of diffusion in a case of a non-parabolic diffusion equation. *International Journal of Engineering Science*. 2005;43(11-12): 977-991.
13. Povstenko Y. *Fractional Thermoelasticity*. Springer; 2015.
14. Kubečka J, Uhlík F, Košovan P. Mean squared displacement from fluorescence correlation spectroscopy. *Soft Matter*. 2016;12(16): 3760-3769.
15. Bolintineanu DS, Grest GS, Lechman JB, Silbert LE. Diffusion in jammed particle packs. *Phys Rev Lett*. 2015;115(8): 088002.
16. Metzler R, Klafter J. The random walk's guide to anomalous diffusion: A fractional dynamics approach. *Physics Reports*. 2000;339(1): 1-77.
17. Tzou DY. *Macro-to microscale heat transfer: The lagging behavior*. 2nd ed. John Wiley & Sons; 2014.
18. Cattaneo C. A form of heat conduction equation which eliminates the paradox of instantaneous propagation. *Compte Rendus*. 1958;247(4): 431-433.
19. Compte A, Metzler R. The generalized Cattaneo equation for the description of anomalous transport processes. *Journal of Physics A: Mathematical and General*. 1997;30(21): 7277.
20. Masoliver J, Weiss GH. Finite-velocity diffusion. *European Journal of Physics*. 1996;17(4): 190.
21. Awad E. On the time-fractional Cattaneo equation of distributed order. *Physica A: Statistical Mechanics and its Applications*. 2019;518: 210-233.
22. Awad E, Metzler R. Crossover dynamics from superdiffusion to subdiffusion: Models and solutions. *Fractional Calculus and Applied Analysis*. 2020;23(1): 55-102.
23. Rukolaine SA, Samsonov AM. (Eds.) A model of diffusion, based on the equation of the Jeffreys type. In: *Proceedings of the International Conference Days on Diffraction 2013*. IEEE; 2013.

24. Rukolaine SA, Samsonov AM. Local immobilization of particles in mass transfer described by a Jeffreys-type equation. *Physical Review E*. 2013;88(6): 062116.
25. Awad E. Dual-Phase-Lag in the balance: Sufficiency bounds for the class of Jeffreys' equations to furnish physical solutions. *Int. J. Heat Mass Trans.* 2020;158: 119742.
26. Awad E, Sandev T, Metzler R, Chechkin A. From continuous-time random walks to the fractional Jeffreys equation: Solution and applications. *Int. J. Heat Mass Transf.* 2021;181C: 121839.
27. Sprague BL, Pego RL, Stavreva DA, McNally JG. Analysis of binding reactions by fluorescence recovery after photobleaching. *Biophysical Journal*. 2004;86(6): 3473-3495.
28. Beaudouin J, Mora-Bermúdez F, Klee T, Daigle N, Ellenberg J. Dissecting the contribution of diffusion and interactions to the mobility of nuclear proteins. *Biophysical Journal*. 2006;90(6): 1878-1894.
29. Anisimov SI, Kapeliovich BL, Perel'man TL. Electron emission from metal surfaces exposed to ultra-short laser pulses. *Sov Phys JETP*. 1974;39(2): 375-377.
30. Qiu TQ, Tien CL. Short-pulse laser heating on metals. *International Journal of Heat and Mass Transfer*. 1992;35(3): 719-726.
31. Rukolaine SA. Unphysical effects of the dual-phase-lag model of heat conduction. *International Journal of Heat Mass Transfer*. 2014;78: 58-63.
32. Rukolaine SA. Unphysical effects of the dual-phase-lag model of heat conduction: higher-order approximations. *International Journal of Thermal Sciences*. 2017;113: 83-88.
33. Awad E. On the generalized thermal lagging behavior: Refined aspects. *Journal of Thermal Stresses*. 2012;35(4): 293-325.
34. Quintanilla R, Rajagopal KR. On burgers fluids. *Mathematical Methods in the Applied Sciences*. 2006;29(18): 2133-2147.
35. Quintanilla R, Racke R. A note on stability in dual-phase-lag heat conduction. *International Journal of Heat and Mass Transfer*. 2006;49(7-8): 1209-1213.
36. Quintanilla R, Racke R. Qualitative aspects in dual-phase-lag heat conduction. *Proceedings of the Royal Society A: Mathematical, Physical and Engineering Sciences*. 2007;463(2079): 659-674.
37. Awad E, Sandev T, Metzler R, Chechkin A. Closed-form multi-dimensional solutions and asymptotic behaviors for subdiffusive processes with crossovers: I. Retarding case. *Chaos, Solitons & Fractals*. 2021;152C: 111357.
38. Awad E, Metzler R. Closed-form multi-dimensional solutions and asymptotic behaviours for subdiffusive processes with crossovers: II. Accelerating case. *Journal of Physics A: Mathematical and General*. 2022;55(20): 205003.
39. Hayamizu K, Aihara Y, Price WS. Correlating the NMR self-diffusion and relaxation measurements with ionic conductivity in polymer electrolytes composed of cross-linked poly (ethylene oxide-propylene oxide) doped with  $\text{LiN}(\text{SO}_2\text{CF}_3)_2$ . *The Journal of Chemical Physics*. 2000;113(11): 4785-4793.
40. Lee SW, McDowell MT, Choi JW, Cui Y. Anomalous shape changes of silicon nanopillars by electrochemical lithiation. *Nano Letters*. 2011;11(7): 3034-3039.
41. Pharr M, Zhao K, Wang X, Suo Z, Vlassak JJ. Kinetics of initial lithiation of crystalline silicon electrodes of lithium-ion batteries. *Nano Letters*. 2012;12(9): 5039-5047.
42. Wang H, Ji X, Chen C, Xu K, Miao L. Lithium diffusion in silicon and induced structure disorder: A molecular dynamics study. *AIP Advances*. 2013;3(11): 112102.
43. Erol S, Orazem ME. The influence of anomalous diffusion on the impedance response of  $\text{LiCoO}_2/\text{C}$  batteries. *Journal of Power Sources*. 2015;293: 57-64.
44. Sibatov RT, Svetukhin VV, Kitsyuk EP, Pavlov AA. Fractional differential generalization of the single particle model of a lithium-ion cell. *Electronics*. 2019;8(6): 650.

45. Bisquert J, Compte A. Theory of the electrochemical impedance of anomalous diffusion. *Journal of Electroanalytical Chemistry*. 2001;499(1): 112-120.
46. Uchaikin VVe, Sibatov R. *Fractional kinetics in solids: anomalous charge transport in semiconductors, dielectrics, and nanosystems*. World Scientific; 2013.
47. Maiza M, Mammeri Y, Nguyen DA, Legrand N, Desprez P, Franco A. Evaluating the impact of transport inertia on the electrochemical response of lithium ion battery single particle models. *Journal of Power Sources*. 2019;423: 263-270.
48. Bardeen J. Diffusion in binary alloys. *Phys Rev*. 1949;76(9): 1403.
49. Erdelyi A, Magnus W, Oberhettinger F, Tricomi FG. *Tables of integral transforms: Based in part on notes left by Harry Bateman and compiled by the staff of the Bateman manuscript project*. New York: McGraw-Hill Book Company; 1954.
50. Sherief HH, Dhaliwal RS. Generalized one-dimensional thermal-shock problem for small times. *Journal of Thermal Stresses*. 1981;4(3-4): 407-20.
51. Sherief HH, Hamza F, Abd El-Latief A. 2D problem for a half-space in the generalized theory of thermo-viscoelasticity. *Mechanics of Time-Dependent Materials*. 2015;19(4): 557-568.
52. Awad E, El Dhaba AR, Fayik M. A unified model for the dynamical flexoelectric effect in isotropic dielectric materials. *European Journal of Mechanics-A/Solids*. 2022;95: 104618.
53. Ezzat MA, Awad ES. Constitutive relations, uniqueness of solution, and thermal shock application in the linear theory of micropolar generalized thermoelasticity involving two temperatures. *Journal of Thermal Stresses*. 2010;33(3): 226-50.
54. Ezzat MA, Awad ES. Micropolar generalized magneto-thermoelasticity with modified Ohm's and Fourier's laws. *Journal of Mathematical Analysis and Applications*. 2009;353(1): 99-113.
55. Ezzat MA, El-Bary AA, Fayik MA. Fractional Fourier law with three-phase lag of thermoelasticity. *Mechanics of Advanced Materials and Structures*. 2013;20(8): 593-602.
56. Kalnaus S, Rhodes K, Daniel C. A study of lithium ion intercalation induced fracture of silicon particles used as anode material in Li-ion battery. *Journal of Power Sources*. 2011;196(19): 8116-24.
57. Boley BA. Discontinuities in integral-transform solutions. *Quarterly of Applied Mathematics*. 1962;19(4): 273-284.
58. Boley BA, Hetnarski RB. *Propagation of discontinuities in coupled thermoelastic problems*. 1968.
59. Schneider W, Wyss W. Fractional diffusion and wave equations. *Journal of Mathematical Physics*. 1989;30(1): 134-144.
60. Chu J, Lee S. Diffusion-induced stresses in two-phase elastic media. *International Journal of Engineering Science*. 1990;28(11): 1085-1109.

## THE AUTHORS

**Fayik M.** 

e-mail: m\_fayik@alexu.edu.eg

**El-Dhaba A.R.** 

e-mail: a.r.eldhaba@sci.dmu.edu.eg

**Awad E.** 

e-mail: emadawad78@alexu.edu.eg



## Mechanical properties and deformation curves of the 3D-printed polycarbonate

I.K. Andrianov , S.I. Feoktistov

Komsomolsk-na-Amur State University, Komsomolsk-on-Amur, Russia

✉ [ivan\\_andrianov\\_90@mail.ru](mailto:ivan_andrianov_90@mail.ru)

**Abstract.** The aim of the study was to evaluate the mechanical characteristics of polycarbonate on the example of polycarbonate samples for 3D printing, to obtain the dependence of stress intensity on strain intensity taking into account compressibility. An experimental study of the mechanical properties of polycarbonate used in 3D printing has been carried out. Polycarbonate samples were made to perform tensile tests on a 3D printer. A series of stretching experiments were carried out in the elastic stage of samples to determine the Poisson's ratio of polycarbonate. To calculate the tensile strength, the conditional yield strength, polycarbonate samples were tested for rupture. Diagrams of conditional stresses from relative deformations are constructed. Since polycarbonate for 3D printing mainly works in the elasticity stage, the study constructed diagrams of polycarbonate deformation taking into account the compressibility of the material. According to the results of the study, the average values of the tensile elastic limit, the conditional yield strength, the tensile strength and the relative deformation at rupture of samples made by the 3d- printing method of polycarbonate were obtained. Deformations curves will allow us to estimate the stress-strain state of loaded polycarbonate elements not only under simple tension, but also under conditions of complex volumetric loading, since they relate the intensity of stresses and deformations.

**Keywords:** polycarbonate, deformation curve, 3D printing, stress, strain, compressibility

**Acknowledgements.** *The reported study was funded by the Russian Fund for Fundamental Research, project “Razrabotka modeli optimizacii form shtampovochnyh osnastok metodom effektivnogo pereraspredeleniya materiala”, project number 19-38-60020\19.*

**Citation:** Andrianov IK, Feoktistov SI. Mechanical properties and deformation curves of the 3D-printed polycarbonate. *Materials Physics and Mechanics*. 2023;51(1): 108-118. DOI: 10.18149/MPM.5112023\_10.

### Introduction

The sustainable development of industry today involves the use of more economical and accurate methods of manufacturing products, one of such methods is the 3D prototyping method, which allows manufacturing parts for the aviation and automotive industries by printing on a 3D printer. The relevance of this direction lies in the possibility of switching from all-metal products to the manufacture of parts from polymers of optimized shape. However, it is important to assess the mechanical properties of polymers, in particular polycarbonate, which is actively used in 3D printing. Modern reference materials are mainly limited to the basic characteristics of the polymer, such as modulus of elasticity, yield strength, tensile strength. It is quite difficult to find stress dependence on polycarbonate deformations during loading, especially for samples obtained by 3D printing methods. Taking into account the compressibility of the material is important, since polycarbonate used for 3D

furnaces practically does not work in the field of plastic deformation, respectively, in the field of elasticity, it is necessary to determine experimentally the value of the Poisson's ratio and take into account when constructing the dependence of stress intensity on strain intensity.

According to the literature review, the issues of sustainable development of domestic industry at the present stage require solving a large number of engineering problems, which is noted in [1]. Modern production automation systems and the design of complex structures are mainly associated with the use of metals [2-4]. At the same time, the transition to the use of polymers in the production of parts is one of the vectors of sustainable development. Issues related to the study of the mechanical and thermal properties of polycarbonate for 3D furnaces were investigated in [5-10]. Structural models and chemical features of the properties of substances used in industry are investigated in [11-13]. A feature of the use of polymers in industry is the possibility of reuse. The problems of recycling of secondary raw materials were investigated in the works [14, 15].

Since many products experience prolonged loads during operation, accompanied by the appearance of fatigue defects, it is important to assess cyclic loads, fatigue failure [16-18]. Experimental studies of the creep and dynamic properties of polycarbonate are presented in [19]. In addition, the peculiarity of polymers is that in the process of cyclic deformation, self-heating phenomena may occur. The problems of temperature modeling, optimization of polymer structures in self-heating conditions are presented in [20-23]. The problems of finite element simulation related to the assessment of the stress-strain state are considered in studies [24-28]. The issues of studying the mechanics of plastics and composite materials are investigated in the works [29-31].

## Methods

The purpose of the study was to construct a diagram of polycarbonate deformation taking into account the compressibility of the material. The peculiarity of the deformation diagram is that it relates the intensity of stresses and the intensity of deformations, in contrast to the diagram for simple stretching. Therefore, the deformation diagram can be used in the study of the volumetric stress state of the elements. Taking into account the compressibility of polycarbonate will allow taking into account the influence of the elastic component of deformation when assessing the stress-strain state.

To achieve this goal, it was necessary to consider a number of subtasks, namely:

- conduct a full-scale experiment on simple stretching of samples made of polycarbonate by 3D printing until destruction;
- build a diagram of conditional stresses;
- to conduct a full-scale experiment on simple stretching in order to calculate the Poisson's ratio when loaded to the yield point;
- construct a deformation diagram for true stresses and logarithmic deformations with and without taking into account the compressibility of the material.

When constructing the polycarbonate deformation diagram, it was necessary to switch to true stresses and logarithmic deformations. This step is due to the need to take into account the change in the cross-sectional area of the sample during deformation, since the conditional stress diagram is constructed under the assumption that the cross-sectional area remains unchanged, while in the process of simple stretching, the transverse dimensions of the sample decrease. Since samples made of polymers by 3D printing methods can be used under repeated loads, it is necessary to take into account the need for summation of deformations. Since relative deformations do not have the additivity property, we will construct the diagram using logarithmic deformations that have the summation property.

To switch to true stresses, taking into account the reduction of the cross-sectional area, we use the condition:

$$\sigma_s F = \sigma F_0, \quad (1)$$

where  $\sigma_s$  – true stresses,  $F$  – current cross-sectional area,  $\sigma$  – conditional stresses,  $F_0$  – initial cross-sectional area of the sample.

Taking into account the incompressibility condition  $F_0 l_0 = Fl$ , the true stresses are determined through the relative longitudinal strain  $\varepsilon$  and conditional stresses according to (1):

$$\sigma_s = \sigma(1 + \varepsilon), \quad (2)$$

To determine the true stresses, taking into account the compressibility of the material, consider the change in the geometric characteristics of the sample: thickness  $a$ , width  $b$  and length  $l$ . Let the dimensions of the body change after deformation according to the ratios:

$$a = a_0(1 + \varepsilon_\perp), \quad b = b_0(1 + \varepsilon_\perp), \quad l = l_0(1 + \varepsilon), \quad (3)$$

where  $a_0$  – the initial thickness,  $b_0$  – the initial width,  $l_0$  – the initial length,  $\varepsilon_\perp$  – relative transverse strain.

The initial cross-sectional area is determined by  $F_0 = a_0 b_0$ . After deformation, the cross-sectional area will change according to (3):

$$F = ab = F_0(1 + \varepsilon_\perp)^2. \quad (4)$$

We express the cross-sectional area (4) in terms of the coefficient of transverse strain:

$$\mu' = -\frac{e_\perp}{e}, \quad (5)$$

where  $e = \ln(1 + \varepsilon)$  – logarithmic longitudinal deformation,  $e_\perp = \ln(1 + \varepsilon_\perp)$  – logarithmic transverse strain.

We express the transverse relative deformation in terms of the coefficient of transverse deformation according to (5):

$$\varepsilon_\perp = \exp(-e\mu') - 1. \quad (6)$$

Substituting (6) into (4), we obtain a change in the cross-sectional area taking into account the compressibility of the material:

$$F = F_0 \exp(-2\mu'e). \quad (7)$$

Then the true stresses according to (1), (7) are determined through the coefficient of transverse deformation:

$$\sigma_s = \sigma \exp(2\mu'e). \quad (8)$$

The coefficient of transverse deformation is determined according to [29]

$$\mu' = \frac{1}{2} - \frac{(1-2\mu)\sigma_s}{2Ee}. \quad (9)$$

Taking into account (9), the true stresses (8), taking into account the compressibility of the material, will be determined:

$$\sigma_s = \sigma \exp\left(e - \frac{1-2\mu}{E}\sigma_s\right). \quad (10)$$

Since the true stresses cannot be expressed explicitly in terms of logarithmic deformations and conditional stresses, we substitute in the right part (10) the value of the true stress obtained without taking into account compressibility:

$$\sigma_s \approx \sigma \cdot \exp(e),$$

then the true stress is determined by

$$\sigma_s = \sigma \exp\left(e - \frac{1-2\mu}{E}\sigma \cdot \exp(e)\right) \quad (11)$$

To construct a deformation diagram, imagine the intensity of logarithmic deformations [32]:

$$e_i = \frac{\sqrt{2}}{3} \sqrt{(e_1 - e_2)^2 + (e_2 - e_3)^2 + (e_3 - e_1)^2} \quad (12)$$

where  $e_1, e_2, e_3$  – main logarithmic strains:

$$e_1 = e, \quad e_2 = e_3 = -\mu'e. \quad (13)$$

Substitute the relations (9), (13) in (12), then the intensity of deformations is expressed in terms of longitudinal deformation by the ratio:

$$e_i = e - \frac{(1 - 2\mu)}{3E} \sigma_s,$$

because  $\sigma_s = \sigma_i$  – the intensity of the stresses, we get

$$e_i = e - \frac{(1-2\mu)}{3E} \sigma_i. \quad (14)$$

In the elasticity stage, the dependence of the intensity of deformations on the intensity of stresses will take the form:

$$e_i = \frac{2(1+\mu)}{3E} \sigma_i, \quad e_i \leq e_{iT} \quad (15)$$

In the case of an incompressible material ( $\mu = 0.5$ ) the deformation diagram and the true stress diagram according to (15) coincide. As a result, the deformation diagram  $\sigma_i - e_i$  can be presented in parametric form according to the diagram  $\sigma_s - e$ :

$$\begin{cases} \sigma_i = \sigma_s \\ e_i = e - \frac{(1 - 2\mu)}{3E} \sigma_s \end{cases}.$$

Thus, according to the discrete data of the diagram of conditional stresses  $\sigma$  from relative deformations  $\varepsilon$ , the construction of the deformation diagram will be determined by the relations:

$$\sigma_i = \sigma \exp \left( \ln(1 + \varepsilon) - \frac{1-2\mu}{E} \sigma(1 + \varepsilon) \right), \quad (16)$$

$$e_i = \ln(1 + \varepsilon) - \frac{(1-2\mu)}{3E} \sigma \exp \left( \ln(1 + \varepsilon) - \frac{1-2\mu}{E} \sigma(1 + \varepsilon) \right). \quad (17)$$

## Results and Discussion

To conduct a simple stretching experiment, samples made by 3D printing from polycarbonate on a Designer X printer of the Picaso3D brand were used (Figure 1). The tests were carried out according to the methodology described in [33]. When printing samples, the Fused Filament Fabrication technology was used.



**Fig. 1.** Simple stretching of a sample made of polycarbonate by 3D printing

To calculate the Poisson's ratio, the tensile force loading was carried out within elastic deformations. The stress from the external load was 25 MPa. The initial geometric characteristics of the cross-section of the sample are presented in Table 1. Measurements of the thickness and width of the cross-section were carried out twice at 5 points along the length of the sample. The results of thickness and width measurements before the start of the tests are presented in Table 1. The length of the sample before and after the test:  $l_0 = 120 \text{ mm}$ ,  $l = 121.425 \text{ mm}$ .

**Table 1.** Geometric characteristics of the cross-section of the sample before deformation

№ point	Thickness, mm		Width, mm	
	First dimension	Second dimension	First dimension	Second dimension
1	4.258	4.258	10.429	10.422
2	4.278	4.273	10.321	10.315
3	4.321	4.315	10.227	10.227
4	4.355	4.358	10.209	10.208
5	4.403	4.401	10.22	10.215

The arithmetic mean values of the thickness  $\bar{a}$  and width  $\bar{b}$  of the sample were determined by the formulas:

$$\bar{a} = \frac{1}{10} \sum_{i=1}^{10} a_i, \quad \bar{b} = \frac{1}{10} \sum_{i=1}^{10} b_i.$$

Accordingly, the average values of thickness and width before the sample test were obtained:

$$\bar{a} = 4,32 \text{ mm}, \quad \bar{b} = 10,28 \text{ mm}$$

The average quadratic error of measuring the average thickness and width of the sample was determined by the formulas:

$$S_{\bar{a}} = \sqrt{\sum_{i=1}^{10} \frac{(a_i - \bar{a})^2}{90}}, \quad S_{\bar{b}} = \sqrt{\sum_{i=1}^{10} \frac{(b_i - \bar{b})^2}{90}}$$

$$S_{\bar{a}} = 0,018, \quad S_{\bar{b}} = 0,028$$

For the confidence probability  $\alpha = 0,98$ , the Student's coefficient was assumed to be equal to  $t_{\alpha} = 3,7$ . As a result, the average values of the cross-section of the sample with a confidence interval were assumed to be equal:  $a = 4,32 \pm 0,065 \text{ mm}$ ,  $b = 10,28 \pm 0,102 \text{ mm}$ .

The relative measurement errors are equal to:  $\delta_{\bar{a}} = 1,5\%$ ,  $\delta_{\bar{b}} = 1\%$ .

The results of measurements of the thickness and width of the sample after stretching are presented in Table 2.

**Table 2.** Geometric characteristics of the cross-section of the sample after deformation

№ point	Thickness, mm		Width, mm	
	First dimension	Second dimension	First dimension	Second dimension
1	4.249	4.240	10.360	10.352
2	4.251	4.259	10.264	10.239
3	4.289	4.295	10.161	10.169
4	4.329	4.330	10.171	10.165
5	4.382	4.369	10.177	10.173

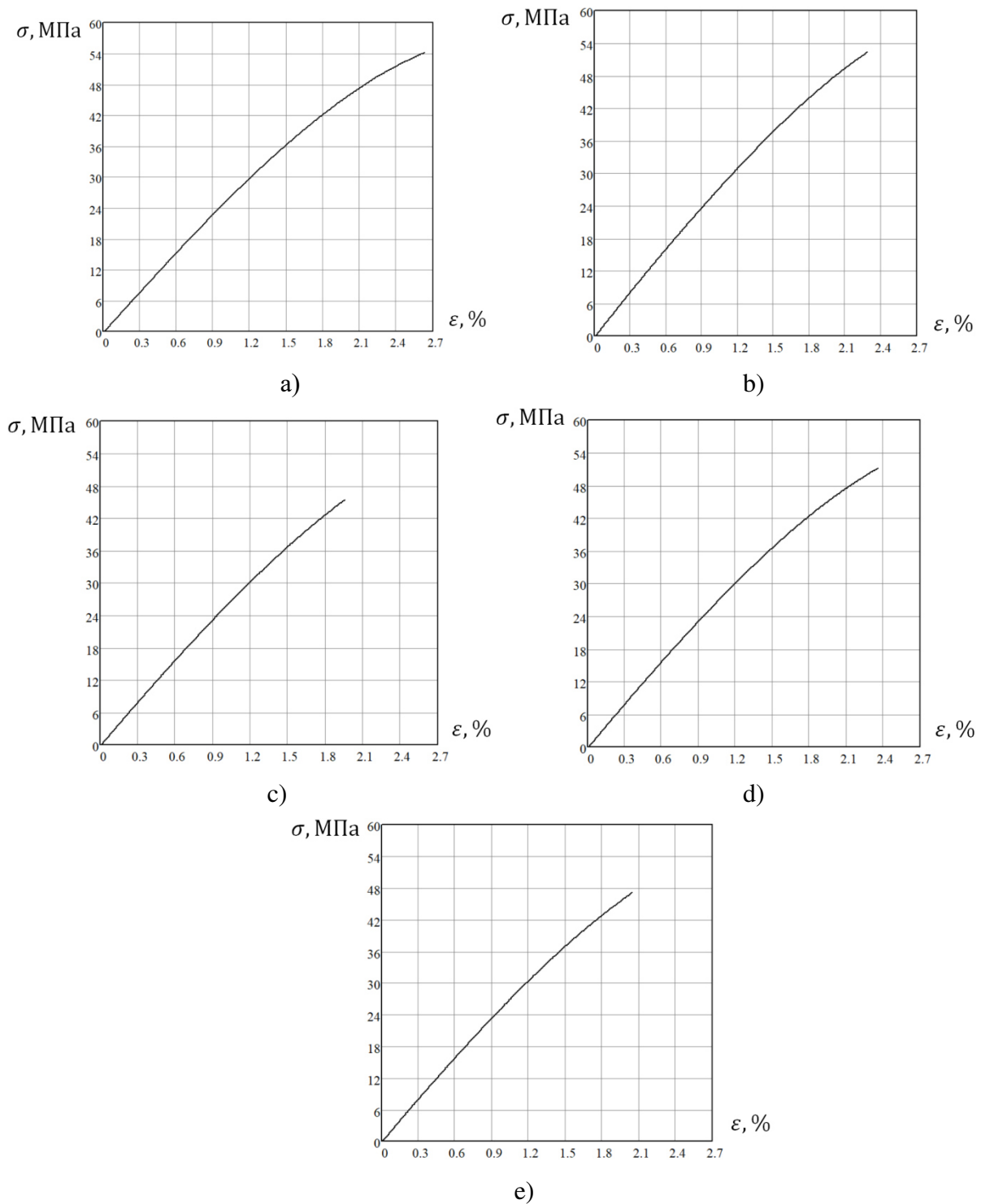


**Fig. 2.** Diagram of the dependence of the conditional stresses on the relative strains of polycarbonate: a) sample 1, b) sample 2, c) sample 3, d) sample 4, e) sample 5

The average quadratic error of measuring the average thickness and width of the sample after deformation:

$$S_{\bar{a}} = 0.01, \quad S_{\bar{b}} = 0.025$$

The average values of the thickness and width of the sample after deformation with a given confidence interval:

$$a = 4.30 \pm 0.06 \text{ mm}, \quad b = 10.22 \pm 0.09 \text{ mm},$$

The relative measurement errors are equal to:

$$\delta_{\bar{a}} = 1.4\%, \quad \delta_{\bar{b}} = 0.8\%$$

Poisson's ratio according to (5) when changing the thickness and width of the sample in the experiment for simple stretching:

$$\mu_a = 0.41, \quad \mu_b = 0.46 \quad (18)$$

According to the calculated values (18), the average value of the Poisson's ratio of polycarbonate under simple tension is determined:

$$\mu = 0.44 \quad (19)$$

Based on the results of the simple stretching experiment, a diagram of the dependence of conditional stresses on relative deformations was taken for 5 different samples (Figure 2).

Table 3 shows the values of the mechanical characteristics of 5 samples: tensile modulus of elasticity, conditional yield strength, tensile strength, relative deformation at the moment of rupture.

**Table 3.** Mechanical properties of polycarbonate based on the results of a simple stretching experiment.

Modulus of elasticity, MPa	Conditional yield strength, MPa	Tensile strength, MPa	Relative strain at the break, %
2602	42.24	54.17	2.64
2756	43.45	52.28	2.28
2679	41.96	45.40	1.96
2687	40.98	51.17	2.36
2719	41.23	47.11	2.05

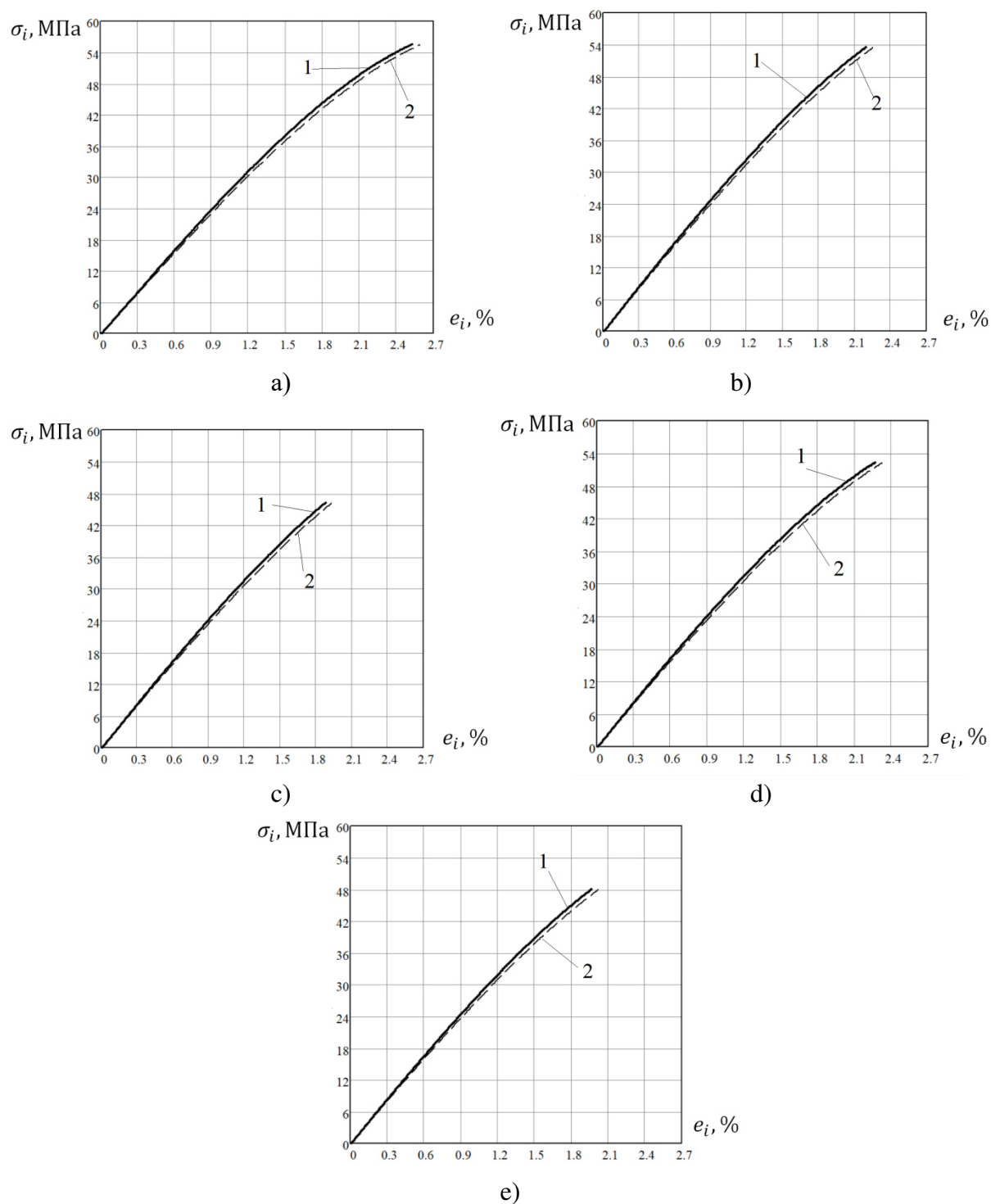
The deformation diagram (Figure 3), taking into account and without taking into account the compressibility of the material, was constructed according to the ratios (20), (21), (25) according to the diagrams of conditional stresses (Figure 2).

Thus, according to the results of the conducted experiments on rupture and stretching in the field of elasticity, the average values of the main mechanical characteristics of polycarbonate used for 3D printing were determined: the elastic modulus at tension, the conditional yield strength, the tensile strength, the relative deformation at the moment of rupture, the Poisson's ratio (table 4).

**Table 4.** Mechanical properties of polycarbonate based on the results of a simple stretching experiment.

Mechanical characteristics of polycarbonate for 3D printing	Average values
Tensile modulus of elasticity	2689 MPa
Conditional yield strength	41.97 MPa
Tensile strength	50.03 MPa
Relative strain at break	2.26 %
Poisson's Ratio	0.44

Deformation diagrams were obtained for 5 samples made by 3D printing from polycarbonate with and without compressibility. Comparing the results in Figures 1 and 2, it should be noted that the maximum error when using a conditional stress diagram instead of a deformation diagram is 5 %; failure to take into account the compressibility of the material during deformation leads to an error of 2 %.



1 – taking into account the compressibility of the material, 2 – without taking into account the compressibility of the material

**Fig 3.** Polycarbonate deformation diagram: a) sample 1, b) sample 2, c) sample 3, d) sample 4, e) sample 5



## Conclusion

The results of the study make it possible to increase the efficiency of industrial production, since the obtained deformation diagrams can be used to assess the stress-strain state of manufactured parts for aviation and automotive purposes by 3D prototyping methods made of polycarbonate. This approach creates the necessary prerequisites for the sustainable development of industry, since the use of polymers instead of metals in the manufacture of parts will allow for more accurate production except for the costs of finishing work.

## References

1. Shakirova OG, Bashkov OV, Khusainov AA. Future challenges on the way to industrial development of equipment and technologies in the digital economy and industry 4.0 (conclusion). In: *Current Problems and Ways of Industry Development: Equipment and Technologies. Lecture Notes in Networks and Systems*. Cham; Springer; 2021. p.1063–1064.
2. Kosmynin AV, Schetinin VS, Khvostikov AS, Smirnov AV. Design of high-speed rotor systems with gas-magnetic bearings. In: Shakirova OG, Bashkov OV, Khusainov AA. (eds) *Current Problems and Ways of Industry Development: Equipment and Technologies. Lecture Notes in Networks and Systems*. Cham: Springer; 2021. p.597-604.
3. Mokritskii BJ, Shelkovnikov VY. Turning and milling conceptual issues. In: Shakirova OG, Bashkov OV, Khusainov AA. (eds) *Current Problems and Ways of Industry Development: Equipment and Technologies. Lecture Notes in Networks and Systems*. Cham; Springer; 2021. p.538-547.
4. Sukhorukov S, Mokritskiy B, Morozova A. Development of a Security Subsystem of a Robotic Laser Welding Complex. In: Radionov AA, Gasiyarov VR. (eds) *Advances in Automation II. RusAutoCon 2020. Lecture Notes in Electrical Engineering*. Cham; Springer; 2021. p.642–652.
5. Pramod T, Jaiprakash N, Sampathkumaran P. Influence of Betel Nut Concentration in the Matrix of Polycarbonate and ABS on the Mechanical Characteristics. In: Vinyas M, Loja A, Reddy K. (eds) *Advances in Structures, Systems and Materials. Lecture Notes on Multidisciplinary Industrial Engineering*. Singapore: Springer; 2019. p.267-275.
6. Sabet M, Mohammadian E. The inclusion of graphene nanoplatelet on the mechanical, thermal, and electrical characteristics of polycarbonate. *Polymer Bulletin*. 2022;15: 1-17.
7. Wu C, Chen C, Chen P. Characteristics of Polycarbonate Soft Segment-Based Thermoplastic Polyurethane. *Applied Sciences*. 2021;11: 5359.
8. Liu Y, Lu X. Chemical recycling to monomers: Industrial Bisphenol-A-Polycarbonates to novel aliphatic polycarbonate materials. *Journal of Polymer Science*. 2022;60(24): 3256-3268.
9. Yongsheng E, Yang F. Study on Synthesizing Polycarbonate with Triphosgene. *Journal of Physics: Conference Series*. 2022;2194: 012033.
10. Bahar A, Belhabib S. Mechanical and Thermal Properties of 3D Printed Polycarbonate. *Energies*. 2022;15(10): 3686.
11. Shakirova OG, Naumov DY, Lavrenova LG, Petkevich SK, Potkin VI. Structural identification of the new binuclear Cu(II) complex with unexpected nitration of a ligand. *Inorganic Chemistry Communications*. 2021;133: 108957.
12. Shakirova OG. Thermally induced spin crossover in iron (ii, iii) complexes with tripodal ligands. In: Shakirova OG, Bashkov OV, Khusainov AA. (eds) *Current Problems and Ways of Industry Development: Equipment and Technologies. Lecture Notes in Networks and Systems*. Cham: Springer; 2021. p.319-330.
13. Shabalin YA, Sarilov MY, Shakirova OG. Demercaptanization of straight-run kerosene fraction according to “demerus jet” technology. In: Shakirova OG, Bashkov OV, Khusainov

- AA. (eds.) *Current Problems and Ways of Industry Development: Equipment and Technologies. Lecture Notes in Networks and Systems*. Cham: Springer; 2021. p.310-318.
14. Kolesnikov AS, Zhakipbaev B, Zhanikulov NN, Kolesnikova OG, Akhmetova YK, Kuraev RM, Shal AL. Review of technogenic waste and methods of its processing for the purpose of complex utilization of tailings from the enrichment of non-ferrous metal ores as a component of the raw material mixture in the production of cement clinker. *Rasayan Journal of Chemistry*. 2021;14(2): 997-1005.
15. Kolesnikov AS, Serikbaev BE, Zolkin AL, Kenzhibaeva GS, Isaev GI, Botabaev NE, Shapalov SK, Kolesnikova OG, Iztleuov GM. Processing of Non-Ferrous Metallurgy Waste Slag for its Complex Recovery as a Secondary Mineral Raw Material. *Refractories and Industrial Ceramics*. 2021;62(4): 375-380.
16. Andrianov IK. Modeling of Forming Die Under Cyclic Loading Conditions. In: *2020 International Multi-Conference on Industrial Engineering and Modern Technologies*. IEEE; 2020. p.20212072.
17. Andrianov IK. Finite Element Calculation of the Polymer Stamp Material Redistribution Under Restrictions on Fatigue Life. *Materials Science Forum*. 2022;1049: 248–254.
18. Andrianov IK, Grinkrug MS, Vakuluk AA. Numerical calculation of the heat sink parameters of the shell turbine vanes at the modeling of the heat-protective coating with a different number of layers. In: Shakirova OG, Bashkov OV, Khusainov AA. (eds) *Current Problems and Ways of Industry Development: Equipment and Technologies. Lecture Notes in Networks and Systems*. Cham; Springer: 2021. p.37-46.
19. Mu Q. Experimental data for creep and dynamic mechanical properties of polycarbonate and polycarbonate. *Data in Brief*. 2022;42: 108264.
20. Andrianov IK. Rod-Based Model for Optimization of a Polymer Die with Self-Heating in Cyclic Loading. *Russian Engineering Research*. 2021;41: 403-406.
21. Andrianov IK. Optimization Model of Thermal Loading of Multilayer Shells Based on the Strength Criterion. In: *2019 International Multi-Conference on Industrial Engineering and Modern Technologies*. IEEE; 2019. p.19229158.
22. Tupitsin M, Trishkina I, Sycheva S, Storozheva E, Novikov R. Study of the influence of structural heritage and operating conditions on the durability of safety valve springs from steel 50KHFA. *Materials Physics and Mechanics*. 2022;48(2): 161-174.
23. Kolesnikov AS, Sergeeva IV, Botabaev NE, Al'Zhanova AZ, Ashirbaev KA. Thermodynamic simulation of chemical and phase transformations in the system of oxidized manganese ore – carbon. *Izvestiya Ferrous Metallurgy*. 2017;60(9): 759–765.
24. Mokritskii B, Morozova A, Sitamov EJ. Simulation Modeling of the Choice of Metal Cutting Tool Coating. In: Radionov AA, Gasiyarov VR. (eds) *Proceedings of the 6th International Conference on Industrial Engineering (ICIE 2020). ICIE 2021. Lecture Notes in Mechanical Engineering*. Cham; Springer: 2021. p.156-162.
25. Andrianov IK. Topological optimization of a complex shape forming stamp. *Journal of Physics: Conference Series*. 2021;2096: 012115.
26. Andrianov IK. Modification of the stamp topological optimization taking into account cyclic fatigue based on the finite element approach. *International Journal of Mechanics*. 2021;15: 145–150.
27. Andrianov IK, Stankevich A. The stress-strain state simulation of the aircraft fuselage stretch forming in the ANSYS. *Journal of Physics: Conference Series*. 2019;1333: 082002.
28. Mokritskii BY, Shakirova OG, Sosnin AA, Sitamov ES, Erukov AI. Estimation of the Results of Predictive Simulation of a Rational Cutting Material. *Russian Metallurgy*. 2020;13: 1613–1618.
29. Pogrebnoi AV. Study of polylactide 3D-printed samples with double-layer weave. *Materials Physics and Mechanics*. 2022;48(2): 289-299.

30. Mzad H. Experimental investigation of the mechanical behavior of honeycomb sandwich composite under three-point bending fatigue. *Materials Physics and Mechanics*. 2022;48(2): 217-231.
31. Belaziz A, Mazari M, Bouamama M, Zahaf S, Mouloud D. Experimental study of ductile and fragile pipe cracked in High-Density Polyethylene (HDPE). *Materials Physics and Mechanics*. 2022;48(2): 199-207.
32. Malinin, N.N. *Applied theory of plasticity and creep*. 1975. (In-Russian)
33. International Organization for Standardization. ISO 527-2:2012. *Plastics - Determination of tensile properties*. 2018.

## THE AUTHORS

**Andrianov I.K.** 

e-mail: ivan\_andrianov\_90@mail.ru

**Feoktistov S.I.**

e-mail: serg\_feo@mail.ru

## Mechanical and microstructural characteristics of underwater friction stir welded AA 6061-T6 joints using a hybrid GRA-artificial neural network approach

Kiran Wakchaure , Ajaykumar Thakur 

Sanjivani College of Engineering, Kopargaon, (SPPU Pune) Maharashtra, 423603, India

✉ [kiran.wakchaure@yahoo.com](mailto:kiran.wakchaure@yahoo.com)

**Abstract.** In this paper hybrid grey relations analysis (GRA) and an artificial neural network (ANN) are applied to study the influence of process parameters on the mechanical properties of friction stir welded aluminum alloy 6061-T6. Thirty experiments were performed by varying tool rotation speed, tool traverse speed, and tool tilt angle to study their effects on ultimate tensile strength, yield strength, percentage elongation, and impact strength of FSW joints. GRA was used to convert all responses into the single response variable, i.e., the grey relation grade (GRG). A feed-forward backpropagation ANN with two hidden layers composed of 9 and 7 neurons each was used to simulate the weld joint characteristics in terms of GRG. ANOVA analysis was used to study the influence of process parameters on grey relation grade. It was found that tool rotation speed has a significant impact on weld characteristics, followed by traverse speed and tilt angle. Based on the results it was revealed that tool rotation speed contributes 39.89% to the mechanical properties of underwater friction stir welding of AA 6061-T6, followed by tool traverse speed and tool tilt angle, respectively, by 29.87% and 19.59%. The tensile test demonstrates that the underwater FSW joint is approximately 8% stronger than the conventional air FSW joint due to grain refinement and increased nugget zone hardness because of less heat exposure and absorption.

**Keywords:** microstructure, underwater friction stir welding, artificial neural network, grey relation analysis, ANOVA

**Citation:** Wakchaure K, Thakur A. Mechanical and microstructural characteristics of underwater friction stir welded AA 6061-T6 joints using a hybrid GRA-artificial neural network approach. *Materials Physics and Mechanics*. 2023;51(1): 119-141. DOI: 10.18149/MPM.5112023\_11.

### Introduction

Friction stir welding (FSW) was developed and patented by the Welding Institute (TWI) in 1991. Earlier, it was limited to laboratory experiments to weld high-strength aluminum alloys (2xxx and 6xxx), which have limited weldability using fusion welding processes [1]. Since FSW is a solid-state welding process, it avoids defects like gas porosity, solidification cracking, residual stresses, weakening of HAZ and nugget zones, reduced corrosion resistance, etc., developed during traditional welding processes [1-2]. FSW is essentially a constrained extrusion process controlled by the non-consumable profiled tool. The tool shoulder constraints softened material, so it cannot escape easily. The material is gradually swept around the probe between the retreating side of the tool and the surrounding material as the tool traverses the joint line. Extruded material forms solid-phase joints behind the tool.

The asymmetrical joint is caused by the extrusion of the deformed material past the RS of the tool [1-3].

This process generates a significant strain and strain rate compared to other solid-state metalworking processes such as rolling, extrusion, and forging. The key parameters affecting weld quality in this welding process are tool geometry, plunging depth, rotational speed, traverse speed, and tool tilt angle [1-3]. In the AA6XXX series, 6061-T6 is a moderately strong heat-treatable alloy containing Al-Mg-Si as its primary alloying element. The  $Mg_2Si$  sediments are responsible for strengthening the AA6061 alloy. This material's high strength-to-weight ratio and corrosion resistance make it ideal for fabricating lightweight structures [5]. AA6061 possesses excellent welding characteristics but suffers a loss in strength due to the dissolution of strengthening precipitates and softening of HAZ. Friction stir welding refines the grain in the nugget zone and improves mechanical properties compared to other welding processes.

Thermal cycle and material flow behavior determine the FSW joint's microstructure evolution and mechanical properties, which are affected by process variables like rotation speed, welding speed, and tool geometry [6]. A fracture of the weld occurred along the LHZs. The tensile strength of the weld increased with increasing welding speed and was independent of tool dimension and rotation speed. Li et al. [7] reported UW-FSW of CNT/Al-Cu-Mg composites reach 94.7% efficiency when compared to FSW. The thermal cycle of underwater trials decreases, and fewer flash faults occur, which facilitates post-weld processing and increases welding productivity.

Underwater or submerged friction stir welding (UFSW/ SFSW) has become a cutting-edge welding technique that offers better mechanical properties while avoiding the welding flaws in traditional FSW [8–10]. During underwater friction stir welding, the entire welding process is carried out in the presence of water. Hofmann et al. [11] proposed using water as a cooling medium to produce ultra-fine grains in the nugget zone of friction stir processed AA6061–T6. As a result of water cooling, Wang et al. [12] found that underwater FSW of spray-formed 7075 Al alloy improves tensile properties and corrosion resistance and reduces the corrosion rate. Compared to conventional FSW, M. Hosseini et al. [13] found underwater friction stir welding to enhance the tensile strength and yield strength of ultrafine-grained AA1050. Furthermore, UFSW was proposed as a method for hardening materials on the surface. According to Rathinasuriyan et al. [14], SFSW requires more torque and power than conventional friction stir welding. Additionally, these values increase as the water head increases during submerged friction stir welding.

Bagheri et al. [15] reported numerical analyses of friction stir welding (FSW) in the air and underwater using smoothed particle hydrodynamics and finite element modelling. Underwater welding results in a lower peak temperature than traditional welding due to its higher cooling impact. In addition, peak temperature and strain rate decreased under both welding conditions as welding speed increased. Abdollahzadeh et al. [16] found that underwater FSW of 60621 T6 significantly reduced the joint temperature. This resulted in a refined microstructure in the stir zone, which improved the welded joint's mechanical properties. UFSW joints have a higher hardness than CFSW joints due to the refined grains' synergetic effect, decreased dissolution of  $\beta''$  precipitates, and fast cooling rate (intensified local deformation). SFSW of AA6061 T6 tensile strength increased with tool rotation speed and decreased with welding speed [17]. Fratini et al. [18] investigated the effects of in-process cooling within normal air, forced air, and water on the mechanical properties of friction stir welding for AA7075-T6. Results show that water is a more powerful cooling medium, improving joint tensile strength due to narrowing the weakest TMAZ and HAZ. FSW samples with water as a cooling medium show increasing microhardness values and low hardness values in the nugget zone of the water FSW sample compared with natural air and forced air

FSW samples. Sharma et al. [19] studied the effects of liquid nitrogen, regular air, and compressed air on the FSW of AA7039. During welding, cooling absorbs the excess heat, which restricts grain growth in the nugget zone and coarsens it in the HAZ. Water was also found to be the best cooling medium for maximum tensile strength and percentage elongation than compressed air and liquid nitrogen. Sinhar et al. [20] found that FSW joints with water cooling show improved yield strength, tensile strength, hardness in HAZ, and corrosion resistance due to more refined microstructure and limited precipitate restrictions as compared with conventional FSW with natural air cooling. Mahto et al. [21] reported that FSW AA6061-T6 and AISI304 form re-crystallized and deformation-textured grains in the SZ, which ultimately transform into dominant shear-and deformation-textured grains in water and air, respectively.

Abbasi et al. [22] evaluated the formability characteristics of tailor-welded blanks created by combining AA6061 aluminum alloy sheets of various thicknesses and devising friction stir vibration welding (FSVW). The results showed that FSVW-ed blanks exhibited better mechanical and formability characteristics than FSW-ed blanks. According to Abbasi et al. [23], grain size decreases from approximately 57  $\mu\text{m}$  for friction stir welding to approximately 34  $\mu\text{m}$  for friction stir vibration welding and approximately 23  $\mu\text{m}$  for underwater friction stir welding. Underwater friction stir welding and friction stir vibration welding effectively reduce precipitation size and interparticle distance. The underwater friction stir welding processed samples have the highest strength and ductility compared to friction stir welding processed samples. The cylindrical and conical tool pins used in FSW are simple in shape and easy to manufacture. Conical pin tools have better mechanical properties than cylindrical, square, and pin tools.

Multiobjective optimization is one of the elements of research in manufacturing processes. Several researchers used AHP, TOPSIS [23-25], and GRA [26-30] for the multiobjective optimization of FSW. The use of empirical non-analytical models, such as Artificial Neural Networks (ANNs), can be an effective alternative in manufacturing problems characterized by complex relationships among variables and unknown relationships among variables [22]. The usefulness of artificial neural networks has been demonstrated in metal forming, fusion welding, and machining [32]. Thapliyal et al. [33] proposed a machine-learning model to predict the ultimate tensile strength of friction stir-welded copper specimens. The result shows that ANN can predict UTS with 94% accuracy. Using five different neural networks, Manvatkar et al. [34] calculated tool and workpiece temperatures, torque, traverse force, and stresses according to the thickness of the plate, welding speed, rotating tool speed, shoulder, pin, and pin length, and the tool material for the friction stir welding. Both experimental and numerical methods were used to evaluate the performance of all ANNs. Ghetiya et al. [35] predicted the tensile strength of FSWed aluminum alloy AA8014. ANN was used to study the influence of welding parameters such as axial force, welding speed, rotational tool speed, and tool shoulder diameter on joint strength. In their study of friction stir lap welding of the Al-Mg and CuZn34 alloys, Shojaeefard et al. [36] developed an ANN model to analyze the relationship between the mechanical properties and the process parameters. Ansari et al. [37] predicted the average grain size of Magnesium ingot under friction stir extrusion processing with the effect of rotational speed, vertical speed, and extrusion hole size (HS) using a 3-6-1 artificial neural network.

Buffa et al. [38] predicted microstructure and microhardness values using ANN for the nugget zone of a Ti-6Al-4V titanium alloy FSW joint. Laubscher et al. [39] proposed a single-layer backpropagation ANN with RSM for predicting friction-welded titanium joint tensile strength based on ANN architecture 3-10-1 and sensitivity analysis. Patel et al. [40] have developed a cellular automata finite element – artificial neural network (CAFE-ANN) hybrid model to predict grain size and yield strength evolution during friction stir welding.

Maleki et al. [41] predicted tensile and hardness properties of the welding zone of FSWed AA-7075-T6 considering input parameters as the rotational and welding speed, pin diameter, shoulder diameter, axial force, and tool hardness as input parameters using ANN.

Since the submerged FSW is gaining a lot of interest nowadays, optimizing the process parameters of submerged FSW for better results would be more critical. In this research, grey relation analysis (GRA) was chosen along with an artificial neural network for the multiobjective optimization and selection of optimum process parameters. FSW is a complex welding mechanism; obtaining all the required responses for a particular set of input parameters is challenging. Hence, it is desired to use a multiobjective decision-making technique to solve this problem. Four output parameters were selected, such as yield strength, ultimate tensile strength, % elongation, and impact strength for the multiobjective optimization of underwater FSW of AA6061-T6. ANOVA analysis was carried out to determine the influence of process parameters on the mechanical properties of the welded joint.

### Methods and materials

The research was carried out on rolled plates of aluminum alloy AA 6061-T6 of 6 mm thickness. A conical tool with an 18 mm shoulder diameter and a pin with a 6 mm diameter, 14° semi-cone angle, and 5.6 mm length were considered to manufacture the tool. The chemical composition and mechanical properties of AA 6061-T6 are shown in Table 1 and Table 2, respectively. Aluminum alloy sheets were cut into sample sizes of 200(L)×75(W)×6(T)mm with an abrasive cutting machine. Edges are machined with a milling machine, and an edge of 200 mm in length, cut to a transverse direction rolling line, was considered to form a weld. Plates were washed with acetone to avoid contamination during the welding procedure. In order to manufacture the tool, a conical tool with a shoulder diameter of 18 mm and a pin diameter of 6 mm, a semi-cone angle of 14°, and a length of 5.6 mm was considered. Hot work dies steel (AISI-H13) was used as a tool material with hardening of 50-55 HRC. The main constituents of the chemical composition of H13 are C-0.4, Mn-0.4, Si-1, Mo-1.35, Cr-0.25, V-1, and Fe-balance (all elements in wt.%). A new fixture was developed to carry out welding trials, which can hold the workpiece properly and withstand the load acting on it. A special vessel-type arrangement was made with an acrylic sheet to store water in the fixture.

**Table 1.** Chemical Composition of AA6061-T6 Alloy

Elements	Mg	Si	Mn	Zn	Fe	Cu	Al
Alloying elements (in %)	1.1	0.6	0.12	0.25	0.35	0.3	Rest

**Table 2.** Mechanical properties of AA6061-T6 Alloy

Properties	UTS	YS	E	% el	$\mu$	MP	H	D
Values	303 MPa	240 MPa	68.9 GPa	20%	0.33	582–652°C	107Hv	2.7 g/cc

All the experiments were carried out on a universal milling machine (G. DUFOUR make) 624D model having a vertical spindle attachment with DRO. The machine consists of the main spindle motor of 15 HP with a spindle speed range of between 24-1180 rpm. There are also two feed motors with 5 HP power, with a feed in the range of 22-1180 mm/min. The experimental setup of underwater friction stir welding is shown in Fig. 1. The Friction Stir welding tool is mounted with a collet on the spindle of a universal milling machine. The fixture was rigidly mounted on the bed of the milling machine. Specimens to be welded were



fixed in the slot made in a fixture with clamps to avoid lateral and transverse movement of specimens during trials. Firstly, the rotating tool shoulder is allowed to touch the top surface of the specimen, and then water is allowed to pour into the fixture vessel to make a 30 mm water head. An arrangement was made to pour and drain hot water from the vessel. At a distance of 14 mm from either side of the weld line and 100 mm from the start point, K-type thermocouples were employed.

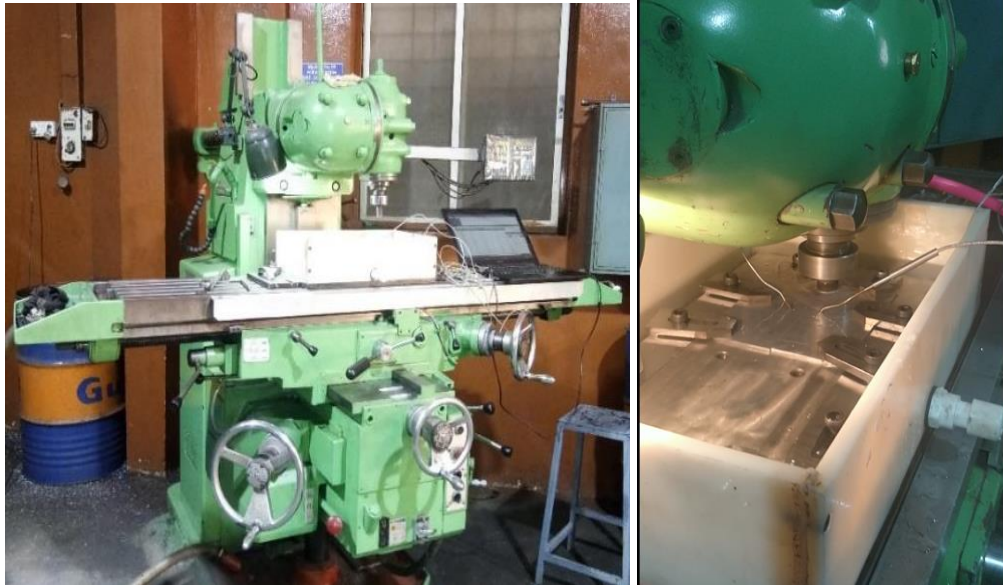


**Fig. 1.** Experimental setup

In this research, rotation speed, welding speed, and tilt angle were chosen as process parameters. Initial trials were performed to derive levels of process parameters by considering defects in the weld zone shown in Table 3.

**Table 3.** Process parameters levels

Parameter (Notation)	Unit	Level					
Tool rotation speed (TRS)	rpm	710		900		1180	
Welding speed (WS)	mm/min	22	29	49	64	83	108
Tilt Angle (TA)	° degree	1°		2°		3°	

The specimens welded with the underwater FSW procedure are shown in Fig. 2 (a) and (b) of final experimentation by considering different levels of process parameters. A total of 30 trials (shown in Table 4) were performed to analyse the effects of process parameters.

After welding trials, all welded samples were cut into the required size per the American Society for Testing of Materials (ASTM) E-8M-08 [ASTM-2008] guidelines using an abrasive water jet machine shown in Figs. 2 and 3. In this study, three samples of tensile strength, one for each impact strength, microstructure, and microhardness, were considered for the characterization. Tensile tests were performed on a 2000KN universal testing machine (UTM) (Make: Universal Motion Inc, Model: MUTCS-20 model). During tensile testing, a crosshead speed of 1 mm/min of UTM was chosen. Selected samples were considered for macro and microstructure evaluation. Optical microscopy has been carried out using a light optical microscope (Make: Conation technologies) with an image analysis system.

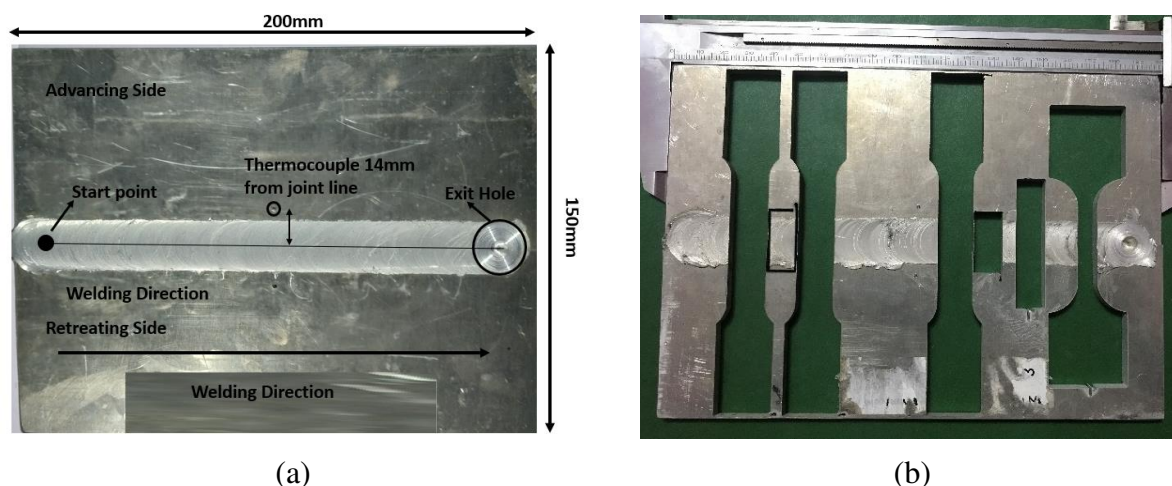


**Table 4.** Grey relation analysis

Sr. No.	Input Parameter			Output Parameters				Normalized Inputs			Normalized Responses				GR G	Rank
	TRS	TT S	TT A	UTS	% El	YS	IS	RP M	WS	TA	UT S	% El	YS	IS		
1	710	22	2	186.56	14.28	105.97	21.76	0.00	0.00	0.50	0.21	0.97	0.32	0.83	0.63	8
2	710	29	2	222.01	7.50	140.26	18.48	0.00	0.08	0.50	0.76	0.20	1.00	0.59	0.65	3
3	710	49	2	174.89	9.37	104.18	24.10	0.00	0.31	0.50	0.03	0.41	0.28	1.00	0.55	16
4	710	64	2	208.94	13.68	123.43	14.09	0.00	0.49	0.50	0.56	0.91	0.66	0.26	0.59	11
5	710	83	2	212.81	11.56	108.69	12.73	0.00	0.71	0.50	0.62	0.66	0.37	0.16	0.50	26
6	710	108	2	172.77	5.78	109.55	10.52	0.00	1.00	0.50	0.00	0.00	0.39	0.00	0.36	30
7	710	22	1	182.22	12.84	97.75	22.23	0.00	0.00	0.00	0.14	0.81	0.15	0.86	0.56	14
8	710	29	1	195.00	9.50	101.00	15.85	0.00	0.08	0.00	0.34	0.43	0.22	0.39	0.44	29
9	710	83	3	210.75	11.12	115.41	13.86	0.00	0.71	1.00	0.59	0.61	0.50	0.25	0.50	25
10	710	108	3	219.05	12.96	102.24	15.46	0.00	1.00	1.00	0.72	0.82	0.24	0.36	0.55	15
11	900	22	2	185.85	13.28	90.12	22.47	0.40	0.00	0.50	0.20	0.86	0.00	0.88	0.58	13
12	900	29	2	198.51	12.03	110.98	18.95	0.40	0.08	0.50	0.40	0.72	0.42	0.62	0.53	20
13	900	49	2	202.06	9.84	95.07	16.85	0.40	0.31	0.50	0.46	0.47	0.10	0.47	0.45	28
14	900	64	2	213.22	11.87	117.06	12.96	0.40	0.49	0.50	0.63	0.70	0.54	0.18	0.52	22
15	900	83	2	217.36	13.43	128.49	15.46	0.40	0.71	0.50	0.69	0.88	0.77	0.36	0.64	6
16	900	108	2	237.05	12.62	140.00	12.57	0.40	1.00	0.50	1.00	0.78	0.99	0.15	0.76	1
17	900	83	1	219.92	10.75	136.46	17.78	0.40	0.71	0.00	0.73	0.57	0.92	0.53	0.64	5
18	900	108	1	232.12	12.84	130.00	12.12	0.40	1.00	0.00	0.92	0.81	0.80	0.12	0.67	2
19	900	49	3	199.07	11.75	110.76	15.46	0.40	0.31	1.00	0.41	0.68	0.41	0.36	0.49	27
20	900	64	3	210.36	13.03	125.41	15.55	0.40	0.49	1.00	0.58	0.83	0.70	0.37	0.59	12
21	1180	83	2	218.28	10.62	129.06	19.89	1.00	0.71	0.50	0.71	0.56	0.78	0.69	0.62	9
22	1180	64	2	208.33	11.81	121.35	16.39	1.00	0.49	0.50	0.55	0.69	0.62	0.43	0.55	17
23	1180	49	2	204.58	10.56	115.28	17.78	1.00	0.31	0.50	0.49	0.55	0.50	0.53	0.51	24
24	1180	29	2	196.19	12.37	111.81	23.63	1.00	0.08	0.50	0.36	0.76	0.43	0.97	0.63	7
25	1180	22	2	188.12	13.43	97.89	18.25	1.00	0.00	0.50	0.24	0.88	0.16	0.75	0.53	21
26	1180	108	2	222.52	12.09	138.00	11.30	1.00	1.00	0.50	0.77	0.72	0.95	0.06	0.65	4
27	1180	49	1	207.16	12.13	106.30	16.62	1.00	0.31	0.00	0.54	0.73	0.32	0.45	0.52	23
28	1180	64	1	206.48	12.43	114.83	16.78	1.00	0.49	0.00	0.52	0.76	0.49	0.46	0.54	19
29	1180	22	3	188.93	13.00	91.23	21.06	1.00	0.00	1.00	0.25	0.83	0.02	0.78	0.54	18
30	1180	29	3	198.54	14.50	117.69	15.46	1.00	0.08	1.00	0.40	1.00	0.55	0.36	0.61	10

For metallographic investigation of welded specimens, a cross-section was taken as they were polished using various grids and etched using Tucker's reagent. Friction stir-welded specimens were polished with emery sheets of various grades. These samples were then etched for 20 seconds with Keller's reagent. EBSD and optical microscopy (OM) were used to

examine these etched specimens. EBSD is a scanning electron microscopy-based microstructural-crystallographic characterization technique used frequently to study crystalline or polycrystalline materials. All the microstructure samples were polished to different grades of emery paper followed by a diamond paste of 1  $\mu\text{m}$  particle size to evolve different zones of the welded specimen SZ, TMAZ, HAZ, and base material. Microhardness testing was carried out on the Vickers Microhardness tester of (Economet make) VH-1MD. The middle of the weld zone (transverse to weld direction) was considered a testing area with a 1mm interval using a 100g indentation load. The sub-size specimen was considered for the Charpy impact test as per ASTM E23 standards.



(a) (b)  
**Fig. 2.** Underwater friction stir welded specimen

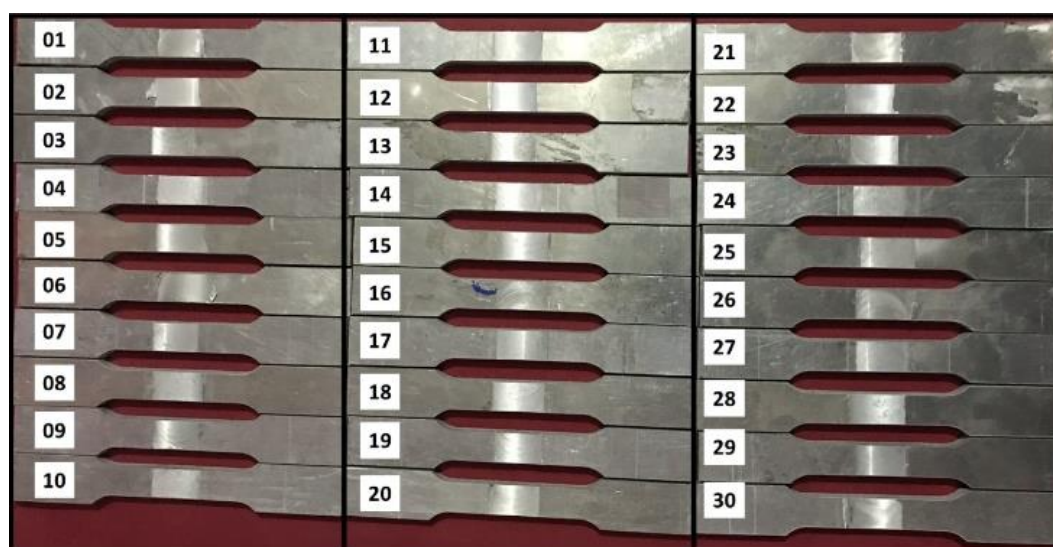


**Fig. 3.** Tensile test specimens as per E-8M-08 [ASTM-2008] guidelines

**Grey relation analysis.** Grey relation analysis is a multi-criteria decision-making technique founded by Chinese professor Julong Deng in the 1980s. GRA is an effective tool for solving inter-relationships among multiple responses and criteria. In GRA, multiple responses are converted into a single grey relation grade, which is convenient for decision-making. GRA gives the appropriate, good solution instead of the best solution for complex real-life problems. Normalization, generation of grey relation coefficient (GRC), and generation of grey relation grade (GRG) are three critical steps in GRA. In normalization, responses are normalized between values 0 to 1 according to three different performance

characteristics – the "larger the better," "smaller the better," and the "nominal the better." In this research, all the response variables, ultimate tensile strength, yield strength, impact strength, and percent elongation, should be at their maximum. Hence, all the variables were normalized with larger performance characteristics (Ref. Eq. 1). Then, the normalized data were turned into a grey relation coefficient (Ref. Eq.2) to show the relationship between the actual data and the data that was wanted. In the last step (Ref. Eq.3), an overall grey relation grade is calculated by averaging weighed grey relation coefficients.

The steps followed in the GRA are shown below:

**Step 1. Normalization** [18-20]

$$x_i^*(k) = \frac{x_i^0(k) - x_i^0(k)}{\max x_i^0(k) - x_i^0(k)}, \quad (1)$$

where  $x_i^*(k)$  is the sequence after the data preprocessing,  $x_i^0(k)$  is the reference sequence,  $x_i^0(k)$  is the smallest value in the reference sequence,  $\max x_i^0(k)$  is the largest value in the reference sequence,  $i = 1, 2, \dots, m$ ;  $k = 1, 2, \dots, n$ ;  $m$  is the number of experiments, and  $n$  is the number of experimental data.

**Step 2. Grey relation coefficient** [18-20]

$$\xi(x_0^*(k), x_i^*(k)) = \frac{\Delta_{\min}(k) + \zeta \Delta_{\max}(k)}{\Delta_{0i}(k) + \zeta \Delta_{\max}(k)}, \quad (\text{Table 5. C16-C19}) \quad (2)$$

$$\Delta_{0i}(k) = \|x_0^*(k) - x_i^*(k)\|, \quad (2.1)$$

$$\Delta_{\min}(k) = \min_{j \in i} \min_{\forall k} \|x_0^*(k) - x_j^*(k)\|,$$

$$\Delta_{\max}(k) = \max_{j \in i} \max_{\forall k} \|x_0^*(k) - x_j^*(k)\|,$$

where  $\Delta_{0i}(k)$  is the deviation sequence of the comparability sequence  $x_i^*(k)$  and reference sequence  $x_0^*(k)=1$ ,  $\zeta$  is the distinguishing coefficient, having a value between 0-1. The value of 0.5 is generally used.

**Step 3. Grey relation grade** [18-20]

$$\gamma_i(x_0^*(k), x_i^*(k)) = \frac{1}{n} \sum_{i=1}^n w_i \xi(x_0^*(k), x_i^*(k)), \quad (3)$$

where  $w_i$  is the weighting value of the  $i^{\text{th}}$  performance characteristic, and here 0.25 is the weight considered for each response variable,  $\gamma_i(x_0^*(k), x_i^*(k))$  is the GRG for an  $i^{\text{th}}$  experiment, and  $n$  is the number of performance characteristics.

First, using Eq. (1), the experimental data consisting of process parameters and responses have been normalized. Tensile strength, yield strength, elongation percentage, and impact strength were evaluated using the largest-the-better (LB) criterion. Based on Eq. (2), grey relational coefficients are calculated for each performance characteristic with weights of  $w_1 = 0.5$  and  $w_2 = 0.5$  [13]. Eq. 3 has been used to calculate the grey relational coefficients for each response. FSW quality is measured by the grey relational grade, a comprehensive measure. GRA transforms the multi-response optimization problem into a single optimization problem with equivalent objective functions. The GRG is the relationship between the reference sequence values and comparability sequence values.

Table 10 indicates the optimal factor combination with a high GRG value. A tool rotation of 900 rpm, a tilt angle of 2 degrees, and a welding speed of 108 mm/min are the optimal conditions for the FSW of aluminum alloy. Table 5 shows the network topology and training parameters of the ANN to GRG, and Table 6 shows each level's mean grey relational grade ratio according to the process parameters. Table 7 shows the absolute error values for different neural networks.

**An artificial neural network (ANN).** An artificial neural network (ANN) is a computational network inspired by biological processes. ANNs are optimization techniques that use data analysis and simulation to model the human brain or neural system. The main benefits of ANNs are that they can access more data and remove noise and insufficient data. ANNs are advantageous because of their calculation speed, ability to learn from examples and

simplicity. Due to these characteristics, ANNs can be applied to materials science. FSW responses have been modeled and predicted by several researchers using ANNs. Manvatkar et al. [36] used a feed-forward network and the backpropagation algorithm for various combinations of welding variables to generate tool durability maps to study tool strength.

Networks are multi-layered, with an input layer for parameters, an output layer for the response, and a hidden layer for processing input using a training function. Four input neurons were used to develop neural networks. In each hidden layer, 1-10 neurons were used to train the data, and one neuron predicted the mechanical properties of welded joints. Input layer nodes represent tool rotation speed, transverse tool speed, and tool tilt angle, which are used to predict response. After training several networks, the number of hidden layers and neurons in each layer was determined. In this study, back propagation neural network with three neurons for the input parameters and one neuron for the response of FSW in terms of grey relation grade.

The training functions "logsig" and "tansig" are used in the first and second hidden layers, respectively. An ANN model was trained with 70% of the readings, validated with 15%, and tested with 15%. A linear regression analysis was also performed between the ANN outputs (predictions) and the corresponding targets (experiments) to evaluate the ANN-based model response. After several trials, the model was developed with two hidden layers containing 1-10 neurons each. A network with minimum absolute relative error and maximum correlation coefficient criteria was used to select the required neural network by training and validating several neural networks. The absolute relative error was calculated with the root to mean square (RSM) error shown in Eq. 4 and the correlation coefficient shown in Eq 5. Neurons in hidden layers one and two were validated with "logsig" and "tagsig" activation functions.

$$\text{Absolute Relative Error} = |RMSE_{Train} - RMSE_{Val}|, \quad (4)$$

$$\text{where } RMSE_{Train} = \left[ \left( \frac{1}{p} \right) \sum_j |t_j - o_j|^2 \right]^{\frac{1}{2}}; \quad RMSE_{Val} = \left[ \left( \frac{1}{p} \right) \sum_j |t_j - o_j|^2 \right]^{\frac{1}{2}}.$$

$$R^2 = 1 - \left[ \frac{\sum_j (t_j - o_j)^2}{\sum_j (o_j)^2} \right]^{\frac{1}{2}}. \quad (5)$$

Network parameters used to train and validate the networks as shown in Table 5.

**Table 5.** Network topology and training parameters of the ANN to GRG

Network parameter	Content
Number of input nodes	3
Number of hidden layers	2
Number of output nodes	1
Number of neurons for each hidden layer	Layer1=9, Layer 2=7
Network type	Feed forward back propagation
Training function	Levenberg–Marquardt
Transfer functions for hidden layers	logsig, tansig
Transfer functions for the output layer	Linear
Performance function	MSE
Training epoch	300
Goal	0.0001

One hundred neural networks were tested with varying neurons in two hidden layers to select the optimal neuron sets in hidden layers. Tables 6 and 7 show that the network with nine neurons in hidden layer 1 and 7 neurons in hidden layer 2 shows the highest correlation

coefficient ( $R^2$ ) is 0.9937, and the slightest absolute error of 0.0021. Hence to train the neural networks, 3-9-7-1 architecture was chosen to predict the grey relation grade.

**Table 6.** Correlation coefficient ( $R^2$ ) for different neural networks

		Layer 2									
Layer 1	Neurons	1	2	3	4	5	6	7	8	9	10
	1	0.6892	0.6636	0.7017	0.4764	0.5315	0.3679	0.6266	0.5031	0.4530	0.6986
	2	0.6760	0.8289	0.6192	0.5921	0.4645	0.6688	0.9691	0.3169	0.5352	0.8687
	3	0.6336	0.7232	0.6495	0.5406	0.9110	0.9875	0.6857	0.6252	0.7901	0.8351
	4	0.9159	0.7816	0.7183	0.5610	0.4624	0.8267	0.6953	0.6191	0.1319	0.5056
	5	0.5753	0.7340	0.6174	0.8097	0.5934	0.6564	0.9065	0.6930	0.6009	0.5936
	6	0.7000	0.8581	0.5812	0.6299	0.9627	0.8522	0.9475	0.6644	0.4279	0.7815
	7	0.7254	0.5310	0.9679	0.6704	0.6573	0.5874	0.9704	0.7635	0.8179	0.5863
	8	0.9436	0.6040	0.5583	0.9227	0.1089	0.8556	0.9184	0.8283	0.7068	0.8041
	9	0.6561	0.8712	0.6353	0.9200	0.6328	0.6823	<b>0.9909</b>	0.9229	0.6204	0.8194
	10	0.8391	0.5643	0.8690	0.9664	0.7029	0.7514	0.9739	0.9806	0.8580	0.8990

**Table 7.** Absolute error values for different neural networks

		Layer 2									
Layer 1	Neurons	1	2	3	4	5	6	7	8	9	10
	1	0.0919	0.0448	0.1190	0.0270	0.1665	0.0578	0.1156	0.0027	0.1484	0.0208
	2	0.1063	0.1749	0.0695	0.1246	0.0651	0.0365	0.0045	0.0319	0.2044	0.1449
	3	0.1275	0.1495	0.0238	0.1930	0.0949	0.0068	0.0499	0.0390	0.2084	0.0310
	4	0.1157	0.0546	0.0417	0.0105	0.1068	0.1738	0.0186	0.0106	0.1169	0.0634
	5	0.0879	0.1094	0.0643	0.1512	0.1244	0.1236	0.0283	0.0403	0.0051	0.0219
	6	0.0834	0.0791	0.0424	0.1089	0.1388	0.1687	0.0640	0.0774	0.2137	0.0062
	7	0.1249	0.0500	0.0131	0.1532	0.1820	0.1360	0.1810	0.0912	0.0024	0.0849
	8	0.1581	0.1281	0.1286	0.1541	0.1032	0.1588	0.2424	0.2220	0.0438	0.1972
	9	0.1207	0.2402	0.1194	0.0733	0.0999	0.1003	<b>0.0021</b>	0.0445	0.2045	0.2543
	10	0.0739	0.0097	0.0481	0.1634	0.0511	0.1650	0.0753	0.2281	0.0588	0.0960

The experimental results and neural network predictions of the process parameters follow each other very closely shown in Table 8, so the developed ANN can accurately predict the grey relation grade. Consequently, it is possible to achieve overall performance without performing any experiments. A neural network model could forecast outcomes better if its mean squared error is lower.

For the GRG, the correlation coefficients were 0.9833, 0.9884, and 0.9938 at the training, validation, and testing stages, respectively shown in Fig. 4. The percentage relative error between the trained and the predicted value by ANN were closely matched, and the maximum percentage of errors was about 3.7% which is within the acceptable level. The low relative error values and average absolute relative error in FSW, as well as the strong correlation coefficients between predicted and experimental results, demonstrate the outstanding capability of artificial neural networks to model mechanical properties without requiring a priori knowledge of thermal and material flow, microstructural and mechanical analysis.

**Table 8.** ANN predictions

Sr. No	1	2	3	4	5	6	7	8	9	10
GRG	0.6268	0.6531	0.5526	0.5944	0.4960	0.3624	0.5623	0.4350	0.5035	0.5544
ANN Pred	0.6492	0.6289	0.5458	0.6073	0.4871	0.3579	0.5566	0.4424	0.4870	0.5609
Error	0.0223	0.0241	0.0067	0.0130	0.0089	0.0044	0.0057	0.0074	0.0166	0.0065
% Error	3.6%	3.7%	1.2%	2.2%	1.8%	1.2%	1.0%	1.7%	3.3%	1.2%
Sr. No	11	12	13	14	15	16	17	18	19	20
GRG	0.5766	0.5308	0.4507	0.5240	0.6359	0.7647	0.6440	0.6656	0.4928	0.5912
ANN Pred	0.5785	0.5248	0.4523	0.5102	0.6503	0.7654	0.6408	0.6665	0.4839	0.5963
Error	0.0019	0.0060	0.0017	0.0138	0.0144	0.0006	0.0032	0.0008	0.0088	0.0051
% Error	0.3%	1.1%	0.4%	2.6%	2.3%	0.1%	0.5%	0.1%	1.8%	0.9%
Sr. No	21	22	23	24	25	26	27	28	29	30
GRG	0.6172	0.5462	0.5104	0.6291	0.5271	0.6491	0.5166	0.5421	0.5434	0.6053
ANN Pred	0.6276	0.5456	0.5183	0.6179	0.5313	0.6504	0.5231	0.5492	0.5518	0.5954
Error	0.0104	0.0005	0.0079	0.0112	0.0042	0.0013	0.0065	0.0071	0.0084	0.0099
% Error	1.7%	0.1%	1.5%	1.8%	0.8%	0.2%	1.3%	1.3%	1.5%	1.6%

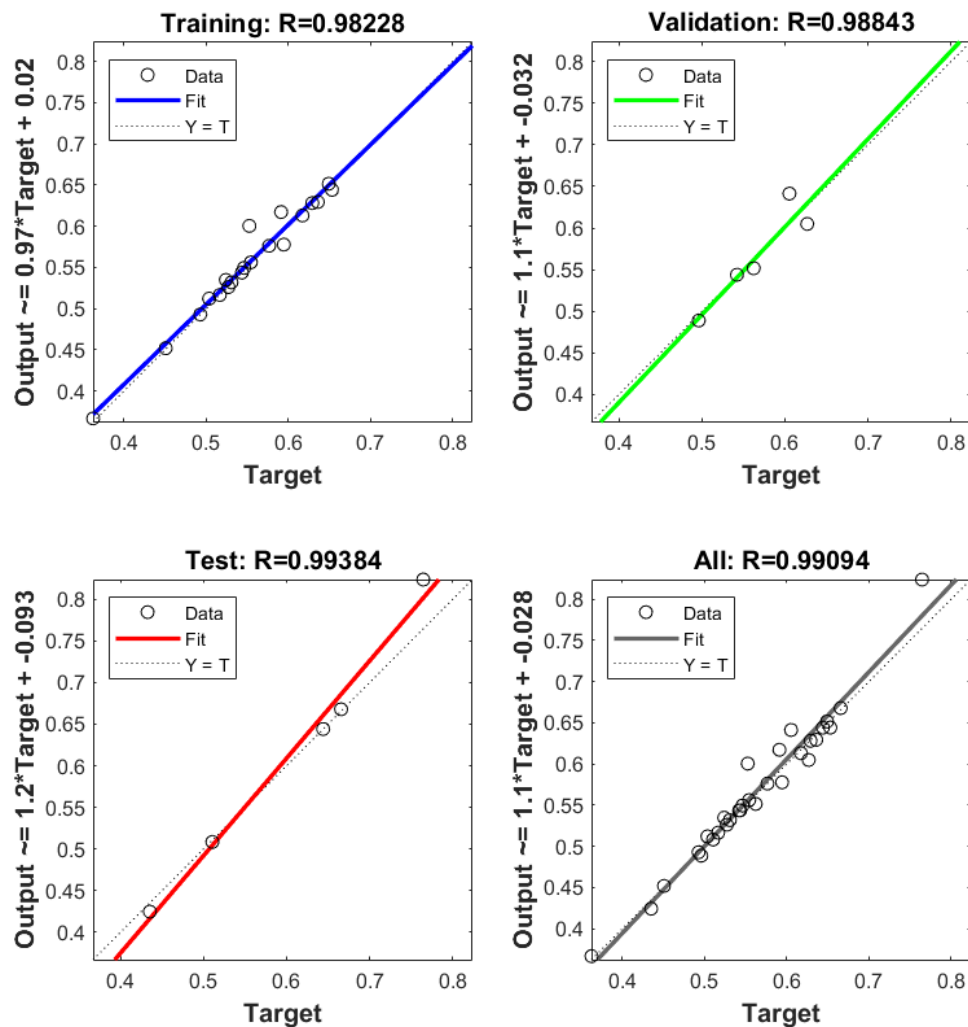


**Fig. 4.** ANN regression values

**Prediction of optimum process parameters.** To predict the optimum process parameters, trained ANN (3-9-7-1) was used. From the grey relation analysis, it was observed that 900 rpm, tool rotation speed, 108 mm/min tool traverse speed, and Tilt angle  $2^\circ$  show the highest value of grey relation grade of 0.7647 (sr. no 16 of Table 4). The same set of parameters was used to obtain the optimum process parameter by varying each parameter by keeping two parameters constant to simulate the neural network. As shown in Fig 5 (a), the effect of tool rotation speed on grey relation grade is predicted using a trained neural network by keeping 108 mm/min of TTS and tilt angle  $2^\circ$  constant. Results show that GRG value increases with an increase in tool rotation speed up to 975 rpm, then decreases.

Also, for the tool traverse speed, the grey GRG value increases with an increase in TTS for TRS 900 rpm and TTA of  $2^\circ$ , as shown in Fig. 5 (b). Maximum grey relation grade obtained at 108 mm/min. Figure 5 (c) shows GRG value increases with an increase in tool tilt angle from  $1-2^\circ$  and then decreases. Maximum grey relation grade obtained at  $2^\circ$ .

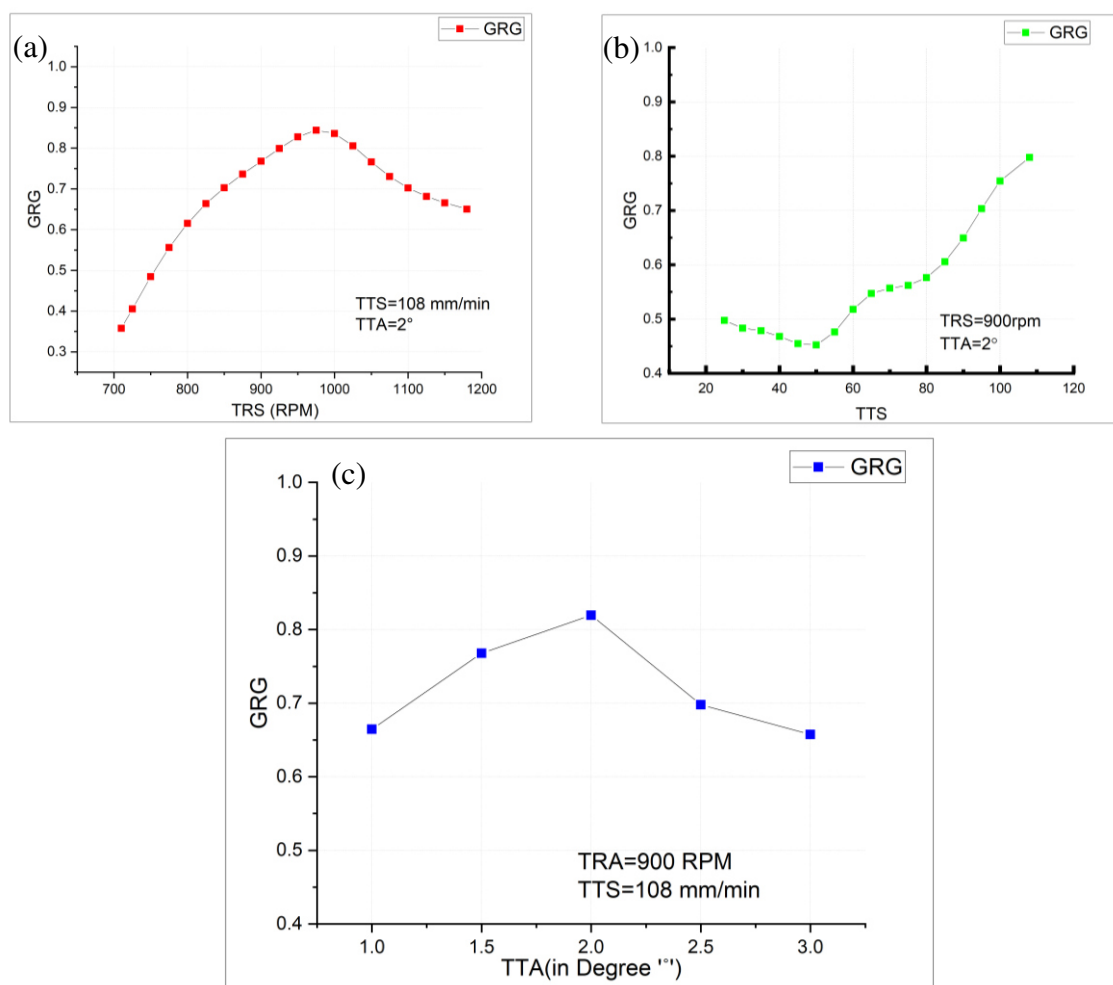


**Fig. 5.** Prediction of GRG using ANN

After simulating the results, optimum parameters predicted by the ANN are Tool rotation speed of 975 rpm, tool transverse speed of 108mm/min, and tool tilt angle of  $2^\circ$ , as shown in Table 9. The grey relation grade obtained using the proposed GRA-ANN approach was 0.8440 with revised optimum parameters tool rotation 975 rpm, tilt angle  $2^\circ$ , and welding speed 108 mm/min, a 9.32% improvement over the 0.7647 obtained experimentally at 900 rpm and 108 mm/min. The results show that the adoption of the GRA-ANN hybrid

optimization method leads to a significant improvement of mechanical properties in friction stir welding.

As the milling machine has limited settings of the tool rotation speed, 975 rpm was not possible with the machine. Hence closed match speed setting of 900 rpm was considered the optimum speed with a transverse tool speed of 108mm/min and tool tilt angle of 2°. The same parameters were used for the conventional in-air friction stir welding experiment after the optimal process parameters were determined for underwater friction stir welding. Mechanical and microscopic investigations were conducted to compare underwater and in-air FSW performance.

**Table 9.** Results of welding performance using the GRA and ANN

Method	Optimum process conditions			GRG	% Improvement in GRG
	TRS	TTS	TA		
GRA	900	108	2°	0.7647	---
GRA-ANN(Pred)	900	108	2°	0.7653	--
<b>TAGUCHI-GRA-ANN (optimized parameters)</b>	<b>975</b>	<b>108</b>	<b>2°</b>	<b>0.8440</b>	<b>9.32%</b>

### Result and discussion

**ANOVA analysis.** The grey relation grade obtained using the proposed GRA-ANN approach was 0.8440 with revised optimum parameters tool rotation 975 rpm, tilt angle 2°, and welding speed 108 mm/min, a 9.32% improvement over the 0.7647 obtained experimentally at 900 rpm and 108 mm/min. [42]. The results of the ANOVA test are shown in Table 10. In addition, a percentage contribution is calculated. In the 1920s, statistician and geneticist R.A. Fisher developed Fisher's F-distribution to test for statistical significance. In this paper, ANOVA analysis was carried out to find the % contribution of each process parameter to the mechanical properties of the welded joint. From Table 10, in ANOVA analysis, it is observed that input parameter tool rotation speed is having highest % contribution of 39.89%, followed by 29.87% and 19.59% of Tool traverse speed and Tool tilt angle, respectively on mechanical properties of underwater friction stir welding of AA 6061-T6.

**Table 10.** ANOVA analysis

Parameters	SS Value	DOF	MS Value	F-Value	P-value	% Contribution
TRS	0.0672	2	0.0336	3.743941	0.041456.	39.89%
TTS	0.1258	5	0.02516	2.803499	0.046358.	29.87%
TTA	0.033	2	0.0165	1.838543	0.188142	19.59%
Error	0.17949	20	0.008975			10.65%
Total	0.40549	29				

Increasing the rotational tool speed improves the grey relation grade to a maximum for a given TTS and TTA. The material is mixed and stirred around the pin due to frictional heating and plastic deformation caused by tool rotation speed. Insufficient tensile strength and yield strength might be caused by low heat generation and plastic deformation at low rotational speeds. On the other hand, a high rotational speed is characterized by turbulent material flow and localized softening due to the abundance of heat created. The presence of strengthening precipitates, dissolution, and coarsening, decreases the strength of the welded joint. Welds produced with tool speeds close to 900 rpm have better mechanical properties because sufficient heat is generated for effective softening and mixing of the deformed material. The strength of the joint tends to increase as welding speed increases.



**Characterization of welded joint.** Macroscopic images of all 30 samples are free from any volumetric defect except flash over the top surface of the weld. Figure 6 shows a macroscopic image of an underwater friction stir welding sample welded with optimum process parameters obtained with ANN-GRA analysis. For the micro and macrostructural investigations, specimens were processed with the optimum process, and parameters were used. For the comparative study, for the same optimum parameters, a new specimen was welded with the conventional in-air friction stir welding process. A macrograph of underwater FSW shows distinct HAZ, TMAZ, and SZ zones, whereas, for in-air FSW, the HAZ and TMAZ are separated by a thin boundary. The macrograph of the weld sample shows well-defined onion rings consisting of bright and dark field regions, which denote uniform material flow in the nugget zone shown in Fig. 6. Exposure to water in UFSW makes the weld smoother compared with FSW.

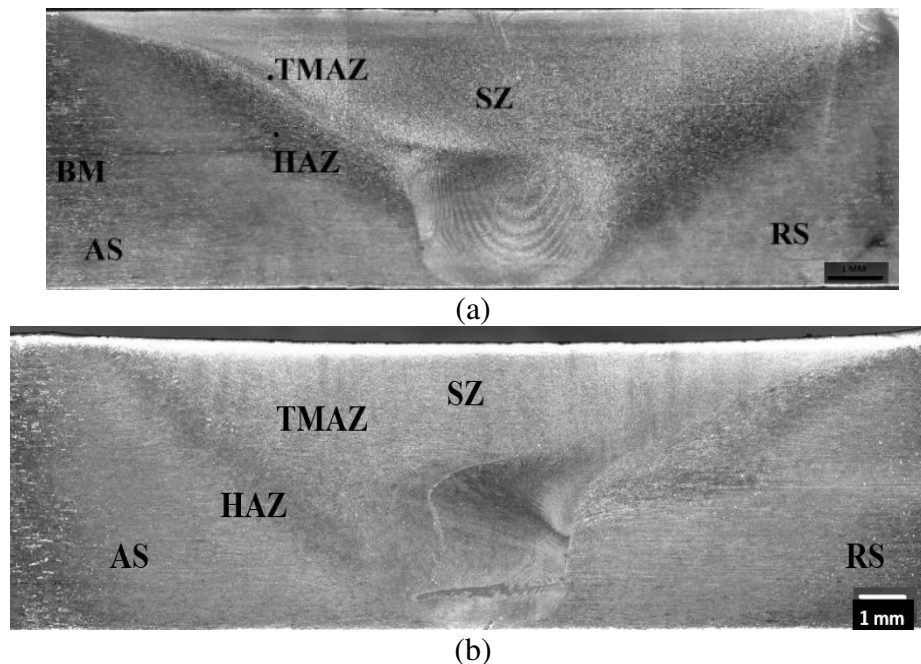


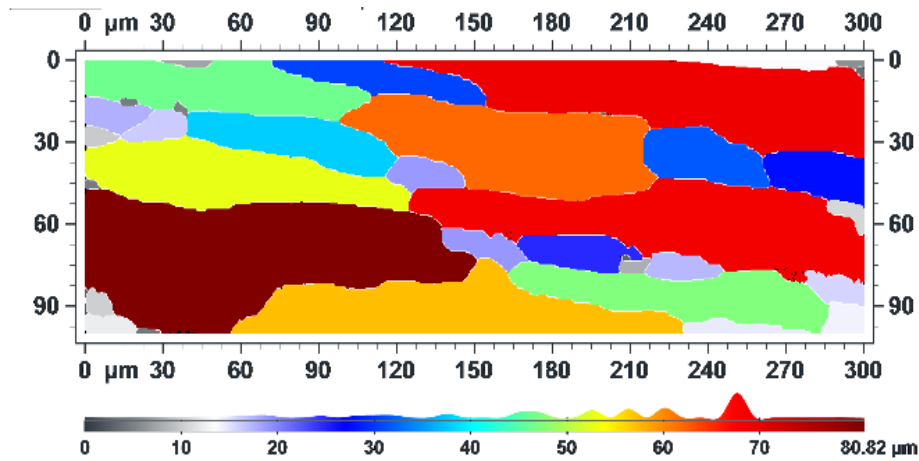
**Fig. 6.** Macroscopic image of an underwater friction stir welding sample welded with optimum process parameters

The plastic deformation generated by the FSW process severely compresses the pre-deformed coarse grains, resulting in the creation of extremely fine recrystallized equiaxed grains within the weld nugget. In addition, the dynamic recrystallisation (DRX) phenomenon, which is theoretical to have been induced by the adsorption of dislocations by sub-grain boundaries, may have also aided in the nucleation and development of ultrafine grains in the FSW weld nugget. As grain refinement takes place, which precedes to increase of microhardness ultimately increases the tensile strength of the joint due to water as a cooling medium carrying out heat from the weld specimens rapidly. This rapid cooling is responsible for restricting grain growth, which leads to refined grains in the weld nugget zone. Slight variation in the grain size of FSW welded samples of both the condition shows that the cooling effect due to water dominates the development of tool pin profiles with the same process parameters. Further, the microstructure analysis the specimen welded in water analysed using EBSD techniques.

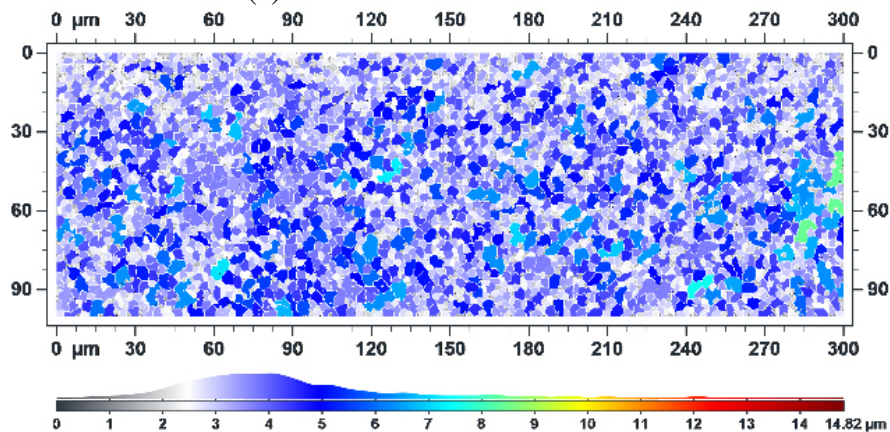
Figure 7 shows the EBSD grain maps of base metal compared with the weld nugget zone of UFSW and CFSW analysed using the ATEX software tool [23]. Figure 7 (a) shows the EBSD maps of base material and which shows elongated grains with an average 84  $\mu\text{m}$

grain size. Figures 7 (b) and 7 (c) shows the components and grains map of TMAZ prepared under water and in air. Where, slightly more refined grains of size  $2.56\text{ }\mu\text{m}$  were observed for water as compared with the air. It was because of effective heat distribution and plastic deformation that occurred due to water which refine grains in the welding zone compared with the air.

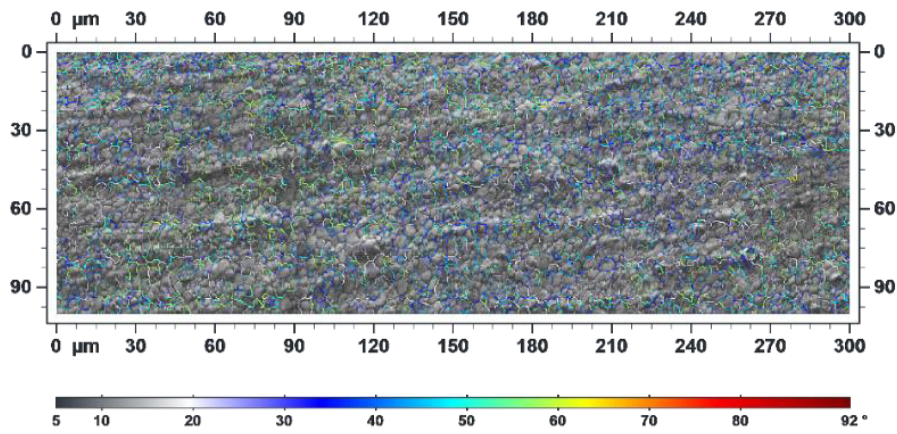
In FSW, the base material of  $84\text{ }\mu\text{m}$  grain size undergoes severe plastic deformation, and grain refinements provide an equiaxed grain size. The average grain size in UFSW is  $2.65\text{ }\mu\text{m}$ , and the CFSW is  $4.91\text{ }\mu\text{m}$ . The water environment in UFSW restricted grain growth in the nugget zone after processing, providing finer grain UFSW compared with CFSW. Due to the shear deformation generated by the rotating tool, the parent grains tend to be reoriented along the flow pattern around the pin, which is a characteristic of TMAZ. Observation of newly-formed equiaxed grains indicates the presence of dynamic recrystallization (DRX). From the exterior to the interior of the TMAZ, there is a trend for more equiaxed grains to develop. With closer proximity to the core of the weld, higher temperatures and more locational deformation are obtained, resulting in an increase in DRX. The texture transition happens on the TMAZ border. The alterations are concentrated in a small area. This region also has significant diversity in grain size.



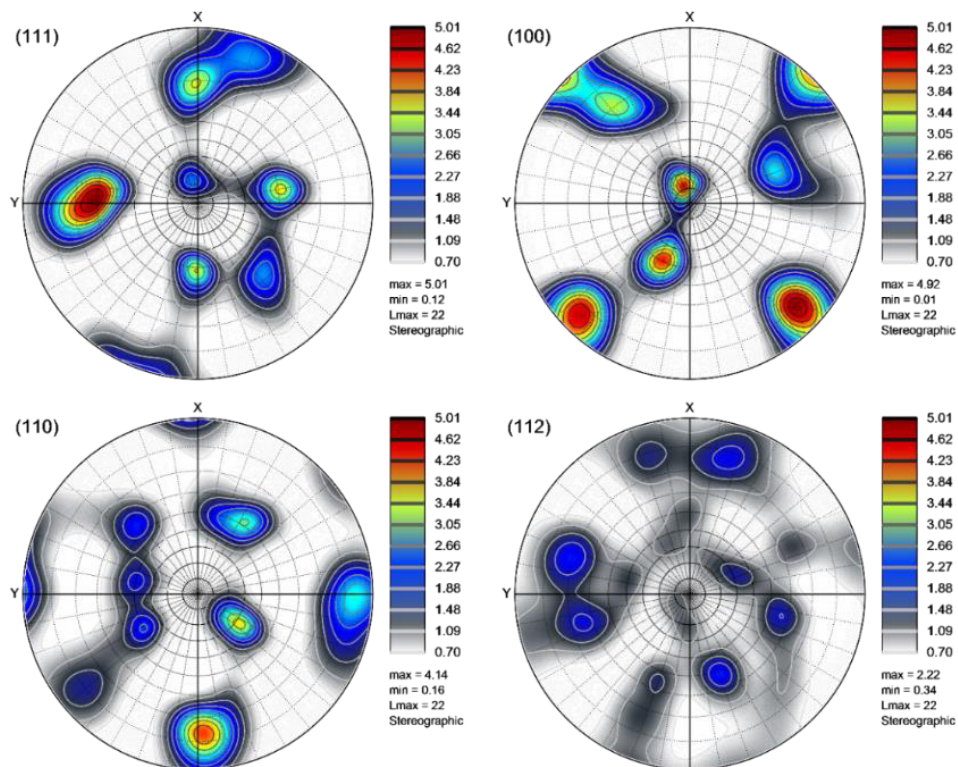
(a) Grain structure of base material



(i) EBSD maps of FSW specimen prepared underwater

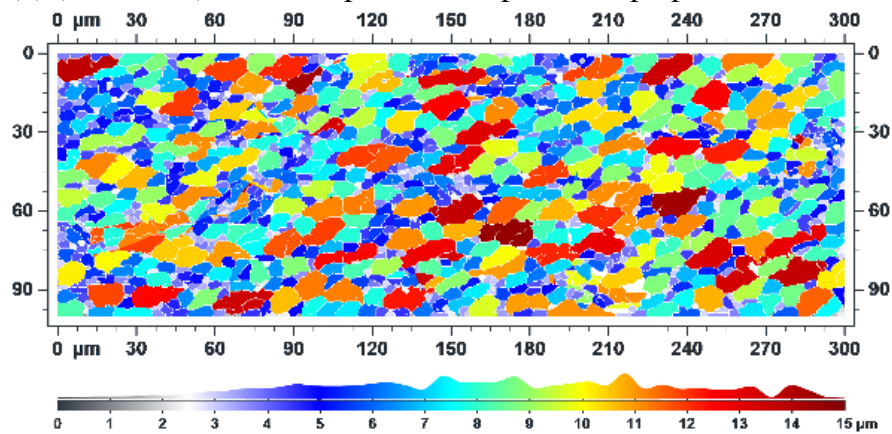


(ii) EBSD maps showing grain boundaries for underwater FSW



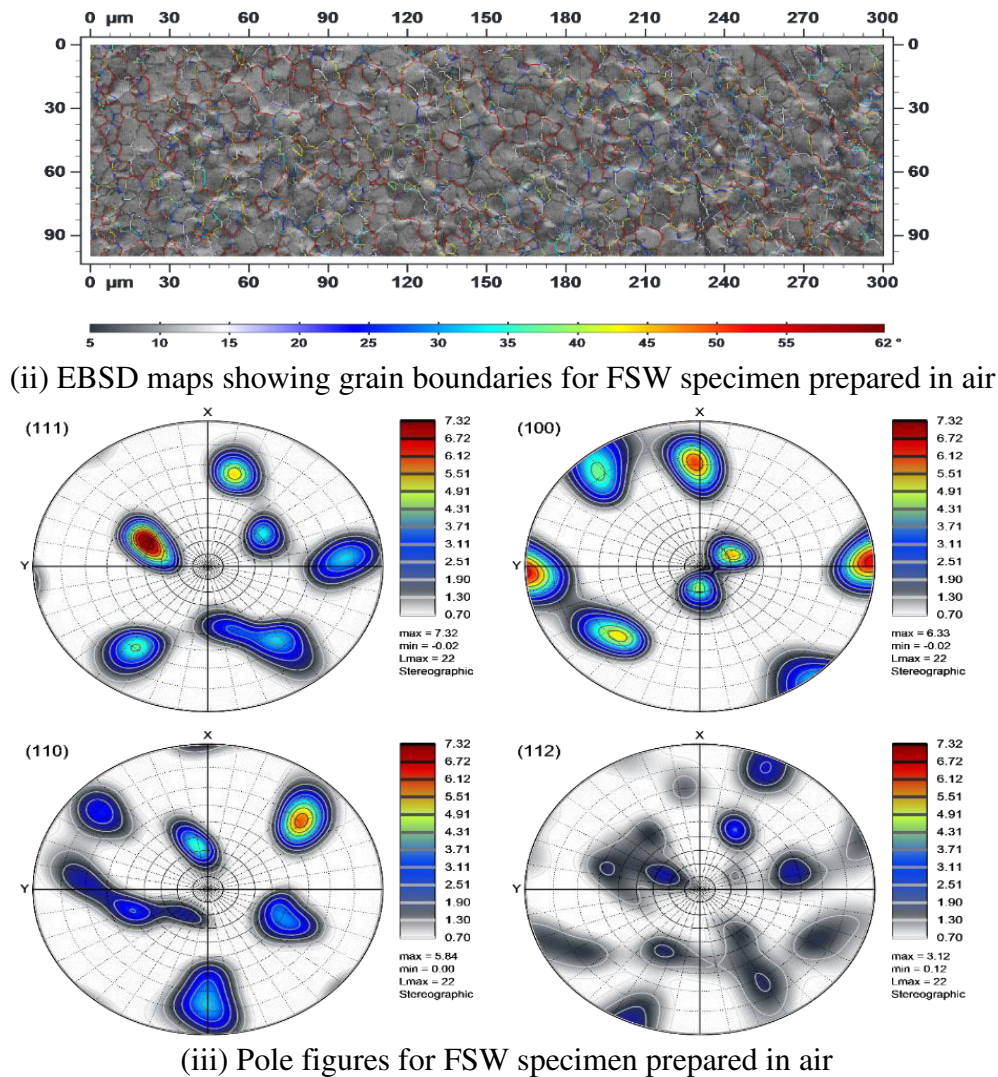
(iii) Pole maps of underwater FSW

(b) (i, ii and iii) EBSD maps of FSW specimens prepared underwater



(i) EBSD maps of FSW specimen prepared in air





In FSW, due to intense recrystallization because of stir action, grain refinement occurs which is responsible for changing mechanical properties in a welded joint. Underwater friction stir welding reduces the thermal exposure in nugget zone, which restricts grain growth due to natural aging during the cooling of the joint, which adds extra benefit to improve the mechanical properties of the joint. The grain refining process is driven by grain subdivision at the cooler perimeter of the tool's deformation zone and the geometric effects of strain, which reduce the overall high-angle border spacing with increasing deformation. Nevertheless, it also involves thermally induced high-angle grain boundary migration, which increases as the temperature approaches the tool. The later, higher-temperature stages of the refining process resemble geometric dynamic recrystallisation. As a result of static annealing in the thermal wake of the tool, the nugget grain structure becomes more equiaxed and coarsens slightly, as well. As indicated previously, sites with relatively large deformation stresses exhibit discontinuous recrystallization; yet, continuous recrystallization is also accompanied by grains refining. In the SZ, a steady change from low-angle borders to high-angle boundaries can be detected, according to studies of grains distribution in the literature [21,22].

The low angle boundaries for the specimen prepared in water are nearly 28.5 % as seen in Fig. 7 (b-ii) whereas high angle boundaries are 71.5 % with an average grain size of 3.21  $\mu\text{m}$  and texture intensity of 5.01 as observed in pole Fig. 7 (b-iii). On the other side, the

low angle boundaries for the specimen prepared in the air are nearly 25.4% as seen in Fig. 7 (c-ii) whereas, high angle boundaries are 74.6 % with an average grain size of 8.1  $\mu\text{m}$  and texture intensity of 7.32 as observed in pole Fig. 7 (c-iii).

The high temperatures and intense deformation experienced during FSW/UFSW result in different textures, precipitates dissolving, and coarsening. The macrostructure has three distinct zones: the stir zone (SZ), the TMAZ, and the HAZ. There is a distinct boundary between TMAZ/HAZ and SZ. The grains of BM are non-deformed and elongated. Typically, the SZ exhibits equiaxed and refined grains that have been dynamically recrystallized. New grains are formed in the SZ due to intensive plastic deformation caused by tool stirring and heat generated by tool rubbing. Figure 8 shows Vickers microhardness profiles measured along the midsections of base material, CFSW, and UFSW specimens. The base material has an average hardness value of 107 HV. The weld regions of HTAAs usually become soft as a result of FSW. The UFSW joints of AA6061 soften due to coarsening and dissolution of strengthening precipitates during FSW/UFSW [43].

It was observed that precipitation-hardened AAs typically have 'W' type hardness profiles (Fig. 8). The advancing side undergoes severe plastic deformation in friction stir welding compared with the retreating side. Due to this, the advancing side undergoes higher temperatures than the retreating side, reducing the region's microhardness. AS in UFSW, with low-temperature exposure in the welding region, the hardness value increases, as shown in Fig. 8. The retreating side in UFSW shows a minimum hardness of 70.2 Hv on the interface of TMAZ /HAZ. For the CFSW minimum hardness value observed in the HAZ zone of the Advancing side.

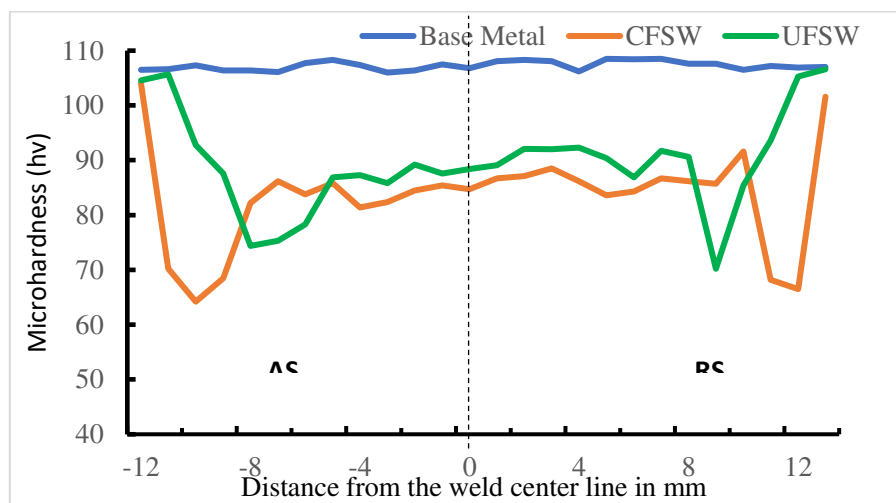


**Fig. 8.** Microhardness profile of UFSW sample

For CFSW samples, due to high heat input on AS, microhardness in AS (64-86 HV) was lower than that in RS (66-87HV). A maximum microhardness of 85 HV was found in the SZ of RS, which was lower than the average microhardness of 107 HV found in the BM. Compared to SZ, TMAZ/HAZ exhibited a noticeable decrease in microhardness. Microstructure analysis revealed that SZ contains fine grains and precipitates. Refined grains with many grain boundaries resist dislocation motion when indented or loaded. As a result, the SZ exhibits a higher microhardness than the TMAZ. There was grain growth (coarsening) in the TMAZ and HAZ. Due to a coarse boundary, there is less resistance to dislocation motion, which makes grain boundaries less available. TMAZ and HAZ have low grain boundary strengthening, contributing to their low hardness. As reported, it was found that in UFSW, TMAZ and HAZ were narrowing, which reduced softening regions in the nugget

zone [7]. TMAZ/HAZ might also have a lower hardness due to the dissolution of strengthening precipitates, Lin et al. [44] observed similar results.

The tensile test results for the base metal, underwater friction stir welding, and conventional in-air friction stir welding (CFSW) samples are shown in Fig 9. Figure 9 shows that welding speed increases from 29-108 mm/min improves mechanical properties. As a result of welding at lower speeds, high heat levels are generated, compromising the growth and dissolution of strengthening precipitates. With higher welding speeds, thermal cycles are reduced, which improves tensile strength and inhibits grain growth and precipitate dissolution. According to Liu et al. [45], the tensile strength first increases with welding speed and then dramatically decreases at 200 mm/min due to the groove defect, which is present at a fixed rotation speed of 800 rpm.

The optimal process parameters used to process both CFSW and UFSW samples are TRS 900 rpm, WS 108 mm/min, with  $TA = 2^\circ$ . Friction stir welding undergoes thermal heating, which reduces mechanical properties compared to a base metal, which results in tensile strength of 303.5 MPa and a 20% elongation. Results show underwater samples show a tensile strength of 237.25 MPa (78.17% of BM) with an elongation of 13.44% (76.08% of BM). FSW samples processed in the air (CFSW) show a tensile strength of 216.88 MPa (71.45% of BM) with an elongation of 12.5% (63.2%) of BM).

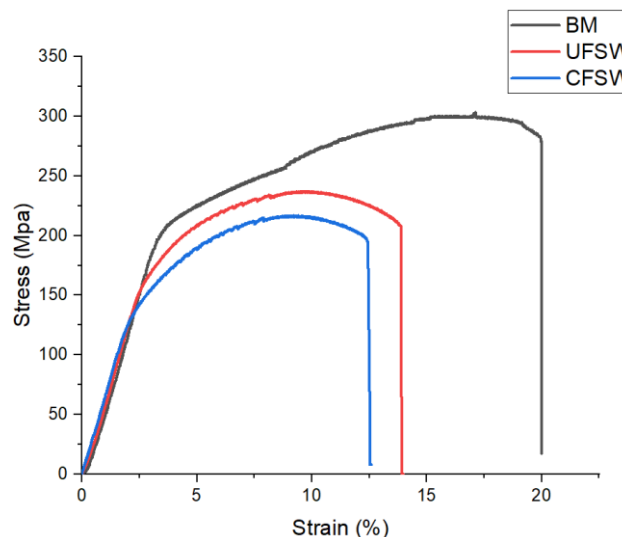


**Fig. 9.** Stress-Strain curves for BM, CFSW, and UFSW

Tensile strength was increased by 10.7% when the welding medium was changed from air to water [46]. The peak temperature in the UFSW is lower than in the FSW due to water's higher heat absorption capacity. In addition, UFSW results in a shorter dwell time above a given temperature and a lower peak temperature due to more significant heating and cooling rates [46]. Water cooling limits the coarsening and dissolution of strengthening precipitates due to reduced temperatures and less thermal gradient. As a result, an optimal underwater FSW joint may be more substantial than a conventional FSW joint.

The hardness minimum is a potential fracture location during transverse tensile loading of heat-treatable Al alloys since the hardening precipitates dominate the strength [46]. In FSW, zones with low hardness distribution are prone to fracture initiation. Figure 10 (a) shows tensile test specimens' fracture surface locations. Based on current research, CFSW tensile test fracture occurs on the AS in the HAZ adjacent to the TMAZ, which has the lowest hardness [43]. Microfractographs (Fig. 10 (b)) show some equiaxed dimples, indicating ductile fracture modes. Dawood et al. [47] attribute small dimples to homogeneous microstructures at the failure site.

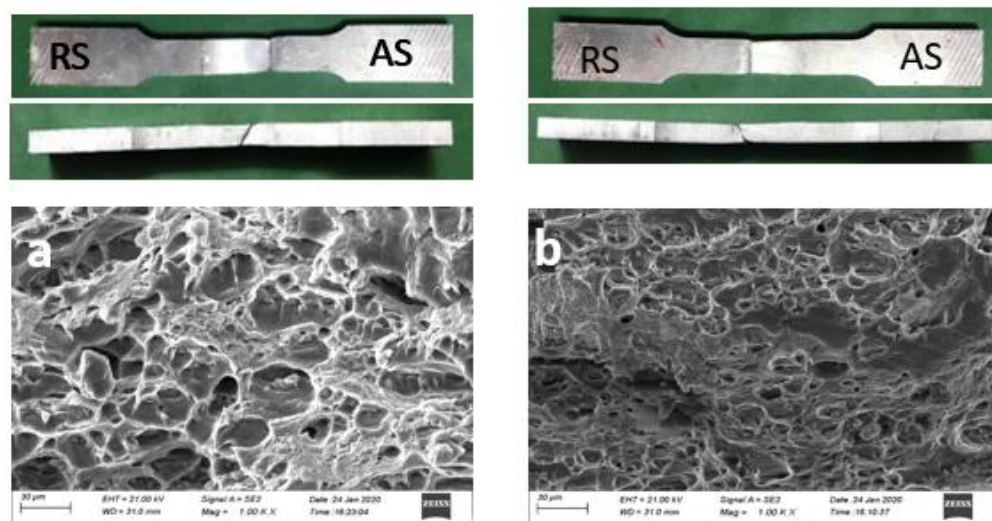


**Fig. 10.** The tensile fracture surfaces of weld joints welded a) CFSW b) UFSW

Typically, the advancing side achieves higher temperatures, causing grain growth, and resulting in the lowest hardness region. The fracture position shifts from advancing to retreating when the cooling medium changes from air to water shown in Fig. 10 (b) for UFSW, fracture occurs in the low hardness zone of the interface of TMAZ and HAZ on the retreating side [48,49]. Several large dimples are evident on the fracture surface of Figs. 10 (a) and (b), indicating significant plastic deformation during tensile testing. Joints welded in air exhibit larger and deeper dimples than joints welded in water; the fracture surfaces of the joints welded in air exhibit ductile characteristics with large dimples. In some positions on the fracture surface of the joint welded in water, there are small dimples with secondary cracks, and quasi-cleavage planes are visible [49].

## Conclusions

In the present investigations, multiobjective optimization was performed using ANN-GRA for UFSW of AA 6061-T6 aluminium alloy using a conical tool. The ultimate tensile strength, yield strength, elongation percentage, and impact strength, optimal process parameters were determined and optimized for tool rotation speed, welding speed, and tilt angle. Based on the results of this study, the following conclusions were drawn:

1. For UFSW the ANN multilayer network 3-9-7-1 shows optimum results in terms of grey relation grade with a correlation coefficient of 0.9909 and an absolute minimum error of 0.0021. In a model trained with an ANN, a grey relation grade increases with tool rotation speed as it increases from 700 to 910 rpm, then decreases. In addition, the grey relation grade increases with an increase in tool traverse speed from 22 to 108 mm/min.
2. Based on GRA-ANN, 0.8440 grey relation grades were predicted with new optimum parameters of 900 rpm, 2° tilt angle, and 108 mm/min welding speed, compared to 0.7647 obtained experimentally at 900 rpm, 2° tilt angle, and 108 mm/min.
3. ANOVA analysis revealed that tool rotation speed contributes 39.89% to the mechanical properties of underwater friction stir welding of AA 6061-T6, followed by tool traverse speed and tool tilt angle, respectively, by 29.87% and 19.59%.
4. Underwater FSW samples show the highest strength of 237.25 MPa (78.17% of BM) compared with the air (CFSW) sample of 216.88 MPa (71.45% of BM).
5. The UFSW produces refined grains in the nugget zone and thus improves the microhardness and tensile strength of the joints compared with in-air friction stir welding.



## References

1. Mishra RS, Ma ZY. Friction stir welding and processing. *Mater. Sci. Eng. R Reports*. 2005;50(1-2): 1–78.
2. Ma ZY. Friction Stir Processing Technology: A Review. *Metall. Mater. Trans. A*. 2008;39: 642–658.
3. Rai R, De A, Bhadeshia HKDH, Deb Roy T. Review: friction stir welding tools. *Sci Technol Weld Join*. 2011;16: 325–342.
4. Mishra RS, Mahoney MW. (Eds.) *Friction Stir Welding and Processing*. ASM International; 2007.
5. Zhou L, Li GH, Liu CL, Wang J, Huang YX, Feng JC, et al. Effect of rotation speed on microstructure and mechanical properties of self-reacting friction stir welded Al-Mg-Si alloy. *Int. J. Adv. Manuf. Technol*. 2017;89: 3509–3516.
6. Liu W, Shen Y, Guo C. Microstructures and mechanical properties of submerged friction stir welding of ME20M Magnesium alloy. In: *16th Int. Bhurban Conf. Appl. Sci. Technol.* IEEE; 2019. p.1–6.
7. Li X, Zhang Z, Peng Y, Yan D, Tan Z, Zhou Q, Wang K, Zhou M. Microstructure and mechanical properties of underwater friction stir welding of CNT/Al-Cu-Mg composites. *J. Mater. Res. Technol*. 2022;18: 405–415.
8. Paramaguru D, Pedapati SR, Awang M. *The Advances in Joining Technology*. Singapore: Springer; 2019.
9. Wahid MA, Khan ZA, Siddiquee AN. Review on underwater friction stir welding: A variant of friction stir welding with great potential of improving joint properties. *Transactions of Nonferrous Metals Society of China*. 2018;28(2): 193–219.
10. Rathinasuriyan C, Muniamuthu S, Mystica A, Senthil Kumar VS. Current Status and Development of Submerged Friction Stir Welding: A Review. *International Journal of Precision Engineering and Manufacturing-Green Technology*. 2021;8: 687–701.
11. Hofmann DC, Vecchio KS. Submerged friction stir processing (SFSP): An improved method for creating ultra-fine-grained bulk materials. *Mater. Sci. Eng. A*. 2005;402: 234–241.
12. Wang Q, Zhao Y, Yan K, Lu S. Corrosion behavior of spray formed 7055 aluminum alloy joint welded by underwater friction stir welding. *Mater. Des*. 2015;68: 97–103.
13. Hosseini M, Danesh Manesh H. Immersed friction stir welding of ultrafine grained accumulative roll-bonded Al alloy. *Mater. Des*. 2010;31: 4786–4791.
14. Rathinasuriyan C, Muniamuthu S, Mystica A, Senthil Kumar VS. Investigation of heat generation during submerged friction stir welding on 6061-T6 aluminum alloy. *Mater. Today Proc*. 2021;46: 8320-8324.
15. Bagheri B, Abbasi M, Abdollahzadeh A, Kokabi AH. Numerical analysis of cooling and joining speed effects on friction stir welding by smoothed particle hydrodynamics (SPH). *Arch. Appl. Mech*. 2020;90: 2275–2296.
16. Abdollahzadeh A, Bagheri B, Abassi M, Kokabi AH, Moghaddam AO. Comparison of the Weldability of AA6061-T6 Joint under Different Friction Stir Welding Conditions. *J. Mater. Eng. Perform*. 2021;30: 1110–1127.
17. Fathi J, Ebrahimzadeh P, Farasati R, Teimouri R. Friction stir welding of aluminum 6061-T6 in presence of watercooling: Analyzing mechanical properties and residual stress distribution. *Int. J. Light Mater. Manuf*. 2019;2: 107–115.
18. Fratini L, Buffa G, Shivpuri R. In-process heat treatments to improve FS-welded butt joints. *Int. J. Adv. Manuf. Technol*. 2009;43: 664–670.
19. Sharma C, Dwivedi DK, Kumar P. Influence of in-process cooling on tensile behaviour of friction stir welded joints of AA7039. *Mater. Sci. Eng. A*. 2012;556: 479–487.




20. Sinhmar S, Dwivedi DK. Enhancement of mechanical properties and corrosion resistance of friction stir welded joint of AA2014 using water cooling. *Mater. Sci. Eng. A*. 2017;684: 413–422.
21. Mahto RP, Rout M, Pal SK. Mechanism of microstructure evolution and grain growth in friction stir welding of AA6061-T6 and AISI304 in air and water media. *Mater. Chem. Phys.* 2021;273: 125081.
22. Abbasi M, Bagheri B, Abdollahzadeh A, Moghaddam AO. A different attempt to improve the formability of aluminum tailor welded blanks (TWB) produced by the FSW. *Int. J. Mater. Form.* 2021;14: 1189–1208.
23. Abbasi M, Abdollahzadeh A, Bagheri B, Ostovari Moghaddam A, Sharifi F, Dadaei M. Study on the effect of the welding environment on the dynamic recrystallization phenomenon and residual stresses during the friction stir welding process of aluminum alloy. *Proc. of the Institution of Mechanical Engineers, Part L: Journal of Materials: Design and Applications*. 2021;235: 1809–1826.
24. Velukkudi Santhanam SK, Ramaiyan S, Rathinaraj L, Chandran R. *Multi Response Optimization of Submerged Friction Stir Welding Process Parameters Using Grey Relational Analysis. Vol 2 Adv Manuf.* American Society of Mechanical Engineers; 2016.
25. Şimşek B, İç YT, Şimşek EH. A TOPSIS-based Taguchi optimization to determine optimal mixture proportions of the high strength self-compacting concrete. *Chemom. Intell. Lab. Syst.* 2013;125: 18–32.
26. Hasan M, Abdi R, Akbari M, Shojaeefard MH, Behnagh RA, Akbari M, Besharati Givi MK, Farhani F. Modelling and pareto optimization of mechanical properties of friction stir welded AA7075/AA5083 butt joints using neural network and particle swarm algorithm. *Mater. Des.* 2013;44: 190–198.
27. Lin JL, Lin CL. The use of the orthogonal array with grey relational analysis to optimize the electrical discharge machining process with multiple performance characteristics. *Int. J. Mach. Tools. Manuf.* 2002;42: 237–244.
28. Sudeepan J, Kumar K, Barman TK, Sahoo P. Mechanical and Tribological Behavior of ABS/TiO<sub>2</sub> Polymer Composites and Optimization of Tribological Properties Using Grey Relational Analysis. *J. Inst. Eng. Ser. C*. 2015;97: 41–53.
29. Hsiao YF, Tarng YS, Huang WJ. Optimization of Plasma Arc Welding Parameters by Using the Taguchi Method with the Grey Relational Analysis. *Mater. Manuf. Process.* 2007;23: 51–58.
30. Wakchaure KN, Thakur AG, Gadakh V, Kumar A. Multi-Objective Optimization of Friction Stir Welding of Aluminium Alloy 6082-T6 Using hybrid Taguchi-Grey Relation Analysis- ANN Method. *Mater. Today Proc.* 2018;5: 7150–7159.
31. Aydin H, Bayram A, Esme U, Kazancoglu Y, Guven O. Application of Grey Relation Analysis (Gra) and Taguchi Method for the Parametric Optimization of Friction Stir Welding (Fsw) Process. *Mater. Tehnol.* 2010;44: 205–211.
32. Ansari MA, Abdi Behnagh R, Lin D, Kazeminia S. Modelling of Friction Stir Extrusion using Artificial Neural Network (ANN). *Neural Computing and Applications*. 2019;31: 7211–7226.
33. Thapliyal S, Mishra A. Machine learning classification-based approach for mechanical properties of friction stir welding of copper. *Manuf. Lett. Society of Manufacturing Engineers (SME)*. 2021;29: 52–55.
34. Manvatkar VD, Arora A, De A, DebRoy T. Neural network models of peak temperature, torque, traverse force, bending stress and maximum shear stress during friction stir welding. *Sci. Technol. Weld. Join.* 2012;17: 460–466.
35. Ghetiya ND, Patel KM. Prediction of tensile strength in friction stir welded aluminium alloy using artificial neural network. *Procedia Technol.* 2014;14: 274–281.

36. Shojaeefard MH, Akbari M, Asadi P. Multi Objective Optimization of Friction Stir Welding Parameters Using FEM and Neural Network. *International Journal of Precision Engineering and Manufacturing*. 2014;15: 2351–2352.
37. Ansari MA, Abdi Behnagh R, Lin D, Kazeminia S. Modelling of Friction Stir Extrusion using Artificial Neural Network (ANN). *Int. J. Adv. Des. Manuf. Technol.* 2018;11(4): 1-12.
38. Buffa G, Fratini L, Micari F. Mechanical and microstructural properties prediction by artificial neural networks in FSW processes of dual phase titanium alloys. *J. Manuf. Process.* 2012;14: 289–296.
39. Laubscher RPIDRF. Application of an artificial neural network model to predict the ultimate tensile strength of friction - welded titanium tubes. *J. Brazilian Soc. Mech. Sci. Eng.* 2019;41: 111.
40. Patel C., Das S., Narayanan RG. CAFE modeling, neural network modeling, and experimental investigation of friction stir welding. *Proc. Inst. Mech. Eng. Part C J. Mech. Eng. Sci.* 2013;227: 1164–1176.
41. Maleki E. Artificial neural networks application for modeling of friction stir welding effects on mechanical properties of 7075-T6 aluminum alloy. *IOP Conf. Ser. Mater. Sci Eng.* 2015;103: 012034.
42. Kumar J, Majumder S, Mondal AK, Verma RK. Influence of rotation speed, transverse speed, and pin length during underwater friction stir welding (UW-FSW) on aluminum AA6063: A novel criterion for parametric control. *Int. J. Light Mater. Manuf.* 2022;5: 295–305.
43. Li D, Yang X, Cui L, He F, Shen H. Effect of welding parameters on microstructure and mechanical properties of AA6061-T6 butt welded joints by stationary shoulder friction stir welding. *Mater. Des.* 2014;64: 251–260.
44. Lin H, Wu Y, Liu S, Zhou X. Effect of cooling conditions on microstructure and mechanical properties of friction stir welded 7055 aluminium alloy joints. *Mater. Charact.* 2018;141: 74–85.
45. Liu HJ, Zhang HJ, Yu L. Effect of welding speed on microstructures and mechanical properties of underwater friction stir welded 2219 aluminum alloy. *Mater. Des.* 2011;32: 1548–1553.
46. Venkateswarulu D, Cheepu M, Krishnaja D, Muthukumaran S. Influence of Water Cooling and Post-Weld Ageing on Mechanical and Microstructural Properties of the Friction-Stir Welded 6061 Aluminium Alloy Joints. *Appl. Mech. Mater.* 2018;877: 163–176.
47. Dawood HI, Mohammed KS, Rahmat A, Uday MB. The influence of the surface roughness on the microstructures and mechanical properties of 6061 aluminium alloy using friction stir welding. *Surf. Coatings Technol.* 2015;270: 272–283.
48. Banik A, Deb Barma J, Saha SC. Effect of Threaded Pin Tool for Friction Stir Welding of AA6061-T6 at Varying Traverse Speeds: Torque and Force Analysis. *Iran J. Sci. Technol – Trans. Mech. Eng.* 2020;44: 749–764.
49. Zhao Y, Wang Q, Chen H, Yan K. Microstructure and mechanical properties of spray formed 7055 aluminum alloy by underwater friction stir welding. *Mater. Des.* 2014;56: 725–730.

## THE AUTHORS

**Kiran Wakchaure**   
e-mail: kiran.wakchaure@yahoo.com

**Ajaykumar Thakur**   
e-mail: ajay\_raja34@yahoo.com

## Effect of Mechanical Properties of AL7075/Mica Powder Hybrid Metal Matrix Composite

K. Arunprasath <sup>1</sup>✉ , P. Amuthakkannan <sup>2</sup> , M. Vijayakumar <sup>1</sup> , R. Sundarakannan <sup>3</sup> , M. Selwin <sup>4</sup> , S. Kavitha <sup>5</sup> , Lavish Kumar Singh <sup>6</sup> 

<sup>1</sup>Department of Mechanical Engineering, PSN College of Engineering and Technology, Tirunelveli, 627152, Tamilnadu, India

<sup>2</sup>Department of Mechanical Engineering, PSR College of Engineering, Sivakasi, 626140, Tamilnadu, India

<sup>3</sup>Institute of Agricultural Engineering, Saveetha school of Engineering, SIMATS, Chennai- 602105, Tamilnadu, India

<sup>4</sup>Department of Mechanical Engineering, SSM Institute of Engineering and Technology, Dindigul - 624002, Tamilnadu, India

<sup>5</sup>School of Mechanical, Aero, Auto and Civil Engineering, Kalasalingam Academy of Research and Education, Krishnankoil, 626126, Tamilnadu, India

<sup>6</sup>Department of Mechanical Engineering, Sharda University, Greater Noida, 201310, India

✉ aruncmr12@gmail.com

**Abstract.** The applications of aluminum-based Metal Matrix Composite (MMC) are very huge and it possesses good output when combined with Mica Powder. Because Mica is one of the naturally available crafted stones of minerals. It can bind with the materials easily in ambient conditions. This research work is to study the mechanical performance of the AL7075/Mica Powder hybrid MMC's. The varying grams of Mica powder (5 g to 25 g) are added with 500 grams of aluminum 7075. From the results obtained for the mechanical properties of AL7075/Mica Powder composite. Specimen 5 (500 g of AL 7075/25 g of Mica Powder) has excellent mechanical properties such as tensile strength of about 285 MPa, impact strength of about 18 J. The Vicker Hardness indentation is about 80 VHN, all these results define that after the addition of Mica Powder in the composite. The bonding nature of Mica with AL7075 always acts as a supporting agent in the defining of excellent mechanical properties of metal matrix composite.

**Keywords:** AL7075, Mica Powder, Tensile strength, Impact strength, Vicker's Hardness test, SEM morphology

**Citation:** Arunprasath K, Amuthakkannan P, Vijayakumar M, Sundarakannan R, Selwin M, Kavitha S, Singh Lavish Kumar. Effect of Mechanical Properties of AL7075/Mica Powder Hybrid Metal Matrix Composite. *Materials Physics and Mechanics*. 2023;51(1): 142-150. DOI: 10.18149/MPM.5112023\_12.

### Introduction

The progression of composite materials with evaluated properties known as practically reviewed materials has reformed mechanical parts fabricating, particularly in the auto, flight, guard, and biomedical businesses. The mix of composite materials is in light of the fact that each layer is unique in relation to different layers. The strength and tribology properties of

each layer rely upon the constituents present in it. On account of appearance, there is a critical improvement in the presentation and lifetime of mechanical parts like pinion wheels, heading, shafts, and cams [1]. The main impetus for AMC's production is fitting the helpful properties of the material by joining the lightweight, intense and flexible aluminum (Al) composite with reasonable earthenware particles. Especially, AMCs supported with SiC have caught much consideration from auto for example brake drums, chamber liners, cylinders and cylinder rings, and so forth, and aviation ventures like rotor vanes, and drive shafts in view of their amazing mechanical properties alongside monetary and natural manageability execution of AMCs relies upon the synthesis of the grid composite, sort of support, and producing strategies [2]. Serious plastic distortion is a productive methodology for making a high thickness of line deserts in metals. The blend of enormous shear strain with high hydrostatic tension, which is brought about, diminishes the grain size of the amalgam, opportunity agglomerates, and nano precipitation. Attributable to these benefits, Serious plastic distortion is frequently applied in the improvement of a wide scope of ultrafine-grained mass metallic composites with ultrahigh strength [3]. Changing reinforcements like Boron Carbide, Silicon Carbide, Aluminum Oxide, and Titanium Diboride are utilized to bear strength in the subsequent parts. Combinations of aluminum are generally utilized in high-temperature application regions where their mechanical properties assume a significant part in the working of the framework. Later investigations are on different scopes of network materials in combinations of Aluminum like A356, Al6061, Al7075, and comparative others are utilized for the creation of composites utilizing different techniques like diffusive projecting, mix projecting, crush projecting, and comparable different procedures [4]. 7075 aluminum composites have superb exhaustive properties and high strength at room temperature. It is one of the greatest strengths of aluminum composites as of now utilized. It has better framing properties however broad erosion opposition and helpless hotness opposition. It is moderately low in extinguishing affectability, appropriate for arrangement treatment at different temperatures, and equipped for fast normal maturing. This high-strength and lightweight combination can be utilized to fabricate climbing hardware and bike parts, and be applied to an auto body board, brake lodging, brake cylinder, guide sheet parts, and other field seat rails in flying [5]. Among different Al combinations grew up until now, the commitment of Al7075 combination to underlying applications in auto and aviation businesses is striking in light of its incredibly high strength, low thickness, high warm steadiness, and great weariness strength. Al7075 is a hotness-treatable combination, in which the development of  $MgZn_2$  hastens and improves its solidarity by scattering fortifying. Mechanical properties of these combinations can be additionally improved by huge refinement of grains by serious plastic disfigurement, which basically fuses cell separation, what's more, disfigurement [6]. Agglomeration is an extremely urgent issue in the utilization of added substances in metal framework materials. This is particularly the situation when metal framework composites are delivered by fluid projecting techniques on the grounds that these fortifications can isolate at grain limits. Furthermore, these techniques require dissolving the metals, which prompts high creation costs [7]. The use of different hard-clay particles like aluminium oxide, boron carbide, titanium carbide, silicon carbide, and rice husk as support has come about in improved mechanical and tribological attributes of composites. Numerous scientists are chipping away at SiC-based metal network composites in light of the fact that of their appealing components. Contrasted with mix projecting, metal penetration, splash deterioration, and mechanical alloying, one of the broadly utilized strategies to foster composites is the Powder metallurgy process [8]. Al7075 MMC was observed to be expanded when contrasted and Al7075 by 20% and 33%, which is because of the great strength and solidness given by the  $Al_2O_3$  which is mixed with Al7075 the particles have a holding ability that bonds with the base material. In mix projecting interaction, the support material is

presented in a persistently mixed liquid grid and afterward cast by sand, long-lasting mold, or strain pass-on projects on the off chance that the blending is done consistently, the B<sub>4</sub>C particles are similarly circulated, which invigorates a uniform all through the material [9]. Al7075 with alumina metal network composite by Stir projecting method. It is tracked down that 8% of Alumina with Al7075 has the most noteworthy mechanical properties. This proportion has the most noteworthy worth in the Brinell hardness test, Impact test, and Extreme load test. A portion of the inventive and effective assembling strategies are effectively carried out in numerous fabricating ventures to create composite materials [10]. With consistently scattered TiB<sub>2</sub> and Gr particles, the high hardness and other great properties of these fortifications can be viably utilized for the improvement of the solidarity of composites. The augmentation in a definitive rigidity of Al7075 combination and it is half and half composites are Hall-Petch reinforcing, load move strength, warm crisscross reinforcing, and precipitation fortifying. Here each fortifying is talked about one by one to see how they impact the strength of Al7075 combination furthermore, its half and half composites. Composites show a decrement in grain size likened to that of unreinforced Al7075 amalgam because of half and half fortifications. Because of the expansion in grain limit thickness, the composites [11, 12]. Al7075 compound by means of contact mix welding and finished up that 20 % volume part of nano particles of SiC with Al7075 expanded the mechanical properties of the welded joint. They announced that the mechanical properties of the welded joint are dependent on grain size, support scattering, and the holding quality among network and fortifications materials. The hardness of the contact mix prepared Cu with the B<sub>4</sub>C was expanded 42 % higher than the without these particulates [13]. Notwithstanding a slight diminishing in the primary hours of the maturing system, the electrical conductivity of the sintered examples for the most part expanded with the expansion in the maturing time [21]. The impact of ball processing time and sintering temperature on the microstructural developments, wear conduct, and mechanical and warm properties of the created composites were researched. X-beam diffractometer and examining electron magnifying lens examination showed that as the ball processing time expanded, the molecule size diminished, the homogeneity expanded the overall thickness of the Al2024 framework diminished with an increment of the nano-ZrO<sub>2</sub> particles while the clear porosity expanded [22]. Besides, critical improvement in mechanical properties, for instance, microhardness, extreme strength, reinforcing productivity, and Young's modulus. The wear rate diminished as the support content expanded while it expanded with the increment of the sliding distance and applied load [23,24]. The objective of the research work is to study the mechanical and morphological properties of chosen Al7075/Mica Powder Metal Matrix Composite for automobile, and aerospace applications.

### Materials and methods

Aluminium7075 powder of about 10-60  $\mu\text{m}$  is purchased from Chandan Steel World, Bhuvaneshwar, Mumbai, Maharashtra. Industrial White Mica powder with a particle size of 10-60  $\mu\text{m}$  purchased from the pearl enterprise, Chennai, Tamil Nadu. The stir casting method is used to prepare the composite with the graphite crucible at 680°C for 25 minutes. The preheated reinforcement is added at regular intervals to avoid unnecessary agglomeration. The reinforcement Al7075 and Mica powder were mixed with 580rpm for 15 minutes. After the mixing of the composite by maintaining 680°C, the molten mixture is pertained in the die and allows for natural cooling at ambient temperature. The same procedure is repeated for the preparation of 5 specimens with varying ratios of Al7075 and Mica powder. Figure 1 represents the experimental setup of stir casting for the preparation of the composite specimens. Table 1 represents the specimen description of the prepared composite.

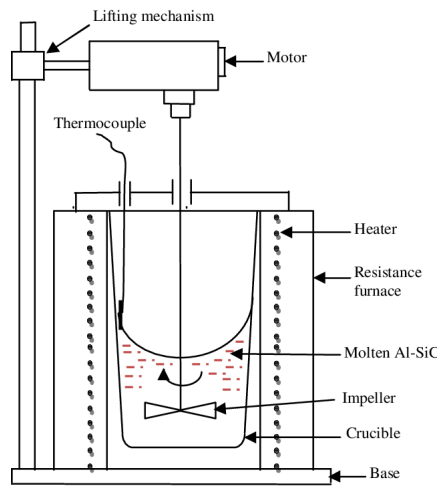


**Fig.1. Stir Casting Setup**

**Table. 1. Composite Specimen Description**

S.no	Weight of Aluminium AL7075(g)	Weight of Mica Powder(g)	Prepared Specimen Designation
1	500	0	Specimen 1
2	500	5	Specimen 2
3	500	10	Specimen 3
4	500	20	Specimen 4
5	500	25	Specimen 5

## Result and discussion

**Tensile test.** The tensile strength analysis is carried out using the universal tensile testing machine. The specimen was prepared as per the ASTM E8 standard and values are recorded with an average of five specimens. The tensile strength of the filler Mica Powder increases the tensile strength of the MMC composite also increase [14, 15]. This type of phenomenon represents the bonding and solid strengthening of the metal and the matrix. The maximum tensile peak is noted for specimen 5 about 285 MPa for the combination which has 25 grams of Mica powder with 500 grams of aluminium. Increasing the homogeneity of the particle size produces a tough bonding at the time of fabrication. This type of pocketing of mica powder may improve the tensile strength of the composite. In addition to this, the different-sized atomic combinations are readily exhibiting this type of intervention on the aluminum-based metal matrix composite [16]. Figure 2 shows the tensile strength analysis of varying grams of AL7075/Mica Powder MMC.

**Impact test.** Impact strength specifies the energy-absorbing capabilities of the material at the time of application of sudden load. At the time of the impact, event happened the workpiece material may withstand the load or break into two halves. The impact test was carried out using the Charpy impact tester with the standard of ASTM A370. For the final value calculation, the average of five specimens is taken. Figure 3 represents the impact strength analysis of AL7075/Mica Powder Metal Matrix Composite. The results of the impact study also, represent the same observation the increase in the content of Mica Powder improves the energy observing capability of the composite about 18 J. While increasing the Mica Powder content increases the bonding strength of the aluminium-reinforced composite [17]. Owing to the quality dispersion of Mica in the aluminum shows this kind of observation, during the happening of the impact event.

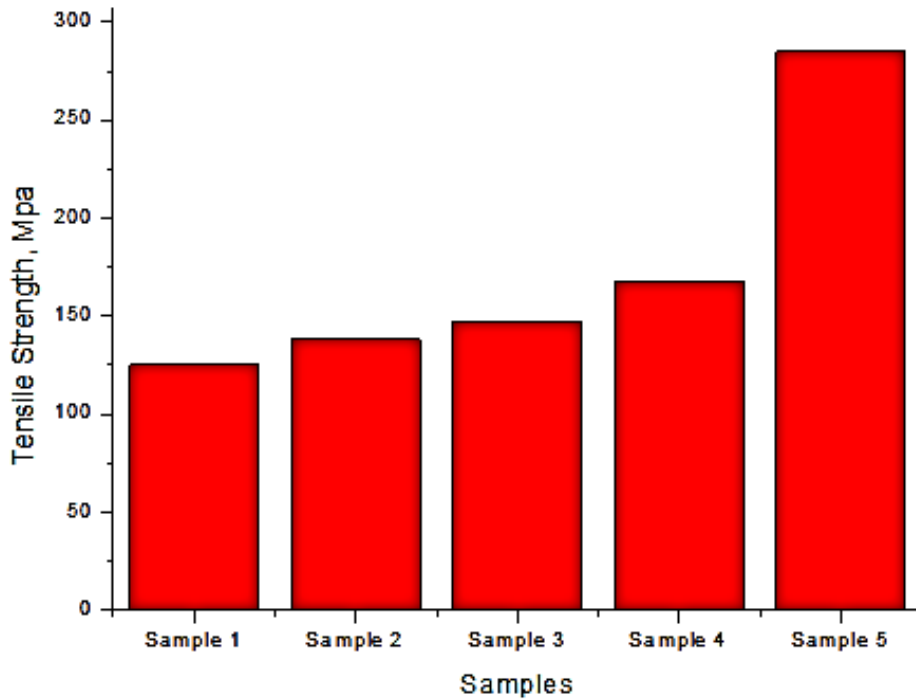


**Fig. 2.** Tensile strength analysis of Al7075/Mica Powder

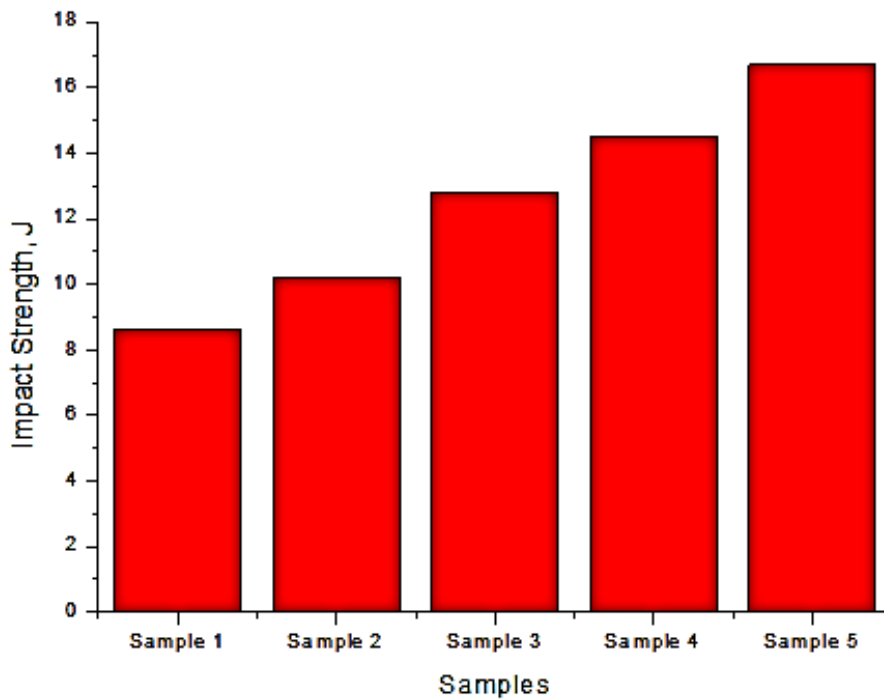


**Fig. 3.** Impact strength analysis of Al7075/Mica Powder

**Hardness test.** Hardness is one of the tests which helps to determine the deformation of the materials by means of indentation. Vicker hardness tester is used to evaluate the hardness of the prepared specimens. A load of 100 kg is applied to the composite for 20 seconds. An average of five specimens are taken for the hardness study. The increase of the filler Mica Powder is an inorganic material that produces an improved hardening condition for the composite [18]. Because the hardness value is only depending on the incorporation of powdered particles in the layers of aluminum which shows about 80 VHN for specimen 5. Figure 4 represents the Vicker Hardness Number of the prepared specimen.



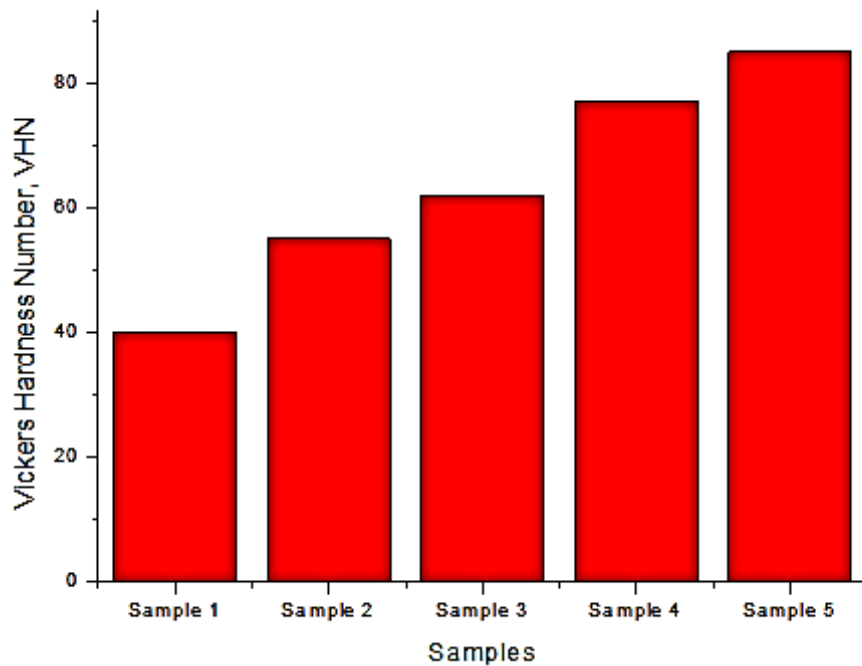


**Fig. 4.** Hardness test analysis of Al7075/Mica Powder

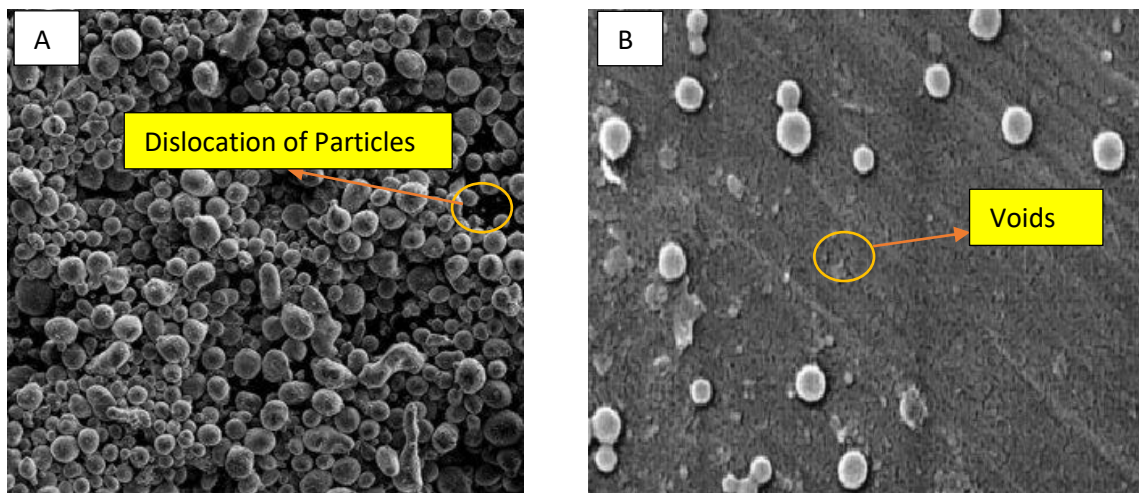


**Fig. 5.** SEM Morphology of tensile and impact fractured specimen

**SEM morphology studies.** Scanning electron microscopy is one of the effective microstructure analysis tools which helps to study the failure pattern of the composite. Figure 5 (a) and (b) show the impact and tensile failure pattern of the Al7075 and Mica powder combination of 15 micron. SEM morphology of tensile fractured specimen 5 (a) clearly locates the potential mismatch on the surface of the composite. Formation of conjunction among the composite may create nucleation of the powdered particles and convert the composite into hard particles. These hard particles of Mica Powder deposited on the surface are responsible for the dislocation of reinforcement particles on the composite. Even though they are having good agglomeration between Al7075 and Mica powder, these types of interventions may occur [19]. The high-pressure compaction of between is responsible for the happening of voids in the composite. Also, the higher stirring time leads to voids in the presence of Mica powder on Al7075 in the composite. The formation of poor



grain boundaries is responsible for the uneven breakdown of the composite at the time of impact load with some voids also noted in Fig. 5(b). The voids and hair line fins are called two-line surface disturbance which completely collapses the impact strength of the metal matrix composite [20].

### Conclusions

Alumium7075 reinforced with Mica Powder metal matrix composite is successfully fabrication using stir the casting method. To study the mechanical properties of the prepared specimens, from the results discussed in the above chapter. The following conclusions are made,

- ✓ The maximum tensile peak is noted for specimen 5 about 285 MPa for the combination which has 25 grams of Mica powder with 500 grams of aluminum. In addition to this, the different-sized atomic combinations are readily exhibiting this type of intervention on the aluminum-based metal matrix composite.
- ✓ The results of the impact study also, represent the same observation the increase in the content of Mica Powder improves the energy-observing capability of the composite by about 18 J. While increasing the Mica Powder content increases the bonding strength of the aluminum-reinforced composite.
- ✓ Owing to the quality dispersion of Mica in the aluminum shows this kind of observation, during the happening of the impact event.
- ✓ The increase of the filler Mica Powder is an inorganic material that produces an improved hardening condition for the composite. Because the hardness value is only depending on the incorporation of powdered particles in the layers of aluminum which shows about 80 VHN for specimen 5.
- ✓ Mica Powder deposited on the surface is responsible for the dislocation of reinforcement particles on the composite. Even though they are having good agglomeration, these types of interventions may occur during tensile loading conditions. The formation of poor grain boundaries is responsible for the uneven breakdown of the composite in the time of impact load with some voids.
- ✓ The better cast ability, high corrosion, low density, and high elasticity of the Al7075/Mica powder composite is one of the potential replacements for the conventional MMC's can utilize transport, automobile, aerospace, and marine applications.

### References

1. Surya MS, Prasanthi G. Effect of silicon carbide weight percentage and number of layers on microstructural and mechanical properties of Al7075/SiC functionally graded material. *Silicon*. 2021;14: 1-10.
2. Kumar A, Kaushik P, Suhrit M. Effects of cryo-FSP on metallurgical and mechanical properties of stir cast Al7075–SiC nano composites. *Journal of Alloys and Compounds*. 2021;852: 156925.
3. Kim H, Ha H, Lee J, Son S, Kim HS, Sung H, Seol JB, Kim JG. Outstanding mechanical properties of ultrafine-grained Al7075 alloys by high-pressure torsion. *Materials Science and Engineering: A*. 2021;810: 141020.
4. Raghuvaran, PJ, Baskaran J, Aagash C, Ganesh A, Gopi Krishna S. Evaluation of mechanical properties of Al7075-SiC composites fabricated through stir casting technique. *Materials Today: Proceedings*. 2021;45: 1914-1918.
5. Honghe X, Zhang Y, Peng R, Zhu L, Lu Y. Simulation and experimental study on the strength of Al7075-T6 clinched joint. *Engineering Failure Analysis*. 2021;129: 105735.

6. Sahoo BP, Das D, Chaubey AK. Strengthening mechanisms and modelling of mechanical properties of submicron-TiB<sub>2</sub> particulate reinforced Al 7075 metal matrix composites. *Materials Science and Engineering: A*. 2021;825: 141873.
7. Arsun O, Akgul Y, Simsir H. Investigation of the properties of Al7075-HTC composites produced by powder metallurgy. *Journal of Composite Material*. 2021;55(17): 2339-2348.
8. Surya MS, Prasanthi G. Effect of SiC weight percentage on tribological characteristics of Al7075/SiC composites. *Silicon*. 2022;14: 1083–1092.
9. Balasubramanian T, Ganesh M, Arunkumar M, Aswin S. Experimental studies on the wear and mechanical properties of Al7075-B<sub>4</sub>C-Al<sub>2</sub>O<sub>3</sub> composite. *IOP Conference Series: Materials Science and Engineering*. 2021;1070(1): 012125.
10. Parthiban A, Mohana Krishnan A, Radha Krishnan B, Vijayan V. Experimental Investigation of Mechanical and Wear Properties of AL7075/Al<sub>2</sub>O<sub>3</sub>/MICA Hybrid Composite. *Journal of Inorganic and Organometallic Polymers and Materials*. 2021;31(3): 1026-1034.
11. Ahmed S, Suhael, Girisha HN. Experimental investigations on mechanical properties of Al7075/TiB<sub>2</sub>/Gr hybrid composites. *Materials Today: Proceedings*. 2021;46(3): 6041-6044.
12. Ghazanlou SI, Eghbali B, Petrov R. Study on the microstructural and texture evolution of Hot Rolled Al7075/graphene/carbon nanotubes reinforced composites. *Materials Chemistry and Physics*. 2021;257: 123766.
13. Shafique J, Alrobei H, Wakeel A, Malik RA, Hussain A, Kim J, Latif M. Structural and mechanical properties of friction stir welded Al<sub>2</sub>O<sub>3</sub> and SiC reinforced Al 7075 alloys. *Journal of Mechanical Science and Technology*. 2021;35(4): 1437-1444.
14. Baba E Sai, Vinitha M, Krishna Prasad DVV. Influence of Heat Treatment on Mechanical Characteristics of Al7075/Al<sub>2</sub>O<sub>3</sub>/TiC Hybrid Metal Matrix Composite. *IOP Conference Series: Materials Science and Engineering*. 2021;1112(1): 012015.
15. Ashwini MV, Patil S, Robionson P. Evaluation of mechanical and tribological properties of AL7075 hybrid metal matrix composite reinforced with fly ash and graphite. *Materials Today: Proceedings*. 2021;45: 311-317.
16. Kumar NS. Fabrication and characterization of Al7075/RHA/Mica composite by squeeze casting. *Materials Today: Proceedings*. 2021;37: 750-753.
17. Gangadhar TG, Girish DP, Prapul Chandra AC, Karthik Raj KV. Effect of hybrid reinforcements on corrosion characteristics of Al7075 based composites. *Materials Today: Proceedings*. 2021;46(13): 5986-5990.
18. Velavan KK, Palanikumar, Senthilkumar N. Experimental investigation of sliding wear behaviour of boron carbide and mica reinforced aluminium alloy hybrid metal matrix composites using Box-Behnken design. *Materials Today: Proceedings*. 2021;44: 3803-3810.
19. James J, Annamalai AR, Muthuchamy A, Jen CP. Effect of Wettability and Uniform Distribution of Reinforcement Particle on Mechanical Property (Tensile) in Aluminum Metal Matrix Composite – A Review. *Nano materials*. 2021;11(9): 2230.
20. Ranjith R, Giridharan PK. Experimental investigation of surface hardness and dry sliding wear behavior of AA7050/B 4 C p. *High Temperature Material Processes: An International Quarterly of High-Technology Plasma Processes*. 2015;19: 3-4.
21. Bezzina S, Moustafa EB, Taha MA. Effects of metastable  $\theta$  precipitates on the strengthening, wear and electrical behaviors of Al 2519-SiC/fly ash hybrid nano composites synthesized by powder metallurgy technique. *Silicon*. 2022;14: 8381-8395.
22. Okumus M, Bulbul B. Study of microstructural, mechanical, thermal and tribological properties of graphene oxide reinforced Al–10Ni metal matrix composites prepared by mechanical alloying method. *Wear*. 2022;15: 204511.

23. Bulbul B, Okumus M. Microstructure, hardness, thermal and wear behaviours in Al–10Ni/TiO<sub>2</sub> composites fabricated by mechanical alloying. *Materials Chemistry and Physics*. 2022;281: 125908.
24. Hakam RA, Taha MA. Study of mechanical properties and wear behavior of nano-ZrO<sub>2</sub>-hardened Al2024 matrix composites prepared by stir cast method. *Egyptian Journal of Xhemistry*. 2022;65: 307-331.

## THE AUTHORS

**K. Arunprasath** 

e-mail: aruncmr12@gmail.com

**M. Vijayakumar** 

e-mail: vijayam74@gmail.com

**M. Selwin** 

e-mail: selwin123@gmail.com

**Lavish Kumar Singh** 

e-mail: lavish.singh2011@gmail.com

**P. Amuthakkannan** 

e-mail: amuthakkannanp@gmail.com

**R. Sundarakannan** 

e-mail: sundarakannan.r@gmail.com


**S. Kavitha** 

e-mail: skavitha@klu.ac.in

## Effect of compression precracking on near threshold region for AISI 4340 steels considering compliance measurements

Salim Çalışkan , Rıza Gürbüz 

Middle East Technical University, Ankara, Turkey

caliskan.salim@metu.edu.tr

**Abstract.** Determining long crack threshold as a design criterion is not a new research topic; however, some anomalies because of different test methods in literature keep it vogueish. Inaccurate estimations may result in considerable variation on corresponding endurance stress for components with small crack size. Accepted approach compared to traditional methods is to perform compression-compression precracking before crack growth tests by eliminating history effects and accurately estimating long crack threshold value. Load history effects may result from specimen configuration and test procedure applied. The scale of yielding during precracking cannot be underestimated and these residual stresses have an effect on crack growth rates, even if limited by stress relief in the plastic region. Naturally formed precrack will propagate until diminishing size of the corresponding tensile zone responsible for crack growth. Compression-compression precracking under constant amplitude loading is performed to form non-propagation crack. The advantage of compression precracking is to provide a fully open crack that eliminates possible closure effects. In the scope of this paper, different stress ratios will be tested and the effect of compression precracking on near threshold will be investigated. To present reliable and accurate crack measurement that affects long threshold directly, compliance curves will be also introduced with this article.

**Keywords:** Steel, Fatigue, Compliance, Crack growth, Threshold

**Acknowledgments.** Authors acknowledge Turkish Aerospace Inc.

**Citation:** Çalışkan S, Gürbüz R. Effect of compression precracking on near threshold region for AISI 4340 steels considering compliance measurements. *Materials Physics and Mechanics*. 2023;51(1): 151-167. DOI: 10.18149/MPM.5112023\_13.

### Introduction

Damage tolerant design approach is used for components having high cycles of operation life such as transmission parts and service life and inspection intervals are specified based on fatigue crack growth data [1]. Fatigue crack propagation behavior is caused by intrinsic and extrinsic mechanisms. Intrinsic mechanism can be controlled by monotonic and cyclic strains ahead of crack tip. Brittle materials exhibit monotonic loading fracture; on the other hand, ductile ones show cyclic deformation because of crack blunting and re-sharpening in the vicinity of steady state crack propagation. Cyclic plastic deformation is the reason for fatigue crack growth with below fracture toughness loading over ductile materials. Generation of residual stresses because of plastic deformation after unloading results in change in local stress ratio and fatigue crack growth behavior is severely affected as if applied additional loading [2]. Steels exhibit strain hardening under deformation and expected stress redistribution is to be less and results as smaller plastic zone size ahead of crack tip [3]. Fatigue cracks grow through slip planes with

maximum resolved shear stress and shear stress changes grain to grain, therefore crack path has a rough surface.

Historically, compression precracking is proposed for materials having low fracture toughness and possible failure occurs under tensile precracking conditions. Compression precracking was proposed by Hubbard to eliminate possible load history effects and generate accurate crack growth rates around near threshold [4]. After compression precracking, non-propagating crack needs to advance at least three monotonic compressive zone sizes to reach steady state crack growth conditions. Compression precracking followed by constant amplitude loading is considered as favorable procedure for analyzing threshold behavior of long cracks at low stress amplitudes.

Pearson observed propagation of small cracks below long crack threshold stress intensities defined by test standards [5]. Then, Newman assessed different behavior of small and long cracks around near threshold on remote crack closure effects that are effective on long cracks under constant amplitude loading [6]. Small cracks below certain length grow faster than long ones because of absence of crack closure. Elber identified crack closure concept under alternating loading that affects residual stress distribution and plastic wake around crack flanks, and this phenomenon is known as load history effects on crack propagation [7]. James et al. studied possible load history effects caused by compression precracking as tensile residual stress that increased threshold value. Load history effects can be due to specimen configuration and applied test procedure. Scale of yielding during precracking cannot be underestimated and has an effect on crack growth rates, even though those residual stresses are limited in plastic zone due to stress relief [8]. Fanning around near threshold is caused by load history and environmental effects resulting in remote closure. Maierhofer et al. described crack growth rate model for small cracks having small scale, yielding by building up crack closure effects and Modified NASGRO equation. Each closure mechanism occurs entirely after certain crack extension. Plasticity induced crack closure increases because of increasing plastic zone size until definite crack size and becomes constant [9]. Some equations were introduced to correlate crack growth rate with  $\Delta K$  (stress intensity factor) for all three regions of  $da/dN$  ( $a$ : crack size and  $N$ : number of fatigue cycles) curve. Steady state and unstable crack growth regions are generally fitted well, but problematic region is around near threshold, especially for lower stress ratios [10].

Fatigue limit can be expressed as resistance of material in terms of propagation of nucleated cracks and corresponding threshold stress for fatigue limit needs to be overcome microstructural barriers for growth process. Therefore, fatigue limit is directly correlated with microstructure properties like grain dimensions at onset of fatigue initiation and initial growth phase can also be called as microstructural threshold. By controlling microstructure through heat treatment enables to have superior fatigue properties of material via excellent mechanical properties. Microstructurally short cracks (on the order of grain size) endure crack propagation because of microstructural barrier resistance and arrest results in preserving fatigue limit unchanged until certain size. Those cracks generally nucleate on surface, and threshold stress is called smooth or plain specimen fatigue limit. However, long cracks have sufficient driving force for growth and fatigue limit decreases by increasing crack size [11]. Applied  $\Delta K$  needs to be higher than threshold value that is related with crack closure phenomenon for growth process for long cracks. Physically small cracks are between microstructural small cracks and long cracks and crack closure starts to become effective, even though they are also sensitive to microstructural changes. This range can be considered as 50  $\mu\text{m}$  and 0.5 mm crack size for low carbon steels [12]. Below 50  $\mu\text{m}$ ; microstructural shot crack is prevailing, and fatigue limit not affected by microstructural barriers. However, fatigue limit starts to decrease parabolically increasing crack size until reaching long crack size region. Then; fatigue limit has a linear relation with increasing crack size because of losing crack closure effects that is responsible

asymptotically decrease for physically short cracks. Number of cycles in terms of fatigue life are spent during propagation phase for most of the short cracks.

Small crack growth is affected by microstructural changes, large scale yielding at crack tip and crack closure as driving force for propagation. In pearlite phase, crack propagation rate decreases because of thin ferrite lamellar on the microstructure; however, cementite part is responsible for rapid propagation Linear Elastic Fracture Mechanics (LEFM). In microstructure containing ferrite and bainite phase; cracks start on ferrite phase and propagate through ferrite across retained austenitic regions [13]. Fatigue growth for small cracks needs to have higher internal and applied stress because of less closure effects. By increasing crack length, internal stresses due to dislocation pile-up to sustain crack growth decrease, which is inversely proportional with R curve change. Specimen with short cracks requires higher stress amplitude and large number of cycles to develop fatigue damage near crack tip, necessary growth of crack [14]. Short cracks grow very slowly by in high propagation rates compared to long cracks. Threshold of stress intensity range for small cracks increases until asymptote to long crack threshold value by increasing crack length and variation of this phenomenon is called R-curve or resistance curve to fatigue crack propagation. This curve serviceably helps to evaluate fatigue limit of materials having small size defects [15]. SN curves can be considered as a function of small crack initiation in classical safe life design approach [16].

Source of internal stresses is stress concentration regions such as notch, hole, microstructural defects etc. and internal stress asymptotically decreases by distance move away. However, applied stress increases by increasing crack length and there exist competitions in terms of total stress. If applied stress is less than  $\Delta K_{th}$  (threshold stress intensity factor) and  $K_{max}$  (maximum stress intensity factor), crack is arrested since total stress is insufficient for propagation. Elimination of internal stress is attributed to fatigue crack growth behavior of long cracks. Local stress ratio will be higher at crack tip than remote load ratio because of existence of internal stresses. Essentially, equal driving forces exist for fatigue crack growth behavior between short and long cracks in case of all the forces included. Compressive residual stresses result in extra stiff characteristic to material and higher driving forces require for crack growth. Therefore, compressive residual stresses enhance crack closure. Change in grain boundary orientation due to strain concentration may be the reason for arresting of small cracks [17].

Short crack behavior exhibits unlike than long crack in terms of difference in crack closure, microstructural sensitivity and relative plastic zone size based on crack length. It is known that short cracks grow at higher propagation rates. Basically, small cracks can be classified into four groups. Microstructural small crack: it is less than grain size. Mechanically small crack: it is less than plastic zone size. Physically small crack: it is less than a unity, so crack closure is fully formed (considered as 1 mm). Chemically small crack: it depends on crack tip environment and may be up to 10 mm in size. Short crack growth rate is faster than long ones, and even they can propagate below long crack threshold region. Long fatigue life can be reached by understanding the near threshold concept and choosing design loads around threshold value. Damage tolerant design allowed to use structures with crack with known propagation rates and specifying inspection interval for remedy. Previously, safe life approach focused only operation lifetime of a component and replacing part after retirement without inspected whether existence of a crack or not. Safe life design is still in use for primary structures based on defining fatigue limit; however, damage tolerant design approach become popular because of extended life of components. Therefore, crack propagation rates become a significant issue during design phase. On material selection phase, it is desired to be high fatigue crack growth resistance with high threshold value fulfilled with soft material that is in contrast with fatigue limit. Therefore, optimum one is chosen for design material by providing less crack growth rate and high fatigue limit [18]. Fatigue crack propagation behavior for small cracks has different curve shape compared to long ones. Many analytical models are introduced to predict



crack growth rate. It is known that short cracks will extend their crack size even though applied stress is below the corresponding long crack threshold value. Therefore, residual life of a component is remarkably affected with altering threshold value. Change in  $1 \text{ MPa}\sqrt{\text{m}}$  on threshold value results in about 18% change in residual characteristics of a component [19].

### Experimental Procedure

Crack growth test specimens were manufactured from AISI 4340 steel with a chemical composition of .38% C, .65% Mn, .7% Cr, 1.65% Ni, .2% Mo, .025% P and S, bal. Fe (in wt%) to discover crack propagation behavior of the steel having high toughness and fatigue performance that makes it good candidate as an aerospace grade material. Crack growth tests were carried out by Single Edge Bending (SEB) specimens. In total, four specimens were used for crack growth tests, and they were extracted in rolling direction. After the material was out of stock, heat treatment was applied per AMS 2759-1D [20]. Accordingly, the rectangular bar was initially normalized at  $900^\circ\text{C}$  for 90 minutes then air cooled, austenitized  $816^\circ\text{C}$  for 60 minutes followed by quickly oil quenched and finally tempered  $600^\circ\text{C}$  for 3 hours. After heat treatment, bainite and ferrite phases are available in microstructures as shown in Fig. 1. Machining parameters were 450 m/min cutting speed, 0.25 rev/min coarse gain and 0.1 rev/min fine gain. The dimensions of specimens were 110 mm in length, 24 mm width and 12 mm thickness by ensuring plain strain condition specified on ASTM E647 [21]. Also, notch section with 8 mm width was produced by Electro Discharge Machining (EDM) method to provide high accuracy in terms of positioning. Mechanical properties can be summarized as 1080 MPa tensile strength and 29 HRC hardness.

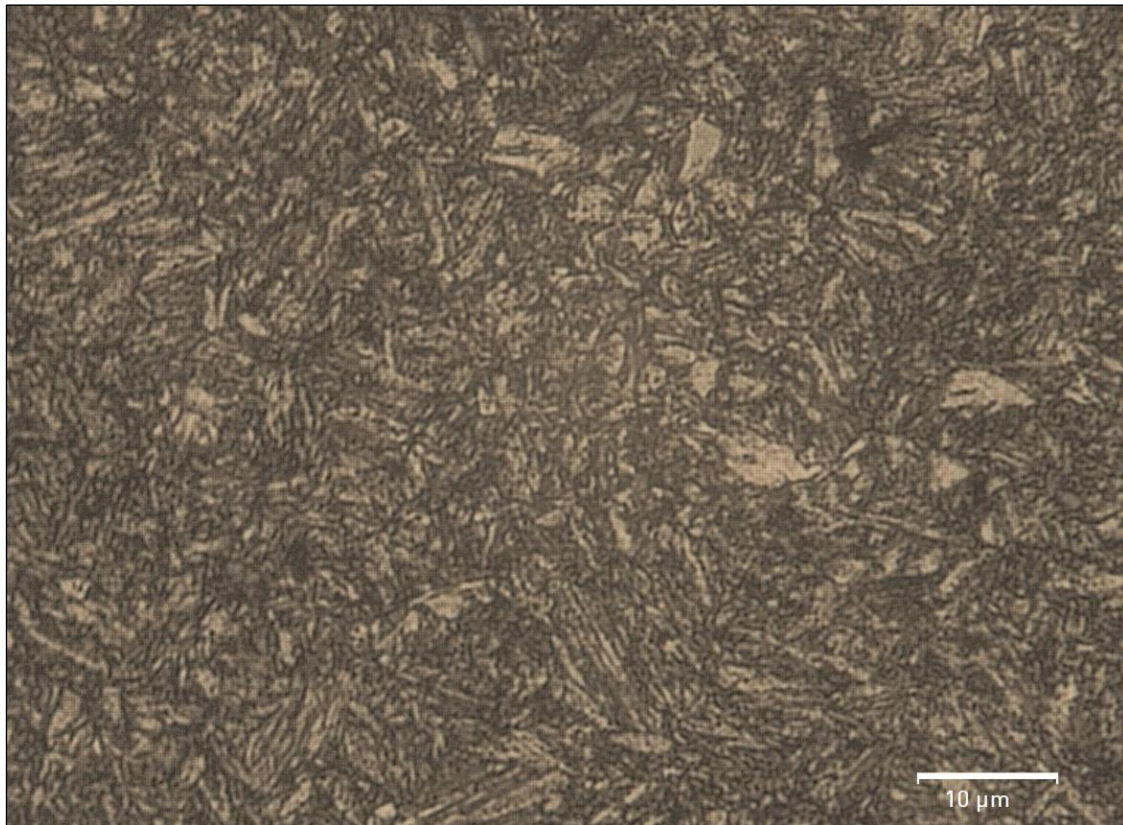


**Fig. 1** Micrograph of steel specimens

Crack propagation tests were carried out under laboratory conditions ( $23\pm 2^\circ\text{C}$  and  $50\pm 5\%$  RH) per ASTM E647. Specimens were cyclically loaded by exciting sinusoidal wave form under 80 Hz test frequency on RUMUL cracktronic test system with stress ratio  $R$  of 0.1.

## Results

### Compliance Method

Crack length measurement can be done by different methods such as compliance, potential drop, laser interferometry and ultrasonic isoscanning. Among them, compliance technique is considered the most common method for estimating crack length. Compliance method is eligible for isotropic materials such as metals that exhibit linear elastic behavior by handling load and displacement data to determine crack propagation. The basic idea behind this method is based on the concept that stiffness decreases with increasing crack length on the specimen. Therefore, calibration curve correlates relationship between crack length and compliance. Compliance method is evaluated for a limited range in terms of normalized crack size. It is also attributed as elastic compliance of specimen because of introducing unloading part of elastic-plastic range, and it is a function of crack length. Therefore, compliance value changes by alternating crack length, which is inversely proportional to specimen size.

Closure phenomenon in fatigue cracks is based on continuously closing from crack tip, resulting in plasticity induced crack closure that alters compliance consistently on load-displacement curve. Friction of contact surfaces and plastic deformation result in hysteresis on the compliance curve that makes determination of opening stress more cumbersome. By introducing  $\Delta K_{eff}$  (effective stress intensity factor) rather than using  $K$  (stress intensity factor) and  $R$  (stress ratio) together, stress ratio effect on fatigue crack growth can be significantly eliminated. As is known, plasticity induced crack closure is the responsible mechanism for varying crack growth rates under different stress ratios. It was observed that crack opening moment leads to change in compliance measurements. Compliance method is useful to monitor crack length of structures under alternating loading. It gives reasonable opening stress value from load-displacement curve in the range of 0.3 to 0.65 times specimen width in terms of crack length. Opening stress can also be estimated by following equation for constant amplitude loading conditions [22]:

$$\frac{S_0}{S_{max}} = A_0 + A_1 * R + A_2 * R^2 + A_3 * R^3 \quad \text{for } R \geq 0 \quad (1)$$

$$\frac{S_0}{S_{max}} = A_0 + A_1 * R \quad \text{for } -1 \leq R < 0 \quad (2)$$

$$A_0 = (0.825 - 0.34 * a + 0.05 * a^2) [\cos (\pi * S_{max} / 2\sigma_0)]^{1/a} \quad (3)$$

$$A_1 = (0.415 - 0.071 * a) * (S_{max} / \sigma_0) \quad (4)$$

$$A_2 = 1 - A_0 - A_1 - A_3 \quad (5)$$

$$A_3 = 2A_0 + A_1 - 1 \quad (6)$$

where  $\sigma_0$  is the flow stress,  $S_0$  is opening stress,  $S_{max}$  is maximum applied stress,  $R$  is stress ratio,  $a$  is constraint factor and  $A_0, A_1, A_2$  and  $A_3$  are the coefficients.

A constraint factor needs to be defined to discover stress state ahead of crack tip. Corresponding factor equals to 1 for plain stress conditions and 3 for plain strain conditions. Crack growth tests around near threshold were conducted under plain strain conditions in a controlled environment; therefore, later one was adopted for crack opening stress evaluation.



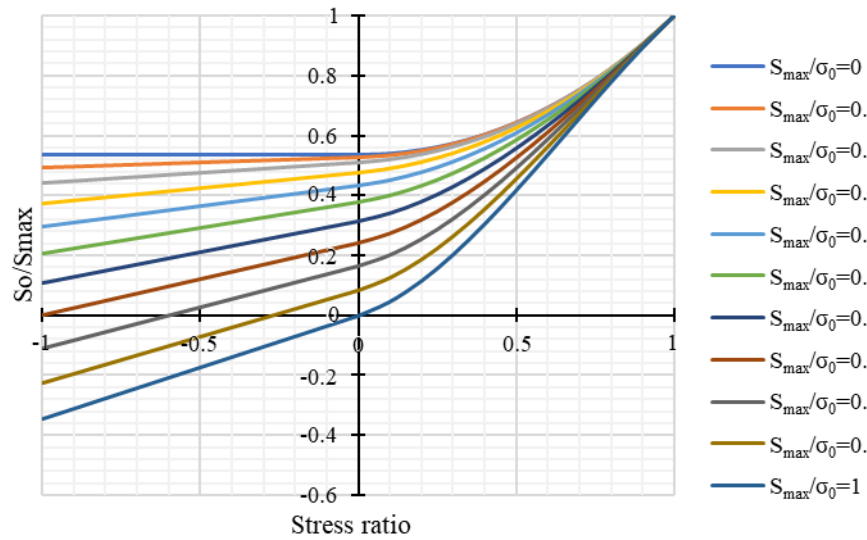


**Fig. 2** Variation of normalized crack opening stress with stress ratio for constraint factor equals to 1

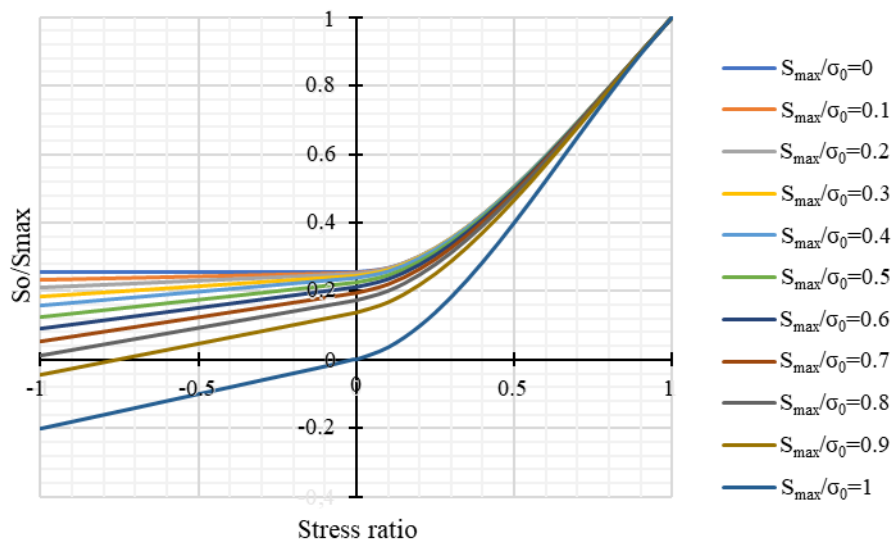


**Fig. 3** Variation of normalized crack opening stress with stress ratio for constraint factor equals to 3

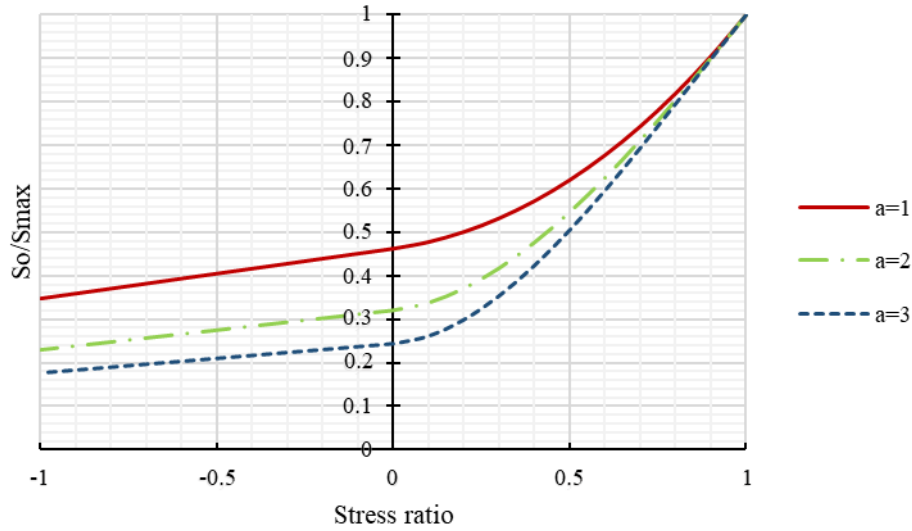


**Fig. 4** Variation of normalized crack opening stress with stress ratio in case of  $S_{max}/\sigma_0=1/3$

As seen from the graph, normalized crack opening stress exhibits lower value with increasing constraint factor, regardless of stress ratio.

Determining compliance by elastic unloading method is proposed by Clarke [23] in order to determine crack length and plastic work fragment ahead of crack tip. Compliance is also called as inverse stiffness function of crack length. Therefore, the relation between crack length and compliance is written in the form of following formulation:

$$EBC = f\left(\frac{a}{w}\right) \quad (7)$$

where  $E$  is elastic modulus of material,  $B$  is thickness,  $C$  is compliance,  $w$  is width and  $a$  is crack size.

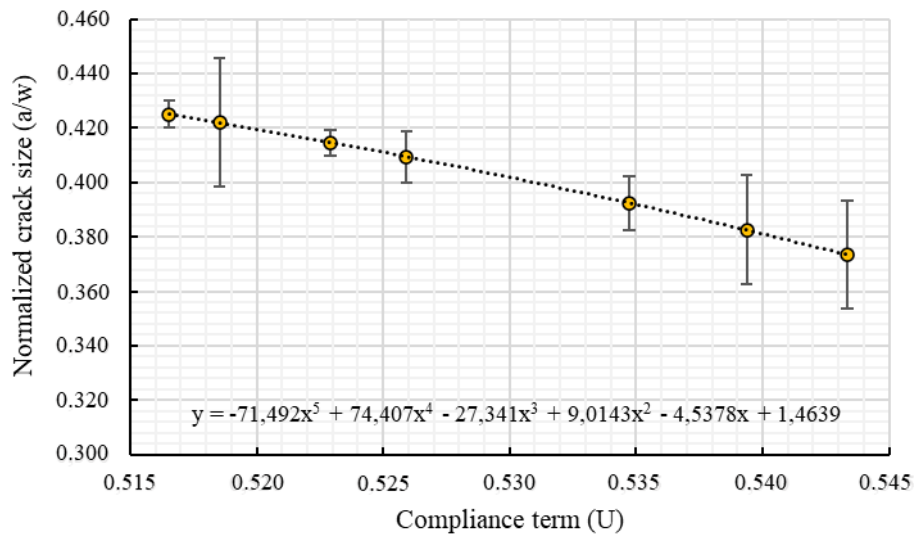


**Fig. 5** Determination of crack size by compliance

For specimens with shallow cracks the following equations can be applied if the normalized crack size ( $a/w$ ) is between 0.05 and 0.45 for SEB specimens [24]. This correlation is performed by least square polynomial regression.

$$\frac{a}{w} = 1.01878 - 4.5367 * u + 9.0101 * u^2 - 27.333 * u^3 + 74.4 * u^4 - 71.489 * u^5 \quad (8)$$

$$u = \frac{1}{\sqrt{\frac{BWCE}{S/4} + 1}} \quad (9)$$

where  $u$  is dimensionless compliance,  $S$  is span length of specimen.

During tests, crack sizes were measured at certain intervals and its correlation with compliance term was examined as shown in Fig. 5.

Compliance measurements were performed on unloading specimen to prevent possible errors because of inelastic strains while calculating slope of displacement versus load data. Compliance is also defined as inverse stiffness of material, and corresponding data contains nonlinearity at maximum and minimum values. Therefore, 10% of upper and lower part was omitted to prevent nonlinear effects and slope was determined via the least square regression fits on unloading part of curve. The accepted approach is to apply the fifth order polynomial fit proposed by Hudak and Saxena [25]. Even though compliance change may not be observed at high stress intensity factors because of stabilized crack, compliance variation can be observed at lower stress intensity factor, especially near thresholds.

To obtain accurate compliance value, 100 data pairs sampling rate is needed per each cycle. Among them, unloading part that is 50 data pairs is used to estimate opening stress. To determine opening stress, fully open crack slope value is firstly determined by help of least square. ASTM method uses the least square fit on the upper part of load-displacement curve which is in the range of about 25% to determine compliance value as shown in Fig. 6.

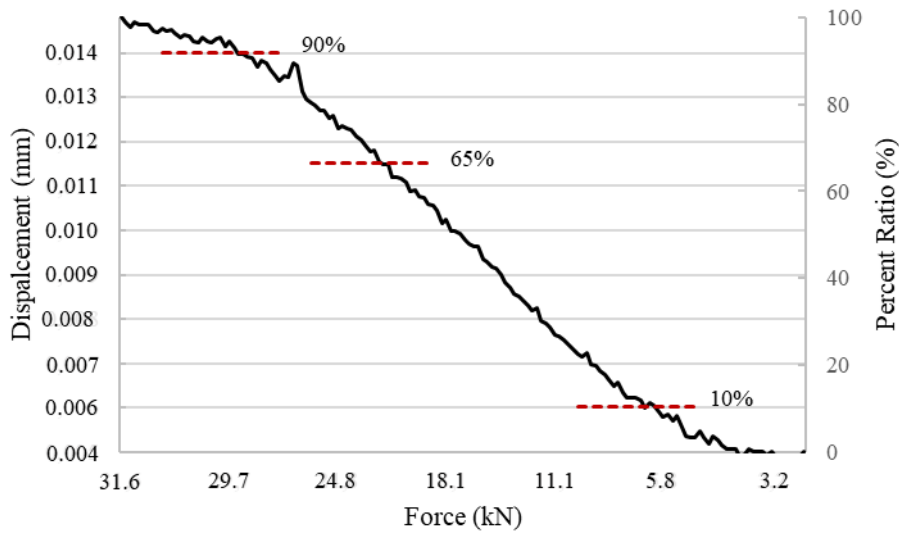


**Fig. 6** Load-displacement curve

Compliance offset method was used to determine opening stress by introducing loading segment and overlapping range. In this study, loading segment was defined as 10% sliding on fully open part and overlapping range between each segment was 5% and variation from this slope gives opening stress by introducing specific deviation on slope value. This deviation can vary with sampling rate, therefore a larger sampling rate gives more reliable results.

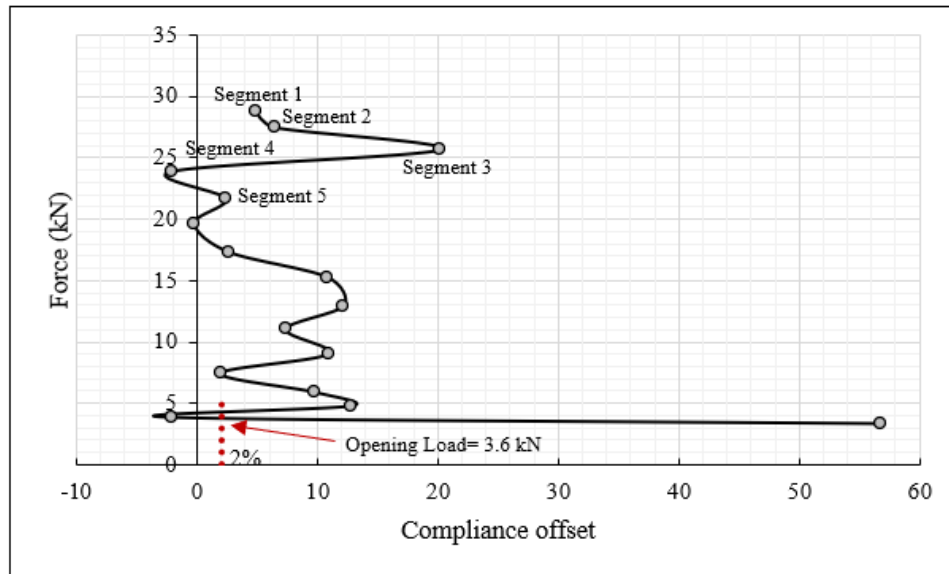


**Fig. 7** Compliance offset method

High variability in compliance offset data resulted because of scattering in the data; nevertheless, the opening load can be estimated at 3.6 kN per ASTM assumption of 2% deviation given on Fig. 7.

Even though compliance change may not be observed at high stress intensity factors because of stabilized crack, compliance variation can be observed at lower stress intensity factor especially near thresholds. Compliance measurements were done throughout threshold tests and variation of crack size with compliance is shown in Fig. 8.

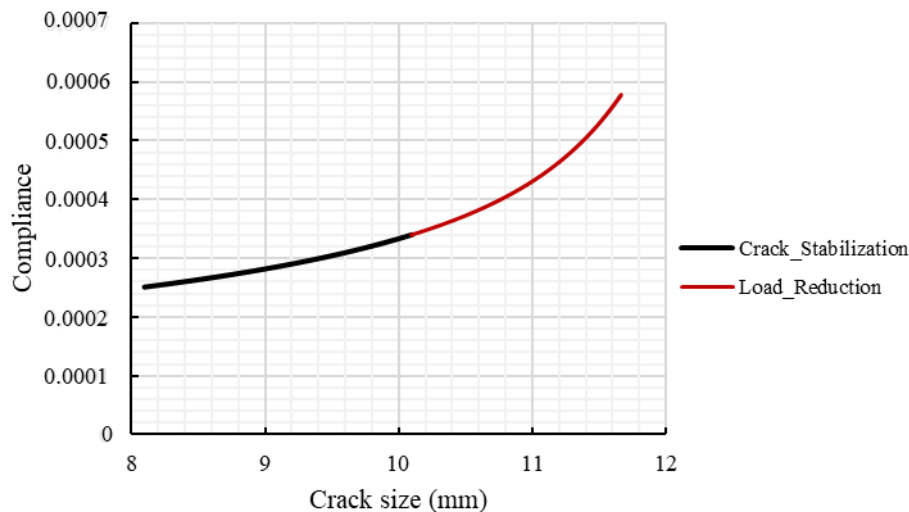


**Fig. 8** Compliance change during each phase of test

### Compression Precracking

Compression precracking is a method to obtain fatigue crack growth data with minimal load history effects. Possible reason for inaccurate threshold value is majorly load history effects arising from test procedure, specimen size and test configuration. In case of higher applied precracking loading, remote closure takes place and reduces driving force and results in higher threshold value. The advantage of compression precracking is that stress intensity is below zero while crack closing on pre-cracking period, therefore crack will directly open and not affected

by load histories under constant amplitude fatigue growth test. During compression precracking, monotonic compressive zone forms after first loading case and tensile yielding ahead of notch takes place after unloading and tensile plastic zone forms inside the compressive zone. As loading continues through testing, a cyclic plastic zone forms that results in small scale yielding and crack propagation. After crack keeps propagation, residual stress will relax and cyclic plastic zone size diminishes. It continues up to monotonic compressive zone size, then crack is arrested because of decreased driving force for crack growth. Advantageous of compression precracking is to provide fully open crack which eliminates possible crack closure effects, therefore it results in less crack propagation rates at low stress intensities. Crack growth rate around near threshold depends on increased stress intensity due to crack growth and ascending threshold because of arising crack closure effects. After certain length propagation near threshold value, crack closure builds up becomes slower and increase of stress intensity gets dominant for crack extension.

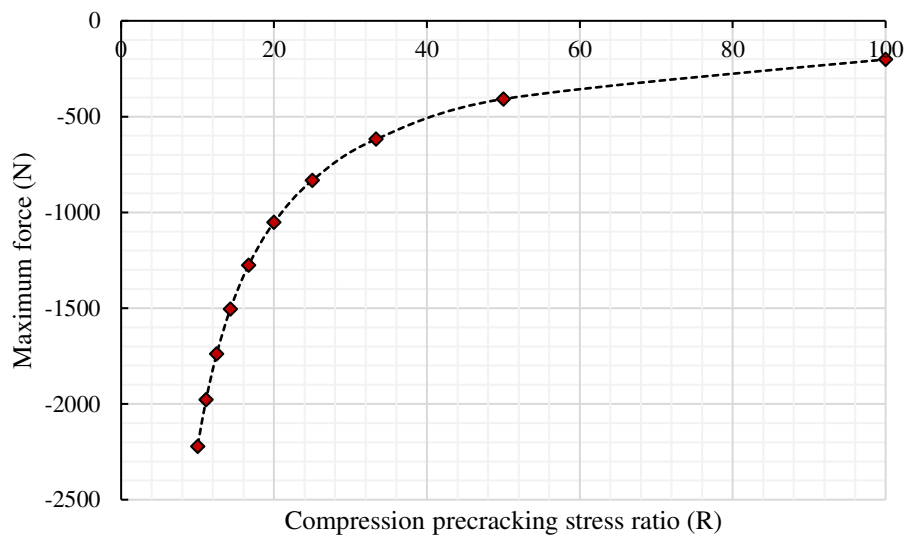


**Fig. 9** Variation of maximum precrack force with stress ratio

Before compression, precracking; stress concentration around crack tip was done via razor blade operation. Razor blade is accepted as beneficial method for forming sharp crack around 20  $\mu\text{m}$  because of little plastic deformation for precracking. After EDM notch preparation, the notch is sharpened by razor blade with 1  $\mu\text{m}$  diamond paste. EDM notch is machined by 30  $\mu\text{m}$  in diameter wires for precise dimensions. Precracking tests were carried out under constant amplitude compressive loading that enables tensile yield ahead of crack tip, and this tensile zone is responsible for straight and natural crack. By extension of fatigue crack, tensile cyclic plastic zone decreases because of relaxation of internal stresses and crack arrests after reaching on monotonic compressive zone. Amount of crack growth for precracking can be correlated with compressive plastic zone size. Arrested crack is called as non-propagating crack under compressive loading because of not available driving force. Compressive precracking tests were performed at stress ratio:  $R=10$ ,  $R=20$  and  $R=40$  via four point bending setup on RUMUL resonant fatigue test system by keeping constant  $\Delta K$  for each case. Test loads were determined based on Irwin plastic zone assumption. Lower and upper roller distance was 24 mm for each case, and oscillatory load was calculated as 20 kN for compression precracking tests. By increasing stress ratio, maximum force converges to zero as shown in Fig. 9 and minimum force converges to -20 kN in case of predetermined 10 kN amplitude loading condition. In other words, fatigue crack threshold values for compression precracked specimens with higher stress ratio converges to proximate threshold values after certain load ratio.

Therefore, R of 40 for compression precracking was chosen as the highest stress ratio, since the threshold values for higher stress ratios will resemble to each other.

To identify the effect of compression precracking on near threshold regime, three specimens were tested under different stress ratios as shown in Fig. 10 and one of the specimens not precracked for comparison. Compression precracking loading is estimated based on an Irwin tip radius of 0.25 mm over plain stress condition. Under subsequent cyclic loading, cyclic plastic zone size decreases because of relation of residual stresses and this results in decreasing driving force for crack propagation and crack arrests around monotonic compressive zone.

$$r_{p, \text{ Plain Stress}} = \left(\frac{1}{2\pi}\right) \left(\frac{K_{max}}{\sigma_y}\right)^2 \quad (10)$$

where  $r_p$  is Irwin radius,  $K_{max}$  is maximum stress intensity factor and  $\sigma_y$  is yield strength of material.  $K_{max}$  can be calculated by given equations below;

$$K_{max} = \left(\frac{Y * M_{max}}{B * \sqrt{(W)^3}}\right) \quad (11)$$

$$Y_{SEB} = 6 * \left(\frac{\sqrt{\left(2 * \tan\left(\frac{a}{W}\right)\right)}}{\cos\left(\frac{a}{W}\right)}\right) * (0,923 + 0,199 * \left(1 - \sin\left(\frac{a}{W}\right)\right)^4) \quad (12)$$

where  $M_{max}$  is maximum moment,  $B$  and  $W$  are thickness and width of specimens respectively,  $Y$  is geometry factor,  $a$  is crack size of specimen including notch length.

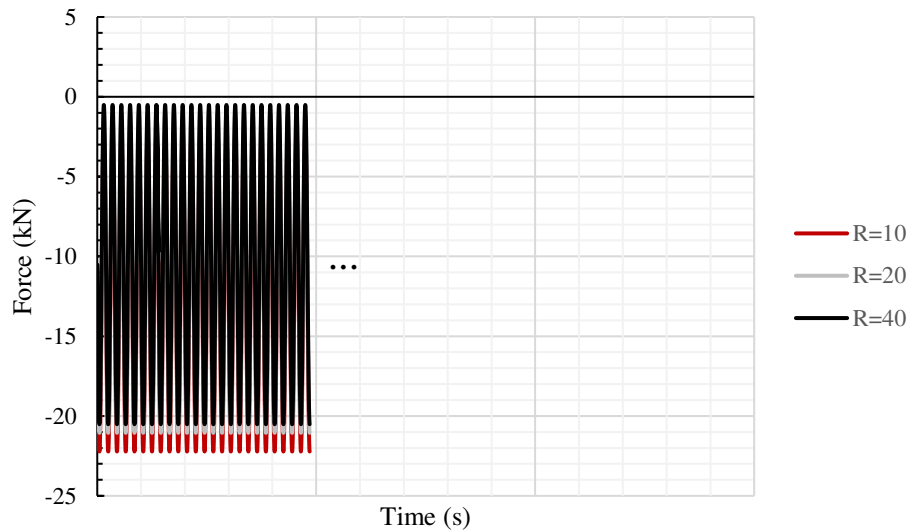


**Fig. 10** Load profile of compression precracking for different stress ratios

Tests were continued until  $2E+06$  cycles, then non-propagating crack was measured through optical microscope for each specimen as shown in Fig. 11. After compression precracking, non-propagating crack needs to advance at least three monotonic compressive zone sizes to reach steady state crack growth conditions. Non-propagating crack size was around 0.2 mm or less, and it is known that precracking size is less than cyclic tensile zone consisting of after unloading. In order to generate reliable fatigue crack growth data, precracking size needs to be outside monotonic compressive zone by ensuring small scale yielding ahead of crack tip. This is achieved by tensile fatigue loading after compression precracking in order to be free in terms of residual stresses.

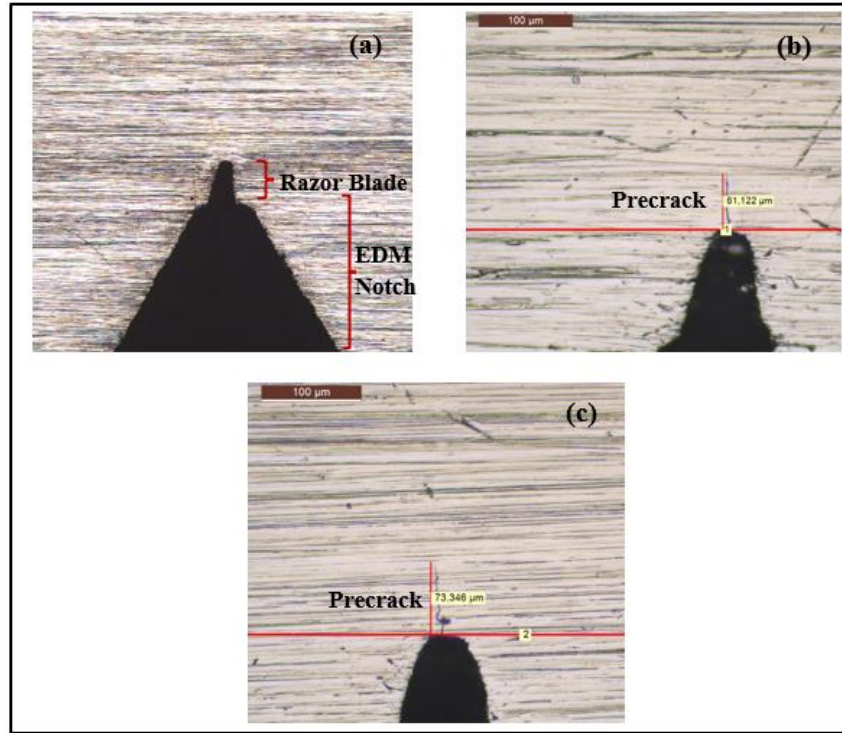


**Fig. 11** Non-propagating crack after compression precracking:  
a) Razor blade application before precracking; b) Front side micrograph;  
c) Back side after formation of non-propagating crack

Constant amplitude loading is performed just below the threshold value until increased crack propagation rate slightly. In this point, most annoying part is to estimate initial  $\Delta K$  value, since initial data is affected by tensile residual stresses from precracking. Tests were initiated at small stress intensities to propagate crack. After  $5E+05$  cycles, load increment was increased as 10% in case of not observed crack propagation. This sequence is continued until crack propagation having stabilized rate. Crack size having at least two- or three-times plastic zone size enables to reach steady state crack growth rate under constant amplitude loading after providing 1-1.5 mm crack advancement. During propagation phase, crack plane is yielded and formed residual stresses affects propagation of crack beyond plastic zone. Crack arrest is caused by residual stresses and loading below threshold stress. Therefore, residual stress effects are eliminated for following constant amplitude testing in case of pre-crack size is around plastic zone size. In this study,  $\Delta K$  initial was chosen as  $4.5 \text{ MPa}\sqrt{\text{m}}$  for  $R$  of 0.1. Then, a minimum of 1.5 mm of crack propagation was allowed to ensure that the crack was stabilized.

Load reduction method was followed after crack stabilization to find out precise threshold value around  $1E-10$  crack growth rate. At least five data points were observed that test was stopped by assuming crack not propagating around near threshold region because of dominant closure effects on crack growth rate.

NASGRO crack growth approach was used to estimate  $\Delta K_{th}$  while post-processing of the data analysis [26]. Expression is given by following equation;

$$\frac{da}{dN} = C \left( \frac{(1-f)}{(1-R)} \Delta K \right)^n \frac{\left( 1 - \frac{\Delta K_{th}}{\Delta K} \right)^p}{\left( 1 - \frac{K_{max}}{K_c} \right)^q} \quad (13)$$

where crack growth rate ( $da/dN$ ) depends on following parameters:  $C$  and  $n$  are constants,  $f$  is Newman's crack opening function,  $p$  and  $q$  are responsible for slope change in threshold and unstable crack growth region respectively,  $\Delta K$  is stress intensity factor range,  $\Delta K_{th}$  is threshold



stress intensity factor range,  $K_{max}$  is maximum applied stress intensity factor,  $K_c$  is critical stress intensity factor and  $R$  is stress ratio.

Newton's crack opening function ( $f$ ) can be calculated by following formula [21];

$$f = \frac{K_{opening}}{K_{maximum}} = \begin{cases} \max R \text{ or } (A_0 + A_1 * R + A_2 * R^2 + A_3 * R^3) & R \geq 0 \\ A_0 + A_1 * R & R < 0 \end{cases} \quad (14)$$

where  $K_{opening}$  is opening stress intensity factor and  $K_{maximum}$  is maximum stress intensity factor.

The equation fits fatigue crack growth data using the logarithmic square method by minimizing errors. The material constants  $C$  and  $n$  were taken as the fitting parameters and the parameter  $q$  was set to zero because of only interested in near threshold region [27].

The following NASGRO equations can be used to evaluate the threshold change as a function of the stress ratio [28].  $C_{th}^p$ ,  $C_{th}^m$  and  $\Delta K_1$  are materials constants, they are estimated by least square fitting with fatigue threshold ( $\Delta K_{th}$ ) data.  $\Delta K_1$  is the stress intensity threshold range as the stress ratio approaches to 1.  $\Delta K_1^*$  takes into account small crack parameter that is called as  $a_0$  [29].

$$\Delta K_{th} = \Delta K_1^* * \left[ \frac{\left( \frac{1-R}{1-f} \right)^{(1+RC_{th}^p)}}{(1-A_0)^{(1-R)(C_{th}^p)}} \right] \quad R \geq 0 \quad (16)$$

$$\Delta K_{th} = \Delta K_1^* * \left[ \frac{\left( \frac{1-R}{1-f} \right)^{(1+RC_{th}^m)}}{(1-A_0)^{(C_{th}^p - RC_{th}^m)}} \right] \quad R \geq 0 \quad (17)$$

$$\Delta K_1^* = \Delta K_1 * \sqrt{\frac{a}{(a+a_0)}} \quad (18)$$

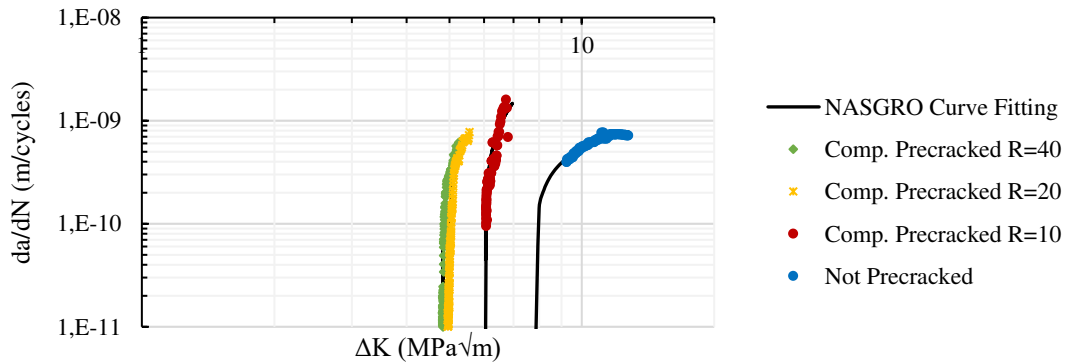


**Fig. 12** NASGRO curve fitting after crack growth tests

Curve fitting by least square method helps to estimate stress intensity threshold range. As a result, the resultant curves were plotted only on near threshold data by applying NASGRO curve fit as shown in Fig. 12. For not precracked specimen; initial  $\Delta K$  was started with 5 MPa√m and at least 2E+06 cycles loaded to observe fatigue crack. Nevertheless, fatigue crack was not initiated on this stress level even though enough stress concentration formed through razor blade nevertheless it was not sufficient to initiate crack ahead of the notch then  $\Delta K$  was increased as %10 of predefined initial  $\Delta K$  value. This procedure was continued until  $\Delta K$  was equal to 15 MPa√m. Then, natural crack was formed on notch region and stabilized after 1.5 mm advancement. During load reduction, crack propagated fast because of high stress level and crack length reached its limit because of specimen geometry. Therefore, crack growth data



points were not recorded around  $10^{-10}$  m/cycles. Nevertheless, NASGRO curve fitting enables to estimate long crack threshold value after least square for not precracked specimen test. Accordingly, long crack threshold values were found 4.82, 4.96, 6.06 and 7.97 MPa $\sqrt{\text{m}}$  for  $R$  of 40, 20, 10 and not precracked specimens respectively.

Long crack threshold values for each case were determined and the effect of compression-compression precracking was evaluated. Accordingly,  $R$  of 40 was resulted as lowest threshold value that means more accurate estimate on threshold value can be done through that stress ratio as design criteria. Indeed, lower stress ratio for compression precracking resulted in remote closure taking place and reducing driving force, hence higher threshold value was obtained. It is suggested that higher stress ratio for compression precracking can be chosen for accurate and reliable fatigue threshold value. If compression precracking was not performed before starting crack growth tests, it was resulted as higher threshold as expected because of load history effects.

## Discussion

The accuracy of compliance measurements provides correlation about assessment of crack closure responsible for stress ratio effect on fatigue crack growth rate, which introduces effective stress intensity factor. In small crack lengths, the compliance value increases with the increase of the load, while the compliance starts to diverge at larger crack lengths. Determining of opening stress through compliance method is difficult and confusing because of hysteresis and measurement noise on data. Compliance variation is caused by change in crack size that alters contacted region and change in plastic zone size. It is generally accepted that usage of 2% deviation from compliance offset gives sensible results. Crack opening stress through compliance method can be attributed more than 3% deviation on load displacement curve. Opening stress can be estimated by assuming an offset of 1.5% on the load-displacement curve. In case total variation of load displacement curve is very small; in other words, where the slope change is not easily seen, opening stress determining can be problematic and brings large scatter on results. For such cases, ASTM compliance offset through 2% deviation leads to evaluating less opening stress value compared to larger variation of compliance instances having distinct slope change. Preference of larger deviation such as 10% on compliance offset value results in less scatter on data but shifting effective stress intensity curve to larger values. Among other methods, ASTM is admitted as compliance offset method. Nevertheless, the downside of the method is that poor precision leads to large scatter on compliance measurements. Another disadvantage is that ASTM offset method may alter with variation of stress ratio.

Compression precracking before crack growth tests causes faster crack growth rates compared to load reduction procedure and resulted as lower threshold value. Threshold values are affected by initial  $\Delta K$  under load reduction scenario. On the other hand, cracks will be fully open after compression precracking and reaches steady state under constant amplitude loading. Therefore, providing stabilized crack before load reduction approaches crack growth to effective stress intensity and deviation around threshold is minimized. Because of difficulties like to control crack growth and keep a sufficient crack length under tensile-tensile precracking; compression precracking is more preferable. Precracking productivity depends on grain boundary orientation in terms of aligned and elongated grains. It is desired to apply small  $\Delta K$  for precracking to minimize tensile residual stresses. After precracking, small scale yielding ahead of crack tip front takes place under cyclic compression. Non-propagating crack size is around 0.2 mm or more, and it is known that precracking size is less than cyclic tensile zone consisting of after unloading. In order to generate reliable fatigue crack growth data, precracking size needs to be outside of monotonic compressive zone by ensuring small scale yielding ahead of crack tip. This is achieved by tensile fatigue loading after compression precracking in order to be free in terms of residual stresses.

Long cracks need to be fully opened on steady state region, then load reduction can be applied to obtain accurate threshold value by assuring fatigue crack growth tests performed with eliminated residual stresses. Even though compression precracking provides minimization of load history effects, crack propagation is desired to be sure on eliminated of closure effects. ASTM E647 load reduction procedure exhibits low crack propagation rate and high threshold values because of having roughness and oxide induced crack closure, which is responsible for observing rough crack flank. Precracking stress value shall be minimum as much as possible to decrease residual stress effects ahead of crack tip.

Crack growth takes place by fulfilled following condition: Applied loading is larger than  $K_{max,th}$  and  $\Delta K_{th}$ . Long crack threshold value is a material property and independent of crack size and specimen geometry. Small cracks advance on regions owning in-situ or pre-existing stress concentration that can be caused by slip bands, dislocation pile-up or existing defects. Cyclic deformation provides fatigue damage formation though dislocation pile-up, persistent slip band formation and accordingly presents available condition for initiation phase of crack. Short crack behavior can be summarized as their dependence on crack length, having higher crack growth rates, advancement even below long crack threshold value and variance of threshold with crack size.

Cracks may not be initiated at maximum allowable rates under load reduction for AISI 4340 steels; however, precracking enables initiation of cracks around  $\Delta K_{th}$  by minimizing load history effects. Even though it is considered that compression precracking provides presenting more accurate fatigue crack growth data with minimal load history effects compared to traditional methods. After compression precracking, non-propagating crack needs to advance at least three monotonic compressive zone sizes to reach steady state crack growth conditions.

Crack closure is caused by tensile part of loading for long cracks under small scale yielding conditions. In small scale yielding, crack closure effect is caused by plasticity, roughness and oxide induced crack closure. Plasticity induced crack closure is not observed on plain strain conditions, since local wedge near crack tip takes place because of plastic shear deformation in wake of crack. Source of internal stresses is stress concentration regions such as notch, hole, microstructural defects etc. And internal stress asymptotically decreases by distance to move away. However, applied stress increases by increasing crack length and there exist competitions in terms of total stress. If applied stress is less than  $\Delta K_{th}$  and  $K_{max}$ , crack is arrested since total stress is insufficient for propagation. Elimination of internal stress is attributed to fatigue crack growth behavior of long cracks. Local stress ratio will be higher at crack tip than remote load ratio because of existence of internal stresses.

Crack closure becomes stabilized by growing from small to long crack, and it increases by increasing crack length until steady state. In this region, closure in terms of crack wake plasticity is maximized then its effectiveness diminishes by increasing effective stress. Presence of crack closure enables to contact of crack flakes under unloading, then results in change in slope on compliance curve. By increasing stress ratio for long cracks, crack closure effects diminish and become R of 0.7 condition. Crack closure for small cracks slowly increases by increasing crack size, that means threshold stress for small cracks increases until certain value that small crack approaches to long cracks.

## Conclusions

Threshold stress becomes significant especially for structures having high cycle loading and resulting in high percentage of initiation and short time for propagation, so life estimation is necessary with accurate threshold stress. Long crack threshold value is basically used in design value for damage tolerant structures, however it is known that small cracks exhibit different crack growth rates than long cracks. To clarify differences in propagation rate, crack closure

concept needs to be well grasped. The following conclusions drawn from this study are listed below:

- Compliance curve is restricted on  $0.25 < a/w < 0.8$  region to represent appropriate calibration result.
- Steady state region on crack growth curve represents crack propagation with constant rate until plastic zone size with unchanged crack sharpness. Threshold value of a component is defined during design phase to estimate safe operation life during service therefore accurate data is significant for durability purposes.
- Residual life of a component is remarkably affected with altering threshold value. For instance, small change on threshold value results in considerable change in residual characteristics of a component.
- Higher stress ratios for compression precracking tests are advised for more accurate fatigue threshold value.
- Crack size after compression precracking is directly related with monotonic compressive zone after first compressive loading.
- Long crack threshold value exhibited high scatter which is around 20% for precracked specimens. By using polynomial fit to entire region; fatigue crack growth rate and threshold value can be estimated.
- The probable cause of the erroneous threshold value is largely due to load history effects from the test procedure, sample size, and test configuration. In case of higher applied precracking loading, remote closure takes place and reduces driving force and results in higher threshold value.

## References

1. James M, Forth S, Newman J. Load history effects resulting from compression precracking. *Journal of ASTM International*. 2005;2(9): 12025.
2. Pippin R, Hohenwarter A. Fatigue crack closure: a review of the physical phenomena. *Fatigue & Fracture of Engineering Materials & Structures*. 2017;40(4): 471–495.
3. Li S, Zhang Y, Qi L, Kang Y. Effect of single tensile overload on fatigue crack growth behavior in DP780 dual phase steel. *International Journal of Fatigue*. 2018;106: 49–55.
4. Hubbard RP. Crack growth under cyclic compression. *Journal of Basic Engineering*. 1969;91(4): 625–630.
5. Pearson S. Initiation of fatigue cracks in commercial aluminium alloys and the subsequent propagation of very short cracks. *Engineering Fracture Mechanics*. 1975;7(2): 235–247.
6. Newman JC. A nonlinear fracture mechanics approach to the growth of small cracks. *AGARD Behaviour of Short Cracks in Airframe Components*. 1983. Available from: <https://ntrs.nasa.gov/citations/19830025829> (Accessed 24<sup>th</sup> Nov 2022).
7. Elber W. The significance of fatigue crack closure. In: *Damage Tolerance in Aircraft Structures*. 1971. p.230-242.
8. James M, Forth S, Johnston W, Newman JA, Everett R. Effects of compression precracking on subsequent crack growth. In: *15th European Conference of Fracture Advanced Fracture Mechanics for Life and Safety Assessments (ECF15)*. Stockholm, Sweden; 2013.
9. Maierhofer J, Pippin R, Gänser H-P. Modified NASGRO equation for short cracks and application to the fitness-for-purpose assessment of surface-treated components. *Procedia Materials Science*. 2014;3: 930–935.
10. Newman Jr. JC, Yamada Y. Compression precracking methods to generate near-threshold fatigue-crack-growth-rate data. *International Journal of Fatigue*. 2010;32(6): 879–885.

11. Chapetti MD. Estimation of the plain high-cycle fatigue propagation resistance in steels. *Materials Research*. 2002;5(2):101–105.
12. Suresh S, Ritchie RO. Propagation of short fatigue cracks. *International Metals Reviews*. 1984;29(1): 445–475.
13. McEvily AJ. The growth of short fatigue cracks: a review. *Transactions on Engineering Sciences*. 1970;13: 93–107.
14. Sadananda K, Nani Babu M, Vasudevan AK. A review of fatigue crack growth resistance in the short crack growth regime. *Materials Science and Engineering: A*. 2019;754: 674–701.
15. Tabernig B, Pippan R. Determination of the length dependence of the threshold for fatigue crack propagation. *Engineering Fracture Mechanics*. 2002;69(8): 899–907.
16. Meggiolaro M, Miranda A, Decastro J. Short crack threshold estimates to predict notch sensitivity factors in fatigue. *International Journal of Fatigue*. 2007;29(9-11): 2022–2031.
17. Sadananda K, Vasudevan AK. Short crack growth and internal stresses. *International Journal of Fatigue*. 1997;19(93): 99–108.
18. Lawson L. Near-threshold fatigue: a review. *International Journal of Fatigue*. 1999;21: 15–34.
19. Grasso M, De IA, Xu Y, Haritos G, Mohin M, Chen YK. Corrigendum to “An Analytical Model for the Identification of the Threshold of Stress Intensity Factor Range for Crack Growth”. *Advances in Materials Science and Engineering*. 2018;2018: 1–2.
20. *Heat Treatment of Carbon and Low-Alloy Steel Parts Minimum Tensile Strength Below 220 ksi (1517 MPa)*, AMS 2759-1D, 2007. Available from: <https://www.sae.org/standards/content/ams2759/1d/>
21. *Standard Test Method for Measurement of Fatigue Crack Growth Rates*, ASTM E647-15e1, December 2016.. Available from: [www.astm.org](http://www.astm.org)
22. Newman JC. A crack opening stress equation for fatigue crack growth. *International Journal of Fracture*. 1984;24(4): R131–R135.
23. Clarke GA, Andrews WR, Paris PC, Schmidt DW. Single Specimen Tests for JIc Determination. Mechanics of Crack Growth, ASTM STP 590. In: *American Society for Testing and Materials*. Philadelphia; 1976. p.27-42.
24. *Standard Test Method for Measurement of Fracture Toughness*, ASTM E1820-11E2, 2011. Available from: [www.astm.org](http://www.astm.org)
25. Saxena A, Hudak SJ. Review and extension of compliance information for common crack growth specimens. *International Journal of Fracture*. 1978;14(5): 453–468.
26. Forman RG, Shivakumar V, Cardinal JW, Williams LC, McKeighan PC. *Fatigue crack growth database for damage tolerance analysis*. National Technical Information Service, Springfield, Virginia, USA. Technical Report number: PB2005-110675, 2005.
27. Patriarca L, Filippini M, Beretta S. Short-crack thresholds and propagation in an AISI 4340 steel under the effect of SP residual stresses. *Fatigue & Fracture of Engineering Materials & Structures*. 2018;41(6): 1275–1290.
28. NASGRO, N. J. S. C. *Fatigue Crack Growth Computer Program Nasgro Version 4.2–Reference Manual*. 2006.
29. El Haddad MH, Topper TH, Smith KN. Prediction of non propagating cracks. *Engineering Fracture Mechanics*. 1979;11(3): 573–584.

## THE AUTHORS

**Caliskan S.**   
e-mail: caliskan.salim@metu.edu.tr

**Gurbuz R.**   
e-mail: rgurbuz@metu.edu.tr

## Mechanical properties of a soil improved with recycled demolition concrete for the construction of shallow foundations

S.P. Munoz Perez<sup>1</sup> , T.M. Salazar Pretel<sup>1</sup> , L.I. Villena Zapata<sup>2</sup> 

<sup>1</sup> Universidad Señor de Sipan, Chiclayo, Perú

<sup>2</sup> Universidad Cesar Vallejo, Trujillo, Perú

✉ msocrates@crece.uss.edu.pe

**Abstract.** To achieve a satisfactory level of safety and stability in the construction of structures in weak soils, one of the best solutions may be soil improvement, the recycling and reuse of construction and demolition materials results in the preservation of natural resources and the reduction of environmental pollution. Therefore, this experimental study proposes to evaluate the mechanical properties of soil for surface foundations incorporating recycled demolition material. The mechanical behavior of a clayey soil improved with recycled concrete from demolition (CRD) was analyzed by means of a series of compaction tests, unconfined compression of soil specimens and direct shear in mixtures with 10 %, 15 %, 20 % and 25 % CRD by weight. As a result, the highest compressive strength of the soil is obtained with 16.67 % CRD according to UCS tests; and an improvement in cohesion and friction angle for all CRD percentages. Thus, it can be demonstrated that CRD has a positive influence on the mechanical properties of a soil with clayey characteristics.

**Keywords:** mechanical properties, shallow foundations, recycled demolition material, soil improvement, unconfined compression of soil specimens, direct shear.

**Citation:** Munoz Perez SP, Salazar Pretel TM, Villena Zapata LI. Mechanical properties of a soil improved with recycled demolition concrete for the construction of shallow foundations. *Materials Physics and Mechanics*. 2023;51(1): 168-178. DOI: 10.18149/MPM.5112023\_14.

### Introduction

To perform different construction works, soil is one of the most important components [1]. Soils used for foundations are the most affected when dealing with loose soils with low shear strength [2], a structure transfers the load to the soil through the foundations at a depth of approximately two to three times its width [3] so avoiding the replacement of these by high quality raw materials [4], finding the suitable materials to treat reinforcement layers for footings in soils with unfavorable bearing capacity [5] and that the generated costs are affordable is one of the purposes of geotechnical engineering [6].

Due to the abundance of construction and renovation of urban buildings in developing and developed countries, there is an increase in the amount of construction and demolition waste [7], this inevitably leads to an increase in the proliferation of construction and demolition waste [8] coupled with the decrease in landfill capacity and the increased difficulty in identifying aggregate quarries [9] the implementation of the reuse of these wastes in civil construction should be developed to mitigate environmental problems [10].

Soils that include loose sands, soft clays, and organics are not suitable for construction projects because they do not possess valuable physical properties for their application [3, 11].

A clayey soil tends to have low shear strength which is further reduced by wetting [12, 13], and a high expansive potential [14] contracting significantly if it dries out and expanding if it absorbs moisture which puts a lot of pressure on the substructure [15], added to this is the heterogeneous condition of these soils at the base of a building and their uneven compression due to poor compaction resulting in variable settlement of the foundation and its subsequent destruction [16, 17]. Therefore, stabilization is often required prior to the construction of civil infrastructures [18] by methods that are economical and environmentally friendly [19].

When we talk about soil improvement, there is a wide range of materials and methods to perform it. R&D materials are those from the construction, rehabilitation and demolition of any type of construction site, whether public or private [20, 21]. The three main demolition waste materials are crushed brick, recycled concrete aggregate (RCA), and reclaimed asphalt pavement [22].

A wide range of soil improvement methods have been developed to support shallow foundations, one of these methods is the in-situ mixing of recycled demolition materials. On a laboratory scale the influence of recycled concrete demolition material (CRD) on the behavior of clayey soils has been studied by several authors concluding that, the addition of this material in a proportion of 22% [23] and 15% [7] results in an increase of the unconfined compressive strength (UCS), permeability coefficient and CBR, as well as the reduction to zero of the free heave; [24] agrees that the optimum percentage of CRD to achieve improvements in the soil is 22%, but this author also compares the results with those obtained by fly ash and lime, concluding that the UCS at 28 days of fly ash is higher than that obtained by CRD waste and the highest CBR is obtained by using lime in the sample, where he states that lime is the best stabilizer to be used as subgrade, but C&D waste is more economical when it is required to have earlier resistances.

The influence of demolition recycled material (R&D) consisting of crushed floor concrete and bricks was also studied, presenting an increase in UCS value and soil shear strength (CBR) by 4 and 4.5 times respectively compared to an untreated soil by adding 20 % of (R&D), as well as, reducing swelling and swelling pressure of the stabilized soil by 80 % [25, 26].

Studies have also been done on the mechanical behavior of soils incorporating different types of reusable materials such as expanded polystyrene (EPS) where the lateral thrust coefficient ( $k_0$ ) was analyzed with the oedometer test at percentages of 0 %, 0.25 %, 0.5 % and 1% EPS by weight, concluding that, as EPS beads are highly deformable, the application of overburden pressure compressed the soft particles, leading to an increase in  $k_0$  [27]; the permeability of the EPS - soil aggregate composite decreases with increasing dry unit weight, where wet compaction of the optimum moisture content contributes to a further increase in permeability variation [28], the influence of EPS bead inclusion on the strength properties of poorly graded stabilized sands was also evaluated [29].

The incorporation of fly ash into soil was studied, concluding that geopolymerization converts clay soil into a non-plastic silt-like material due to the fact that the clay particles are covered by geopolymer gels, thus forming coagulated particles with considerably less likelihood of swelling, consolidation and drying shrinkage [30]; results also indicate that a fly ash-based geopolymer could be a simple solution to increase the sorption and metal removal capacity of local clay to mitigate potential contaminants due to leachate penetration into the soil [31].

Likewise, an attempt was made to examine the effect of lime-zeolite stabilization on the behavior of a natural soil the size of a low plasticity silt, by performing standard compaction tests, as well as unconfined compression experiments specimens were subjected to consecutive cycles of freezing and thawing showed a significant improvement in the mechanical performance of the treated soil in terms of strength and durability [32].

A study was conducted with direct shear tests on a rubber-sand composite along a nonwoven geotextile layer, demonstrating that the addition of 40 % granulated rubber to pure sand caused an approximately 50 % reduction in the maximum mobilized interface shear stress as loading cycles progressed [33].

In addition, literature reviews have been conducted: on cementitious composites, common unconventional stabilizers, reinforcing fibrous inclusions, and the simultaneous use of a stabilizer and a reinforcing agent where the most prominent studies are detailed and laid out in a logical sequence to present the most practical mixtures used for soil stabilization purposes [34]; also, the effects of EPS incorporation in different types of mixtures were investigated by reviewing the most prominent studies on EPS beads and blocks subjected to static and cyclic loading, the study proposes some essential practical issues to be followed for future research that are lacking in the current literature [35].

Therefore, the objective of this research is to evaluate the mechanical properties of a soil with clayey characteristics by adding 10 %, 15 %, 20 % and 25 % by weight of recycled concrete from demolition; subjecting it to unconfined compressive strength tests UCS and direct shear to verify the mechanical behavior of the soil in parameters of shear strength, cohesion, and friction angle in the construction of shallow foundations.

## Methods

**Materials used.** Figure 1 shows the flow diagram of the processes followed for the development of this research, from the location of the land to obtain the soil samples and the collection of the CRD samples, their crushing process and the laboratory tests performed.

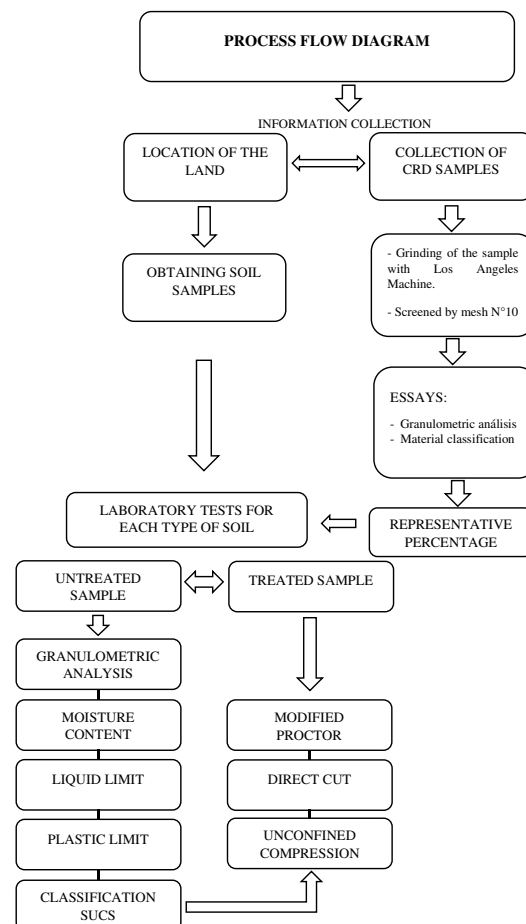


**Fig. 1.** Process flow diagram



**Soil.** Soil samples were collected through 9 soil pits in the locality of Ferreñafe, Lambayeque, Peru with a depth of 1.50 meters to avoid the presence of vegetation and loose soils. The representative clay samples were collected in polyethylene bags in order to avoid any variation in moisture content. The geotechnical properties of the soil are given in Table 1.

**Table 1.** Physical properties of soil

POINT	DEPTH	MOISTURE CONTENT (%)	LIMITS OF ATTERBERG			GRANULOMETRY				CLASS. USCS	$\gamma_{max}$ g/cm <sup>3</sup>	OCH %
			LL (%)	LP (%)	IP (%)	% PASS N°4	% PASS N°10	% PASS N°40	% PASS N°200			
C1	1.5 m	26.29	22.07	17.40	4.17	100.0	99.5	86.4	17.8	SC-SM	1.973	9.44
C2	1.5 m	15.09	22.16	16.94	5.22	100.0	99.5	93.8	22.7	SC-SM	1.978	9.08
C3	1.5 m	21.98	41.96	23.23	18.74	100.0	99.2	96.7	35.1	SC	2.018	10.44
C4	1.5 m	21.83	29.98	16.43	13.56	100.0	98.7	94.0	66.2	CL	1.930	13.06
C5	1.5 m	18.22	49.46	20.82	28.64	100.0	99.0	96.6	51.7	CL	1.981	10.34
C6	1.5 m	15.11	38.64	17.11	21.53	100.0	99.2	95.0	53.1	CL	1.968	10.71
C7	1.5 m	18.99	44.71	16.35	28.35	99.9	98.4	94.2	60.0	CL	2.010	11.38
C8	1.5 m	21.57	44.16	15.90	28.26	100.0	98.5	92.8	62.4	CL	2.016	11.40
C9	1.5 m	19.49	52.59	23.19	29.40	100.0	99.6	94.2	74.4	CH	1.896	14.37

**Recycled demolition material.** The CRD material consisted of concrete rubble obtained from demolition activities of sidewalks, columns of a building under renovation and laboratory cores.

Due to the large size of these blocks and that they cannot be directly implemented in experimental studies because of the small/medium scale of the laboratory equipment, the chosen CRD material was dried, crushed and filtered through a 2 mm No. 10 sieve and kept in air-tied polyethylene bags at a controlled temperature. The crushing process was carried out in the Los Angeles Abrasion Machine, in a time span of 15 min per sample. The physical properties of the residues are presented in Table 2.

**Table 2.** Physical properties of CRD

Characteristic	Worth
Uniformity coefficient, Cu	1.4
Curvature coefficient, Cc	0.9
Classification according to USCS	SP

## Experimental work

A series of laboratory tests were performed consisting of Modified Proctor, Unconfined Compressive Strength USC and Direct Shear testing on natural soil and recycled concrete demolition waste at (10 %, 15 %, 20 %, 25 %). Sample preparation and laboratory testing were performed in accordance with the appropriate ASTM standards.

**Compaction Testing.** Modified Proctor compaction tests (ASTM D-1557) were performed to determine optimum moisture content (OCH) and maximum dry density (MDS). The soil and composite mixtures were thoroughly mixed for 12 hours prior to compaction. First, compaction tests were performed to determine the compaction characteristics of the unstabilized soil. Subsequently, tests were conducted on the composite mixtures consisting of soil plus CRD in all their percentages under study. A soil sample weighing 2.5 kg was taken

and passed through a 4.75 mm No. 4 sieve to perform the compaction test in a modified Proctor mold of 943 cm<sup>3</sup> capacity. The water is then added to the soil and mixed thoroughly without the formation of lumps. This sample is divided into 5 equal parts, poured into standard mold in five layers and compacted by applying 25 blows per layer using a modified rammer weight of 44.48 N weight dropped from a height of 47.52 cm.



**Fig. 2.** Materials used and experimental work

**Unconfined compressive strength tests.** Unconfined compressive strength tests (ASTM D-2166) were performed on 41 mm diameter and 88 mm high cylindrical specimens at optimum moisture content, compacted to maximum dry density. The specimens were prepared by compacting them by simulating the Modified Proctor dynamic compaction energy in five equal layers in the standard 99.99 cm<sup>3</sup> mold by applying 19 blows per layer using a rammer weight of 17.18 N dropped from a height of 16 cm. Three specimens were made per sample, and these were cured by keeping them in plastic bags to prevent moisture loss and tested at 24 hours. The UCS was determined as the average of values. UCS tests were performed on the specimens at a strain rate of 1.68 mm/min. Stress and strain values were recorded, and a graph was plotted between stress as the ordinate and strain as the abscissa.

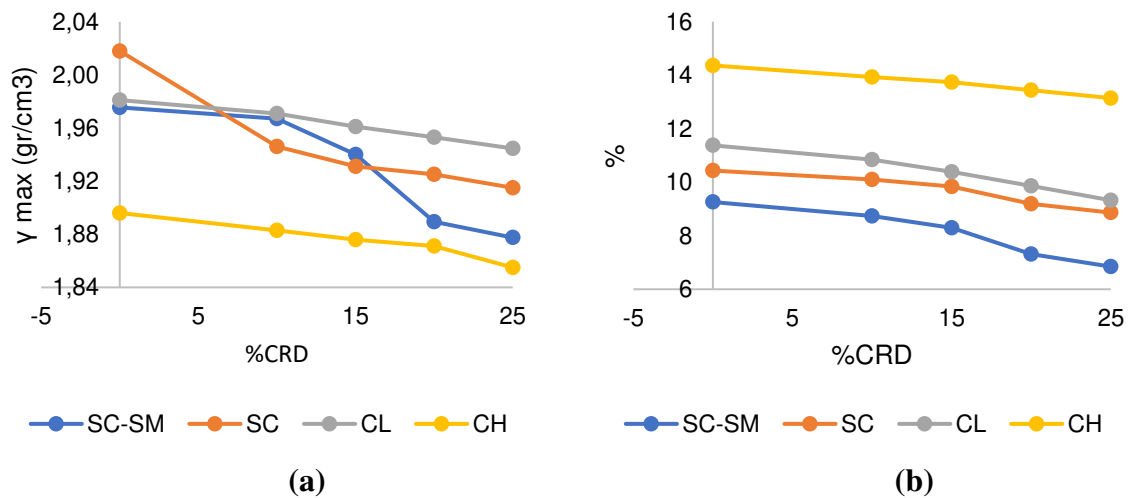
**Shear strength tests.** The shear strengths of the RCA clay mixtures were determined using the direct shear test method (ASTM D-3080). The conventional direct shear apparatus implemented consisted of a shear box that accommodates a 60 mm diameter soil sample with 22 mm depth. During vertical (normal) tension tests, it is applied mechanically using dead weights and a lever arm, while shear tension is exerted by a displacement-controlled motor. The displacement gauges have a resolution of 0.01 mm and 0.001 mm respectively, while shear force measurements are accurate to 0.05 kg.

Specimen fabrication, performed in three layers (each approximately 7-8 mm), is generally similar to that described for unconfined compression testing, i.e., each specimen is made at optimum moisture content compacted to maximum dry density; simulating modified Proctor compaction energy in a 67.85 cm<sup>3</sup> mold applying in this case 22 strokes per layer using a rammer weight of 17.18 N dropped from a height of 16 cm. The specimens are cut under vertical stresses of  $\sigma_n = 0.48, 1.12$  and  $1.61 \text{ kg/cm}^2$ . After applying vertical tension, the specimen is gradually immersed in water and soaked for 24 h before cutting (the specimens had no prior curing). Throughout the soaking period, any settlement and compression of the sample is monitored. Soil samples were sheared at a constant rate of 1 mm / min up to the maximum horizontal displacement (u) of 6 mm. This rapid shear rate would significantly deny the samples the time required for drainage, and therefore conditions resembling an undrained shear would prevail.

## Results and discussion

As a result of the experimental studies, the characteristics of unconfined compressive strength UCS and shear strength were determined; according to the USCS classification, the soils were grouped into 4 groups with similar physical characteristics.

**Soil compaction tests.** The Modified Proctor results are shown in Figure 3, these show a tendency to decrease both OCH and MDS as the percentage of CRD increases; OCH decreases due to the presence of coarser particles of CRD waste compared to those of soil, which results in reduced surface area and therefore a lower affinity for water [23], the decrease in MDS occurs because the specific gravity of CRD waste is lower than those of natural soil and also CRD aggregates present unreacted cement that flocculates with clay to provide less densification [25].

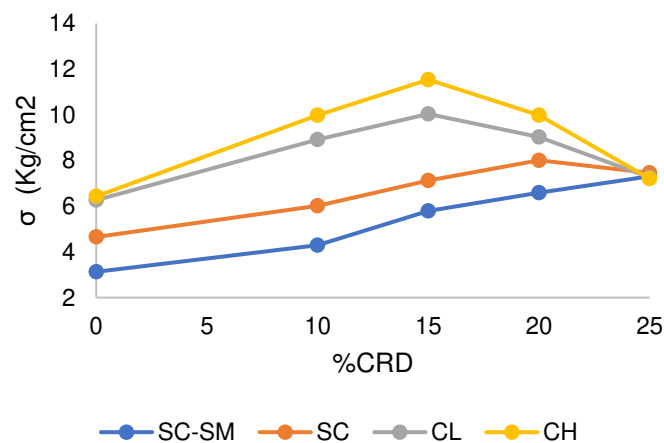


**Fig. 3.** Compaction test results: (a) maximum dry density, (b) optimum moisture content

**Table 3.** Preliminary laboratory results, Modified Proctor test

MODIFIED PROCTOR RESULTS FOR SOIL / CRD			
CALICATA	CRD	MDS	OCH
	%	g/cm3	%
SC-SM	0	1.976	9.26
	10	1.967	8.74
	15	1.940	8.30
	20	1.890	7.31
	25	1.878	6.85
SC	0	2.018	10.44
	10	1.946	10.10
	15	1.931	9.84
	20	1.925	9.19
	25	1.915	8.87
CL	0	1.981	11.38
	10	1.971	10.84
	15	1.961	10.39
	20	1.953	9.87
	25	1.945	9.33
CH	0	1.896	14.37
	10	1.883	13.93
	15	1.876	13.74
	20	1.871	13.45
	25	1.855	13.15

**Unconfined compressive strength tests.** Figure 4 shows the behavior of the soil after incorporating CRD by weight in different percentages and subjecting it to compressive strength tests with 24 hours of curing in a humid chamber. In all the research points (test pits), an improvement in strength is observed with the addition of CRD. The average optimum CRD % is calculated by interpolating all the results of the 04 soil types.

**Fig. 4.** Unconfined Compressive Strength Test Results

The Shapiro Wilk normality test presented a p-value of significance lower than 0.05 ( $p=0.023<0.05$ ), for the variable percentage of recycled concrete from demolition (%), i.e. the normality assumption was not met, while the p-value was greater than 0.05 ( $p=0.918>0.05$ ) for the variable Unconfined compressive strength ( $\text{kg/cm}^2$ ), complying with the normality assumption, therefore, the correlation was quantified with Spearman's correlation test, which presented a p-value of significance lower than 0.05 ( $p=0.041<0.05$ ), rejecting the null hypothesis, showing that there is a significant relationship between both variables, likewise Spearman's correlation coefficient reached a positive value ( $r_s=0.460$ ), that is, there is a low direct correlation between both variables.

According to Figure 5 the approximate dispersion equation which is:

$$\sigma = -119.06\%CRD^2 + 39.705\%CRD + 5.0079 \quad (1)$$

Deriving the equation with respect to the %CRD we obtain:

$$\sigma = -238.12\%CRD + 39.705 = 0 \quad (2)$$

And if the equation equals zero, the average optimal %CRD of the 4 soil types can be obtained: %CRD = 16.67 % y  $\sigma = 8.32 \text{ kg/cm}^2$ .

From Figure 5, as a result, the average optimum percentage of CRD is 16.67 % reaching a compressive strength of  $8.32 \text{ kg/cm}^2$ , with higher percentages of CRD the compressive strength decreases progressively.

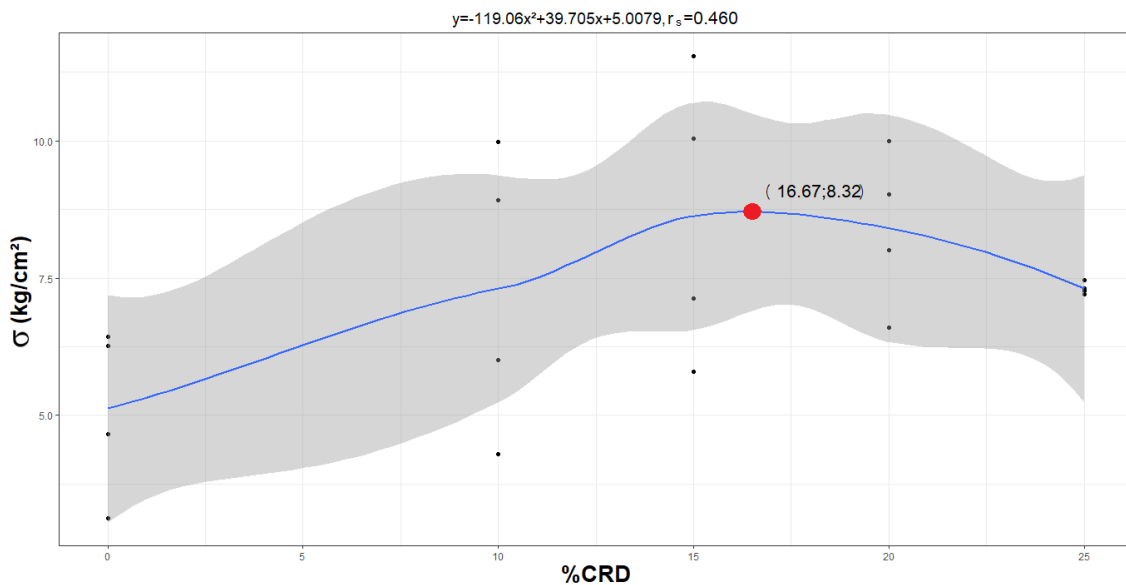


**Fig. 5.** Dispersion of the UCS test results and their respective approximate equations

On the other hand other authors, [23] argues that, in their research the addition of 22 % CRD increases the UCS to 1062 kPa, which was more than two and a half times that of the UCS of natural soil, with 22 % CRD the UCS increases to 1062 kPa, after the addition of 24 % CRD, the USC increases to 1012 KPa which is less than the UCS of the soil + 22 % composite CRD waste, therefore, he concluded that 22 % CRD can be considered as the optimum percentage for stabilization of that type of soil.

The researcher [25] considered 20 % CRD as the optimum percentage with a 4-fold increase over natural soil for a curing period of 28 days, at more days of curing the strength growth is marginal. [7] also analyzed the UCS strength of a clayey soil at different curing periods and sample percentages, having at 15 % CRD at 28 days of curing a compressive strength of 1567 KPa compared to UCS= 275 KPa for an unstabilized soil without any curing. These results are similar to the present investigation, which in this case the optimum percentage is 16.67 %, beyond this percentage the compressive strength of the soil decreases.

**Shear strength tests.** The results of the shear strength tests are shown in Figure 6. These results present an upward trend with a downward curve in some cases. For its part [7] argues that for RCA - natural clayey soil mixtures, the increase in %CRD results in dilatant behavior and higher shear strength as reflected in results with high cohesion and high peak internal friction angle, since, mixing RCA with clayey soils results in stronger, stiffer and less compressible mixtures that are particularly suitable for construction purposes as subbase / subgrade of road pavements.

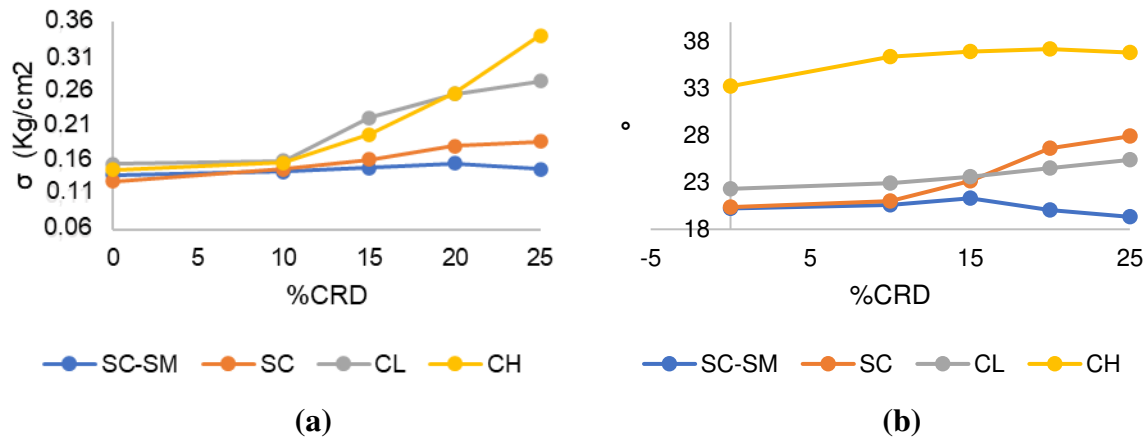


**Figure 6.** Shear strength test results: (a) Cohesion, (b) Internal friction angle

## Conclusions

1. The physical tests of the soils defined the type of soil to which they belonged; there was no previous information on the type of soil in the sampling area; but after the pertinent analysis in the laboratory, SC-SM, SC, CL and CH soils were obtained according to the USCS classification.
2. By means of the Modified Proctor test, information was obtained for the subsequent elaboration of the compacted specimens according to their OCH and MDS; these results showed a tendency to reduce as a higher percentage of CRD was added to the sample.
3. According to the unconfined compressive strength test of cylinders of natural soil and soil improved with CRD, it was obtained through a dispersion analysis that the addition of this aggregate in a 16.67% by weight in a soil with clay properties presents the greatest improvements according to the UCS test.
4. For the RCA - natural soil mixtures, the increase in %CRD results in an increase in the angle of friction and cohesion with respect to the soil in its natural state.

## References

1. Bhat A, Marathe S, Ashmitha N. Stabilization of Locally Available Soil using CNSA and Glass Industry Waste. *International Journal of Recent Technology and Engineering*. 2019;8(3): 4245-4249.
2. Khan MS, Tufail M, Mateeullah M. Effects of Waste Glass Powder on the Geotechnical Properties of Loose Subsoils. *Civil Engineering Journal*. 2018;4(9): 2044-2051.
3. Neami M, Alsoudany K, Dawod A, Ehsan E. Remediation of cohesive soils using waste glass. *Conference of the International Journal of Arts & Sciences*. 2016;09(01): 125–138.
4. Henzinger C, Schömig P. *Prognose der Festigkeitsentwicklung zementbehandelter Böden mit dem Porosity/Binder-Index*. Geotechnik; 2020.
5. Consoli N, Bittar J, Quiñónez A, Salvagni K, Johann A. Use of Sustainable Binders in Soil Stabilization. *Journal of Materials in Civil Engineering*. 2019;31(02): 125-137.




6. Zhilkina T, Sychugov S, Gumeniuk A, Mackevicius R, Turchin V, Vasilev V, Zakirov V, Ilinsky A. Technology of soil stabilization with cementsand grouting mortar with optimal aggregate grading. *MATEC Web of Conferences*. 2018;193: 05046.
7. Kianimehr M, Shourijeh P, Binesh S, Mohammadinia A, Arulrajah A. Utilization of recycled concrete aggregates for light - stabilization of clay soils. *Construction and Building Materials*. 2019;227: 116792.
8. Ministerio del Ambiente. *Informe anual de residuos sólidos municipales y no municipales en el Perú Gestión 2012*. Perú; 2012.
9. Malasavage N, Gallagher P, Grubb D, Wartman J, Carnivale M. Modifying plastic clay with crushed glass: Implications for constructed fills. *Soils and Foundations*. 2007;47(6): 1017-1027.
10. Olufowobi J, Ogundaju A, Michael B, Aderinlewo O. Clay soil stabilisation using powdered glass. *Journal of Engineering Science and Technology*. 2014;9(5): 541-558.
11. Fauzi A, Nazmi M, Rahman A, Jauhari Z. Utilization Waste Material as Stabilizer on Kuantan Clayey Soil Stabilization. *Procedia Engineering*. 2013;53: 42-47.
12. Gowtham S, Naveenkumar A, Ranjithkumar R, Vijayakumar P, Sivaraja M. Stabilization of Clay Soil by Using Glass and Plastic Waste Powder. *International Journal of Engineering and Techniques*. 2018;4(2): 146-150.
13. Asadollahi F, Dabiri R. Effects of Glass Fiber Reinforced Polymer on Geotechnical Properties of Clayey Soil. *Journal of Structural Engineering and Geotechnics*. 2017;02: 73-83.
14. Ayala G, Rosadio A, Durán G. Study of the effect of the addition of ash from artisan brick kilns in the stabilization of clay soils for pavements. In: *Proceedings of the LACCEI international Multi-conference for Engineering, Education and Technology, 2019*. 2019.
15. Nuruzzaman M, Hossain A. Effect of Soda Lime Glass Dust on the Properties of Clayey Soil. *Global Journal of Researches in Engineering*. 2014;14(E5): 19-24.
16. Mikolainis M, Ustinovičius M, Sližytė D, Zhilkina T. Analysis of static and dynamic deformation modulus. *Engineering Structures and Technologies*. 2016;8(2): 79-84.
17. Alvarez A., Sosa J., Ramirez G, Miranda L. Improved mechanical properties of a high plasticity clay soil by adding recycled PET. *IOP Conference Series: Materials Science and Engineering*. 2019; 758 012075.
18. Bahadori H, Hasheminezhad A, Alizadeh S. The Influence of Natural Pozzolans Structure on Marl Soil Stabilization. *Transportation Infrastructure Geotechnology*. 2020;7: 46–54.
19. Ormeño E, Rivas N, Duran G, Soto M. Stabilization of a Subgrade Composed by Low Plasticity Clay with Rice Husk Ash. *Materials Science and Engineering*. 2019;758; 012058.
20. Cabrera F, Gómez J, Almaral J, Arredondo S, Gómez M, Mendivil J. Properties in fresh state of mortars with recycled aggregate concrete and effect of c/a relation. *Ingeniería y Desarrollo*. 2017;35(01): 198-218.
21. Deshmukh R, Patel S, Shahu J. Laboratory and FEM Study on Construction and Demolition Waste and Fly Ash for Use as Pavement Material. In: Sundaram R, Shahu J, Havanagi V. (eds.) *Geotechnics for Transportation Infrastructure. Lecture Notes in Civil Engineering*. Singapore: Springer: 2019. p.177-187.
22. Arulrajah A, Mohammadinia A, D'Amico A, Horpibulsuk S. Effect of lime kiln dust as an alternative binder in the stabilization of construction and demolition materials. *Construction and Building Materials*. 2017;152: 999-1007.
23. Hymavathi J, Navya B, Kumar Y. Enhancing the strength characteristics of clayey soil by addition of fly ash and construction demolition waste. *International Journal of Civil Engineering and Technology*. 2018;9(6): 1048-1054.

24. Sharma R, Hymavathi J. Effect of fly ash, construction demolition waste and lime on geotechnical characteristics of a clayey soil: a comparative study. *Environmental Earth Sciences*. 2016;75: 377.
25. Varaprasad B, Reddy J, Rajesh T, Kumar Y, R. Reddy. Soil Improvement by Fine Fraction Residue from Recycling Construction and Demolition Waste. *International Journal of Scientific & Technology Research*. 2019;8(10): 3389-3393.
26. Hidalgo C, Carvajal G, Muñoz F. Laboratory Evaluation of Finely Milled Brick Debris as a Soil Stabilizer. *Sustainability*. 2019;11(4): 967.
27. Kazempour S, Jamshidi R, Ahmadi H, Payan M. Assessment of the compression characteristics and coefficient of lateral earth pressure of aggregate-expanded polystyrene beads composite fill-backfill using large oedometer experiments. *Construction and Building Materials*. 2021;302: 124145
28. Alizadeh S, Jamshidi R, Khaksar E, Payan M. Assessment of the Hydraulic Characteristics of Aggregate-Expanded Polystyrene Beads Composite Using Enhanced Standard Proctor Compaction Test Configuration. *Iranian Journal of Science and Technology. Transactions of Civil Engineering*. 2022.
29. Khajeh A, Ebrahimi S, Molaabasi H, Jamshidi C, Payan P. Effect of EPS beads in lightening a typical zeolite and cement-treated sand. *Bulletin of Engineering Geology and the Environment*. 2021;80: 8615–8632.
30. Khaksar E, Jamshidi R, Payan M, Arabani M. A sustainable landfill liner material: clay-fly ash geopolymers. *Bulletin of Engineering Geology and the Environment*. 2021;80: 4111–4124.
31. Khaksar E, Jamshidi R, Payan M, Arabani M. Compositional effects of clay–fly ash geopolymers on the sorption process of lead and zinc. *Journal of Environmental Quality*.
32. Shirmohammadi S, Ghaffarpour S, Payan M, Senetakis K. Effect of Lime Stabilization and Partial Clinoptilolite Zeolite Replacement on the Behavior of a Silt-Sized Low-Plasticity Soil Subjected to Freezing–Thawing Cycles. *Coatings*. 2021;11(8): 994.
33. Madani N, Hosseinpour I, Payan M, Senetakis K. Cyclic and Postcyclic Interface Characteristics of Geotextile-Embedded Sand-Rubber Composites. *Journal of Materials in Civil Engineering*. 2023;35(2).
34. Khajeh A, Jamshidi R, Payan M. A Simple Review of Cemented Non-conventional Materials: Soil Composites. *Geotech. Geol. Eng.* 2020;38: 1019–1040.
35. Khajeh A, Jamshidi R, Payan M. A Review of the Studies on Soil-EPS Composites: Beads and Blocks. *Geotech Geol Eng.* 2020;38: 3363–3383.

## THE AUTHORS

**Socrates Pedro Muñoz Pérez**   
e-mail: msocrates@crece.uss.edu.pe

**Tatiana Marilu Salazar Pretel**   
e-mail: spreteltatianam@crece.uss.edu.pe

**Luigi Italo Villena Zapata**   
e-mail: lvillenaz@ucvvirtual.edu.pe





### **Submission of papers:**

Manuscript should be submitted (**both MS Word and PDF**) by e-mail to: **mpmjournal@spbstu.ru**

After a confirmation of the paper acceptance, the authors should send the signed hard copy of the "Transfer of Copyright Agreement" form (available at <http://www.mpm.spbstu.ru> section "Authors") by regular post to "Materials Physics and Mechanics" editorial office:

*Periodicals Editorial Office, Institute of Advanced Manufacturing Technologies, Peter the Great St.Petersburg Polytechnic University, Polytechnicheskaya, 29, St.Petersburg 195251, Russia.*

The scanned copy of the signed "Transfer of Copyright Agreement" should be send by e-mail to: **mpmjournal@spbstu.ru**.

### **Filetype:**

Authors are invited to send their manuscripts **as MS Word file with PDF format copy**.

MS Word file should be prepared according to the general instructions bellow; we are kindly asking the authors to look through the detail instruction at: <http://www.mpm.spbstu.ru>.

### **Length:**

Papers should be limited to 30 typewritten pages (including Tables and Figures placed in the proper positions in the text).

### **Structure of the manuscript:**

**PAPER TITLE: CENTERED,**

**TIMES NEW ROMAN 14 BOLD, CAPITAL LETTERS**

**A.B. Firstauthor<sup>1</sup>, C.D. Secondauthor<sup>2\*</sup>** -Times New Roman 12, bold, centered

<sup>1</sup>Affiliation, address, country - Times New Roman 10, centered

\*e-mail: e-mail of the corresponding author - Times New Roman 10, centered

**Abstract.** Times New Roman 12 font, single line spacing. Abstract should not exceed 12 lines.

**Keywords:** please, specify paper keywords right after the abstract.

**Paper organization.** Use Times New Roman 12 font with single line spacing. Use *Italic* font in order to stress something; if possible, please, use **bold** for headlines only.

**Page numbering.** Please, do not use page numbering.

**Tables, Figures, Equations.** Please, see the sample file at <http://www.mpm.spbstu.ru> for more details.

### **References**

References should be subsequently numbered by Arabic numerals in square brackets, e.g. [1,3,5-9], following the sample style below:

[1] Koch CC, Ovid'ko IA, Seal S, Veprek S. *Structural Nanocrystalline Materials: Fundamentals and Applications*. Cambridge: Cambridge University Press; 2007.

[2] Hull D, Bacon DJ. *Introduction to Dislocations*. 5nd ed. Amsterdam: Butterworth-Heinemann; 2011 Available from: <https://www.sciencedirect.com/science/book/9780080966724?via%3Dihub> [Accessed 19th June 2018].

[3] Romanov AE, Vladimirov VI. Disclinations in crystalline solids. In: Nabarro FRN (ed.) *Dislocations in Solids*. Amsterdam: North Holland; 1992;9. p.191-402.

[4] Mukherjee AK. An examination of the constitutive equation for elevated temperature plasticity. *Materials Science and Engineering: A*. 2002;322(1-2): 1-22.

- [5] Soer WA, De Hosson JTM, Minor AM, Morris JW, Stach EA. Effects of solute Mg on grain boundary and dislocation dynamics during nanoindentation of Al–Mg thin films. *Acta Materialia*. 2004;52(20): 5783-5790.
- [6] Matzen ME, Bischoff M. A weighted point-based formulation for isogeometric contact. *Computer Methods in Applied Mechanics and Engineering*. 2016;308: 73-95. Available from: [doi.org/10.1016/j.cma.2016.04.010](https://doi.org/10.1016/j.cma.2016.04.010).
- [7] Joseph S, Lindley TC, Dye D. Dislocation interactions and crack nucleation in a fatigued near-alpha titanium alloy. To be published in *International Journal of Plasticity*. Arxiv. [Preprint] 2018. Available from: <https://arxiv.org/abs/1806.06367> [Accessed 19th June 2018].
- [8] Pollak W, Blecha M, Specht G. *Process for the production of molded bodies from silicon-infiltrated, reaction-bonded silicon carbide*. US4572848A (Patent) 1983.
- [9] Brogan C. *Experts build pulsed air rig to test 3D printed parts for low carbon engines*. Available from: <http://www.imperial.ac.uk/news/186572/experts-build-pulsed-test-3d-printed/> [Accessed 19th June 2018].

### **Правила подготовки статей:**

Рукопись (**английский язык, MS Word и копия PDF**) должна быть направлена в редакцию журнала по электронной почте: **mpmjournal@spbstu.ru**.

После подтверждения принятия статьи в печать, авторы должны отправить подписанные:

1. Соглашение о передаче авторских прав (<http://www.mpm.spbstu.ru>, раздел «Авторам»);
2. Экспертные заключения о том, что материалы статьи не содержат сведений, составляющих государственную тайну, и информацию, подлежащую экспортному контролю; по адресу:

*Россия, 195251, Санкт-Петербург, Политехническая, д. 29, Санкт-Петербургский политехнический университет Петра Великого, Институт передовых производственных технологий, Редакция периодических изданий.*

Скан-копии подписанных документов просим направить по электронной почте: **mpmjournal@spbstu.ru**

### **Тип файла:**

Редакция принимает **файлы MS Word с копией в формате PDF**. Статья должна быть подготовлена в соответствии с настоящей инструкцией, мы просим авторов также следовать более подробным инструкциям на сайте журнала <http://www.mpm.spbstu.ru> в разделе «Авторам».

### **Длина статьи:**

Статья не должна превышать 30 страниц формата А4, включая Таблицы и Рисунки, размещенные непосредственно в соответствующих местах.

### **Общие правила оформления статьи:**

**НАЗВАНИЕ СТАТЬИ: ВЫРОВНЯТЬ ПО ЦЕНТРУ,**

**ШРИФТ, TIMES NEW ROMAN 14 BOLD, ЗАГЛАВНЫЕ БУКВЫ**

Автор(ы): **А.Б. Первыйавтор<sup>1</sup>, В.Г. Автор<sup>2\*</sup>** - шрифт Times New Roman 12, bold, по центру

<sup>1</sup>Наименование организации, адрес, страна - шрифт Times New Roman 10, по центру

\* e-mail автора, представившего статью - шрифт Times New Roman 10, по центру

**Аннотация.** Аннотация статьи составляет не более 12 строк. Используйте шрифт Times New Roman 12, одинарный межстрочный интервал.

**Ключевые слова:** укажите ключевые слова после аннотации.

**Как организовать текст статьи.** Используйте шрифт Times New Roman 12, одинарный межстрочный интервал. При необходимости выделить какую-либо информацию используйте *курсив*. Используйте **полужирный** шрифт только для заголовков и подзаголовков.

**Номера страниц.** Пожалуйста, не используйте нумерацию страниц

**Таблицы, Рисунки, Уравнения.** Подробные правила оформления данных элементов статьи приведены в инструкции на сайте журнала <http://www.mpm.spbstu.ru>

### **Литература**

Ссылки приводятся в тексте в квадратных скобках [1,3,5-9]. Стиль оформления ссылок:

[1] Koch CC, Ovid'ko IA, Seal S, Veprek S. *Structural Nanocrystalline Materials: Fundamentals and Applications*. Cambridge: Cambridge University Press; 2007.

[2] Hull D, Bacon DJ. *Introduction to Dislocations*. 5nd ed. Amsterdam: Butterworth-Heinemann; 2011 Available from: <https://www.sciencedirect.com/science/book/9780080966724?via%3Dihub> [Accessed 19th June 2018].

[3] Romanov AE, Vladimirov VI. Disclinations in crystalline solids. In: Nabarro FRN (ed.) *Dislocations in Solids*. Amsterdam: North Holland; 1992;9. p.191-402.

[4] Mukherjee AK. An examination of the constitutive equation for elevated temperature plasticity. *Materials Science and Engineering: A*. 2002;322(1-2): 1-22.

- [5] Soer WA, De Hosson JTM, Minor AM, Morris JW, Stach EA. Effects of solute Mg on grain boundary and dislocation dynamics during nanoindentation of Al–Mg thin films. *Acta Materialia*. 2004;52(20): 5783-5790.
- [6] Matzen ME, Bischoff M. A weighted point-based formulation for isogeometric contact. *Computer Methods in Applied Mechanics and Engineering*. 2016;308: 73-95. Available from: [doi.org/10.1016/j.cma.2016.04.010](https://doi.org/10.1016/j.cma.2016.04.010).
- [7] Joseph S, Lindley TC, Dye D. Dislocation interactions and crack nucleation in a fatigued near-alpha titanium alloy. To be published in *International Journal of Plasticity*. Arxiv. [Preprint] 2018. Available from: <https://arxiv.org/abs/1806.06367> [Accessed 19th June 2018].
- [8] Pollak W, Blecha M, Specht G. *Process for the production of molded bodies from silicon-infiltrated, reaction-bonded silicon carbide*. US4572848A (Patent) 1983.
- [9] Brogan C. *Experts build pulsed air rig to test 3D printed parts for low carbon engines*. Available from: <http://www.imperial.ac.uk/news/186572/experts-build-pulsed-test-3d-printed/> [Accessed 19th June 2018].

# МЕХАНИКА И ФИЗИКА МАТЕРИАЛОВ

51 (1) 2023

Учредители: Санкт-Петербургский политехнический университет Петра Великого,

Институт проблем Машиноведения Российской академии наук

Издание зарегистрировано федеральной службой по надзору в сфере связи,  
информационных технологий и массовых коммуникаций (РОСКОМНАДЗОР),

свидетельство ПИ №ФС77-69287 от 06.04.2017 г.

## Редакция журнала

Профессор, д.т.н., академик РАН, А.И. Рудской – главный редактор

Профессор, д.ф.-м.н., член-корр. РАН, А.К. Беляев – главный научный редактор

Профессор, д.ф.-м.н. И.А. Овидько (1961 - 2017) – основатель и почетный редактор

Профессор, д.ф.-м.н. А.Л. Колесникова – ответственный редактор

Л.И. Гузилова – выпускающий редактор, корректор

## Телефон редакции

+7(812)552 77 78, доб. 224

E-mail: [mpmjourn@spbstu.ru](mailto:mpmjourn@spbstu.ru)

Компьютерная верстка Л.И. Гузилова

---

Подписано в печать xx.xx.2023 г. Формат 60x84/8. Печать цифровая

Усл. печ. л. 10,0. Тираж 100. Заказ \_\_\_\_.

---

Отпечатано с готового оригинал-макета, предоставленного автором  
в Издательско-полиграфическом центре Политехнического университета Петра  
Великого. 195251, Санкт-Петербург, Политехническая ул., 29.

Тел.: +7(812)552 77 78, доб. 224.





<b>Epitaxial stabilization of <math>\alpha</math>-Ga<sub>2</sub>O<sub>3</sub> layers grown on r-plane sapphire</b> V.I. Nikolaev, A.Y. Polyakov, S.I. Stepanov, A.I. Pechnikov, L.I. Guzilova, M.P. Scheglov, A.V. Chikiryaka	<b>1-9</b>
<b>Deformations properties of glassy epoxy doped with SiO<sub>2</sub> and Al<sub>2</sub>O<sub>3</sub> nanoparticles of different synthesis methods</b> V. Syzrantsev	<b>10-18</b>
<b>Effect of nickel incorporation on structural and optical properties of zinc oxide thin films deposited by RF/DC sputtering technique</b> Mohibul Khan, Md Shahbaz Alam, Sk. Faruque Ahmed	<b>19-32</b>
<b>Deformation and Heat-Insulating Characteristics of Light Concrete on Porous Burned Binder Under Heating</b> V.T. Erofeev, S.A. Korotaev, N.I. Vatin	<b>33-41</b>
<b>Wave propagation in a nonlocal rotating micropolar piezoelectric solid</b> Baljeet Singh, Asha Sangwan, Jagdish Singh	<b>42-60</b>
<b>Simulation of the plastic deformation of shape memory alloys considering shear anisotropy on the slip plane</b> F.S. Belyaev, M.E. Evard, A.E. Volkov	<b>61-67</b>
<b>On the unloading dynamics in an elastic/viscoplastic material predeformed by viscometric twisting</b> A.A. Burenin, E.A. Gerasimenko, L.V. Kovtanyuk	<b>68-83</b>
<b>Gas-abrasive wear of shut-off valves and process piping of compressor and gas distribution stations</b> O.Yu. Elagina, A.G. Buklakov, Yu.S. Dubinov, D.V. Dedok	<b>84-92</b>
<b>Diffusion-induced stresses due to an impulsive mass source under non-Fickian mass transfer models</b> M. Fayik, A.R. El-Dhaba, E. Awad	<b>93-107</b>
<b>Mechanical properties and deformation curves of the 3D-printed polycarbonate</b> I.K. Andrianov, S.I. Feoktistov	<b>108-118</b>
<b>Mechanical and microstructural characteristics of underwater friction stir welded AA 6061-T6 joints using a hybrid GRA-artificial neural network approach</b> Kiran Wakchaure, Ajaykumar Thakur	<b>119-141</b>
<b>Effect of Mechanical Properties of AL7075/Mica Powder Hybrid Metal Matrix Composite</b> K. Arunprasath, P. Amuthakkannan, M. Vijayakumar, R. Sundarakannan, M. Selwin, S. Kavitha, Lavish Kumar Singh	<b>142-150</b>
<b>Effect of compression precracking on near threshold region for AISI 4340 steels considering compliance measurements</b> Salim Çalışkan, Rıza Gürbüz	<b>151-167</b>
<b>Mechanical properties of a soil improved with recycled demolition concrete for the construction of shallow foundations</b> S.P. Munoz Perez, T.M. Salazar Pretel, L.I. Villena Zapata	<b>168-178</b>